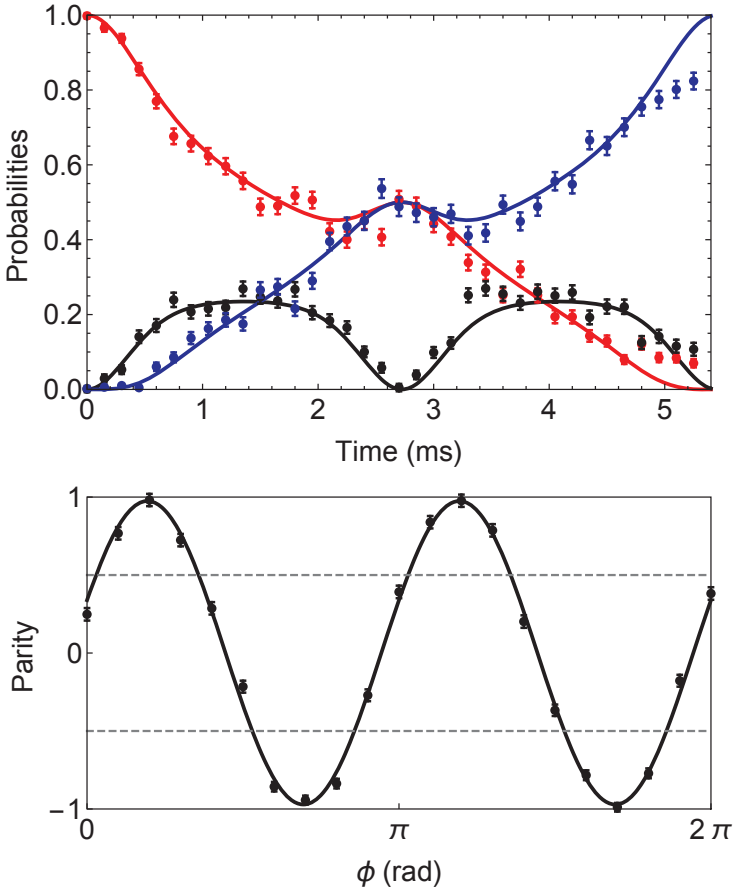
High-Fidelity Entanglement of Trapped Ions using Long-Wavelength Radiation



Joseph Aidan Delf Randall

Department of Physics

Imperial College London

Submitted for the degree of

Doctor of Philosophy

February 2016

Declaration

I hereby declare that except where specific reference is made to the work of others, the contents of this thesis are original and have not been submitted in whole or in part for consideration for any other degree or qualification in this, or any other university.

Joseph Aidan Delf Randall
February 2016

The copyright of this thesis rests with the author and is made available under a Creative Commons Attribution Non-Commercial No Derivatives licence. Researchers are free to copy, distribute or transmit the thesis on the condition that they attribute it, that they do not use it for commercial purposes and that they do not alter, transform or build upon it. For any reuse or redistribution, researchers must make clear to others the licence terms of this work.

Abstract

This thesis describes experimental work in which the spin and motional states of one and two trapped atomic ions are manipulated with long-wavelength radiation in the microwave and radio frequency (RF) regime. This allows single- and two-qubit quantum logic gates to be implemented with long-wavelength radiation, in contrast to laser frequency radiation used in the majority of work to date. The two-qubit gate scheme developed represents a significant advance towards a large scale quantum computing architecture in which laser light is not needed for coherent manipulation.

An experimental setup is built in which a macroscopic linear Paul trap is fitted with permanent magnets to create a strong axial magnetic field gradient. This addition allows the spin and motional states of the ions to be coupled using long-wavelength radiation. The coherence time of qubits that are sensitive to the magnetic field gradient is increased by nearly three orders of magnitude with the use of dressed states and the lifetime and coherence time are measured to be $T_1 = 0.63(4)\,\mathrm{s}$ and $T_2 = 0.65(5)\,\mathrm{s}$, respectively. Using the dressed-state qubit, sideband cooling of a single ion to the motional ground state is demonstrated, and the final mean phonon number after cooling is measured to be $\bar{n} = 0.13(4)$. Finally, a two-qubit gate is demonstrated using the dressed-state qubits in conjunction with the magnetic field gradient, and a Bell state fidelity of $\mathcal{F}_{\mathrm{Bell}} = 0.985(12)$ is determined. This is a significant increase in fidelity for a two-qubit gate based on long-wavelength radiation compared to previous work. The errors are analysed and it is shown that with the next generation of microfabricated traps being developed in the group, the gate fidelity using this scheme can be pushed far into the fault tolerant regime. This makes this scheme promising as an integral part of a large scale quantum computing architecture.

Acknowledgements

I would like to thank my supervisor Prof. Winfried Hensinger for playing a major part in my development so far as a physicist. During my undergraduate degree, with his encouragement and guidance, I secured funding through the junior research associate scheme for a summer placement in the group, which I then followed with a final year project. With his help, I then managed to get a place in the controlled quantum dynamics centre for doctoral training (CDT) in Imperial College, which allowed me to develop essential skills for my PhD. Throughout my PhD, Winfried has offered advice and enthusiasm that helped me see my work through to the end, and my thanks go to him for everything. Next I would like to thank Dr. Seb Weidt, my 'other supervisor', who has been my first point of contact since my undergraduate placement. In my final year undergraduate project four years ago, Seb and I thought a lot about the little known scheme to entangle ions using a magnetic field gradient, and from then until the point a few months ago when we managed to implement the scheme in the lab, Seb has been an invaluable colleague. His motivation and enthusiasm are unrivalled, and without his attention to detail and forward planning, we would probably still be waiting for the magnets to arrive. Thanks to Dr. Simon Webster for being the 'go-to guy' for any difficult (or not so difficult) physics questions, whose knowledge and experience in quantum and atomic physics has been a huge help to me. Thanks also to him for reading my thesis and giving me helpful and critical feedback. Thanks to Tomas 'T.J' Navickas for fixing the locking at the drop of a hat and making working in the lab fun. Thanks to David Murgia, the other Imperial guy, for bringing a great atmosphere to the team, from the after lunch espressos to the big nights out. Thanks to Anna Webb for her brilliant job in mastering the experiment so far, and for her upbeat attitude even when everything is going wrong. I look forward to working with her in experiments to come. Thanks also to Eamon Standing and Dr. Kim Lake, who worked on the experiment when we first put the magnets in and made the shifts entertaining and enjoyable. Thanks to the old guys who were there when I started in the lab to advise me and who got the experiment up and running in the first place: Dr. James Siverns, Dr. James McLoughlin, Dr. Robin Sterling, Dr. Altaf

Nizamani, Dr. Marcus Hughes, Darren De Motte, Dr. Gouri Giri and especially Dr. Bjoern Lekitsch who has always been willing to give me plenty of help and advice on electronics and technology in the lab. Thanks also to the new(ish) guys: Anton Grounds, Ethan Potter, Andrea Rodriguez Blanco, Weikang Fan and Adrian Parra Rodriguez for their help and advice over the past year, and also Nikolaus Lorenz for reading my thesis and providing insightful comments. Thanks also to my second supervisor Prof. Myungshik Kim, as well as the others in cohort 3 of the CDT, aka 'wundercohort': Howard Dale, Devin Dunseith, Mercedes Gimeno-Segovia, Darren Holland, Jake Iles-Smith, Kyle Major, Mark Mitchison, Naomi Nickerson, Emilio Pisanty Alatorre, Andre Ranchin and Mihai-Dorian Vidrighin for the many discussions on the foundations of quantum physics, as well as quantum drinking games. Having a connection with a group of physicists studying related but slightly different topics has been invaluable for broadening my understanding of the quantum information and atomic physics research community, and I would recommend this route to anyone thinking of doing a PhD. Further thanks to Prof. Terry Rudolph and Prof. Danny Segal for creating the CDT along with Myungshik, accepting me into it, and for teaching me a small part of what they know. Additionally I would like to thank my family and friends for all their support during my PhD. To my mum Regan, dad Chris and sister Mairead, thanks for all of your love and support, and for regularly listening to me talk about whatever had happened in the lab over the last week or two. Thanks also to my nans Jeanne and Pat, aunt Angela, uncle Steve and cousins Harri, Eve and Fred for their support over the past years. Finally, thanks to Lucy, who has been there for me through my whole time at university, never complained if I worked late in the lab, and made my life outside of the lab a whole lot more enjoyable.

Publications

- **Generation of spin-motion entanglement in a trapped ion using long-wavelength radiation**

  K. Lake, S. Weidt, J. Randall, E. D. Standing, S. C. Webster, and W. K. Hensinger, Phys. Rev. A 91, 012319 (2015)

- **Efficient preparation and detection of microwave dressed-state qubits and qutrits with trapped ions**

  J. Randall, S. Weidt, E. D. Standing, K. Lake, S. C. Webster, D. F. Murgia, T. Navickas, K. Roth, and W. K. Hensinger, Phys. Rev. A 91, 012322 (2015)

- **Ground-State Cooling of a Trapped Ion Using Long-Wavelength Radiation**

  S. Weidt, J. Randall, S. C. Webster, E. D. Standing, A. Rodriguez, A. E. Webb, B. Lekitsch, and W. K. Hensinger, Phys. Rev. Lett. 115, 013002 (2015)

Table of contents

List of figures **15**

List of tables **19**

1 Introduction **21**

1.1 Quantum computing . . . 23

1.1.1 Requirements for a quantum computer . . . 25

1.1.2 Trapped ions . . . 26

1.2 Trapped ion quantum computing with long-wavelength radiation . . . 28

1.2.1 Issues with using long-wavelength radiation . . . 29

1.2.2 The static magnetic field gradient scheme . . . 30

1.3 Summary of the thesis . . . 32

2 Background and Experimental Setup **33**

2.1 Introduction . . . 33

2.2 Trapped ion basics . . . 33

2.2.1 Trapping ions . . . 33

2.2.2 Normal modes of a trapped ion string . . . 36

2.2.3 Trapped ion qubits . . . 39

2.3 Energy level structure of $^{171}Yb^{+}$ . . . 43

2.3.1 Ionisation . . . 43

2.3.2 Doppler cooling . . . 44

2.3.3 $^{2}S_{1/2}$ ground state . . . 45

2.4 Experimental setup . . . 47

2.4.1 Ion trap . . . 47

2.4.2 Optical setup . . . 51

2.4.3 Microwave and RF setup . . . 55

2.5 Initial experiments . . . 59

2.5.1 Initial trapping and cooling . . . 59

2.5.2 State preparation and detection . . . 60
2.5.3 Rabi oscillations . . . 66
2.5.4 Magnetic field noise . . . 68
2.5.5 Magnetic field drifts . . . 69
2.5.6 Maximising the magnetic field gradient . . . 72

3 Coupling spin and motion with a magnetic field gradient 75
3.1 Introduction . . . 75
3.2 Spin-motion coupling with a single ion . . . 76
3.2.1 Spin-motion coupling with photon momentum . . . 76
3.2.2 Spin-motion coupling with a magnetic field gradient . . . 80
3.2.3 The effective Lamb-Dicke parameter . . . 84
3.2.4 Driving motional sidebands with microwaves . . . 86
3.3 Multiple ions in a magnetic field gradient . . . 88
3.3.1 Individual addressing . . . 88
3.3.2 Generalising spin-motion coupling to multiple ions . . . 91
3.3.3 Spin-spin coupling . . . 96

4 Dressed states 99
4.1 Introduction . . . 99
4.2 Dressed state theory . . . 100
4.2.1 Dressing a two-level atom . . . 100
4.2.2 Adding an auxiliary state . . . 105
4.2.3 Dressed states with three levels . . . 107
4.3 Dressed states in $^{171}Yb^{+}$ . . . 112
4.3.1 Magnetic field noise in $^{171}Yb^{+}$ . . . 116
4.3.2 Preparation and detection of the dressed system . . . 120
4.3.3 Individual addressing of the clock transitions . . . 123
4.3.4 T_1 and T_2 time measurements . . . 124
4.4 Combining dressed states with a magnetic field gradient . . . 128
4.4.1 Dressed states in a magnetic field gradient . . . 128
4.4.2 Dressed spin-spin coupling . . . 131
4.4.3 Dressed state sidebands . . . 132

5 Sideband cooling 135
5.1 Introduction . . . 135
5.2 Doppler cooling . . . 136
5.3 Measuring the temperature . . . 137

5.4 Sideband cooling . . . 139
5.4.1 Sideband cooling with dressed states . . . 143
5.4.2 Heating . . . 145
5.4.3 Sideband cooling two ions . . . 147

6 Two ion entanglement 151
6.1 Introduction . . . 151
6.2 Spin-motion entanglement with a single ion . . . 152
6.2.1 The Mølmer-Sørensen interaction . . . 152
6.2.2 Spin-motion entanglement with the dressed-state qubit . . . 157
6.3 Two-ion entanglement . . . 159
6.3.1 Mølmer-Sørensen interaction for multiple ions . . . 159
6.3.2 Sources of Error . . . 166
6.3.3 Experimental Results . . . 180

7 Conclusion 187
7.1 Summary . . . 187
7.2 Future work . . . 189
7.3 Scalability . . . 190

References 197

Appendix A Pure dephasing of a driven two-level atom 205

Appendix B Normalising detection errors 209
B.1 Single ion . . . 209
B.2 Two ions . . . 210
B.3 Probability estimation and errors . . . 211

Appendix C Magnus Expansion 213

Appendix D Gate recipe 215

List of figures

2.1 Diagram of a linear Paul trap . . . 34
2.2 The potential felt by two ions . . . 37
2.3 Normal modes of a two ion string . . . 38
2.4 Single qubit rotations on the Bloch sphere . . . 42
2.5 State probabilities for the two-level Rabi problem . . . 42
2.6 Two-photon ionisation process for ytterbium . . . 44
2.7 Energy level structure of $^{171}Yb^{+}$ . . . 45
2.8 $^{2}S_{1/2}$ ground state manifold of $^{171}Yb^{+}$ . . . 46
2.9 Schematic of the ion trap . . . 48
2.10 Diagram of the magnets used to create a magnetic field gradient . . . 50
2.11 Schematic of the optical setup . . . 53
2.12 Schematic of the RF and microwave setup . . . 57
2.13 CCD images of trapped ion strings . . . 60
2.14 Optical pumping for state preparation . . . 62
2.15 Single ion state detection histograms . . . 63
2.16 Two ion state detection histograms . . . 65
2.17 Frequency and time scans demonstrating Rabi oscillations on the $|0\rangle \leftrightarrow |0'\rangle$ clock transition . . . 67
2.18 Rabi oscillation on the $|0\rangle \leftrightarrow |+1\rangle$ magnetic field sensitive transition . . . 70
2.19 Magnetic field drift due to running the atomic ovens . . . 71
2.20 Stabilising the magnetic field to an atomic transition . . . 71
2.21 Maximising the magnetic field gradient . . . 73

3.1 Illustration of red and blue sideband transitions . . . 78
3.2 The Lamb-Dicke parameter as a displacement of the harmonic oscillator wavefunctions . . . 79
3.3 The effect of a magnetic field gradient on a single ion . . . 82
3.4 Motional sidebands in a single ion . . . 87

3.5 Individual addressing of two ions in frequency space 90
3.6 Motional sidebands for two ions 95
3.7 Spin-spin coupling due to the magnetic field gradient 96

4.1 Two level dressed states 100
4.2 Eigenenergies and populations for the two level dressed system 102
4.3 Coupling an auxiliary state to the two level dressed system 106
4.4 Three level dressed states 108
4.5 Eigenenergies and populations for the three level dressed system . . . 110
4.6 Coupling an auxiliary state to the three level dressed system 111
4.7 Dressed states in $^{171}Yb^{+}$ 113
4.8 The effect of magnetic field noise on the dressed system 117
4.9 Illustration of the insensitivity of the dressed state qubit to magnetic field drifts 119
4.10 Preparation and detection method for the dressed states 120
4.11 Frequency scan of the dressed state transitions and Rabi oscillation on the $|0'\rangle \leftrightarrow |D\rangle$ transition 122
4.12 Individual addressing of the clock transitions for two ions in frequency space 124
4.13 Lifetime measurement of $|D\rangle$ 125
4.14 Coherence time measurement of the dressed-state qubit 126
4.15 Spin-spin coupling in the dressed states 132
4.16 Motional sidebands in the dressed states 134

5.1 Measuring the ion temperature using a sideband interaction 138
5.2 Illustration of a sideband cooling experiment using long-wavelength radiation 140
5.3 Simulated motional state populations after sideband cooling 141
5.4 Demonstration of ground state cooling 144
5.5 Heating rate measurement 146
5.6 Rabi oscillations on the sidebands after ground state cooling 147
5.7 Ground state cooling and heating rate measurement for the stretch mode of two ions 148

6.1 Internal and motional state evolutions for the Mølmer-Sørensen interaction with a single ion 153
6.2 Theoretical spin state probabilities for the Mølmer-Sørensen interaction with a single ion 156

6.3 Demonstration of the Mølmer-Sørensen interaction with a single ion . 158
6.4 Internal and motional state evolutions for the Mølmer-Sørensen interaction with two ions 160
6.5 Reduced density matrix evolution and spin state populations for the Mølmer-Sørensen interaction with two ions 164
6.6 Gate infidelity due to motional heating 167
6.7 Gate infidelity due to depolarisation 170
6.8 Effect of amplitude modulating the Rabi frequency for a two-level system 171
6.9 Infidelity as a function of window length t_w for an amplitude shaped pulse 173
6.10 Demonstration of pulse amplitude shaping with the dressed-state qubit 174
6.11 Gate infidelity due to a mis-set symmetric detuning 174
6.12 Gate infidelity due to a mis-set asymmetric detuning 176
6.13 Gate infidelity due to Kerr coupling between the axial stretch and radial rocking modes 177
6.14 Gate infidelity due to spin-spin coupling 178
6.15 Total gate infidelity as a function of trap frequency for the two axial modes 180
6.16 Measured populations for the Mølmer-Sørensen interaction applied to two ions 182
6.17 Parity as a function of the phase of a carrier $\pi/2$ pulse applied after the Mølmer-Sørensen gate 183

7.1 X-junction in a scalable quantum computing architecture 191
7.2 Example experimental sequence to implement simultaneous single qubit gates in the scalable architecture. 192
7.3 Dressed-state qubits with local magnetic fields 195

A.1 Evolution of the density matrix for a driven two-level system undergoing dephasing 208

List of tables

4.1 Approximate functions for the magnetic field sensitivity of the dressed states 118

6.1 Error budget for the two-qubit gate 185

Chapter 1

Introduction

The advent of electronic computing technology over the past 50 years has revolutionised the modern world. The processing and storage capacities of modern computers have increased rapidly since the invention of the transistor in 1947, with the density of transistors in a circuit roughly doubling every two years according to Moore's law [1, 2]. Supercomputers represent the forefront of computational processing power, reaching up to 33.86 petaFLOPS (quadrillion floating point operations per second) at the time of writing [3], and are essential for many computationally intensive tasks such as climate modelling, code breaking and molecular dynamics as well as biological simulations. Despite the impressive increase in processing power over the years, many tasks are out of reach of being computable in the foreseeable future, and therefore new computing technologies that offer an increase in processing capacity are highly desirable.

A fundamental feature of the theory of information is the fact that it can be abstracted away from a physical device. The basic component of an information processor is a bit, labelled b, which can be in one of two states 0 or 1. In reality, the bits will be encoded in a physical system such as the beads on an abacus or the voltage of a transistor, but these details are unimportant as long as a small set of operations, such as 'flipping' the bit between 0 and 1, can be carried out. Although the details of the physical system used for the computation are not required for the theory, it does assume that the bits are classical systems that can be in one of two macroscopically distinct states. However, it is known that the world is quantum, and therefore a system that has two distinct states also has the potential to be in a linear superposition of the two states according to quantum theory. It was for this reason that in 1982, Richard Feynman suggested that controllable quantum systems may be useful for simulating other quantum systems, and thereby gave rise to the

field of quantum simulation [4].

The advantage of quantum information processing compared to classical becomes apparent when considering the numerical simulation of a quantum many-body system. In many fields of research a simulation may need to consider the quantum degrees of freedom of a system containing many thousands of atoms or molecules, such as the simulation of chemical reactions or of the properties of a material. If these systems consist of N spin-1/2 particles (which is an oversimplification in most cases), in general $O(2^N)$ bits are required to store the quantum state of the overall system in a classical memory. Furthermore, to solve the Schrödinger equation and thereby find the time evolution for such a system requires exponential time with system size N for a classical computer. This unfavourable scaling means that many approximations have to be made in order to be able to simulate a quantum many-body system larger than a few tens of spin-1/2 particles on a classical supercomputer, severely limiting the scope of problems that can be tackled. A quantum system on the other hand has the same scaling with system size as the problem to be simulated for the same reasons. This makes such a quantum processor inherently more efficient for simulating a quantum many-body system. If a quantum processor consisting of two-level quantum bits, or 'qubits', can be created and controlled in such a way that the desired unitary evolution for a simulation is carried out, a quantum many-body system consisting of N spin-1/2 particles can be simulated with only $O(N)$ qubits, a much more favourable scaling. In the same way as with classical information, quantum information theory is independent of the physical system considered, and could be implemented in a range of systems that can demonstrate the required basic operations.

Besides the clear advantage of simulating a quantum-many body system with another controlled quantum system over that of a classical computer, quantum information processors have other advantages that are less immediately apparent. In 1985, Deutsch showed that an arbitrary unitary operator acting on N qubits can be decomposed into a sequence of 'quantum gates' acting on small numbers of qubits [5]. Such a quantum processor that can be programmed to carry out arbitrary unitary evolution is known as a 'universal' quantum computer, as opposed to a processor that can only perform a particular evolution such as a quantum simulator. A quantum algorithm involves applying a sequence of operations to a number of qubits in a universal quantum computer, and can offer substantial speed advantages compared to equivalent classical algorithms with the same goal. The most famous example is Shor's algorithm, which allows a large number to be factorised in polynomial time (i.e. the time to factorise the number is a polynomial

function of its length n) [6]. This problem is thought to be exponentially hard with a classical computer, and is used as the basis of some encryption techniques for secure data transmission. Furthermore, quantum computing has been shown to offer significant speedup for search and optimisation algorithms compared to the best known algorithms in classical computers [7], providing motivation for many disciplines in science and industry.

Motivated by the applications of quantum information processing discussed so far, a basic outline of how quantum computing works will be given in the following sections, as well as the requirements to build a quantum computer experimentally, and it will be shown how these requirements can be met using trapped atomic ions.

1.1 Quantum computing

An ideal quantum bit, or qubit, is a two-level quantum system that is perfectly isolated from its surroundings and can be manipulated perfectly by some external control. We can write the state of the qubit in terms of two basis states which can be labelled $|0\rangle$ and $|1\rangle$ in analogy with a classical bit. An arbitrary state of the system is then $|\psi\rangle = \alpha|0\rangle + \beta|1\rangle$, where α and β are complex coefficients and $|\alpha|^2 + |\beta|^2 = 1$. It is immediately apparent from this definition that quantum information is fundamentally different from classical information, as the coefficients α and β are continuous variables, unlike the discrete states of a classical computer. An operation on a qubit is then a unitary operator that manipulates the state in a particular way, which can be rephrased as a single qubit gate in analogy with a single bit gate in classical information processing. The equivalent of a NOT gate in QIP is a σ_x operator, which applies the unitary $U_x = \sigma_x = |0\rangle\langle 1| + |1\rangle\langle 0|$ to the qubit. The phase-flip gate $U_z = \sigma_z = |0\rangle\langle 0| - |1\rangle\langle 1|$ does not have a classical analogue, and flips the relative phase of a superposition of the two basis states.

The gate model of QIP is the most widely used and has a close analogy with the logic gate methods used to process information in classical computers. Other methods also exist, such as cluster state quantum computing and adiabatic quantum computing, which can offer some advantages compared to the gate model for certain implementations. In the gate model, small subsets of qubits are manipulated in order to perform quantum logic gates, which can be built up into an algorithm. As mentioned previously, Deutsch showed that an arbitrary unitary operator can be decomposed into a sequence of gates out of a set including a number of single qubit gates as well as one gate acting on two qubits [5]. The two-qubit gate must be

capable of creating maximally entangled Bell states, and a commonly used gate that fulfils this requirement is the controlled-not (CNOT) gate, defined by the unitary operator

$$U_{\mathrm{CNOT}} = |00\rangle\langle 00| + |01\rangle\langle 01| + |10\rangle\langle 11| + |11\rangle\langle 10|\,. \tag{1.1}$$

The CNOT gate can be thought of as having a 'control' and 'target' qubit. If the control qubit is in the state $|0\rangle$, the gate does nothing, whereas if the control qubit is in the state $|1\rangle$, the target qubit is flipped. If the control qubit is prepared in the equal superposition state $(|0\rangle + |1\rangle)/\sqrt{2}$ and the target qubit is prepared in $|0\rangle$, the output state after application of the CNOT gate is $(|00\rangle + |11\rangle)/\sqrt{2}$, which is a maximally entangled Bell state. Therefore, if all of the basic gates can be performed on small sets of one or two qubits perfectly, an arbitrarily large unitary evolution on an arbitrarily large number of qubits can theoretically be constructed.

So far, we have assumed that all operations are free from error. In reality, all quantum systems will be coupled to their surroundings at some level, and no experimental control parameters to implement the quantum gates can be set perfectly. Therefore there will always be some error in the operations applied to the qubits. Furthermore, due to the continuous nature of quantum states, small errors in a single gate will add when performing multiple gates, and so at first it would naïvely seem that a quantum algorithm would quickly fail as the number of gates is increased. In classical computation, information is protected from errors using redundancy, where for example a single bit is encoded in three identical bits. The three bits are then periodically checked throughout an algorithm and if they do not all read the same value due to an error, the majority value will be taken and all three bits will be reset to this value. If the probability for an error during the interval between the bits being checked is ϵ, this error correction scheme reduces the probability to ϵ^2, the probability for two errors to occur. Adding further bits would then reduce the error further. The same approach cannot be taken in quantum computing however as the no-cloning theorem forbids quantum states to be copied and measurement of a quantum system collapses the state. Fortunately, in 1996, it was shown that a quantum version of error correction can be achieved [8, 9]. Rather than copying the individual qubits to achieve redundancy, the quantum information is instead spread over many qubits in an entangled state. For example an arbitrary superposition state $\alpha|0\rangle + \beta|1\rangle$ could be encoded in many qubits as $\alpha|00...0\rangle + \beta|11...1\rangle$. The states $|0_L\rangle \equiv |00...0\rangle$ and $|1_L\rangle \equiv |11...1\rangle$ are then the states of the 'logical' qubit that can be protected from errors. To detect and correct for errors without destroying the

quantum state, a particular type of measurement, known as a syndrome measurement, can be performed that reveals the type of error and which qubit was affected without revealing the actual state of the qubits. With this information, an extra gate can be applied to the affected qubit, thereby correcting for the error and consequently protecting the quantum information. In order to perform such error correction, many operations must be performed in order to create the logical qubits, detect any errors and correct for them. If the errors of each of the required operations are below a certain 'threshold' value, the error correction corrects for errors faster than they occur, and hence the computation becomes 'fault-tolerant'. The exact value of the threshold depends on the error correction scheme used and the number of qubits making up each logical qubit, and is usually in the range 10^{-4} to 10^{-2} [10–12]. This then provides a target regime to be reached for any experimental demonstration of a quantum operation.

1.1.1 Requirements for a quantum computer

From the previous section it is possible to obtain a basic understanding of the requirements that may be needed for a physical implementation of a quantum computer following the gate model. A system in which qubits can be prepared, manipulated and measured should be identified, and these operations should be performed with errors small enough to be compatible with quantum error correction schemes. There should also be a deterministic way to couple the qubits together in pairs in order to perform the required two-qubit gates. These requirements were formalised by DiVincenzo in 2000 and are reproduced from Ref. [13] in the following for convenience:

1. A scalable physical system with well characterised qubits,
2. The ability to initialise the state of the qubits to a simple fiducial state, such as $|000...\rangle$,
3. Long relevant decoherence times, much longer than the gate operation time,
4. A "universal" set of quantum gates,
5. A qubit-specific measurement capability.

The first point simply states that the chosen system should contain two quantum states that can be isolated from other states to make a qubit. So for example a quantum harmonic oscillator would not be a good system for a qubit as all the states

are equally spaced in energy and hence two levels cannot be addressed individually. Furthermore, the system should be scalable to many qubits. The second point refers to the fact that most quantum systems in a thermal environment will be in a mixed state, and so a procedure to 'purify' the qubits should be available. The third point says that the decoherence times for the qubits must be much longer than the gate times. This ensures that the errors for each gate will be low, which as stated previously is a requirement for fault-tolerant quantum computation. The fourth point ensures that all of the required gates outlined by Deutsch for a universal quantum computer can be carried out and finally the fifth point requires that each qubit can be measured independently from the other qubits. This is required for the error correction syndrome measurements as discussed previously and also for reading the output after performing a quantum algorithm.

The DiVincenzo criteria summarise the requirements for a physical implementation of a quantum computer. Many possible implementations are being investigated experimentally including neutral atoms [14], ions [15], photons [16], superconducting qubits [17] and quantum dots [18] (for a review and comparison, see Ref. [19]). Trapped ions are one of the most mature implementations and many fundamental demonstrations of the basic operations required for quantum computation have been demonstrated using them. In the following section, a background of trapped ions for quantum computing will be given and it will be shown how they meet all of the DiVincenzo criteria.

1.1.2 Trapped ions

Trapped atomic ions have many features that are ideal for quantum information purposes, and their potential as candidates for a large scale quantum computer was soon realised after the work of Deutsch and Shor. Ion trap experiments are conducted in ultra-high vacuum (UHV) environments and ions can be trapped by electric fields, meaning they are very well isolated from potential sources of noise. Ions were first laser cooled in 1978 [20], and soon after a single ion [21] and small ion crystals [22] were trapped. The large trap potentials that can be created for charged ions combined with strong laser cooling results in long ion lifetimes of days or weeks, which is useful for robust storage of quantum information. Qubits can be stored in the internal electronic states of 'alkali-like' ions containing one electron in the valence shell, and if a single isotope and species of ion is used, the qubits are perfectly identical. Examples of commonly used ions include $^{9}Be^{+}$, $^{25}Mg^{+}$, $^{43}Ca^{+}$, $^{87}Sr^{+}$, $^{137}Ba^{+}$ and $^{171}Yb^{+}$. The qubits can be prepared in a pure state using

optical pumping, and single qubit rotations can be performed using electromagnetic radiation near resonant with the qubit energy splitting. Measurements can be made using state-selective fluorescence, where photons are only scattered by the ion and subsequently detected if it is in one of the qubit states. To couple ions together, the Coulomb coupling between them can be utilised. Small numbers of ions in a shared trap form structures known as Coulomb crystals, which exhibit collective normal modes of motion. When cooled sufficiently, these motional modes can be well approximated as independent quantum harmonic oscillators. By coupling the qubits to such shared motional quantum states, a link between different qubits is formed which can be used to implement the required two-qubit gates. The first theoretical proposal showing how a two-qubit gate could be implemented in such a system was outlined by Cirac and Zoller in 1995 [15].

In 2002, Kielpinski et al. discussed how trapped ion quantum information processing could be scaled to many ions using a 2D array of connected ion trap structures in a 'quantum charge-coupled device' (QCCD) architecture [23]. The architecture would involve different 'zones' where different operations would occur. Trapped ion qubits would be stored, processed and detected in dedicated zones in the array, and shuttled between zones. This would require ions to be separated, shuttled through junctions and recombined. Alternative methods to scale ion trap quantum information processing have also been suggested, including schemes in which the ions are not shuttled but instead coupled to photons, which can then be interfered to create entanglement between ions that are located in different traps [24].

Many of the required proof-of-principle demonstrations have been carried out over the past three decades. Quantum jumps were first observed in a single ion in 1986 [25], demonstrating that the quantum state of a single atom can be detected. Following this in 1989, it was demonstrated that the motional states of a trapped ion could be cooled to the ground state using a technique known as sideband cooling [26]. Next, the first demonstration of a two-qubit quantum logic gate between the internal states of a single ion and the two lowest energy states of one of its motional modes was performed [27]. In 1998, the first demonstration of deterministic entanglement between two trapped ion qubits was presented [28]. These demonstrations followed the ideas of Cirac and Zoller in Ref. [15], which involved cooling the motional mode used to the ground state. In 1999, new theoretical methods were developed by both Mølmer and Sørensen [29–31] and Milburn [32], in which geometric phases were used to implement a two-qubit gate that is independent of the initial motional state, even if it is a mixed thermal state. These schemes considerably eased some of the challenges towards achieving high fidelity two-qubit gate operations. The Mølmer-Sørensen

scheme was demonstrated experimentally in 2000 with the entanglement of four ions [33]. In 2003, a two-qubit gate based on the ideas of using geometric phase was demonstrated with a fidelity of 0.97 [34]. The required ion transport operations have also been demonstrated including shuttling around a corner [35] and through an X-junction [36], as well as fast transport, separation and recombination [37, 38].

Currently many of the required operations have been demonstrated in trapped ions with fidelities at or close to that required for fault tolerant quantum computing. State preparation and readout have been demonstrated with a fidelity of 0.9993 [39], single qubit gates with a fidelity of 0.999999 [39] and a two-qubit gate with a fidelity of 0.999 [40]. Therefore with the combination of methods so far reported, all of the requirements presented by DiVincenzo have been met with trapped ions. The remaining challenge, as will be discussed in the following section, is scaling these proof-of-principle experiments to a large number of ions in order that useful quantum computations can be carried out.

1.2 Trapped ion quantum computing with long-wavelength radiation

There are two types of qubits commonly used in trapped ion quantum information experiments. The first are optical qubits, which consist of two states that are separated in energy by an amount corresponding to a frequency in the optical regime. Typically, the $S \leftrightarrow D$ transition in alkali-like ions is chosen due to the relatively long lifetime of the D state (typically around 1 second). To drive coherent rotations between the two states to perform quantum logic gates, a laser with a linewidth similar to the natural linewidth of the transition ($\approx 1\,\mathrm{Hz}$) must be used. Stabilising a laser to such a linewidth is a large engineering challenge, and combined with the finite lifetime of the upper qubit state, makes this choice of qubit less favourable for achieving high-fidelity gate operations. Single qubit gates for optical qubits have been demonstrated with a fidelity of 0.997 [41]. The second type of qubits commonly used are hyperfine qubits, which consist of two states in the electronic ground state in ion isotopes where the nuclear spin is non-zero, giving rise to states with different F quantum numbers. These states have near infinite lifetimes, giving them a clear advantage compared to optical qubits. For commonly used ion species, the states are typically separated by a few GHz and are therefore in the microwave frequency regime. Coherent rotations can be driven using a microwave source connected to an emitter which broadcasts the radiation over a wide area in space. Microwave

sources typically have frequency stability better than 0.1 mHz, and therefore do not require any additional stabilisation, substantially reducing the engineering overhead compared to laser sources. Single qubit gates in the microwave frequency regime have been demonstrated with a fidelity of 0.999999 [39].

1.2.1 Issues with using long-wavelength radiation

For single qubit gates, hyperfine qubits driven by long-wavelength radiation in the microwave regime have a clear advantage over optical qubits driven by optical radiation. However, as mentioned previously, to implement two-qubit gates the qubits encoded in the internal states should be coupled to the shared motional modes of a multi-ion string. The coupling strength between the internal and motional states is characterised by a parameter known as the Lamb-Dicke parameter (LDP), which if the motion considered is in the z-direction, is given by $\eta_l = z_0|\vec{k}|$, where $z_0 = \sqrt{\hbar/2m\nu_z}$ is the position spread of the ion's ground state wavefunction, m is the ion's mass, ν_z is the trap frequency in the z-direction and $\vec{k}$ is the wavevector of the laser, which is inversely proportional to the wavelength. Rotations between the qubit states that also change the motional state by one quanta will occur with a frequency approximately equal to $\sqrt{n}\eta_l\Omega_0$, where n is the motional quantum number and Ω_0 is the Rabi frequency for a transition that does not change the motional state. For optical frequencies, the LDP is typically on the order 0.1, and consequently the time to make a transition that changes the motional state is approximately 10 times slower than the single qubit gate time. For microwave frequencies however, the LDP is around 10^{-6}, which typically would make two-qubit gate times much slower than the coherence time of the qubits. Therefore an alternative approach has to be taken if hyperfine qubits are to be used for quantum computing.

The most commonly used method that allows two-qubit gates to be performed between hyperfine qubits uses a two-photon Raman transition. In this method, two lasers couple the hyperfine qubit states via a third state by setting the difference frequency to be near resonant with the qubit frequency. The LDP is then proportional to the difference wavevector $\Delta\vec{k}$, which is maximised if the two laser beams are counter-propagating and is of similar magnitude to the case of optical qubits. This therefore allows the advantages of optical radiation and hyperfine qubits to be combined, and two-qubit gates using this method have been demonstrated with a fidelity of 0.999 [40]. Despite these impressive results, such Raman laser gates have disadvantages that could cause issues when scaling to a large number of ions. One issue is off-resonant scattering from the third state. Since the upper state used in

the Raman transition typically has a short lifetime, unwanted scattering events are reduced by detuning the laser by a large amount so that population is only ever virtually excited. However, the effective Rabi frequency between the qubit states decreases with this detuning, and therefore high Raman laser powers ($\approx 5\,\mathrm{mW}$ in Ref. [40]) are needed in order to produce fast, high-fidelity gates. Achieving such high Raman laser powers on a large scale is a substantial engineering challenge. A further issue is maintaining the amplitude and beam pointing stability of the lasers required for high-fidelity gates. Unlike microwave technology, achieving such stability in a laser requires additional work that would be hard to achieve on a large scale. Additionally, ions trapped in a 2D array structure such as that envisioned by Kielpinski would all need to be addressed by individual laser beams which would all have to be carefully aligned. Microwave emitters on the other hand broadcast over a wide area from a distance, allowing all ions to be addressed without the need for such careful alignment. For these reasons, it would be advantageous if microwave frequencies that directly drive the hyperfine qubits could also be used for two-qubit gates, thereby removing the need for optical radiation for any coherent operations in a scalable ion trap quantum computer.

1.2.2 The static magnetic field gradient scheme

In 2001, Mintert and Wunderlich proposed an idea to add a static magnetic field gradient to the ion trap system in order to create a substantial coupling between the qubit states and the ions' motional states using only long-wavelength radiation in the microwave or radio frequency (RF) regime [42]. Such a coupling was demonstrated in 2009 by Johanning et al. [43], and a two-qubit gate using a spin-spin coupling that arises from the gradient was demonstrated in 2012 with a fidelity of 0.64 [44]. An alternative laser-free coupling method was also developed by Ospelkaus et al. in which the ion string is placed close to a microwave waveguide so that it is in the near field of the microwave radiation [45]. Being in the near field causes the ions to experience strong oscillating magnetic field gradients which can also produce the required coupling to the motional states. A two-qubit gate using this method was demonstrated in 2011 with a fidelity of 0.76 [46]. Both of these methods remove the need for coherent manipulation with laser light and therefore are advantageous for scalability, but have some issues that must be resolved if the fidelities are to be increased to the high levels required for fault-tolerant quantum computation. For the oscillating gradient scheme, one issue is that the ions need to be trapped close to the surface of the ion trap chip, which causes the ions' motional states to be heated

at a fast rate which can limit the gate fidelities. A further issue is that due to the geometry of the trap and waveguide structure, the gate must be implemented on the motional modes in the radial direction. The frequency of these modes depends on the amplitude of the required high-power RF voltage creating the trapping potential, which is difficult to stabilise to the level required for high-fidelity gates.

For the static magnetic field gradient scheme, the hyperfine states used for qubit states must be chosen to have different magnetic moments so that the qubit energy splitting is sensitive to magnetic fields. This requirement however also makes the qubit sensitive to magnetic field noise, which causes the coherence time to be significantly reduced compared to qubit states with equal magnetic moments. In 2011, Timoney et al. devised a method to significantly increase the coherence time of qubits formed of states with different magnetic moments using dressed states [47]. Combining this method with the static magnetic field gradient scheme would therefore allow for high-fidelity two-qubit gates to be implemented using long-wavelength radiation. This idea has been the focus of much of the work in our group for the last few years.

In the work described in this thesis, a $^{171}Yb^{+}$ ion trap experiment is developed which incorporates a static magnetic field gradient and uses dressed states to increase the coherence time of magnetic field sensitive qubits. Using this combined approach, a two-qubit gate is performed with a fidelity of 0.985(12) using long-wavelength radiation. This is the highest fidelity two-qubit gate using long-wavelength radiation reported to date by far, and therefore represents a significant advance towards a large scale quantum computing architecture in which laser light is not needed for coherent manipulation. Due to the long coherence time of the qubits formed from the dressed states, magnetic field noise is no longer the dominant error source as in previous two-qubit gate implementations based on the static magnetic field gradient scheme. Consequently, gate fidelities far in the fault-tolerant regime are predicted for the next generation of microfabricated ion traps where much higher magnetic field gradients, and hence much faster two-qubit gate times, can be generated. Furthermore, the gate can form an integral part of a 'blueprint' quantum computing architecture developed in our group [48], based on long-wavelength radiation. An important feature of this architecture is that it removes the correlation between the number of long-wavelength fields applied and the number of qubits. Contrasting to a laser-based architecture, where laser beams would have to be individually aligned to each entanglement zone, this represents a major simplification for the prospects of scaling to a large number of ions. Therefore, the dressed-state two-qubit gate scheme developed in this work is an essential step towards a scalable ion trap quantum computing architecture based on long-wavelength radiation.

1.3 Summary of the thesis

The thesis is structured as follows. In chapter 2, the background theory for ion trap quantum information processing is presented and the $^{171}Yb^{+}$ ion species used in this work is introduced. Following this the experimental setup is discussed and some initial results are presented. In chapter 3, it is shown how laser light can be used to couple the spin and motional states of trapped ions for two-qubit gate operations. It is then shown that by adding a magnetic field gradient, a similar coupling can be achieved when only driving the ions with long-wavelength radiation. In chapter 4, dressed states are introduced and it is shown how they protect against magnetic field noise and thereby increase the coherence time of qubits composed of states with different magnetic moments. It is then shown how these states can still be coupled to the ions' motional states using the magnetic field gradient. In chapter 5, the magnetic field gradient and dressed state schemes are combined to demonstrate sideband cooling of one and two ions to the motional ground state with a mean phonon number of $\bar{n} = 0.13(4)$ in the single ion case. This is the lowest temperature achieved using long-wavelength radiation and as well as being advantageous for achieving a high-fidelity two-qubit gate, it is also useful in a range of applications including precision measurements and quantum simulations. In chapter 6, it is shown how the Mølmer-Sørenson interaction can be applied to one and two ions. In the single ion case, such an interaction produces spin-motion coupled 'Schrödinger cat' type states, while in the two ion case the interaction gives rise to a two-qubit quantum logic gate. The two-qubit Mølmer-Sørenson gate is demonstrated with a Bell state fidelity of 0.985(12), demonstrating that this scheme is promising for use in a large scale quantum computer.

Chapter 2

Background and Experimental Setup

2.1 Introduction

Trapped ions have been used for quantum information purposes for over two decades, and consequently much of the basic theoretical and experimental aspects have been extensively reviewed in the literature. In this chapter a summary of the background theory relevant for the rest of the thesis is presented, as well as a description of the main experimental setup used in this work. Following this, the results of some initial experiments to characterise the system are presented.

2.2 Trapped ion basics

2.2.1 Trapping ions

Gauss' law states that the divergence of an electric field in free space must be zero, and therefore no static electric field can be created that will trap a charged particle in three dimensions. Two common trapping methods that circumvent this problem are commonly used. The first is a Penning trap, in which a combination of static electric and magnetic fields are used to achieve the required three-dimensional trapping. The second is the Paul trap, in which time-dependent electric fields create a potential that mimics a three-dimensional confining potential when averaged in time. In this work a variant on the original Paul trap design is used, which is known as a linear Paul trap. An illustration of the electrode configuration for a linear Paul trap is shown in Fig. 2.1. In the $x - y$ plane, an oscillating RF voltage of the form

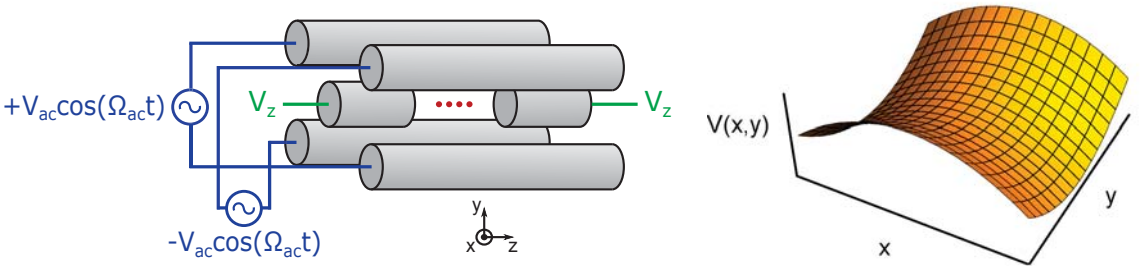


Fig. 2.1 Illustration of the electrode configuration for a linear Paul trap. An oscillating RF voltage (blue) is applied to the four rod electrodes, with opposite phase for the two pairs that are diagonally opposite. This creates an oscillating quadrupole potential in the $x-y$ plane that can confine ions. A plot of this potential at one instant of time is shown in the right graph. To confine the ions in the z direction, a static voltage V_z (green) is applied to two endcap electrodes, creating a static harmonic potential. If the voltages are set so that the trap potential is much weaker in the z direction compared to the x and y directions, the ions can form a linear string, illustrated by the red points.

$V_{ac}\cos(\Omega_{ac}t)$ is applied to two of the four rod electrodes, while the opposite voltage $-V_{ac}\cos(\Omega_{ac}t)$ is applied to the other two. This creates a 2D quadrupole electric field with amplitude $Q_{ac} = \alpha_{ac}V_{ac}/\rho_0$, where α_{ac} is a geometrical factor that is equal to 1 if the electrodes are perfectly hyperbolic and ρ_0 is the distance from the trap centre to the RF electrodes. The potential in the z direction is created using two 'endcap' electrodes, with an equal static voltage V_z applied to both. This creates a static electric field with amplitude $Q_z = \alpha_z V_z/\sigma_0$, where α_z is another geometrical factor and σ_0 is the distance in the z direction from the centre of the trap to the endcap electrodes. The total electric potential is therefore

$$V(x,y,z,t) = Q_{ac}(x^2-y^2)\cos(\Omega_{ac}t) + Q_z\Big(z^2 - \frac{x^2+y^2}{2}\Big). \tag{2.1}$$

A plot of $V(x,y,z=0,t=t_0)$ for an instant of time t_0 is also shown in Fig. 2.1. The motion of an ion with charge e and mass m in such a potential can be calculated from the force $\vec{F} = -e\vec{\nabla}V$. In the z direction, we therefore arrive at the differential equation

$$\frac{\partial^2 z}{\partial t^2} = -\frac{2eQ_z}{m}z, \tag{2.2}$$

which is simply the equation for a harmonic oscillator with angular frequency $\nu_z = \sqrt{2eQ_z/m}$. In the x and y directions, the motion is more complicated and the equations of motion are in the form of the well known Mathieu equation. The dynamics of ions in such an oscillating quadrupole potential are discussed in detail

in Refs. [49–51] and summarised here. We can define two parameters q and a as

$$\begin{aligned} q &= \frac{4eQ_{ac}}{\Omega_{ac}^2 m}, \\ a &= -\frac{4eQ_z}{\Omega_{ac}^2 m}, \end{aligned} \tag{2.3}$$

which determine whether the ion's motion is stable. In the limit $q \ll 1$ and $a \ll q$, the motion in the x direction can be shown to approximately be [49, 51]

$$x(t) \approx x_0 \cos(\nu_r t)\Big(1 + \frac{q}{2}\cos(\Omega_{ac} t)\Big), \tag{2.4}$$

where x_0 is a constant that can be determined from initial conditions and $\nu_r = \nu_x = \nu_y$ is the secular frequency in the 'radial' directions, given by

$$\nu_r = \frac{\Omega_{ac}}{2}\sqrt{\frac{q^2}{2} - \frac{2\nu_z^2}{\Omega_{ac}^2}}. \tag{2.5}$$

The motion in the y direction can also be calculated in a similar way. The motion is therefore a combination of a slow secular oscillation at frequency ν_r, superimposed with a higher frequency, lower amplitude oscillation at frequency Ω_{ac}, which is known as micromotion. If $\nu_r \ll \Omega_{ac}$, we can neglect the micromotion and the motion in the radial directions can be approximated as harmonic with frequency ν_r. The above analysis assumes that the ion sits at the minimum of the RF potential, known as the RF nil. If however, additional static electric fields are present, the ion position may be away from the RF nil. In this case, the amplitude of the micromotion is increased and hence is termed 'excess micromotion'. Excess micromotion can be detrimental for high fidelity quantum logic operations and should therefore be minimised. Importantly for the linear Paul trap, the RF nil is a line along the z axis and not just a single point as in other types of Paul trap design. This means that multiple ions can be confined without experiencing any excess micromotion. The ions can be made to form such a linear string by adjusting the voltages of the endcap and RF electrodes so that the trap potential is much weaker along the z axis than in the x and y directions. The dynamics of a string of ions in such a linear configuration is discussed in the following section.

2.2.2 Normal modes of a trapped ion string

Multiple ions in a trap repel each other due to the Coulomb interaction, but are pushed together due to the trapping potential. When the ions are sufficiently cold, these two forces combined cause the ions to form crystal structures known as Coulomb crystals. Their motion is then strongly coupled together, which can be used to transfer quantum information between ions. The DC and RF voltages are typically set so that the secular frequency in the axial (z) direction is much less than the secular frequencies in the radial (x and y) directions. In this case, a small number of ions will form a linear string along the z axis of the trap and the system dynamics can be separated into independent axial and radial oscillations*. In this work only the axial motion is used, and therefore the radial motion is ignored. The quantum dynamics of ions in such a one-dimensional harmonic potential are derived in Ref. [52] and summarised here. The total potential from the trap and the Coulomb interaction in the axial direction is given by

$$V = \sum_{j=1}^{N} \frac{1}{2} m\nu_z^2 z_j(t)^2 + \sum_{\substack{j,k=1 \\ j\neq k}}^{N} \frac{e^2}{8\pi\epsilon_0} \frac{1}{|z_j(t) - z_k(t)|}, \tag{2.6}$$

where $z_j(t)$ is the position of ion j and ϵ_0 is the permittivity of free space. If the ions are cold, we can approximate that $z_j(t) \approx z_j^e + q_j(t)$, where z_j^e is the equilibrium position of ion j and $q_j(t)$ is a small displacement about its equilibrium. The equilibrium positions can be determined by finding the zero points of the gradient of the potential with respect to each ion position z_j. This leads to a set of coupled differential equations which in general have to be solved numerically. For two ions, the equations can be solved analytically and we find that the equilibrium ion positions are

$$\begin{aligned} z_1^e &= -\frac{1}{2^{2/3}} \left(\frac{e^2}{4\pi\epsilon_0 m\nu_z^2} \right)^{1/3}, \\ z_2^e &= +\frac{1}{2^{2/3}} \left(\frac{e^2}{4\pi\epsilon_0 m\nu_z^2} \right)^{1/3}. \end{aligned} \tag{2.7}$$

These equilibrium positions are simply the minima of the potential felt by each ion due to the trap and the other ion, as illustrated in Fig. 2.2.

*This is only approximately true for situations where the ions have relative motion, in which case a non-linear Kerr-type coupling between the axial and radial motion exists. This can be a source of infidelity for two-qubit gate operations and is discussed further in Sec. 6.3.2.

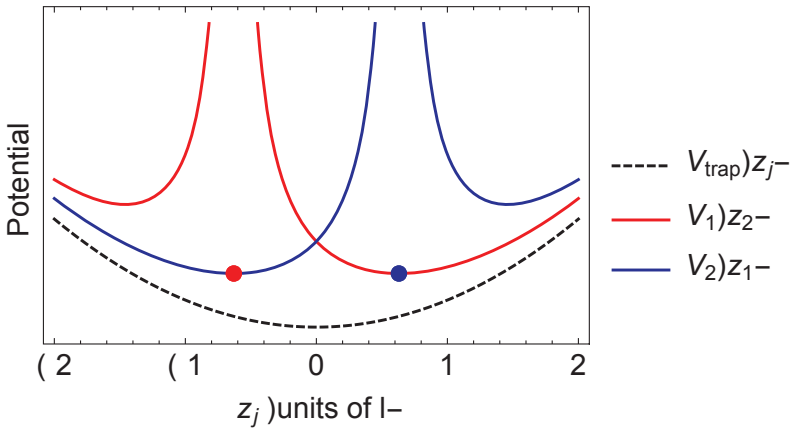


Fig. 2.2 The potential felt by two ions due to the trap (dashed black line), as well as the combined potential due to the trap and ion 1 felt by ion 2 (red) and the potential due to the trap and ion 2 felt by ion 1 (blue) as a function of the respective ion positions in units of the characteristic distance scale $l = (e^2/4\pi\epsilon_0 m\nu_z^2)^{1/3}$. The equilibrium positions can be calculated by finding the positions at which both ions sit at the minimum of their respective potentials.

We will now consider the small displacements about the equilibrium positions $q_j(t)$. The dynamics of the trapped ion system can be described as a series of N coupled harmonic oscillators. Such a system is best described in terms of normal modes with coordinates $Q_k(t)$ and momenta $P_k(t) = m\dot{Q}_k(t)$, for $k = 1, ..., N$, which are uncoupled and oscillate independently. The individual ion positions can be written in terms of the normal mode coordinates as

$$q_j(t) = \sum_{k=1}^{N} S_{jk} Q_k(t), \tag{2.8}$$

where S_{jk} gives the relative motion of ion j for normal mode k. The values of the elements S_{jk} are the jth element of the kth eigenvector of the matrix $\mathbf{A}$, where the eigenvectors are numbered according to increasing eigenvalue and where the matrix elements of $\mathbf{A}$ are given by

$$A_{jk} = \frac{1}{m}\left[\frac{\partial^2 V}{\partial z_j \partial z_k}\right]_{z_j=z_j^e, z_k=z_k^e}. \tag{2.9}$$

The normal mode frequencies are then found to be $\nu_k = \sqrt{\mu_k}$, where μ_k are the eigenvalues of $\mathbf{A}$. The lowest frequency mode for any number of ions has frequency $\nu_1 = \nu_z$ and $S_{j1} = 1/\sqrt{N}$ for all j. This corresponds to all ions oscillating in phase with the same amplitude at the trap frequency, as if the string was a single particle situated at the centre of mass position. This mode is therefore often referred to as

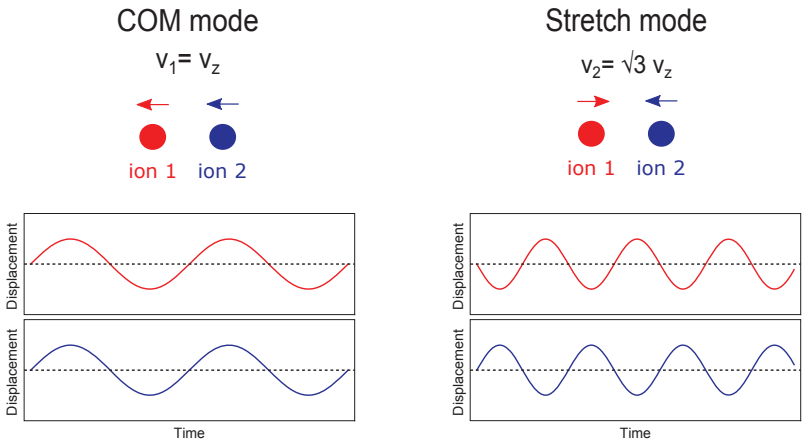


Fig. 2.3 Illustration of the normal modes of motion for a pair of co-trapped ions. The dynamics of the ions for any initial condition can be described as a sum of the two normal modes of motion. The normal modes are the centre of mass (COM) mode (left) with frequency ν_z and the stretch mode (right) with frequency $\sqrt{3}\nu_z$. The graphs show the ion displacements about their equilibrium positions as a function of time.

the centre of mass (COM) mode. All higher order modes have frequencies greater than ν_z and involve relative motion between the ions. In the case of two ions in a shared trap with trap frequency ν_z, there are two normal modes with frequencies $\nu_1 = \nu_z$ and $\nu_2 = \sqrt{3}\nu_z$. For the first mode we find that $S_{11} = S_{21} = 1/\sqrt{2}$ as expected for the COM mode, while for the second mode, we obtain $S_{12} = -1/\sqrt{2}$ and $S_{22} = 1/\sqrt{2}$. The ions therefore move with equal amplitude and opposite phase, and hence this mode is often referred to as the stretch mode. The two modes of motion are illustrated in Fig. 2.3.

Quantization of the motion

The normal mode coordinates can be quantized in the same way as the usual harmonic oscillator by defining the normal mode position and momentum operators

$$\begin{aligned} Q_k \to \hat{Q}_k &= \sqrt{\frac{\hbar}{2m\nu_k}}(a_k + a_k^\dagger), \\ P_k \to \hat{P}_k &= i\sqrt{\frac{\hbar m\nu_k}{2}}(a_k - a_k^\dagger), \end{aligned} \tag{2.10}$$

where a_k, $a_k^\dagger$ are the ladder operators for normal mode k. The Hamiltonian describing the motion of the ion string is then

$$H_m = \sum_{k=1}^{N} \hbar \nu_k a_k^\dagger a_k. \tag{2.11}$$

The quantum dynamics of the ion string can therefore be described as a series of N independent harmonic oscillators, each with a different frequency ν_k. In most cases, all ions participate in a given mode*, and therefore each mode can be used as a route for quantum information to be communicated between ions. This is a key feature that is used in much of the work discussed later in this thesis, and methods to couple the motional states of the ions with their internal electronic states will be the focus of chapter 3.

2.2.3 Trapped ion qubits

Qubits can be formed from two electronic internal states of a trapped ion and manipulated by an oscillating electromagnetic field. Labelling the two states $|\downarrow\rangle \equiv (0,1)^T$ and $|\uparrow\rangle \equiv (1,0)^T$ and setting the zero point of energy to be halfway between the two states, the Hamiltonian term describing the internal states is

$$H_0 = \frac{\hbar\omega_0}{2}\Big(|\uparrow\rangle\langle\uparrow| - |\downarrow\rangle\langle\downarrow| \Big), \tag{2.12}$$

where $\hbar\omega_0$ is the energy splitting. We now consider applying an electromagnetic field to the ion. In the work discussed in this thesis, the qubits are formed from hyperfine atomic levels, and therefore there is no electric dipole coupling. The lowest order coupling of the ion to an electromagnetic field is therefore a magnetic dipole coupling, and the Hamiltonian is therefore $H = H_0 + H_I$, where H_I is given by

$$H_I = -\vec{\mu} \cdot \vec{B}, \tag{2.13}$$

where $\vec{\mu}$ is the magnetic moment and $\vec{B}$ is the applied magnetic field. We can apply an oscillating magnetic field of the form $\vec{B} = \vec{B}_0 \cos(\omega t - \vec{k} \cdot \vec{r} - \phi)$, where $\vec{k}$ is the wavevector, $\vec{r}$ is the ion position, ω is the frequency of the oscillating field and ϕ is the phase. If the wavelength of the field is much larger than the spatial extent of the ion's

*This is always true for the COM mode, however some ions do not participate in higher order modes, which is the case if $S_{jk} = 0$ for ion j and mode k. This is the case for instance for the centre ion of a three ion string for the second mode, in which the two outer ions oscillate with opposite phase, while the middle ion is stationary. Similar 'stretch' modes also exist in larger strings with an odd number of ions.

wavefunction, we can approximate that $e^{i\vec{k}\cdot\vec{r}} \approx 1$ by expanding to lowest order, and therefore neglect the $\vec{k}\cdot\vec{r}$ term in the cosine. This is known as the magnetic dipole approximation, and is a good approximation when the field is of similar frequency to the resonant frequency of the hyperfine qubit, which would typically correspond to wavelengths on the order of several centimetres. We can write the Hamiltonian term H_I in terms of it's matrix elements in the $\{|\downarrow\rangle, |\uparrow\rangle\}$ basis as

$$\begin{aligned} H_I &= -\Big(\langle\downarrow| \vec{\mu}\cdot\vec{B}_0 |\uparrow\rangle |\downarrow\rangle\langle\uparrow| + \langle\uparrow| \vec{\mu}\cdot\vec{B}_0 |\downarrow\rangle |\uparrow\rangle\langle\downarrow| \Big)\cos(\omega t - \phi) \\ &= \hbar\Omega_0 \Big(|\uparrow\rangle\langle\downarrow| + |\downarrow\rangle\langle\uparrow| \Big)\cos(\omega t - \phi), \end{aligned} \tag{2.14}$$

where we have defined the Rabi frequency $\Omega_0 = -\langle\uparrow| \vec{\mu}\cdot\vec{B}_0 |\downarrow\rangle/\hbar = -\langle\downarrow| \vec{\mu}\cdot\vec{B}_0 |\uparrow\rangle/\hbar$. We can now move to the interaction picture with respect to H_0 as $H \to H' = e^{iH_0 t/\hbar}(H - H_0)e^{-iH_0 t/\hbar}$, giving

$$H' = \frac{\hbar\Omega_0}{2}\Big(|\uparrow\rangle\langle\downarrow| e^{i\omega_0 t} + |\downarrow\rangle\langle\uparrow| e^{-i\omega_0 t}\Big)\Big(e^{i\omega t}e^{-i\phi} + e^{-i\omega t}e^{i\phi}\Big). \tag{2.15}$$

If ω is set close to the resonant frequency of the qubit ω_0, the interaction Hamiltonian H' will contain two terms slowly rotating at frequency $\delta = \omega - \omega_0$, known as the detuning, as well as two terms rotating at a much higher frequency $\omega + \omega_0$. The rotating wave approximation (RWA) is a well known approximation in which these two faster rotating terms are neglected, which is valid as long as $\Omega_0 \ll \omega_0$. With this, H' becomes

$$H' = \frac{\hbar\Omega_0}{2}\Big(|\uparrow\rangle\langle\downarrow| e^{-i\delta t}e^{i\phi} + |\downarrow\rangle\langle\uparrow| e^{i\delta t}e^{-i\phi}\Big). \tag{2.16}$$

To find the unitary operator resulting from H', we can insert H' into the Schrödinger equation $i\hbar\frac{\partial}{\partial t}|\psi(t)\rangle = H'|\psi(t)\rangle$ and solve for an arbitrary spin state $|\psi(t)\rangle = c_\downarrow(t)|\downarrow\rangle + c_\uparrow(t)|\uparrow\rangle$. This gives a set of two coupled first-order differential equations

$$\dot{c}_\uparrow(t) = -\frac{i\Omega_0}{2}e^{i\delta t}e^{-i\phi}c_\downarrow(t), \tag{2.17a}$$

$$\dot{c}_\downarrow(t) = -\frac{i\Omega_0}{2}e^{-i\delta t}e^{i\phi}c_\uparrow(t), \tag{2.17b}$$

By differentiating Eq. 2.17a with respect to t and substituting in Eq. 2.17b, we can write the problem as a single second-order differential equation in terms of $c_\uparrow(t)$ only

as

$$\ddot{c}_{\uparrow}(t) - i\delta\dot{c}_{\uparrow}(t) + \frac{\Omega_0^2}{4}c_{\uparrow}(t) = 0. \tag{2.18}$$

The general solution is then given by

$$c_{\uparrow}(t) = e^{i\delta t/2}\Big(ae^{-i\Omega_\delta t/2} + be^{i\Omega_\delta t/2}\Big), \tag{2.19}$$

where we have defined $\Omega_\delta = \sqrt{\Omega_0^2 + \delta^2}$ and a and b are constants that depend on the initial conditions. The solution for $c_{\downarrow}(t)$ can then be found be differentiating Eq. 2.19 with respect to t and substituting into Eq. 2.17a to get

$$c_{\downarrow}(t) = -\frac{e^{-i\delta t/2}e^{i\phi}}{\Omega_0}\Big(\delta(ae^{-i\Omega_\delta t/2} + be^{i\Omega_\delta t/2}) - \Omega_\delta(ae^{-i\Omega_\delta t/2} - be^{i\Omega_\delta t/2})\Big). \tag{2.20}$$

The unitary operator in the $\{|\downarrow\rangle, |\uparrow\rangle\}$ basis can then be calculated by finding a and b for the initial conditions corresponding to the two basis states. For an initial state $|\downarrow\rangle$, the initial conditions are $c_{\downarrow}(0) = 1$ and $c_{\uparrow}(0) = 0$, and we therefore find that $a = -b = \Omega_0 e^{-i\phi}/2\Omega_\delta$. If the initial state is instead $|\uparrow\rangle$, the initial conditions are $c_{\downarrow}(0) = 0$ and $c_{\uparrow}(0) = 1$, and we find that $a = (1 + \delta/\Omega_\delta)/2$ and $b = (1 - \delta/\Omega_\delta)/2$. Inserting these two sets of of parameters for the two initial conditions into Eqs. 2.19 and 2.20, we obtain the unitary operator

$$U(\delta, \Omega_0, \phi, t) = \begin{pmatrix} e^{i\delta t/2}\Big[\cos(\Omega_\delta t/2) - \frac{i\delta}{\Omega_\delta}\sin(\Omega_\delta t/2)\Big] & -\frac{i\Omega_0}{\Omega_\delta}e^{i\delta t/2}e^{-i\phi}\sin(\Omega_\delta t/2) \\ -\frac{i\Omega_0}{\Omega_\delta}e^{-i\delta t/2}e^{i\phi}\sin(\Omega_\delta t/2) & e^{-i\delta t/2}\Big[\cos(\Omega_\delta t/2) + \frac{i\delta}{\Omega_\delta}\sin(\Omega_\delta t/2)\Big] \end{pmatrix}. \tag{2.21}$$

If the field is set to resonance ($\delta = 0$), the unitary operator reduces to

$$U(\Omega_0, \phi, t) = \begin{pmatrix} \cos(\Omega_0 t/2) & -ie^{-i\phi}\sin(\Omega_0 t/2) \\ -ie^{i\phi}\sin(\Omega_0 t/2) & \cos(\Omega_0 t/2) \end{pmatrix}. \tag{2.22}$$

In the Bloch sphere picture, this unitary operator rotates the Bloch vector by an angle $\theta = \Omega_0 t$ around an axis at an angle ϕ in the $x - y$ plane, as shown in Fig. 2.4. With sequences of such pulses, any point on the Bloch sphere can be reached and therefore this interaction allows arbitrary rotations of the qubit to be performed. In experiments, the state probabilities $P_{\uparrow}$ and $P_{\downarrow} = 1 - P_{\uparrow}$ are measured. It is therefore useful to calculate these probabilities, which can be used to compare with experimental data. For a state initialised in $|\downarrow\rangle$, the probability to be in the state

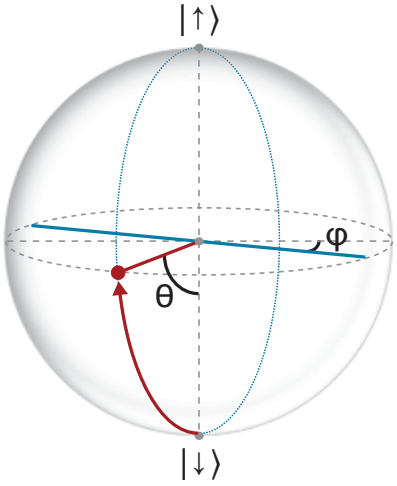


Fig. 2.4 Illustration of the effect of the unitary operator given in Eq. 2.22 on a qubit initialised in $|\downarrow\rangle$. The Bloch vector (red) rotates by an angle $\theta = \Omega_0 t$ around an axis (blue) at an angle ϕ in the $x - y$ plane. By applying sequences of such pulses, arbitrary rotations on the Bloch sphere can be implemented.

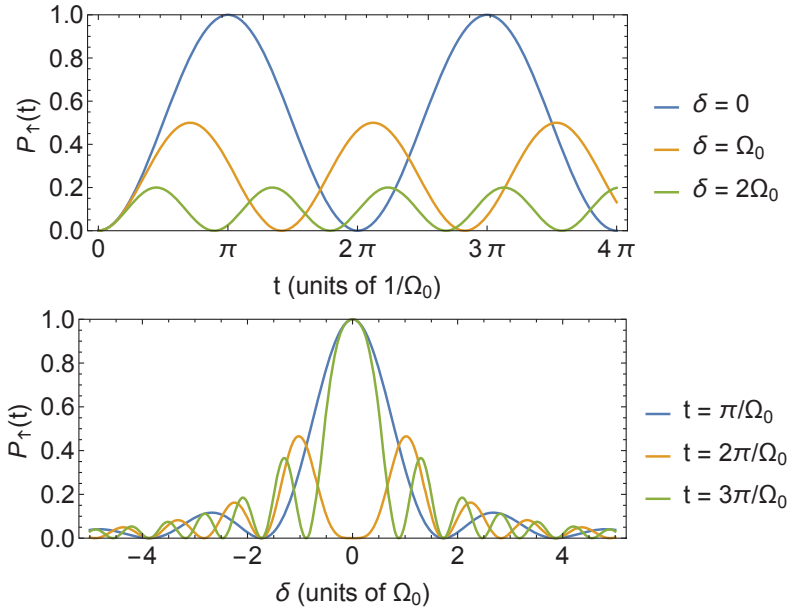


Fig. 2.5 Plots of the probability to be in the state $|\uparrow\rangle$ after applying a near-resonant field as a function of time (top) and detuning (bottom) when the state is initialised in $|\downarrow\rangle$, following Eq. 2.23. It can be seen that a larger detuning gives rise to faster oscillations of frequency Ω_δ with a lower amplitude. If the pulse time is an odd integer multiple of π/Ω_0, the population will have transferred completely to the state $|\uparrow\rangle$ if the field is resonant.

$|\uparrow\rangle$ is found to be

$$P_{\uparrow}(t,\delta) = \frac{\Omega_0^2}{\Omega_\delta^2}\sin^2(\Omega_\delta t/2) = \frac{\Omega_0^2}{2\Omega_\delta^2}\Big(1-\cos(\Omega_\delta t)\Big). \tag{2.23}$$

Plots of $P_{\uparrow}(t,\delta)$ as a function of both time and detuning are shown in Fig. 2.5.

2.3 Energy level structure of $^{171}Yb^{+}$

Various ion species are commonly used experimentally, each with certain advantages and disadvantages that can be considered depending on the specific application. In this work, the element ytterbium (Yb) is used, and in particular the isotope $^{171}Yb^{+}$. $^{171}Yb^{+}$ is one of seven naturally occuring stable isotopes of ytterbium, and is the only isotope with a nuclear spin of 1/2. The non-zero nuclear spin means that the ion has a hyperfine structure, which can be used for encoding quantum information. The fact that the nuclear spin is the lowest non-zero possible value makes the hyperfine structure relatively simple compared to other isotopes or ion species. In this section the energy level structure of $^{171}Yb^{+}$ will be described.

2.3.1 Ionisation

To load the trap with ytterbium ions, firstly ytterbium metal is resistively heated in an atomic oven situated close to the trap structure (decribed in Sec. 2.4.1). In our setup there are two ovens, one of which contains a sample of 'natural' ytterbium with a naturally occurring abundance of each isotope*, while the other contains a sample enriched to contain >95% $^{171}Yb^{+}$. It can sometimes be useful to trap $^{174}Yb^{+}$ instead of $^{171}Yb^{+}$, as the lack of nuclear spin in the former isotope simplifies the energy level structure and therefore makes the Doppler cooling simpler. In this case, it may be useful to use the natural ytterbium oven, however we found that the ytterbium in this oven was depleted after several years of running the experiment, leaving only the enriched ovens.

The heated ytterbium atoms are directed by the oven across the centre of the trapping region, at which point they are ionised using a two-photon ionisation process involving two optical transitions. Firstly a laser with a wavelength near 399 nm excites the $^1S_0 \leftrightarrow {}^1P_1$ transition, as shown in Fig. 2.6. The exact wavelength of this transition is isotope dependent, and therefore the ionisation process is isotope selective. This is a useful feature for the experiments discussed in this work, where

*14.3% ^{171}Yb, 31.8% ^{174}Yb, 53.9% other.

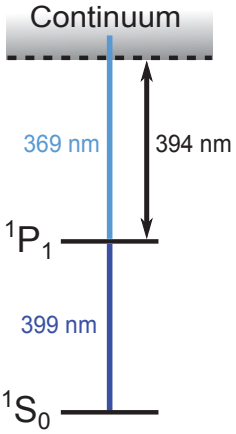


Fig. 2.6 Energy level diagram of the relevant levels in neutral ytterbium, showing the transitions required for the two step ionisation process. The $^1S_0 \leftrightarrow {}^1P_1$ transition wavelength near 399 nm depends on the isotope, and therefore an isotope can be selected by choosing the wavelength appropriately. A 369 nm laser, which is also used for Doppler cooling, then provides the second excitation of the electron to the continuum.

multiple ions of the same isotope are required to be trapped together. In the second step, a laser with a wavelength near 394 nm excites the electron from $^1P_1$ to the continuum, thereby ionising the atom. As will be seen in the following section, a laser with wavelength near 369 nm is required for Doppler cooling. Since the wavelength is less than the maximum of 394 nm required for ionisation, this laser is also used for the second step of the ionisation process.

2.3.2 Doppler cooling

A closed Doppler cooling cycle can be formed using three lasers and one microwave field resonant with three transitions in $^{171}Yb^+$. The main Doppler cooling cycle is on the $^2S_{1/2}, F = 1 \leftrightarrow {}^2P_{1/2}, F = 0$ transition, requiring a laser with a wavelength near 369 nm. Population in $^2P_{1/2}, F = 0$ then decays back to $^2S_{1/2}, F = 1$ with a rate equal to the natural linewidth $\Gamma/2\pi = 19.6$ MHz. Off-resonant excitation to the $^2P_{1/2}, F = 1$ state can occur, which can decay to $^2S_{1/2}, F = 0$. A microwave field resonant with the $^2S_{1/2}, F = 0 \leftrightarrow {}^2S_{1/2}, F = 1$ transition at ≈ 12.6 GHz can then be used to repopulate $^2S_{1/2}, F = 1$. In 0.5% of cases, the population decays from $^2P_{1/2}$ to $^2D_{3/2}$, from which it can be excited to the state $^3[3/2]_{1/2}$ by a laser of wavelength near 935 nm and can then decay back to $^2S_{1/2}$, thereby closing the cooling cycle. The hyperfine structure of the $^2D_{3/2}$ and $^3[3/2]_{1/2}$ levels can be addressed either by applying 3 GHz sidebands to the 935 nm laser, or by increasing the power to broaden over all transitions. The latter method is chosen in this work. Occasionally collisions

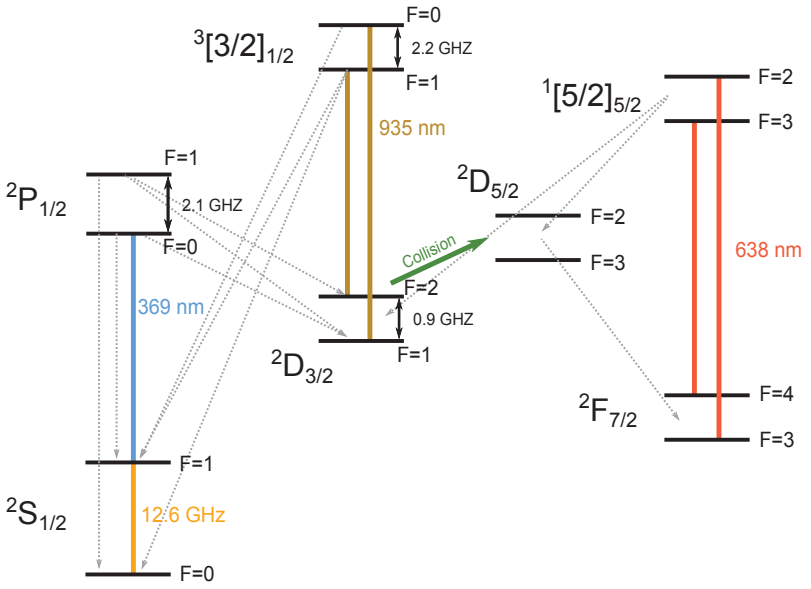


Fig. 2.7 Energy level structure of $^{171}Yb^{+}$ showing the relevant energy levels. A closed Doppler cooling cycle for $^{171}Yb^{+}$ can be formed with three lasers and a microwave field. If an even isotope of Yb^{+} was chosen, such as $^{174}Yb^{+}$, there would be no hyperfine structure and therefore the microwave field would not be required. This makes such isotopes simpler to trap.

with background gas will cause the population to transition from $^2D_{3/2}$ to $^2D_{5/2}$, from which it can decay to the state $^2F_{7/2}$. In our experiment, we observe such a process in a two ion string with a frequency on the order 1 per day. A third laser with wavelength near 638 nm can then be used to transfer population from $^2F_{7/2}$ to $^1[5/2]_{5/2}$, from which it can decay back to either $^2D_{3/2}$ or $^2D_{5/2}$. Here since the transition to $^2F_{7/2}$ is very unlikely, the wavelength of the 638 nm laser can be slowly scanned, allowing the required frequencies for all hyperfine levels to be covered.

2.3.3 $^2S_{1/2}$ ground state

All coherent operations in this work are performed in the $^2S_{1/2}$ hyperfine ground state manifold. The manifold consists of four states, which are shown in an energy level diagram in Fig. 2.8. In zero magnetic field the state $|0\rangle \equiv F = 0, m_F = 0$ is separated from the $F = 1$ sub-manifold by $\hbar\omega_{\mathrm{hf}} = 2\pi \times \hbar \times 12.6428121\,\mathrm{GHz}$. The three states $|-1\rangle \equiv F = 1, m_F = -1$, $|0'\rangle \equiv F = 1, m_F = 0$ and $|+1\rangle \equiv F = 1, m_F = +1$ are degenerate in this zero field case, however when a magnetic field is applied, the three states acquire an energy difference. In our experiment, a weak magnetic field of $\approx 10\,\mathrm{G}$ is applied in the z direction to lift the degeneracy of the $F = 1$ sub-manifold and to define a quantization axis with respect to the polarisation of any incident

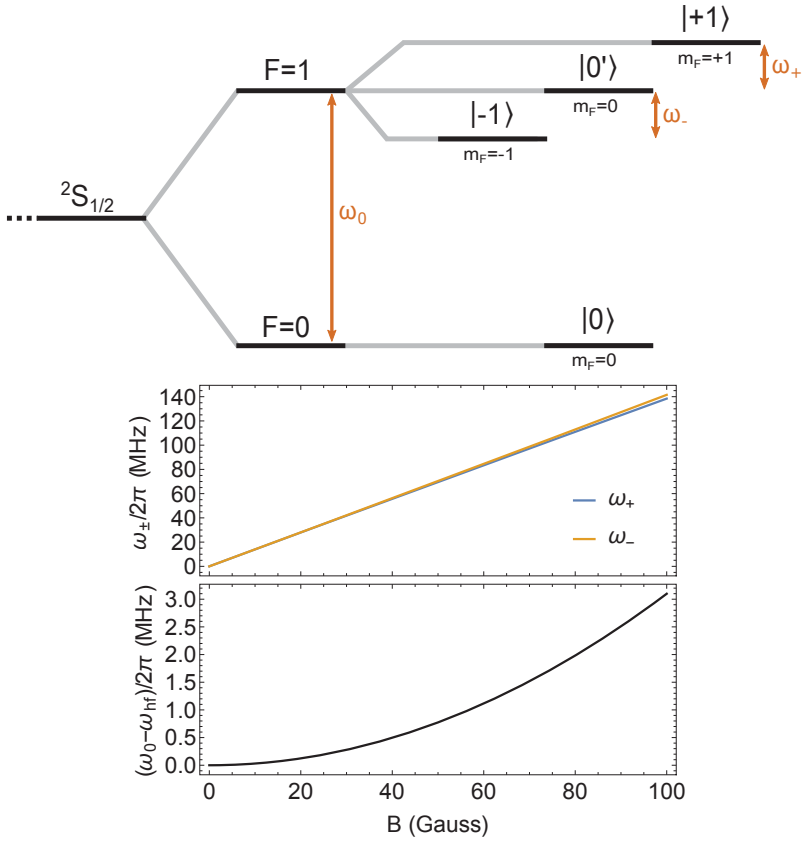


Fig. 2.8 Top: Energy level diagram of the ${}^2S_{1/2}$ ground state manifold of ${}^{171}\mathrm{Yb}^+$. The ground state consists of two hyperfine manifolds $F = 0$ and $F = 1$, separated by $\omega_0/2\pi \approx 12.6\,\mathrm{GHz}$. In a magnetic field, the three m_F sub-levels of the $F = 1$ manifold are separated in energy by amounts $\omega_+ \approx \omega_-$ (defined in Eqs. 2.24a and 2.24b), where the approximation holds for low magnetic fields. Bottom: Plots of the three frequencies indicated in above figure following Eqs. 2.24a, 2.24b and 2.24c as a function of the magnetic field. Note the different scales on the y axes. It can be seen that $\omega_+ \approx \omega_-$ and $\omega_0 \approx \omega_{\mathrm{hf}}$ for low magnetic fields.

electromagnetic radiation. The energies of the states $|-1\rangle$ and $|+1\rangle$ are linearly dependent on the applied magnetic field, while the energies of the states $|0\rangle$ and $|0'\rangle$ are only sensitive to second order. The transition frequency between any two states can be calculated using a combination of the three frequencies indicated in Fig. 2.8, which can be derived from the Breit-Rabi formula [53] and are given by

$$\omega_+ = \frac{\omega_{\mathrm{hf}}}{2}\left(1 + \chi - \sqrt{1 + \chi^2}\right), \tag{2.24a}$$

$$\omega_- = -\frac{\omega_{\mathrm{hf}}}{2}\left(1 - \chi - \sqrt{1 + \chi^2}\right), \tag{2.24b}$$

$$\omega_0 = \omega_{\mathrm{hf}}\sqrt{1 + \chi^2}, \tag{2.24c}$$

where $\chi = g_J \mu_B B/\hbar\omega_{\mathrm{hf}}$ and we have neglected the contribution from the nuclear spin as the nuclear magneton μ_N is much smaller than the Bohr magneton μ_B. Plots of the three frequencies are shown in Fig. 2.8. In weak magnetic fields it can be approximated that $\sqrt{1+\chi^2} \approx 1$, in which case the three transition frequencies reduce to $\omega_0 \approx \omega_{\mathrm{hf}}$ and $\omega_+ \approx \omega_- \approx \mu_B B/\hbar$. For a typical magnetic field of 10 G, we find that $\omega_+ \approx \omega_- \approx 14$ MHz, which is in the radio frequency (RF) region, and $\Delta\omega_\pm \equiv \omega_- - \omega_+ \approx 31$ kHz. In Sec. 2.5, it will be shown how electromagnetic radiation in the radio and microwave frequency regions can be used to coherently drive transitions between these states in the $^2S_{1/2}$ manifold.

2.4 Experimental setup

In this section, the main components of the experimental setup will be described. Many of the components are described in detail elsewhere, and in this case appropriate references are provided. The experiment is controlled by a computer running LabVIEW, which is connected to a field-programmable gate array (FPGA, National Instruments PXI-7842R). The FPGA has 8 analog output voltages, 8 analog inputs, 96 digital inputs/outputs (DIOs) and runs with a clock speed of 40 MHz, allowing fast control of various aspects of the experiment.

2.4.1 Ion trap

The ion trap used in this work is a linear 'blade' Paul trap as discussed in Sec. 2.2.1. A schematic of the trap is shown in Fig. 2.9, and a few small differences to the standard design can be observed. Firstly, the oscillating RF voltage is only applied to two of the four blade shaped electrodes, while static DC voltages are applied to the other two. This is because it is experimentally much easier to generate, amplify and apply a single RF signal compared to two with opposite phase. The consequence is that the whole quadrupole potential, including at $x = y = 0$, oscillates at the RF frequency Ω_{ac}. However, since the forces felt by the ions are proportional to the gradient of the potential, which is unchanged, this modification has no effect in the $x - y$ plane. In the z direction, the RF potential is grounded at the endcaps, and therefore an oscillating RF potential at $x = y = 0$ can create a small oscillating gradient along the trap axis, which can cause axial micromotion. This effect is considered to be small in the centre region of the trap and is therefore ignored. The DC blades are segmented into three sections, each of which can have a different DC voltage applied. The two outer electrodes on either blade can therefore be used as

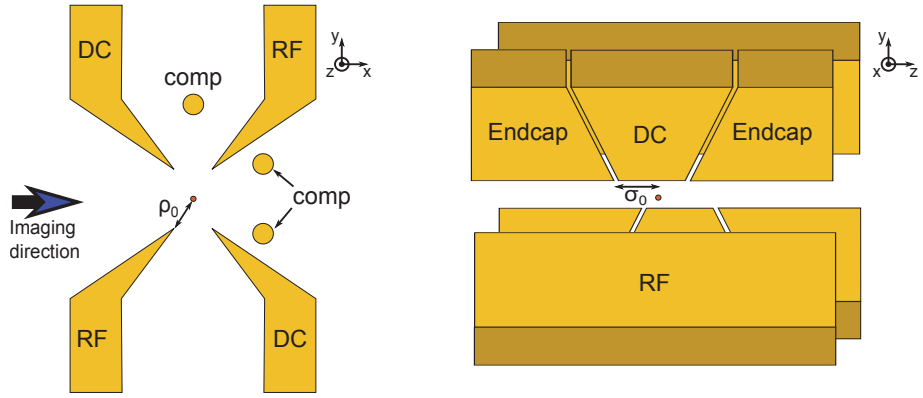


Fig. 2.9 Schematic of the ion trap used in this work. Left: In the $x-y$ plane an RF voltage is applied to two opposite electrodes, which along with the DC electrodes creates the required oscillating quadrupole field. The centre point is at a distance $\rho_0 = 310(10)\,\mu$m from the RF electrodes. The direction in which the ions are viewed by the imaging system is shown for reference. Two compensation rod electrodes are also shown, which allow for micromotion compensation (the right compensation electrode is separated into two electrically connected rods, allowing for laser access through the gap between them). Right: The trap in the $y-z$ plane, showing the segmented DC electrodes. The outer 'endcap' electrodes create confinement in the z direction, and are spaced by $\sigma_0 \approx 500\,\mu$m from the centre of the trap structure. The compensation electrodes are not shown here for clarity.

the endcap electrodes to create the axial static potential. Further to the six DC blade electrodes, there are also two compensation electrodes, shown in Fig. 2.9. These electrodes together with the centre DC electrodes allow the ion position to be moved in the $x-y$ plane, which can be used to ensure that the ions sit exactly on the RF nil line and therefore have no excess micromotion (known as micromotion compensation). During the baking of the vacuum system containing the trap, one of the compensation electrodes moved and became electrically connected to one of the endcaps. Fortunately, there are enough remaining electrodes to be able to move the ions in all directions and change the axial trap frequency. The ion electrode distance, which is also the distance to the RF electrodes ρ_0, was found to be $310(10)\,\mu$m, while the distance to the endcap electrodes in the z direction is $\sigma_0 \approx 500\,\mu$m. Further details of the trap design can be found in Ref. [54].

Vacuum system

The ion trap is housed in a vacuum system that is held at an ultra-high vacuum (UHV) pressure of $\approx 10^{-12}$ Torr. Further details regarding the vacuum system design and trap mounting are given in Ref. [55]. The vacuum system has feedthroughs for 50 DC connections and one RF connection, which can be used to connect the

DC and RF electrodes. Additionally, there are 6 DC feedthroughs for the atomic oven connections. The pressure is maintained using an ion pump (Varian StarCell 9191145) and monitored using an ion gauge (Varian 9715015).

Voltage generation

To create the required DC voltages, a low noise multi-channel voltage supply was used*. The supply has 7 channels that can supply $\pm 10\,\mathrm{V}$, plus one channel that can supply $\pm 150\,\mathrm{V}$, which is used for the two electrodes that are electrically connected. The required RF voltage to create the oscillating quadrupole potential is generated by a HP8640 signal generator. The signal is then amplified by 47 dB (NP Technologies NP-541), before being sent to a helical resonator. The helical resonator allows the RF source to be impedance matched to the trap, as well as increasing the RF voltage further and filtering the signal. With the resonator attached to the RF source and to the trap through RF vacuum feedthroughs, the resonant frequency was found to be 19.212 MHz and the Q factor was found to be 200(20). The RF voltage can then be calculated as $V_{ac} = \kappa\sqrt{2PQ}$, where P is the RF power applied to the resonator, $\kappa = (L/C)^{1/4}$ and C and L are the capacitance and inductance of the ion trap-resonator system, which was measured to be $\kappa = 13(1)$ [56]. RF powers in the range 0 W to 3 W are typically applied to the helical resonator in this work, corresponding to voltages in the range $0 - 450\,\mathrm{V}$, however powers of up to 10 W (820 V) have been applied previously.

Magnetic field gradient

A large magnetic field gradient along the z axis of the trap was required for the experiments discussed in this thesis in order to create a coupling between the spin and motional states of trapped ions using long-wavelength radiation. The reason a magnetic field gradient produces such a coupling is the subject of Chapter 3. To create the gradient, Samarium Cobalt (SmCo) rare earth permanent magnets were retrofitted to the existing ion trap structure, as shown in Fig. 2.10. The magnets were placed so that the magnetic north poles of each pair are facing, approximately centred around the centre of the trap. This arrangement creates a large magnetic field gradient in the z direction, which in the centre region is well approximated as linear and has an absolute magnetic field close to zero. The latter feature was important in the design, as a large absolute magnetic field at the ion positions will shift the internal energy levels of the ions and can lead to undesired effects such as reduced detection

*designed and built by Dr. Bjoern Lekitsch.

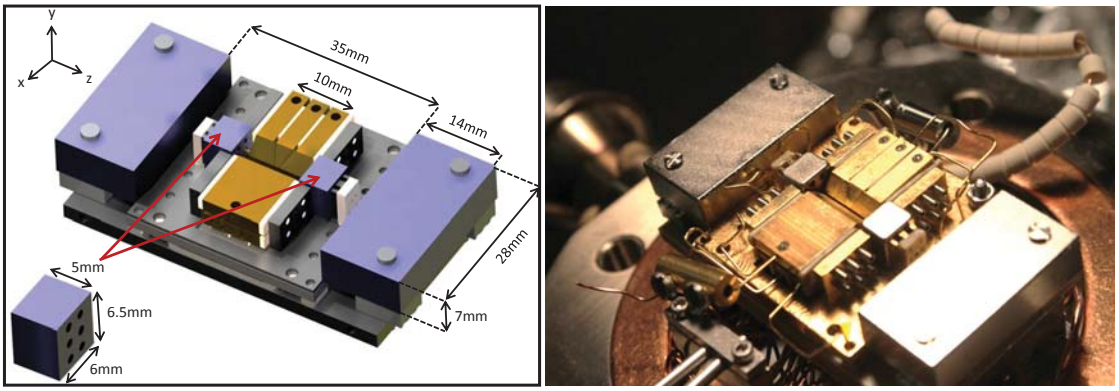


Fig. 2.10 Left: Solidworks diagram of the ion trap with fitted SmCo permanent magnets (coloured purple). The larger magnets have two holes each to allow screws to be passed through in order to attach the magnets to the base of the trap structure. Two aluminium blocks are placed under each magnet to raise them up so that they are approximately centred with the ion positions. The smaller magnets have six holes, three of which allow the compensation electrodes to pass through (the other three ensure that the magnetic field is symmetric about the centre of the magnet). The electrodes are electrically insulated from the grounded magnets by thin Kapton tape which is placed inside the holes. Right: Photograph of the trap after the magnets have been fitted.

fidelities. The magnets were coated with three thin layers consisting of Nickel, Copper and Nickel, which were chosen to suppress outgassing of the porous SmCo material during baking to create the required vacuum. Due to an unforeseen machining error in the electrode mounting block, some of the coating had to be removed from the magnets to allow them to be positioned properly. No issues were encountered during the baking procedure and low vacuum was reached, and therefore the SmCo material was found to be UHV compatible. A simulation of the setup predicted a magnetic field gradient along the trap axis of $\partial_z B = 42\,\mathrm{T/m}$, however when measured using the ions*, the actual gradient was found to be $\partial_z B = 24.50(1)\,\mathrm{T/m}$. A further simulation after adding the magnets to the trap found that the protective coating reduces the magnetic field gradient, which could explain the lower measured value compared to the simulated one. Further details of the magnet design can be found in Ref. [57]. A higher magnetic field gradient may be achievable if a new trap was designed specifically to incorporate magnets close to the ion positions, as there would be less constraints compared to the retrofit discussed here.

As stated previously, the absolute magnetic field at the ion positions should be

*The method used to measure the gradient is discussed in Sec. 3.3.1

small (typically $\approx 10\,\mathrm{G}$). Since the magnets are only coarsely aligned, there could be a substantial magnetic field at the ion positions. Therefore, a set of high field Helmholtz coils were required for each spatial direction. Estimates of possible magnet misalignments corresponded to additional magnetic fields of up to $\approx 200\,\mathrm{G}$ at the ion positions. To compensate such a field, each Helmholtz coil consists of 185 turns of 1.08 mm diameter copper wire, for which up to 10 A can be applied. The coil formers incorporate copper pipes which are attached to rubber tubes, allowing water to be passed through to reduce the temperature of the coils if high currents are used. Further details of the Helmholtz coil setup can be found in Ref. [57]. With the use of additional permanent magnets placed outside the vacuum system, the current required in each coil to bring the magnetic field to the desired value was reduced to the range $1 - 3\,\mathrm{A}$. Therefore the temperature of the coils can be kept at a reasonable value without the need for water cooling.

2.4.2 Optical setup

As seen in the previous sections, three lasers are needed for Doppler cooling $^{171}Yb^{+}$ ions, plus one additional laser for ionisation. With the exception of the 369 nm laser, all of the lasers are home built external cavity diode lasers (ECDL). Details of the construction of these lasers can be found in Ref. [58]. For the majority of the work discussed in this thesis, a Toptica frequency doubled system was used to generate the 369 nm light for Doppler cooling (TA-SHG 36). The Toptica system comprises an ECDL (DL pro) to generate 739 nm light, a tapered amplifier (TA) to amplify the light from 40 mW to 400 mW and a bow-tie cavity containing a second harmonic generation (SHG) doubling cystal, which converts the light to the required 369 nm with an output power of up to 60 mW. For the later experiments, mainly in Chapter 6, a newer 369 nm laser system was used. This is a MSquared system, comprising a Ti:sapphire laser (SOLSTIS CW) for the 739 nm light and a bow cavity with a SHG crystal (ECD-X) to double the frequency, with a 369 nm output power of 1.3 W.

Fig. 2.11 shows a schematic of the experimental setup showing the main features used to deliver the required light to the ions. The main elements of this setup will be discussed in the following paragraphs. The vacuum system containing the ion trap along with some optics were placed inside a Faraday cage* in order to reduce electrical noise. The Faraday cage has two doors on two of the four sides to allow for access. One issue encountered was that if all doors were closed, the heat from the high current coils inside the cage caused the temperature to increase significantly,

*designed by Eamon Standing

causing the pressure inside the vacuum system to increase. For this reason, the Faraday cage was left open for all experiments discussed in this thesis. A method to reduce the heating effect remains to be investigated.

All four lasers are situated outside of the Faraday cage. The three home built lasers have identical simple optical setups consisting of an optical isolator, a beam picker to send a small amount of light to the wavemeter and steering mirrors to couple the light into an optical fibre. The optical fibres are then passed through small holes in the walls of the Faraday cage. For the 369 nm laser, the optical setup is almost identical for both the Toptica and MSquared laser systems. Before being sent to the doubling cavity, some 739 nm light is picked off to be sent to both the wavemeter and the locking setup (discussed in the following section). The 739 nm light also passes through an electro-optic modulator (EOM, MSquared system: Qubig EO-T1055M3, Toptica System: New Focus 4441), which if switched on adds ≈ 1 GHz sidebands. The reason for such a modulation will be discussed in the following sections. For the MSquared system, the EOM is driven using a purpose built module (Qubig EDU high res + AMP - 2H) with an output frequency of 1.055 GHz and maximum power of 4 W, while for the Toptica system, a frequency source (Rohde and Schwarz SML 01) is used along with a switch (Mini Circuits ZFSWA2-63DR+) and amplifier (RF Bay MPA-0925). One difference between the Toptica and MSquared systems is that in the Toptica system the EOM is placed before the light is picked off for frequency stabilisation, while in the MSquared system the EOM is placed afterwards. The consequence of this is that in the case of the Toptica, turning on the EOM affects the stabilisation lock, while for the MSquared it is unaffected. After the doubling cavity, the 369 nm light enters a double pass acousto-optic modulator (AOM, Isomet 1212-2-949) setup, which allows the light to be switched on and off on timescales less than 1 μs. The AOM is driven with an adjustable frequency near 200 MHz, and a power of up to 3 W. The required frequency is generated by a voltage controlled oscillator (VCO, Mini Circuits ZX95-200-S+), whose output frequency can be varied through a analog voltage output of the FPGA. The signal is passed through a variable attenuator (Mini Circuits ZX73-2500-S+) which is used to adjust the laser power using a second analog output of the FPGA, a switch (Mini Circuits ZASW-2-50DR+) controlled with a digital FPGA output and two amplifiers (Mini Circuits ZFL-750+ and ZHL-035WF+).

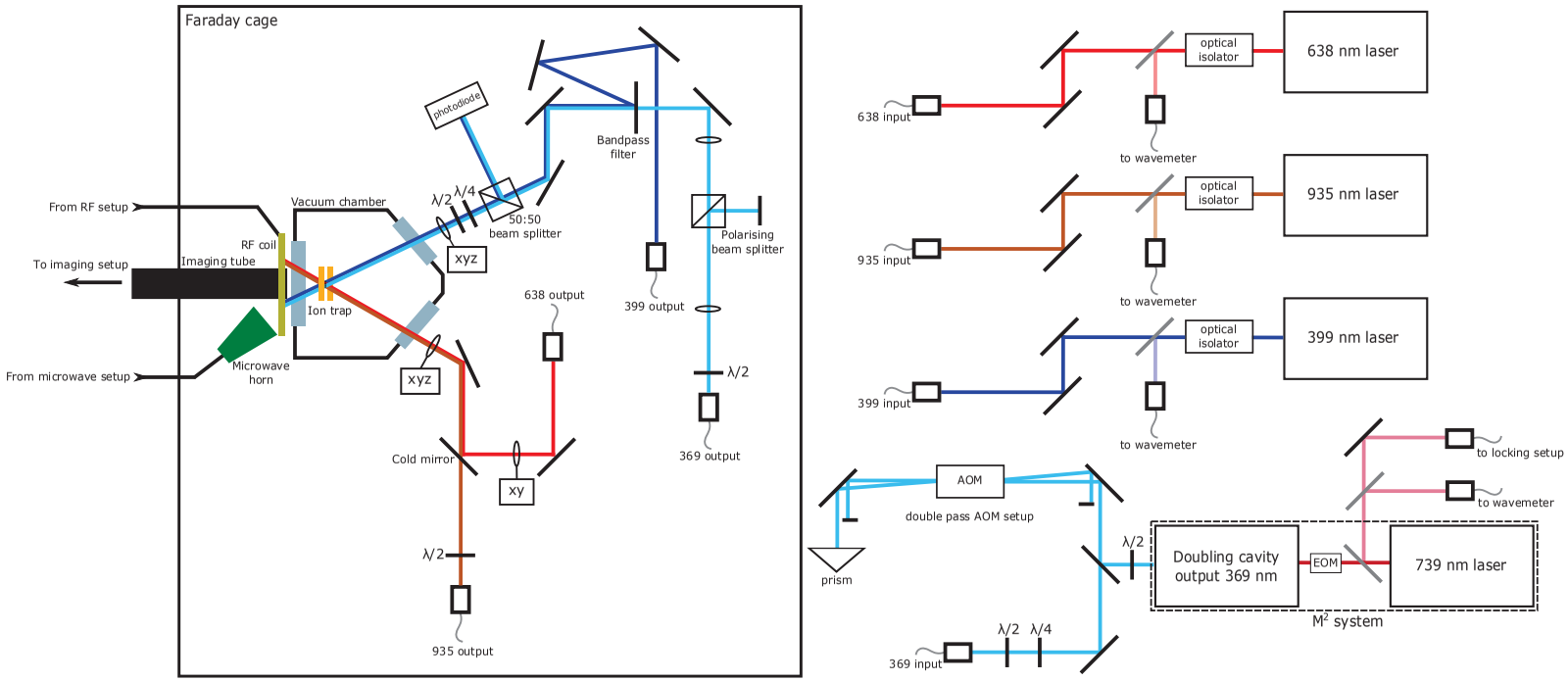


Fig. 2.11 Schematic of the experimental setup used in this work, where each of the main elements are discussed in the text. The box represents a Faraday cage which is positioned around the vacuum system and some of the optics. Light is transferred through the cage using optical fibres. The imaging tube, RF coil and microwave horn are all positioned near the front window of the vacuum system close to the ion trap, and the tube as well as RF and microwave connection cables pass through holes in the wall of the cage.

Inside the Faraday cage, the beams are overlapped and sent through two viewports of the vacuum system to the centre of the ion trap. The 935 nm and 638 nm lasers are overlapped using a cold mirror (Thorlabs, M254C45), which when placed at 45^o to a beam transmits light with wavelength greater than ≈ 700 nm and reflects light of lower wavelength. The overlap of the two beams is adjusted using an xy translation stage holding a lens in the 638 nm beam path only, and both beams are focussed and imaged to the centre of the ion trap using an xyz translation stage holding a lens. After exiting the optical fibre, the 369 nm light passes through a polarising beam splitter (Eksma 430-1157). The beam splitter only allows horizontal polarisation light to pass through, and therefore any fluctuations or drifts in the laser polarisation due to the optical fibre will be turned into intensity fluctuations and drifts. The 369 nm and 399 nm lasers are overlapped using a bandpass filter (Semrock FF01-370/36-25), which is also used as a mirror, with a centre frequency of 370 nm and a bandwidth of 36 nm, thereby allowing 369 nm light to pass through while reflecting 399 nm light. The beams are overlapped using an adjustable mirror in the 399 nm beam path. The light then passes through a 50:50 beam splitter (Eksma 355-1105), which sends half of the 369 nm light to a photodiode. The photodiode signal is used for a 'noise eater' intensity stabilisation system, consisting of a digital PID circuit in LabVIEW that feeds back a voltage to an attenuator controlling the RF power sent to the 369 nm AOM*. After trapping, the 399 nm light is blocked using an iris (not shown) so that only 369 nm light is detected by the photodiode during an experiment. The beams are then focussed and imaged to the centre of the trap using an xyz translation stage holding a lens.

739 nm Frequency Stabilisation

The 369 nm laser wavelength needs to be stabilised against drifts and fluctuations to ensure Doppler cooling, state preparation and state detection are optimised and repeatable. To achieve this, a three-stage stabilisation setup is used to lock the 739 nm wavelength to the $5^2S_{1/2} \leftrightarrow 5^2P_{3/2}$ transition in rubidium. The stabilisation setup is discussed in detail in Ref. [59], and summarised here. A home built 780 nm ECDL laser is first locked to an atomic transition in ^{87}Rb using a saturation absorption spectroscopy setup. This stabilised laser is then sent into a cavity and the cavity length is locked to the 780 nm laser. The 739 nm laser is then locked to the cavity, and hence through the chain, the 739 nm laser has been locked to the atomic transition. An AOM double pass setup is incorporated into the 780 nm beam path, allowing the

*system designed by Tomas Navickas and Tom Crane.

wavelength of the 780 nm laser, and hence the wavelength of the 739 nm laser, to be fine tuned by tuning the RF frequency sent to the AOM. Substantial improvements to the locking setup have been made since the original design* including adding and replacing PID, amplifier and filtering electronics to reduce noise, adding new larger bandwidth photodiodes, adding a new improved cavity and replacing some analog feedback electronics with a digital FPGA based feedback system.

Imaging

The 369 nm light scattered by the ions is collected by a series of lenses and focussed onto either a CCD camera or photomultiplier tube (PMT). The CCD camera is used for aligning the laser beams and initially detecting ions when trapping, while the PMT is used to take fluorescence measurements during experiments. This setup is discussed in detail in Ref. [60] and summarised here. The optics in the imaging setup are placed in a long lens tube to minimise background light. On the end of the tube a triplet lens is placed close to the window of the vacuum system nearest to the ion trap. The distance between the ion and the triplet lens is approximately 2 cm. The light is focussed by the triplet lens to a point at which an iris is placed, which can be partially closed to allow light from the ions to pass through while blocking light scattered by the electrodes of the ion trap. The light then passes through a doublet lens, before passing through a 370 nm bandpass filter (Semrock FF01-370/36-25) and onto a CCD camera. A flipper mirror is positioned between the filter and the camera, which when positioned upright diverts the light to instead hit a PMT. The total magnification of the system is 35.1. The fraction of photons scattered by the ion that are detected on the PMT (known as the collection efficiency) has been measured to be 0.1% in our system [56].

2.4.3 Microwave and RF setup

In order to drive transitions between the $^2S_{1/2}$ hyperfine states in $^{171}Yb^+$, RF and microwave fields of different frequencies are needed. Furthermore, as will be shown in Sec. 3.3.1, the magnetic field gradient causes the resonant frequencies of the hyperfine transitions in different ions to be separated, and therefore additional frequencies are required for multiple ions. It is also desirable for all required signals to be high power, as a higher power will increase the amplitude of the field at the ion position and thereby increase the Rabi frequency. Higher Rabi frequencies lead to faster single

*improvements carried out by Tomas Navickas.

and multi qubit gates, and consequently higher gate fidelities. For the majority of the work described in this thesis, Analog Devices AD9959 evaluation boards were used to generate the required RF frequencies. These boards output four separate RF signals using direct digital synthesis (DDS), and hence are commonly referred to as 'DDS' boards. With a single 25 MHz clock reference frequency input for all DDS boards, frequencies up to 500 MHz can be generated with a maximum peak to peak output voltage of approximately 700 mVpp (+7 dBm). The frequency, phase and amplitude of the DDS boards are controlled from the experimental computer by USB. Further details of the boards can be found in Ref. [61]. The control of the boards has been modified since the design in Ref. [61] to bypass an Arduino board and communicate directly between the computer and DDS boards via USB, which was found to be more reliable*. A total of four boards are used to create the required signals to implement all of the experiments described in this thesis, totalling 16 frequencies. Two boards are used for the RF signals, while the other two boards are mixed with a microwave oscillator to create the required microwave signals. A schematic of the microwave and RF setups is shown in Fig. 2.12. Each DDS output is first amplified by +18 dB (Mini Circuits ZFL-750+), before passing through a switch (Mini Circuits ZASWA-2-50DR+). The switches can be controlled on fast timescales (rise time ≈ 10 ns) by TTL pulses that are input from the FPGA controlled by the experimental computer. After the switches, the four channels from each DDS are combined using a four-way combiner (Mini Circuits ZMSC-4-3+).

In the RF setup, two further switches allow either of two DDS boards, or an arbitrary waveform generator (AWG, Agilent 33522A) to be selected. The AWG can be used to generate more complex waveforms incorporating features such as pulse amplitude shaping, which is required for some experiments towards the end of this thesis. A directional coupler placed after the switches allows a small fraction of the signal to be diverted to a USB oscilloscope (PicoScope 2208A). This is used to measure the phase relationships of the four fields from one of the DDS boards. For the Mølmer-Sørensen gate described and implemented in Chapter 6, the relative phase relationships ($\phi_i - \phi_j$ for fields i and j) between the six RF fields applied is important. For the setup described here, the phase of each individual field will change for every pulse as the DDS boards continuously output and each pulse start time is defined by a switch turning on, which is uncorrelated with the output frequencies. The relative phases between the fields can however remain constant, but are unknown and vary when the frequencies are changed. The USB oscilloscope therefore allows

*update implemented by Anna Webb.

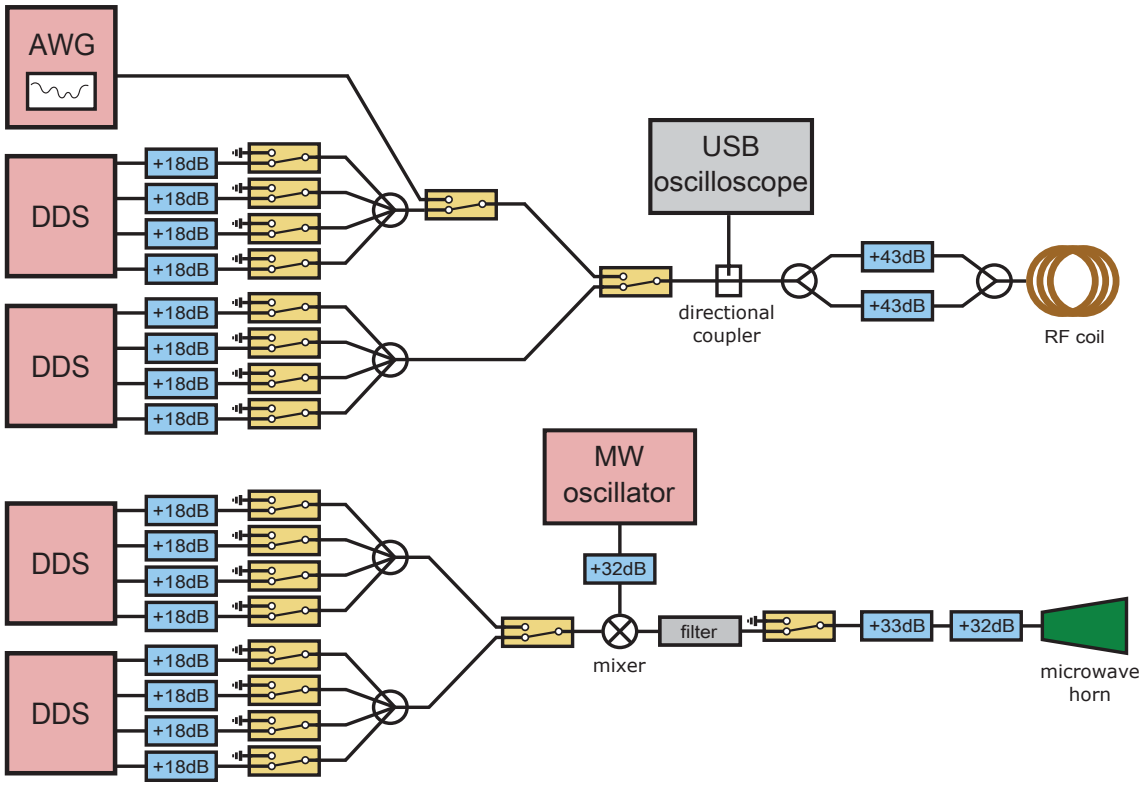


Fig. 2.12 Schematic of the RF and microwave experimental setups, as described in the text. Red boxes indicate frequency sources, blue represent amplifiers and yellow correspond to switches, which can be controlled on fast timescales using TTL pulses from the FPGA.

the waveform to be sampled, from which the relative phases can be extracted and set to the correct value. If the AWG is instead used for generating such a signal, the phases of each field are well defined and identical for each pulse, and therefore this procedure is not required. After the directional coupler, the RF signal is amplified to high power. This is achieved by splitting the signal using a two-way splitter (Mini Circuits ZFSC-2-1-S+), passing the signals through two +43 dB amplifiers (Mini Circuits LZY-22X+) and recombining with a high power two-way combiner (Werlatone D1635-102). The reason for splitting and recombining is to ensure that the signals are kept below the 1 dB compression point (the point at which the gain drops by 1 dB due to amplifier saturation) of the amplifiers to achieve higher powers and reduce unwanted intermodulation frequencies. The signal is then sent to a three turn copper coil* (wire diameter 3.35 mm, coil radius 51 mm) placed close to the front window of the vacuum chamber, which radiates the RF field across the ion trap.

For the microwave setup†, the combined outputs from the two DDS boards are sent to a switch allowing one board to be selected. The RF signal is then mixed with a microwave signal close to 12.6 GHz (Marki Microwave T3-0316MQP). The microwaves are generated by a vector signal generator (VSG, Keysight E8267D) with a power of −12 dBm, which is then amplified by +32 dB (Microwave Amps AM25-12-13-30-33). The microwave frequency is chosen to be 100 MHz less than $\omega_{\mathrm{hf}}/2\pi$ (defined in Sec. 2.3.3), and therefore only the positive modulation sidebands are resonant with hyperfine transitions in the ion, while the carrier and negative modulation sidebands are far off-resonant. With this choice, all of the microwave frequencies can be adjusted individually. To suppress the unwanted carrier and negative modulation sidebands, a custom passband filter (A1 Microwave WG 18) with a sharp passband region from 12.593 GHz to 12.793 GHz is used. The microwave signal then passes through a final switch (AMC SWN-218-2DT), after which it is amplified in two stages (Ciao Wireless CA1020-503 +33 dB gain and Microwave Amps AM25-12-13-30-33 +32 dB gain) and sent to a microwave horn (Flann Microwave 18240-10) positioned close to the front window of the vacuum chamber. The horn emits linearly polarised radiation and is orientated approximately 45° to the z-axis of the trap, and rotated so that the polarisation is approximately 45° from horizontal. This ensures that the microwave field contains σ_-, σ_+ and π components with respect to the quantization axis along the z-direction. Since the microwave field may be distorted by the trap electrodes and vacuum chamber, the polarisation at the ion

*designed by Anna Webb
†designed by Dr. Seb Weidt and Alastair Price

position is not well known and therefore fine adjustment of the horn position and orientation is carried out by optimising the Rabi frequencies of the transitions in the ion.

2.5 Initial experiments

2.5.1 Initial trapping and cooling

To trap $^{171}Yb^{+}$ ions, all required lasers and the imaging are aligned to the centre of the trap. The 369 nm laser is focussed to a beam waist of $\approx 30\,\mu$m and a power of $\approx 50\,\mu$W, corresponding to an intensity at the ion of 3.5×10^4 Wm^{-2}. For this laser it is important to focus the beam to a small waist in order to reduce scatter on the trap electrodes, whereas light from the other lasers will be blocked by the 370 nm filter in the imaging setup and therefore the beams can have larger diameters. The 399 nm laser has a power of $\approx 200\,\mu$W, while the 638 nm laser has a power of ≈ 1 mW. The 935 nm laser has a much larger power of ≈ 6 mW, which is required to power broaden over the hyperfine structure in the $^2D_{3/2}$ and $^3[3/2]_{1/2}$ manifolds. After aligning the optics, a current of 6.2 A is applied to the atomic ovens and the 739 nm laser is red detuned by approximately 50 MHz from the predicted resonance of the $^2S_{1/2}, F = 1 \leftrightarrow {}^2P_{1/2}, F = 0$ transition. After a few minutes, one or more ions can be seen by the CCD camera, after which the 399 nm iris is closed and the oven current is turned off. Fig. 2.13 shows images of linear strings of ions taken using the CCD camera.

For Doppler cooling, the 369 nm beam intensity is set near the saturation intensity and detuned by the natural linewidth $\Gamma/2\pi = 19.6$ MHz. In our experiment the laser power can be switched between two different values, and these are set by the powers required for state preparation and detection. State detection requires a laser intensity near the saturation intensity, and therefore this power is also used for Doppler cooling. We measure a power optimised to give the highest state detection fidelity (discussed in the following section) of $2.6\,\mu$W for our experiment. The AOM frequency is scanned to set the frequencies corresponding to resonance, as well as the frequency corresponding to a detuning of one natural linewidth to the red of the transition for Doppler cooling. These frequencies can then be switched between during each experiment.

To measure the trap frequencies, an RF signal can be applied to the RF coil (normally used to broadcast RF signals to manipulate the ions' internal states) with frequency near that of the trap frequency. Previously, the signal was applied to one

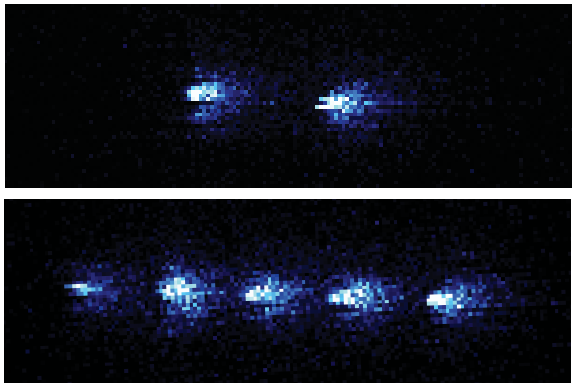


Fig. 2.13 CCD images of linear strings of ions trapped in the experimental setup described in the previous sections. In both cases, the axial trap frequency was measured to be $\nu_z/2\pi = 265\,\text{kHz}$, corresponding to an ion-ion spacing of $8.4\,\mu\text{m}$ for the two ion case (top) and an average ion-ion spacing of $5.8\,\mu\text{m}$ for the five ion string (bottom).

of the endcap electrodes of the trap, which produces an oscillating electric field that can be tuned to resonance with the ion's secular motion. When the field frequency is resonant, the motion of the ion is excited, which can be observed in the fluorescence. We observed a similar effect when applying a signal to the RF coil, which is assumed to arise from small electric fields produced. Since the coil is already integrated into the experiment, this provides an easy way to measure the trap frequencies. We found that axial trap frequencies in the range 100 kHz to 450 kHz could be created using the voltage supply discussed in Sec. 2.4.1. Theoretically the frequency could be lowered by further lowering the endcap voltages, however this was not investigated in detail. Higher axial trap frequencies have also been produced previously using voltage supplies with higher output voltages. The upper limit for the axial trap frequency is determined by the maximum DC voltage that can be applied to the trap electrodes before electrical breakdown, which is expected to be >200 V for a macroscopic trap. Radial trap frequencies in the range 1.5 MHz to 2.0 MHz were measured, corresponding to RF powers in the range 1.6 W to 3 W. For most of the experiments discussed in this work, the RF power was set so that the radial frequencies are 1.524 MHz and 1.56 MHz in the x and y directions.

2.5.2 State preparation and detection

In order to perform coherent quantum operations, it is desirable to prepare the ion in a pure quantum state with high fidelity. In atomic systems this is often achieved using optical pumping, where lasers resonant with certain atomic transitions cause

population to spontaneously decay into a state that is not coupled to the lasers. In $^{171}Yb^{+}$, such a process can be achieved using the three lasers used for Doppler cooling as shown in Fig. 2.7 with the microwave field switched off and by shifting the frequency of the 369 nm laser to be resonant with the $^2S_{1/2}, F = 1 \leftrightarrow {}^2P_{1/2}, F = 1$ transition. The $^2P_{1/2}, F = 1$ states can decay to $^2S_{1/2}, F = 0$, which is not directly coupled by any laser. Therefore any population that falls to this state is trapped, and after some time the population will all be pumped into $^2S_{1/2}, F = 0$. To shift the laser frequency by the required ≈ 2.1 GHz corresponding to the energy splitting between the $F = 0$ and $F = 1$ states in the $^2P_{1/2}$ manifold, the EOM discussed in Sec. 2.4.2 is used. The EOM sits in the 739 nm beam path before it is sent to the doubling cavity, and modulates the 739 nm laser with sidebands at 1.055 GHz. The power of the signal sent to the EOM is adjusted so that the carrier frequency, corresponding to the resonant frequency of the $^2S_{1/2}, F = 1 \leftrightarrow {}^2P_{1/2}, F = 0$ transition, is strongly suppressed.

Coherent manipulation is performed in the $^2S_{1/2}$ manifold, and therefore a method to discriminate between states in this manifold is required. To achieve this, the three lasers used for Doppler cooling are applied with the microwave field switched off. This causes the ion to fluoresce if it is in one of the $^2S_{1/2}, F = 1$ states ($\{|-1\rangle, |0'\rangle, |+1\rangle\}$), and remain dark if in the state $^2S_{1/2}, F = 0$, ($|0\rangle$). It should be ensured that the 369 nm laser polarisation with respect to the quantization axis (z) has equal parts σ_- (right circular), σ_+ (left circular) and π (linear). This can be optimised using the $\lambda/4$ and $\lambda/2$ waveplates situated before the trap in the 369 nm beam path (see Fig. 2.11). By applying the laser for a fixed amount of time and recording the number of photons scattered on the PMT, the two hyperfine levels can therefore be discriminated by setting a threshold number of photons. If the number of photons detected is above the threshold, the ion is recorded as 'bright', while if the number of photons is equal to or below the threshold, the ion is recorded as 'dark'. A limitation to this method is off-resonant coupling of the 369 nm laser to other hyperfine levels in both the $^2S_{1/2}$ and $^2P_{1/2}$ manifolds. If the ion is in the state $^2S_{1/2}, F = 0$, the 369 nm laser is off-resonant by ≈ 14.7 GHz*, which gives a small chance that a dark ion will be detected as bright. An even more likely event can occur if the ion is in the $^2S_{1/2}, F = 1$ manifold, in which case the laser is only ≈ 2.1 GHz off-resonant from the $^2S_{1/2}, F = 1 \leftrightarrow {}^2P_{1/2}, F = 1$ transition. Since population can decay from $^2P_{1/2}, F = 1$ to $^2S_{1/2}, F = 0$, such an event can cause the ion to stop fluorescing during the detection. Since only a small fraction of the scattered photons are detected, this can

*this corresponds to the $^2S_{1/2}, F = 0 \leftrightarrow {}^2P_{1/2}, F = 1$ transition, as the transition $^2S_{1/2}, F = 0 \leftrightarrow {}^2P_{1/2}, F = 0$ is forbidden.

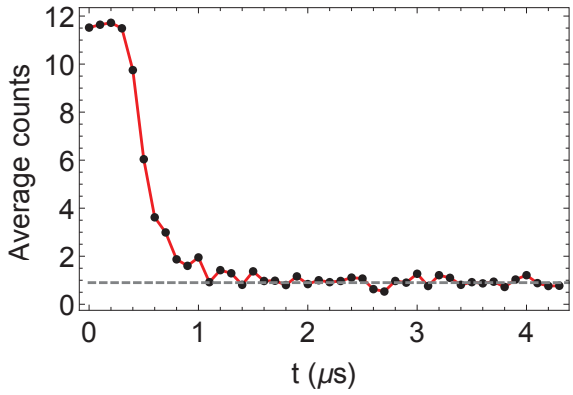


Fig. 2.14 Average photon counts detected after applying the 369 nm laser to a single ion with the EOM switched on for a time t, and detecting for 1.5 ms. Each point is the result of 100 repetitions. The modulated 369 nm laser should cause population to be optically pumped to the state $|0\rangle$ as described in the text, in which case the ion should not scatter any photons during the detection period. The average number of counts detected on the PMT can be seen to reach a steady state of ≈ 0.9 average photons (dashed grey line) after approximately 2 μs. The excess photons are attributed mainly to background scatter of the 369 nm laser on the trap electrodes, which agrees with the result of a similar experiment performed when no ion is in the trap.

cause a bright ion to be detected as dark. The likelihood of such an off-resonant scattering event increases with time, and therefore the time in which the 369 nm light can be applied for detection is limited.

The state preparation and detection fidelities are hard to separate, and therefore are usually combined into a single error or infidelity known as SPAM (state preparation and measurement) error. A rate equations simulation of the $^{171}Yb^{+}$ system* predicts that a state preparation infidelity of $<10^{-4}$ should be achievable in our system, and therefore most of the infidelity is predicted to come from the limitation in detection due to off-resonant coupling, as described in the previous paragraph. To determine the time required for preparation, the ion is first Doppler cooled, after which a pulse of 369 nm light is applied for a variable time. The power in this case is set to approximately 50 μW, the EOM is switched on and the AOM frequency is set to be resonant with the $^2S_{1/2}, F = 1 \leftrightarrow {}^2P_{1/2}, F = 1$ transition. The ion fluorescence is then detected after applying the 369 nm light for 1.5 ms, where the power is set to approximately 2.6 μW, the EOM is switched off and the AOM frequency is set to resonance. The average number of photons detected after such an experiment is then obtained by repeating the experiment multiple times. The result

*written by Dr. Kim Lake and discussed in Ref. [59].

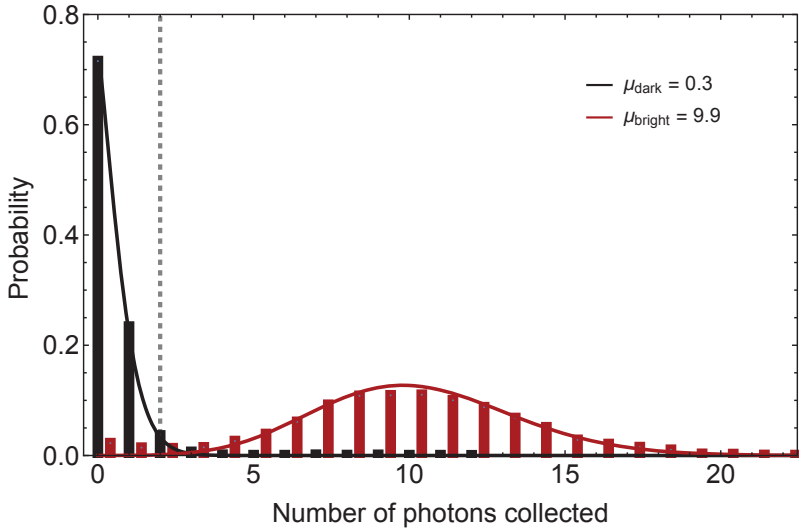


Fig. 2.15 Histograms of detected photons after preparing a single ion in the state $|0\rangle$ (black) or the state $|0'\rangle$ (red) and detecting for 0.7 ms. Each histogram is the result of 5000 repetitions. The data is fitted with a Poissonian function given in Eq. 2.25, with mean photon values of $\mu_{\text{dark}} = 0.3$ for the dark measurement and $\mu_{\text{bright}} = 9.9$ for the bright measurement. The slight deviations from Poissonian shapes of the histograms are attributed to off-resonant coupling of the 369 nm detection beam as discussed in the text. Setting a threshold of 2 photons (dashed grey line), the probabilities to measure the correct state are $P(\text{dark}|0) = 0.986$ and $P(\text{bright}|0') = 0.950$, and therefore the detection fidelity is 0.968.

is shown in Fig. 2.14, and it can be seen that the population reaches a steady state after approximately 2 μs. Ideally there would be zero average photons recorded at this point. The excess photons are attributed to background scatter of the 369 nm laser on the trap electrodes, while the off-resonant coupling of the 369 nm laser is considered negligible for this detection time.

To characterise the detection, firstly the ion is prepared in $|0\rangle$ by applying the 369 nm light with the EOM switched on for a time greater than the time to reach the steady state as measured in the previous experiment. The state is then detected and the experiment is repeated several times, allowing a histogram of the number of photons detected to be recorded. Secondly the same experiment is repeated, except that after preparation in $|0\rangle$ a microwave field transfers the population to $|0'\rangle$. This is achieved through a coherent process introduced in Sec. 2.2.3 which is discussed in further detail in the following section. It is estimated that the transfer is achieved with an infidelity $<10^{-3}$. The histograms from the two experiments can then be plotted together, and the overlap between the two indicates the detection fidelity. The histograms should approximately follow Poissonian statistics if off-resonant coupling effects are neglected, and therefore can be fitted with a Poissonian function

as a function of the photon number n, given by

$$f_{\text{poisson}}(n) = \frac{\mu^n}{n!} e^{-\mu}, \tag{2.25}$$

where μ is the mean photon number. A fluorescence detection measurement gives n photons, and for a threshold t_1, if $n \leq t_1$, the measurement result is dark, whereas if $n > t_1$, the measurement result is bright. For a given t_1, the fraction of events in which an ion was prepared in $|0\rangle$ and was detected as dark, $P(\text{dark}|0)$, can be calculated, as well as the fraction of events in which an ion was prepared in $|0'\rangle$ and detected as bright, $P(\text{bright}|0')$. The average of these two numbers is then the detection fidelity. t_1 is chosen to maximise this fidelity. Fig 2.15 shows the result of such an experiment, giving a detection fidelity of 0.968. This is significantly lower than the threshold required for fault-tolerant quantum computation, and is mainly limited by the low proportion of scattered photons that are collected by the imaging system (known as the collection efficiency) as well as the background photons scattered from the trap electrodes. As discussed previously, the 369 nm light can off-resonantly couple to other levels in the $^{171}Yb^+$ ion, causing errors in detection. The chance of such an event occurring increases with the detection time, and therefore the detection time should be kept short. However, if only a small fraction of the photons scattered by the ion are collected, it may be the case that no photons are detected even when the ion is in the bright state. A larger collection efficiency increases the chance of detecting photons for a given detection time, and therefore increases the detection fidelity. In Ref. [62], a specially designed optic was built that achieves a collection efficiency of 10%, and using this a detection fidelity of 0.99915(7) was achieved for the $^{171}Yb^+$ hyperfine levels. Therefore the low detection fidelity is not a fundamental problem, and future experimental setups will incorporate optics with higher collection efficiencies to remove this limitation.

Assuming that errors in state preparation can be neglected, an experiment such as that shown in Fig. 2.15 gives a linear map between the probabilities for the ion to be in the $F = 0$ or $F = 1$ manifolds of $^2S_{1/2}$ and the probabilities for the ion to be detected as dark or bright. For an experiment that is repeated multiple times, this map can then be used to infer the state of the ion given a set of dark or bright measurements. The method to achieve this, as well as the associated error in the measurement, is discussed in Appendix B.

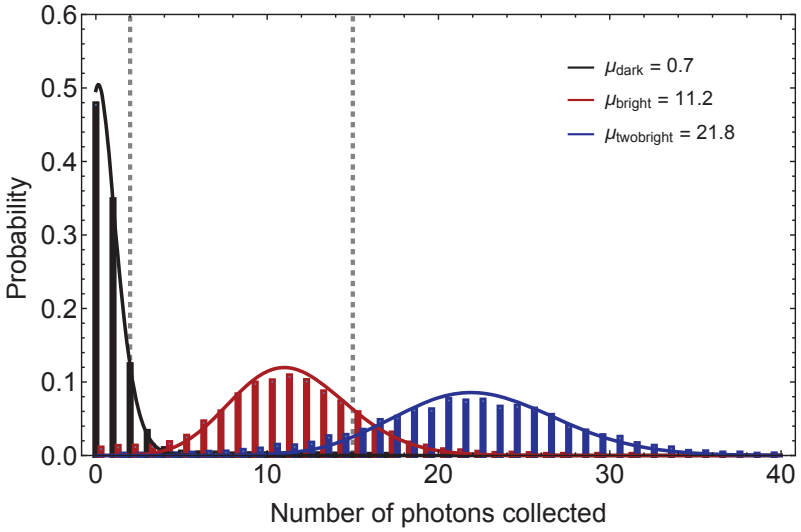


Fig. 2.16 Histograms of detected photons after preparing a two ions in the state $|00\rangle$ (black), $|0'0\rangle$ (red) or $|0'0'\rangle$ (blue) and detecting for 0.7 ms. Each histogram is determined from 5000 repetitions. The data is fitted with Poissonian functions, with mean photon values of 0.7 for the dark measurement, 11.2 for the bright measurement and 21.8 for the two bright measurement. Setting the two thresholds to be 2 and 15 (dashed grey lines), the probabilities to detect the correct state are $P(\text{dark}|00) = 0.946$, $P(1\text{ bright}|0'0) = 0.855$ and $P(2\text{ bright}|0'0') = 0.853$, giving a two ion detection fidelity of 0.885.

Two ion detection

For two ions, there are four possible final states that could be detected for which $\{F_1, F_2\} = \{0,0\}$, $\{0,1\}$, $\{1,0\}$ and $\{1,1\}$, where F_j is the F quantum number in the ${}^2S_{1/2}$ manifold for ion j. Using a PMT, only the total fluorescence from both ions can be recorded and with two thresholds, there are three possible detection outcomes; 'dark', 'one bright' and 'two bright'. As discussed in Sec. 3.3.1, the addition of a magnetic field gradient to the experimental setup allows the ions to be individually addressed by microwave and RF fields, and therefore all four states can be prepared, but only three can be discriminated. The fluorescence histograms after a detection event follow Poissonian statistics (Eq. 2.25), for which the mean photon number μ is the only variable. Therefore the two histograms for the one bright and two bright events have a significantly larger overlap with each other compared to the dark and one bright histograms. This causes the detection fidelity for two ions to be much lower than the single ion case. Fig. 2.16 shows the state detection histograms after preparing the ion in the states $|00\rangle$, $|0'0\rangle$ and $|0'0'\rangle$, giving a detection fidelity of 0.885. As in the single ion case, the histograms can be used to normalise the state detection errors from subsequent experiments, allowing the state of the ions

to be inferred from the measurements. Again, this is discussed in further detail in Appendix B. The detection fidelity for two ions is much lower than for a single ion when using a PMT, and as the ion number increases, the overlap between histograms gets larger and hence the detection fidelity gets worse. Therefore this detection method is not scalable to a large ion array. To achieve higher fidelities and a more scalable solution, a CCD camera could be used instead of a PMT, for which the ions can be spatially resolved. Such a detection method could be implemented using our experimental setup and is currently being investigated for future experiments. Alternatively, ions could be shuttled to 'detection zones', in which they are detected away from other ions. This would require microfabricated trapping structures that allow for ions to be shuttled, separated and recombined and is also being investigated in the group.

2.5.3 Rabi oscillations

In Sec. 2.2.3, the theory of two hyperfine states interacting with an electromagnetic field was described. This theory can be applied to microwave and radio frequency fields interacting with the states making up the $^2S_{1/2}$ manifold in $^{171}\mathrm{Yb}^+$. As discussed in Sec. 2.3.3, for typical magnetic fields of $\approx 10\,\mathrm{G}$, the resonant frequencies corresponding to the energy splittings between the states $\{|-1\rangle, |0'\rangle, |+1\rangle\}$ in the $F = 1$ sub manifold are in the radio frequency region. Therefore an RF field can drive transitions between these states. Transitions between $|0\rangle$ and the three $F = 1$ states can be driven using microwave fields with a frequency near $\omega_{\mathrm{hf}}/2\pi \approx 12.6\,\mathrm{GHz}$. The Rabi frequency for a transition between two states $|i\rangle$ and $|j\rangle$ can be calculated from the magnetic field amplitude of the oscillating field, $\vec{B}_0$, as $\Omega_{ij} = \langle j| \vec{\mu} \cdot \vec{B}_0 |i\rangle$. In our setup, the microwave and RF fields are applied using antennae external to the vacuum chamber and are only coarsely aligned. For this reason, and also due to the potential interference between the fields and the trap structure, the magnetic field magnitude and polarisation at the ion position are not well known. The Rabi frequencies for the different transitions are therefore found and optimised experimentally.

Rabi oscillations between hyperfine states in $^{171}\mathrm{Yb}^+$ can be implemented using the RF and microwave setups described in Sec. 2.4.3. To find the centre frequency of a microwave transition, a single frequency microwave pulse with fixed time should be applied to the ion after preparing in $|0\rangle$ using the preparation method described in Sec. 2.5.2. The frequency of the microwave field can then be scanned over a range near the estimated frequency. Fig. 2.17 shows the result of such an experiment when a microwave field is scanned over the resonance of the $|0\rangle \leftrightarrow |0'\rangle$ 'clock'

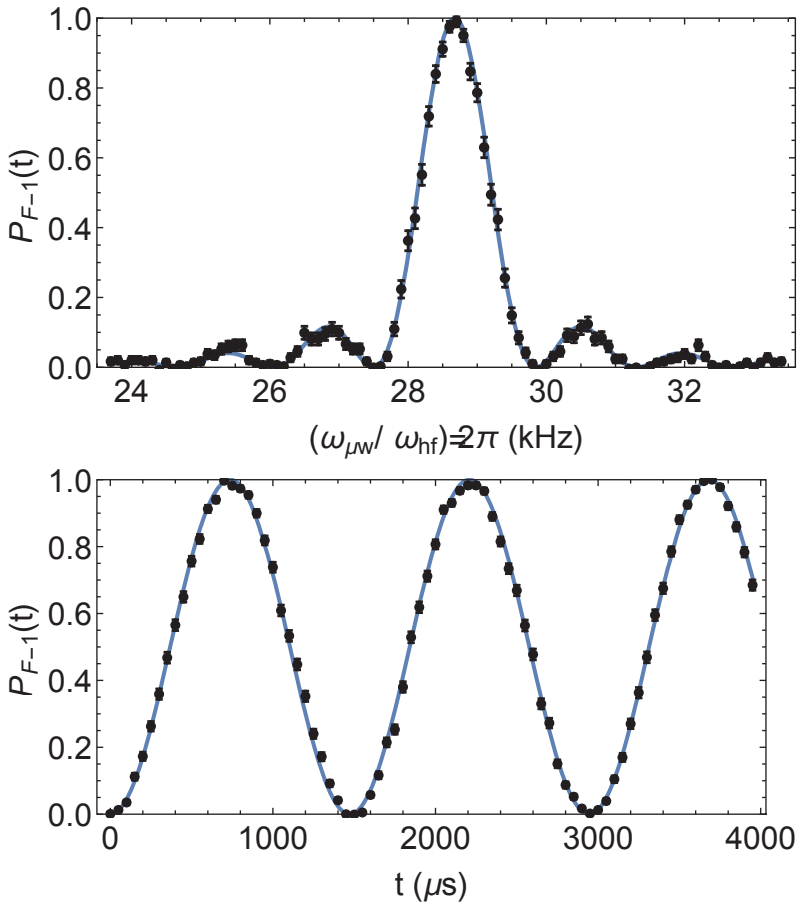


Fig. 2.17 Top: Population in F=1 after preparing in $|0\rangle$ and applying a microwave field near-resonant with the $|0\rangle \leftrightarrow |0'\rangle$ 'clock' transition for a time $t = \pi/\Omega_c$, where Ω_c is the Rabi frequency, and varying the detuning δ_c. Each point is the result of 300 repetitions, where a threshold of 2 photons has been used to discriminate between the two states and the data has been normalised as discussed in the text. The blue curve is a fit to the data following Eq. 2.23, which gives a centre frequency compared to the zero magnetic field frequency ω_{hf} of $(\omega_0 - \omega_{\mathrm{hf}})/2\pi = 28.675(3)\,\mathrm{kHz}$. Bottom: After setting the frequency to the centre of the transition determined by the top graph, the time of the microwave pulse is scanned. The population can be seen to sinusoidally oscillate between the two states, known as Rabi oscillations. Each data point consists of 1000 repetitions. The data is fitted with Eq. 2.23 with $\delta_c = 0$ and Ω_c as the only free parameter. The fit gives $\Omega_c/2\pi = 679.0(4)\,\mathrm{Hz}$.

transition, with the pulse time set to $t = \pi/\Omega_c$, where Ω_c is the Rabi frequency. The data is fit with a theory curve following Eq. 2.23, giving a centre frequency $(\omega_0 - \omega_{\mathrm{hf}})/2\pi = 28.675(3)\,\mathrm{kHz}$. After finding the centre frequency, a similar experiment can be performed where the frequency of the microwave field is fixed and the pulse time is varied. This results in Rabi oscillations, also shown in Fig. 2.17. A fit using Eq. 2.23 gives a Rabi frequency of $\Omega_c/2\pi = 679.0(4)\,\mathrm{Hz}$. It can be seen that there is almost no decay in the contrast of the Rabi oscillations on the timescale shown in the figure. This is due to the fact that the energies of the two states $|0\rangle$ and $|0'\rangle$ are independent of the magnetic field to first order, and therefore fluctuations in the magnetic field do not affect the qubit coherences. This is not the case for transitions involving the magnetic field sensitive states $|-1\rangle$ and $|+1\rangle$, as will be shown in the following section.

2.5.4 Magnetic field noise

Magnetic field noise causes dephasing of superpositions of states whose energy difference depends on the magnetic field. To see this, consider two atomic states $|\downarrow\rangle$ and $|\uparrow\rangle$. If the energy of the state $|\uparrow\rangle$ has a linear dependence on magnetic field so that $\epsilon_\uparrow = \mu_B B$ (for $g_F m_F = 1$) and the energy of the state $|\downarrow\rangle$ is independent of the magnetic field, magnetic field noise will have a Hamiltonian

$$H_{\mathrm{noise}} = \mu_B \Delta B(t) \left|\uparrow\right\rangle \left\langle\uparrow\right|, \tag{2.26}$$

where $\Delta B(t)$ is an arbitrary time dependent magnetic field noise term. To see the effect of such a Hamiltonian, we can consider a noise function of the form

$$\Delta B(t) = B_0 \cos(\omega_f t + \phi_f). \tag{2.27}$$

For an arbitrary state $|\psi(t)\rangle = c_\downarrow(t)\,|\downarrow\rangle + c_\uparrow(t)\,|\uparrow\rangle$, the Schrödinger equation with this Hamiltonian gives a set of two uncoupled differential equations, given by

$$\begin{aligned} i\dot{c}_\downarrow(t) &= 0, \\ i\dot{c}_\uparrow(t) &= \frac{\mu_B}{\hbar} B_0 \cos(\omega_f t + \phi_f) c_\uparrow(t), \end{aligned} \tag{2.28}$$

with solutions

$$\begin{aligned} c_\downarrow(t) &= c_\downarrow(0), \\ c_\uparrow(t) &= c_\uparrow(0) e^{-i\mu_B B_0 \sin(\omega_f t + \phi_f)/\hbar\omega_f}. \end{aligned} \tag{2.29}$$

If we start in an equal superposition state, where for simplicity we set the initial phase to zero so that $c_\downarrow(0) = c_\uparrow(0) = 1/\sqrt{2}$, the state at time t is then

$$|\psi(t)\rangle = \frac{1}{\sqrt{2}}\Big(|\downarrow\rangle + \exp(-i\mu_B B_0 \sin(\omega_f t + \phi_f)/\hbar\omega_f)\, |\uparrow\rangle \Big). \tag{2.30}$$

The effect of the noise is therefore an oscillation in the relative phase between the two qubit states at frequency ω_f, phase ϕ_f and amplitude $\mu_B B_0/\hbar\omega_f$. If these parameters are unknown and vary between experiments, the average effect is a dephasing of the qubit coherences, exponentially reducing the off-diagonal elements of the density matrix with a characteristic timescale T_2, known as the coherence time.

A simple approximation, known as pure dephasing, is that the off-diagonal density matrix elements decay exponentially at a rate $\Gamma = 1/T_2$. An analytical solution for the population in $|\uparrow\rangle$ after preparing in $|\downarrow\rangle$ and applying a resonant field for time t is derived in appendix A, and is found to be

$$P_\uparrow(t) = \frac{1}{2}\left[1 - e^{-\Gamma t/2}\left(\cos(\Omega_\Gamma t/2) + \frac{\Gamma}{\Omega_\Gamma}\sin(\Omega_\Gamma t/2)\right)\right], \tag{2.31}$$

where $\Omega_\Gamma = \sqrt{4\Omega_0^2 - \Gamma^2}$. Fig. 2.18 shows the result of an experiment in which a microwave field was applied near resonant with the $|0\rangle \leftrightarrow |+1\rangle$ transition. The energy of $|+1\rangle$ is linearly dependent on the magnetic field, and therefore this system is identical to the one described above. A fit to Eq. 2.31 gives a coherence time of $T_2 = 2.2(1)\,\mathrm{ms}$.

In a real experimental environment, magnetic field noise will typically exhibit a spectrum that is inversely proportional to frequency. This feature can be utilised to suppress dephasing with the use of dressed states, where the coupling of the noise to the atomic states is limited to a specific frequency bandwidth. This subject is the focus of chapter 4.

2.5.5 Magnetic field drifts

Changes in the magnetic field that are slow compared to typical timescales of the experiments cause the resonant frequencies of transitions involving magnetic field

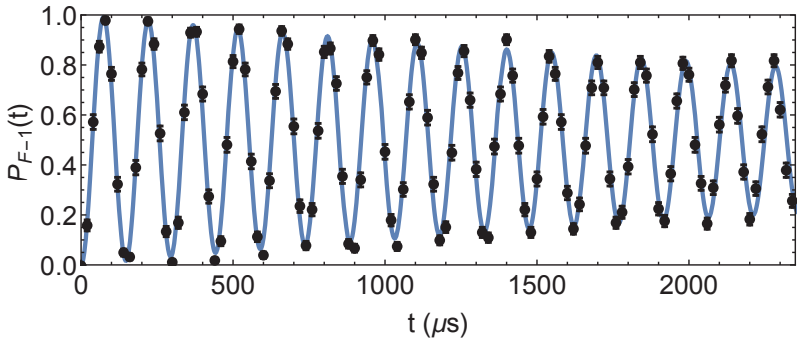


Fig. 2.18 Population in $F = 1$ after preparing in $|0\rangle$ and applying a microwave field resonant with the $|0\rangle \leftrightarrow |+1\rangle$ transition. Each point consists of 300 repetitions. The data is fit with Eq. 2.31 with the Rabi frequency and decoherence time as free parameters, giving $\Omega_+/2\pi = 6.783(2)\,\text{kHz}$ and $T_2 = 2.2(1)\,\text{ms}$.

sensitive states to drift. We find that on timescales of several minutes to hours, the transition frequencies of the microwave and RF transitions in the ${}^2S_{1/2}$ manifold can vary by 10s of kHz. One less common feature in our setup compared to a typical ion trap experiment is that due to the large magnetic field gradient, a change in the position of the ion(s) will also cause the resonant frequencies to shift. It is therefore difficult to distinguish between magnetic field drifts and drifts in the position of the centre of the trapping potential. One observation is that the transition frequencies drift by a large amount after initially running the atomic oven. This is possibly the result of charge build up on the trap electrodes as they are coated with neutral ytterbium atoms, thereby causing the ion positions to move, and such movement is also observed on the CCD camera. Smaller frequency drifts however cannot be observed in this way. Fig. 2.19 shows the result of an experiment where the resonant frequency of the $|0\rangle \leftrightarrow |+1\rangle$ transition was measured over a period of several minutes after the oven has been switched off. It can be seen that the frequency drift reduces after approximately one hour. Consequently, ions are typically left for around one hour after trapping before experiments are performed.

Magnetic field stabilisation

An experiment that involves several repetitions and steps may last many minutes or hours. Therefore during the experiment the magnetic field may drift, causing the transition frequencies to change. To prevent this from occurring, a method to stabilise the magnetic field to a transition in one of the ions is used. To achieve this, a separate experiment is performed between each experimental step in which the ion is prepared in $|0\rangle$ and a weak microwave field is applied near resonant with

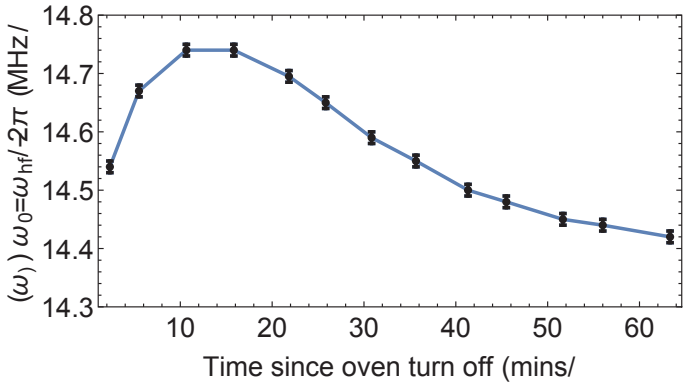


Fig. 2.19 Frequency of the $|0\rangle \leftrightarrow |+1\rangle$ transition for a single ion as a function of time after turning off the atomic oven. The frequency is measured by scanning the frequency of the microwave field over the transition after applying a pulse of length equal to the π-time, similar to the experiment shown in Fig. 2.17.

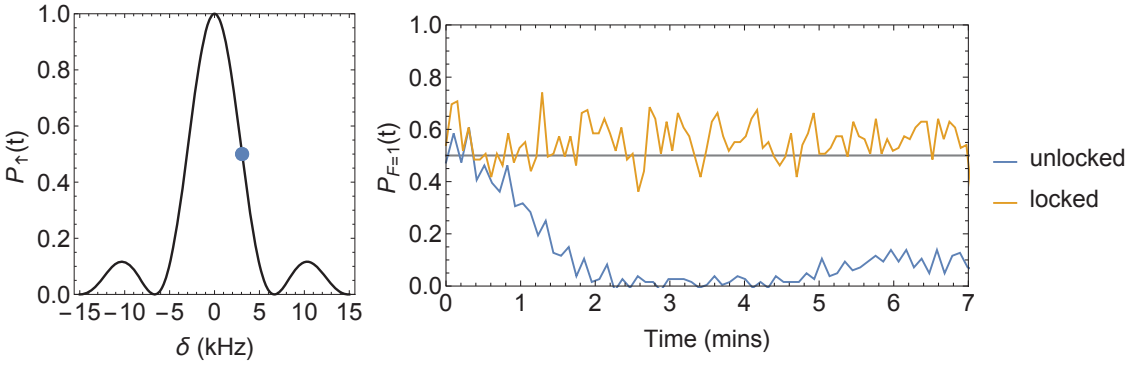


Fig. 2.20 Left: Plot of the theoretical population in $|+1\rangle$ as a function of the detuning of the microwave field from the $|0\rangle \leftrightarrow |+1\rangle$ transition, calculated from Eq. 2.23 with a Rabi frequency $\Omega_s/2\pi = 3.8\,\text{kHz}$. The magnetic field is stabilised to a point halfway up the side of the peak (indicated by the blue point). Right: Population in F = 1 after preparing in $|0\rangle$ and applying a microwave field whose frequency is initially set to halfway up the Rabi peak where a higher Rabi frequency of $\Omega_+/2\pi = 20\,\text{kHz}$ has been used and the pulse applied for a time $t = \pi/\Omega_+ = 25\,\mu\text{s}$. The blue data is for the case in which the magnetic field is unlocked, while the orange data is for the case where it is stabilised as discussed in the text.

the $|0\rangle \leftrightarrow |+1\rangle$ transition with a pulse length equal to the π-time. The frequency of this field is set to be detuned from the transition so that the population in $|+1\rangle$ is 0.5, which is on the side of the transition peak, as shown in Fig. 2.20. If the magnetic field drifts, the population in $|+1\rangle$ will change, which is detected. The difference between the detected population and the original population (0.5) is then calculated, multiplied by a constant factor and sent to a current controller (Delta Elektronika ES030-5) which controls a small coil placed approximately 30 cm away from the ion and centred with the z axis of the trap. This allows the magnetic field to be stabilised to the transition frequency. Fig. 2.20 shows the resulting measured population with and without the magnetic field locking. It is estimated that the magnetic field is stabilised to within 0.2 mG of the required value.

2.5.6 Maximising the magnetic field gradient

As mentioned previously, the permanent magnets creating the magnetic field gradient are only coarsely aligned, and therefore high field Helmholtz coils are required to adjust the magnetic field to reduce it to the required value at the ion positions. As well as adjusting the absolute magnetic field, it should also be ensured that the magnetic field gradient is aligned along the axis of the trap. Simulations of the magnetic field show that as well as the desired magnetic field gradient in the z direction, there is also a gradient of approximately 11 T/m in the x and y directions. The gradient in the z direction is largest when only the B_z component of the magnetic field is non-zero, and therefore the field in the x and y directions should be minimised. The magnetic field can be measured using a magnetic field sensitive transition in the ion as demonstrated previously, and adjusted in the x and y directions using the x and y magnetic field coils. Fig. 2.21 shows an example experiment where the current in the x coil is varied and the $|0\rangle \leftrightarrow |+1\rangle$ transition frequency is measured. After setting this coil current to correspond to the minimum magnetic field, the experiment can be repeated in the y direction after which the magnetic field gradient is aligned along the z axis. The z coil can then be used to adjust the absolute magnetic field felt by the ion to the desired value. The coil currents are typically set between $1 - 2$ A, corresponding to magnetic fields of $15 - 30$ G according to the analysis in Ref. [57].

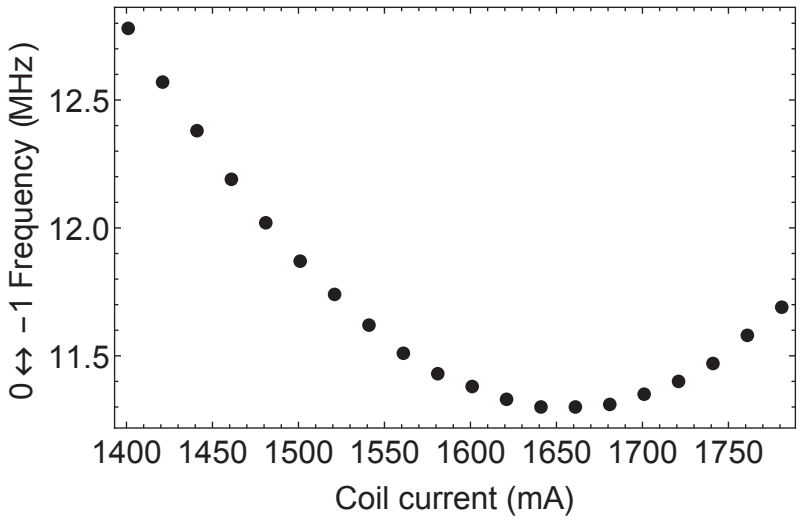


Fig. 2.21 Example data showing the variation of the $|0\rangle \leftrightarrow |+1\rangle$ transition frequency as a function of the current applied to the Helmholtz coil pair in the x direction. The magnetic field in this direction as well as the y direction should be minimised in order to align the magnetic field gradient with the z axis of the trap.

Chapter 3

Coupling spin and motion with a magnetic field gradient

3.1 Introduction

The oscillations of trapped ions in a shared harmonic trap are strongly coupled together due to the Coulomb interaction, and can be described in terms of a series of collective normal modes, as described in Sec. 2.2.2. The collective motion of the ions can be utilised to implement multi-ion quantum logic, such as the two-qubit gates required for quantum computing. Since the qubits are stored in the internal spin states of the ions, the spin and motional states need to be coupled together to transfer quantum information between them in order to implement such gates. A common way to achieve this uses the photon momentum $\hbar k$ of an oscillating electromagnetic field, where k is proportional to ω, the frequency of the radiation. The frequencies associated with the energy splittings between the electronic ground states of trapped ions are in the microwave and radio frequency range, for which the photon momentum produces a negligible coupling strength between the spin and motional states. For this reason, for qubits stored within such states, two-photon Raman transitions using lasers have to be used since the photon momentum is appreciable. Although this method has been hugely successful for small numbers of qubits, there are issues with scalability* that make it desirable to search for an alternative coupling mechanism. In this chapter, it will be shown that the addition of a magnetic field gradient to an ion trap provides a spin-motion coupling that is independent of the frequency of the radiation coupling to the qubit states, as first proposed in Ref. [42] and first demonstrated in Ref. [43]. With this, the transitions

*see chapter 1 for details.

between motional states that are required for multi ion gates can be achieved using long-wavelength radiation.

3.2 Spin-motion coupling with a single ion

The effect of a magnetic field on the energy of a hyperfine state of a trapped ion depends on it's magnetic moment with quantum number m_F. Consider two hyperfine states consisting of $|\downarrow\rangle$ with quantum numbers $F = 0, m_F = 0$ and $|\uparrow\rangle$ with quantum numbers $F = 1, m_F = 1$. Neglecting second-order Zeeman effects, the frequency corresponding to the energy splitting between the two states is therefore given by $\omega_B = \omega_0 + \mu_B B/\hbar$, where ω_0 is the frequency splitting in the absence of any magnetic field, B is the magnetic field, $\mu_B = e\hbar/2m_e$ is the Bohr magneton and m_e is the mass of the electron. The Hamiltonian H_0 describing the ion can be split into two parts H_B and H_m, describing the internal and motional states respectively. Defining the zero point of energy to be halfway between the two states, these Hamiltonian terms are given by

$$\begin{aligned} H_0 &= H_B + H_m, \\ H_B &= \frac{\hbar\omega_0}{2}\Big(|\uparrow\rangle\langle\uparrow| - |\downarrow\rangle\langle\downarrow| \Big) + \mu_B B\, |\uparrow\rangle\langle\uparrow|, \\ H_m &= \hbar\nu_z a^\dagger a, \end{aligned} \tag{3.1}$$

where ν_z is the axial trap frequency and $a, a^\dagger$ are the ladder operators for that motional mode. In this situation, the spin and motional states of the ion are uncoupled and independent of one another. In the following sections, it will be shown how the states can be coupled together in the usual method using the photon momentum of an electromagnetic field, and also an alternative method using a magnetic field gradient.

3.2.1 Spin-motion coupling with photon momentum

Consider an electromagnetic plane wave of frequency ω propagating in the $+z$ direction so that $\vec{k}\cdot\vec{z} = kz$, where $\vec{k}$ is the wavevector with magnitude $k = |\vec{k}| = \omega/c$. The additional Hamiltonian in terms of the internal states of the ion is therefore

$$H^{(l)} = \frac{\hbar\Omega_0}{2}\Big(|\uparrow\rangle\langle\downarrow| + |\downarrow\rangle\langle\uparrow| \Big)\Big(e^{i(kz-\omega t+\phi)} + e^{-i(kz-\omega t+\phi)} \Big), \tag{3.2}$$

where Ω_0 is the Rabi frequency as defined in Sec. 2.2.3 and here we have not made the magnetic dipole approximation where the kz term in the exponentials can be neglected. We can write z in terms of the harmonic oscillator ladder operators as $z = z_e + q = z_0(a + a^\dagger)$, where $z_e = 0$ is the ion's equilibrium position, q is a small displacement about the equilibrium position, $z_0 = \sqrt{\hbar/2m\nu_z}$ is the position spread of the ion's ground state wavefunction and m is the ion's mass. We can define the Lamb-Dicke parameter $\eta_l = kz_0$ such that $kz = \eta_l(a + a^\dagger)$, and then go into the interaction picture with respect to H_0, giving a Hamiltonian term

$$H_I^{(l)} = \frac{\hbar\Omega_0}{2}\Big(|\uparrow\rangle \langle\downarrow| \, e^{i(\omega_B - \omega)t} e^{i\phi} e^{i\eta_l(\tilde{a} + \tilde{a}^\dagger)} + \text{H.c.}\Big), \tag{3.3}$$

where $\tilde{a} = ae^{-i\nu_z t}$, $\tilde{a}^\dagger = a^\dagger e^{i\nu_z t}$ and we have made a rotating wave approximation that neglects terms oscillating at $\omega_B + \omega$. If $\Omega_0 \ll \nu_z$, the Hamiltonian can be decomposed into independent transitions between $|\downarrow\rangle |n\rangle$ and $|\uparrow\rangle |n + m\rangle$, where m is an integer, which can be selected by choosing the appropriate detuning $\delta_m = \omega - (\omega_B + m\nu_z)$ where $\delta_m \ll \nu_z$. The Hamiltonian term for a given n and m is then

$$H_{I,n,m}^{(l)} = \frac{\hbar\Omega_{n,n+m}}{2}\Big(e^{-i\delta_m t} e^{i\phi} |\uparrow\rangle \langle\downarrow| \otimes |n + m\rangle \langle n| + \text{H.c.}\Big), \tag{3.4}$$

where $\Omega_{n,n+m} = \Omega_0 \langle n| \, e^{i\eta_l(a^\dagger + a)} |n + m\rangle$ is the Rabi frequency of the transition. The exponential can then be expanded in powers of η_l. The second order terms contain factors proportional to $\eta_l^2 n$, and so if $\eta_l^2 n \ll 1$, we can discard terms greater than first order in the expansion, which is known as the Lamb-Dicke regime. With this approximation, the zeroth order term is

$$H_c = \frac{\hbar\Omega_0}{2}\Big(e^{-i\delta_c t} e^{i\phi} |\uparrow\rangle \langle\downarrow| + e^{i\delta_c t} e^{-i\phi} |\downarrow\rangle \langle\uparrow| \Big), \tag{3.5}$$

which is a carrier transition where $\delta_c = \delta_{m=0}$ is the detuning from the carrier and the Rabi frequency is $\Omega_{n,n} = \Omega_0$. The first order term consists of two parts which are known as red and blue sideband transitions, given by

$$\begin{aligned} H_r &= \frac{i\hbar\eta_l\Omega_0}{2}\Big(e^{-i\delta_r t} e^{i\phi} a |\uparrow\rangle \langle\downarrow| + e^{i\delta_r t} e^{-i\phi} a^\dagger |\downarrow\rangle \langle\uparrow| \Big), \\ H_b &= \frac{i\hbar\eta_l\Omega_0}{2}\Big(e^{-i\delta_b t} e^{i\phi} a^\dagger |\uparrow\rangle \langle\downarrow| + e^{i\delta_b t} e^{-i\phi} a |\downarrow\rangle \langle\uparrow| \Big), \end{aligned} \tag{3.6}$$

where $\delta_r = \delta_{m=-1}$ and $\delta_b = \delta_{m=+1}$ are the detunings from the red and blue sidebands respectively. The corresponding Rabi frequencies are $\Omega_r = \Omega_{n,n-1} = \sqrt{n} i\eta_l\Omega_0$ and $\Omega_b = \Omega_{n,n+1} = \sqrt{n+1} i\eta_l\Omega_0$. These transitions are illustrated in Fig. 3.1.

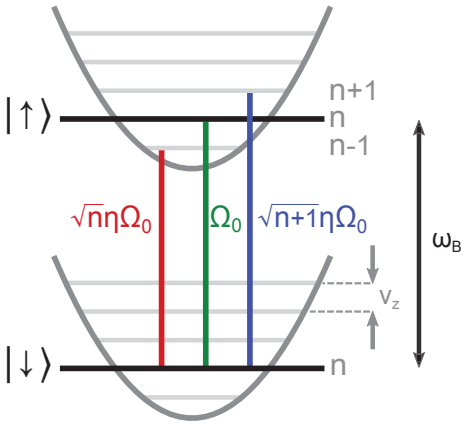


Fig. 3.1 By setting the frequency of the applied field appropriately, the spin state can be changed along with a change in the motional state. Assuming the spin is prepared in $|\downarrow\rangle$, if the frequency is set to $\omega = \omega_B$, a carrier transition to $|\uparrow\rangle$ is driven with Rabi frequency Ω_0, where the motional state is left unchanged. If the frequency is set to $\omega = \omega_B - \nu_z$, a red sideband is driven where the motional state n is reduced by 1, with a Rabi frequency $\sqrt{n}\eta_l\Omega_0$. Finally, if the frequency is set to $\omega = \omega_B + \nu_z$, a blue sideband is driven where the motional state n is increased by 1, with a Rabi frequency $\sqrt{n+1}\eta_l\Omega_0$.

The transition rates between different spin and motional states can be understood by considering the overlap between the harmonic oscillator wavefunctions for different Fock states. The transition rate between two states $|\downarrow\rangle|n\rangle$ and $|\uparrow\rangle|m\rangle$ for a general Hamiltonian H is given by the matrix element $\langle m|\langle\uparrow|H|\downarrow\rangle|n\rangle$. For the interaction Hamiltonian term $H_I^{(l)}$ (Eq. 3.3), the transition rate is therefore proportional to $\langle m|e^{i\eta_l(a+a^\dagger)}|n\rangle = \langle m|D(i\eta_l)|n\rangle$, where $D(\alpha) = e^{\alpha a^\dagger - \alpha^* a}$ is the displacement operator. This is just the overlap between the Fock state $|m\rangle$ and the Fock state that has been displaced in momentum space by an amount η_l, $D(i\eta_l)|n\rangle$. Fig. 3.2 illustrates this overlap for the case that the two motional states are the ground and first excited states. It can be seen that if the displacement is small (i.e. in the Lamb-Dicke regime), then the overlap between the two wavefunctions is approximately linear with η_l, which explains the linear dependence of the sideband Rabi frequencies on η_l. The n dependence of the Rabi frequencies arises from the increase in the number of nodes in the wavefunctions with increasing n, causing the overlap between them to be amplified for a given displacement [63].

We have therefore shown that the spin and motional states of a single trapped ion can be coupled using the photon momentum of an electromagnetic wave. The Lamb-Dicke parameter η_l characterises the relative coupling strength between the carrier and sidebands, and is proportional to the frequency of the oscillating field. For microwave and RF couplings and with typical trap frequencies, the Lamb-Dicke

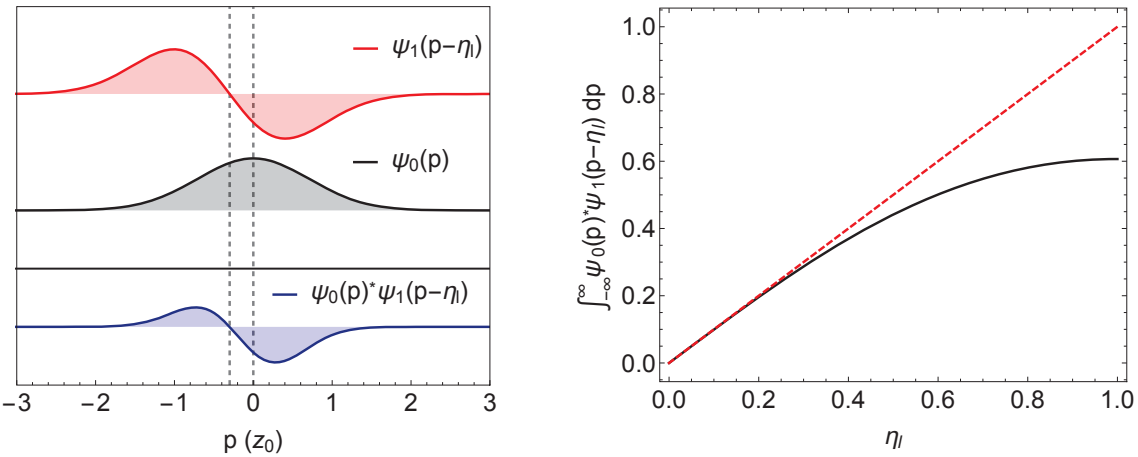


Fig. 3.2 Left: plots of the momentum wavefunctions of the ground (black) and first excited (red) Fock states, where the first excited state has been displaced by an amount $-\eta_l$. The wavefunctions are plotted in units of the variance of the ground state wavefunction z_0. The blue curve shows the multiple of the two wavefunctions. It can be seen that when integrating over momentum, the overlap between the two wavefunctions will be non-zero, indicating that the transition rate between the two states for a Hamiltonian that gives such a displacement will be non-zero. Right: The overlap between the two wavefunctions as a function of the displacement η_l (black). It can be seen that for small η_l, which is equivalent to the Lamb-Dicke regime for the ground state, the overlap is approximately linear (dashed red line). This explains the linear dependence of the sideband Rabi frequencies on η_l.

parameter is negligible. As an example, for the 12.6 GHz microwave transition in $^{171}\mathrm{Yb}^+$ and a trap frequency of $\nu_z/2\pi = 500\,\mathrm{kHz}$, we obtain $\eta_l = 2\times10^{-6}$. Therefore if this spin-motion coupling mechanism is to be used with hyperfine qubits, two-photon Raman transitions with laser light have to be used. In this case, the Lamb-Dicke parameter is $\eta_l = \Delta k_z z_0$, where $\Delta k_z = |k_{z,1} - k_{z,2}|$ is the difference wavevector, which is maximised at $2k_z$ for counter-propagating Raman beams. For the 369 nm transition in $^{171}\mathrm{Yb}^+$ with the same trap frequency, this gives $\eta_l = 0.26$.

3.2.2 Spin-motion coupling with a magnetic field gradient

We will now see that a magnetic field gradient can couple the spin and motional states of a trapped ion and give rise to sideband transitions with a relative carrier-sideband coupling strength that is independent of the frequency of the electromagnetic field. For a magnetic field gradient along the z direction, $B \to B(z) = B_0 + z\partial_z B$, where B_0 is the offset magnetic field and $\partial_z B$ is the magnetic field gradient. Expanding in terms of ladder operators ($z = z_0(a + a^\dagger)$), the modified system Hamiltonian $H_0 = H_B + H_m$ is then

$$\begin{aligned} H_B &= \frac{\hbar\omega_0}{2}\Big(|\uparrow\rangle\langle\uparrow| - |\downarrow\rangle\langle\downarrow|\Big) + \mu_B B_0 |\uparrow\rangle\langle\uparrow|, \\ H_m &= \mu_B \partial_z B z_0 |\uparrow\rangle\langle\uparrow|(a + a^\dagger) + \hbar\nu_z a^\dagger a. \end{aligned} \tag{3.7}$$

H_B therefore determines the qubit energy splitting due to the constant magnetic field component at the ion's equilibrium position $z_e = 0$, while H_m describes the harmonic oscillator and the coupling between the spin and motional states. To see how the ion's motional state is affected, we can write the Hamiltonian H_m as the sum of two parts depending on the spin state as

$$H_m = H_m^\downarrow |\downarrow\rangle\langle\downarrow| + H_m^\uparrow |\uparrow\rangle\langle\uparrow|, \tag{3.8}$$

where the parts are given by

$$\begin{aligned} H_m^\downarrow &= \langle\downarrow| H_m |\downarrow\rangle = \hbar\nu_z a^\dagger a \\ H_m^\uparrow &= \langle\uparrow| H_m |\uparrow\rangle = \mu_B \partial_z B z_0 (a + a^\dagger) + \hbar\nu_z a^\dagger a. \end{aligned} \tag{3.9}$$

In the case of $H_m^\downarrow$, the Hamiltonian is that of the usual harmonic oscillator with eigenstates $|n\rangle$ and ground state $|n = 0\rangle$. For the case of $H_m^\uparrow$, we can introduce new

operators b and $b^\dagger$ with the definitions [64]

$$\begin{aligned} b &= a + \eta, \\ b^\dagger &= a^\dagger + \eta, \end{aligned} \tag{3.10}$$

where we have defined $\eta = \mu_B \partial_z B z_0 / \hbar \nu_z$, allowing $H_m^\uparrow$ to be re-written as

$$H_m^\uparrow = \hbar \nu_z b^\dagger b - \hbar \nu_z \eta^2. \tag{3.11}$$

This is now in the form of the usual harmonic oscillator with ladder operators b and $b^\dagger$ and a constant shift in eigenenergies by an amount $-\hbar\nu_z\eta^2$. The eigenstates are $|n'\rangle$ and the ground state is $|n' = 0\rangle$. In the position basis the wavefunctions can be written in terms of a new position coordinate z', and we can write z' in terms of z by expanding in terms of ladder operators and using the known relationships between $a, a^\dagger$ and $b, b^\dagger$ as

$$\begin{aligned} z' &= z_0(b + b^\dagger) \\ &= z_0 \left(a + a^\dagger + 2\eta\right) \\ &= z + 2z_0\eta. \end{aligned} \tag{3.12}$$

Therefore the effect of the gradient is to displace the motional state by an amount $2z_0\eta$ in the $-z$ direction. This is a similar mechanism to that discussed in Sec. 3.2.1 for the case of spin-motion coupling with photon momentum. In this case however, the displacement is in position rather than momentum. Furthermore, in the magnetic field gradient case, the coupling is present at all times, unlike the photon momentum case where the coupling is only present when the field is interacting with the ion. We can write the energy eigenstates $|n'\rangle$ in the original Fock state basis $|n\rangle$ by using the fact that $b\,|n' = 0\rangle = 0$ and therefore $a\,|n' = 0\rangle = -\eta\,|n' = 0\rangle$. A coherent state $|\alpha\rangle$ is defined as the eigenstate of the annihilation operator a, i.e. $a\,|\alpha\rangle = \alpha\,|\alpha\rangle$, and therefore $|n' = 0\rangle$ is a coherent state in the original basis with $\alpha = -\eta$. A coherent state can be written as a displaced vacuum state, and therefore we find that the relationship between the original and displaced ground state is

$$|n' = 0\rangle = D(-\eta)\,|n = 0\rangle = e^{-\eta(a^\dagger - a)}\,|n = 0\rangle\,. \tag{3.13}$$

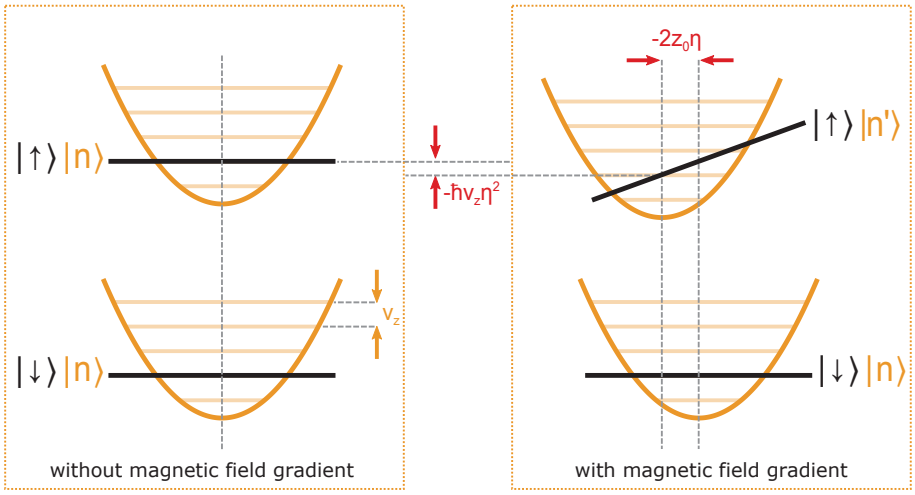


Fig. 3.3 Illustration of a simplified ion consisting of two spin states $|\uparrow\rangle$ and $|\downarrow\rangle$ and a motional mode with Fock states $|n\rangle$. Left: Without a magnetic field gradient, the spin and motional states are decoupled. Right: If the energy of the state $|\uparrow\rangle$ is magnetic field dependent, a magnetic field gradient causes the centre of the harmonic oscillator to be displaced by an amount $-2z_0\eta$ conditional on the spin being in the state $|\uparrow\rangle$, accompanied by a shift in energy $-\hbar\nu_z\eta^2$. The displaced oscillator has displaced Fock states $|n'\rangle = D(-\eta)\,|n\rangle$.

Using this relationship, we can find the excited states of the displaced oscillator as

$$\begin{aligned}
|n'\rangle &= \left(b^\dagger\right)^n |n'=0\rangle \\
&= e^{-\eta(a^\dagger - a)}\left(a^\dagger\right)^n e^{\eta(a^\dagger - a)}\,|n'=0\rangle \\
&= e^{-\eta(a^\dagger - a)}\left(a^\dagger\right)^n e^{\eta(a^\dagger - a)} e^{-\eta(a^\dagger - a)}\,|n=0\rangle \\
&= e^{-\eta(a^\dagger - a)}\left(a^\dagger\right)^n |n=0\rangle \\
&= e^{-\eta(a^\dagger - a)}\,|n\rangle\,,
\end{aligned} \tag{3.14}$$

where we have used the fact that $b^\dagger = e^{-\eta(a^\dagger - a)} a^\dagger e^{\eta(a^\dagger - a)}$(*). The excited states of the displaced oscillator are therefore just the displaced Fock states, as expected. The Hamiltonian term H_m in Eq. 3.1 can now be re-written in terms of the two harmonic oscillators as

$$H_m = \hbar\nu_z a^\dagger a\,|\downarrow\rangle\langle\downarrow| + \hbar\nu_z b^\dagger b\,|\uparrow\rangle\langle\uparrow| - \hbar\nu_z\eta^2\,|\uparrow\rangle\langle\uparrow|\,, \tag{3.15}$$

which is illustrated in Fig. 3.3.

In the above we have seen that a magnetic field gradient causes a displacement

*This can be shown using the identity $e^X Y e^{-X} = Y + [X,Y] + \frac{1}{2!}[X,[X,Y]] + \ldots$

of the harmonic oscillator depending on the spin state. The two displaced oscillators have different motional states $|n\rangle$ and $|n'\rangle$ and operators $a, a^\dagger$ and $b, b^\dagger$, which are related to each other by a displacement operator $e^{-\eta(a^\dagger - a)}$. It would be useful to define new spin states for which the harmonic oscillator states are the same. Such a spin is known as a polaron, which is a quasi-particle that incorporates the harmonic oscillator displacement when the spin is changed. The polaron spin and motional states can be defined by the relations

$$\begin{aligned} |\downarrow_p\rangle |n_p\rangle &= |\downarrow\rangle |n\rangle , \\ |\uparrow_p\rangle |n_p\rangle &= |\uparrow\rangle |n'\rangle = e^{-\eta(a^\dagger - a)} |\uparrow\rangle |n\rangle . \end{aligned} \tag{3.16}$$

The polaron spin states $\{|\uparrow_p\rangle , |\downarrow_p\rangle\}$ and motional states $|n_p\rangle$ cannot be defined in terms of the original states $\{|\uparrow\rangle , |\downarrow\rangle , |n\rangle\}$ individually, and so all calculations must explicitly include both the spin and motional states. The polaron ladder operators are

$$\begin{aligned} a_p &= a |\downarrow\rangle \langle\downarrow| + b |\uparrow\rangle \langle\uparrow| = a + \eta |\uparrow\rangle \langle\uparrow| , \\ a_p^\dagger &= a^\dagger |\downarrow\rangle \langle\downarrow| + b^\dagger |\uparrow\rangle \langle\uparrow| = a^\dagger + \eta |\uparrow\rangle \langle\uparrow| , \end{aligned} \tag{3.17}$$

for which it can be confirmed that the motional operators and states obey the usual harmonic oscillator algebra by finding that $a_p\Big(|s_p\rangle |n_p\rangle \Big) = \sqrt{n_p}\Big(|s_p\rangle |n_p - 1\rangle \Big)$, $a_p^\dagger\Big(|s_p\rangle |n_p\rangle \Big) = \sqrt{n_p + 1}\Big(|s_p\rangle |n_p + 1\rangle \Big)$ and $[\mathbb{I}_p \otimes a_p, \mathbb{I}_p \otimes a_p^\dagger] = 1$, where s refers to either $\uparrow$ or $\downarrow$ and $\mathbb{I}_p = |\uparrow_p\rangle \langle\uparrow_p| + |\downarrow_p\rangle \langle\downarrow_p|$. The full Hamiltonian H_0 can then be written in terms of the polaron states and operators as

$$\begin{aligned} H_B &= \frac{\hbar\omega_0}{2}\Big(|\uparrow_p\rangle \langle\uparrow_p| - |\downarrow_p\rangle \langle\downarrow_p| \Big) + \mu_B B_0 |\uparrow_p\rangle \langle\uparrow_p| , \\ H_m &= \hbar\nu_z a_p^\dagger a_p - \hbar\nu_z \eta^2 |\uparrow_p\rangle \langle\uparrow_p| , \end{aligned} \tag{3.18}$$

where we have used the fact that $\sum_n |s\rangle \langle s| \otimes |n\rangle \langle n| = \sum_{n_p} |s_p\rangle \langle s_p| \otimes |n_p\rangle \langle n_p|$. In this basis, the Hamiltonian now looks like a normal two level system decoupled from the harmonic oscillator, with an extra energy shift on the $|\uparrow_p\rangle$ state in H_m. It should be noted that a unitary transformation can be applied for which the polaron spin and motional states are transformed back to the original basis, known as a polaron

transformation. The unitary operator is given by

$$U_p = e^{\eta(a^\dagger - a)|\uparrow\rangle\langle\uparrow|}, \tag{3.19}$$

for which it can be shown that $U_p |s_p\rangle |n_p\rangle = |s\rangle |n\rangle$, $U_p a_p U_p^\dagger = a$ and $U_p a_p^\dagger U_p^\dagger = a^\dagger$. Although this transformation simplifies the notation, it should be remembered that the real decoupled spin and motional states for an ion in a magnetic field gradient are the polaron states and not the usual spin and motional states, which are intrinsically coupled together. In the following section, it will be shown that by applying an oscillating field near resonant with the qubit transition, transitions between motional states can be realised using the magnetic field gradient.

3.2.3 The effective Lamb-Dicke parameter

We have seen in the previous section that a magnetic field gradient couples the internal and motional states of a trapped ion, however in the appropriate basis, the system can still be viewed as decoupled spin and motional states. We will now add an oscillating field near resonant with the qubit resonance frequency and it will be shown that the magnetic field gradient can drive motional transitions between states in the polaron basis. We will neglect the photon momentum terms $e^{\pm ikz}$ in the Hamiltonian, implying that the field is low frequency (and hence η_l is small). The effects of a magnetic field gradient combined with a field that has significant photon momentum are not considered in this thesis. The Hamiltonian is

$$H_{\text{osc}} = \frac{\hbar\Omega_0}{2}\Big(|\uparrow\rangle\langle\downarrow| + |\downarrow\rangle\langle\uparrow| \Big)\Big(e^{i(\omega t-\phi)} + e^{-i(\omega t-\phi)}\Big), \tag{3.20}$$

where ω is the frequency of the field and ϕ is the phase. We can write this in the polaron basis using the identity

$$\begin{aligned} |\uparrow\rangle\langle\downarrow| &= \sum_n |\uparrow\rangle\langle\downarrow| \otimes |n\rangle\langle n| \\ &= \sum_{n_p} e^{\eta(a_p^\dagger - a_p)} |\uparrow_p\rangle\langle\downarrow_p| \otimes |n_p\rangle\langle n_p| \\ &= e^{\eta(a_p^\dagger - a_p)} |\uparrow_p\rangle\langle\downarrow_p| , \end{aligned} \tag{3.21}$$

where we have used the fact that $a = a_p - \eta \left|\uparrow_p\right\rangle \left\langle\uparrow_p\right|$ and $a^\dagger = a_p^\dagger - \eta \left|\uparrow_p\right\rangle \left\langle\uparrow_p\right|$ to obtain $e^{\eta(a^\dagger - a)} = e^{\eta(a_p^\dagger - a_p)}$. Eq. 3.20 then becomes

$$H_{\text{osc}} = \frac{\hbar\Omega_0}{2}\Big(e^{\eta(a_p^\dagger - a_p)} \left|\uparrow_p\right\rangle \left\langle\downarrow_p\right| + e^{-\eta(a_p^\dagger - a_p)} \left|\downarrow_p\right\rangle \left\langle\uparrow_p\right|\Big)\Big(e^{i(\omega t - \phi)} + e^{-i(\omega t - \phi)}\Big). \tag{3.22}$$

We can now go into the interaction picture with respect to H_0 (Eq. 3.7) to give

$$\begin{aligned} H_I &= e^{iH_0 t/\hbar} H_{\text{osc}} e^{-iH_0 t/\hbar} \\ &= \frac{\hbar\Omega_0}{2}\Big(e^{i(\omega_B - \omega)t} e^{i\phi} e^{\eta(\tilde{a}_p^\dagger - \tilde{a}_p)} \left|\uparrow_p\right\rangle \left\langle\downarrow_p\right| + \text{H.c.}\Big), \end{aligned} \tag{3.23}$$

where $\omega_B = \omega_0 + \mu_B B_0/\hbar - \nu_z\eta^2$ is the resonant frequency of the qubit, $\tilde{a}_p = a_p e^{-i\nu_z t}$, $\tilde{a}_p^\dagger = a_p^\dagger e^{i\nu_z t}$ and we have made a rotating wave approximation that neglects terms rotating at $\omega_B + \omega$. This Hamiltonian is almost identical to that obtained in the case of spin-motion coupling with photon momentum in Eq. 3.3, where η is analogous to the Lamb-Dicke parameter η_l and can hence be thought of as an effective Lamb-Dicke parameter. Unlike the Lamb-Dicke parameter arising from the photon momentum, the effective Lamb-Dicke parameter is only dependent on the magnetic field gradient and the trap frequency and is independent of the frequency of the radiation. This makes transitions between motional states possible using long-wavelength radiation.

We can therefore follow the same derivation as for the photon momentum case, and if we are in the Lamb-Dicke regime for the effective Lamb-Dicke parameter, where $\eta^2 n_p \ll 1$, we arrive at the analogous carrier and sideband Hamiltonians given by

$$\begin{aligned} H_c &= \frac{\hbar\Omega_0}{2}\Big(e^{-i\delta_c t} e^{i\phi} \left|\uparrow_p\right\rangle \left\langle\downarrow_p\right| + e^{i\delta_c t} e^{-i\phi} \left|\downarrow_p\right\rangle \left\langle\uparrow_p\right|\Big), \\ H_r &= -\frac{\hbar\eta\Omega_0}{2}\Big(e^{-i\delta_r t} e^{i\phi} a_p \left|\uparrow_p\right\rangle \left\langle\downarrow_p\right| + e^{i\delta_r t} e^{-i\phi} a_p^\dagger \left|\downarrow_p\right\rangle \left\langle\uparrow_p\right|\Big), \\ H_b &= +\frac{\hbar\eta\Omega_0}{2}\Big(e^{-i\delta_b t} e^{i\phi} a_p^\dagger \left|\uparrow_p\right\rangle \left\langle\downarrow_p\right| + e^{i\delta_b t} e^{-i\phi} a_p \left|\downarrow_p\right\rangle \left\langle\uparrow_p\right|\Big). \end{aligned} \tag{3.24}$$

The corresponding Rabi frequencies for the sidebands are therefore $\Omega_r = \Omega_{n_p, n_p - 1} = \sqrt{n_p}\eta\Omega_0$ and $\Omega_b = \Omega_{n_p, n_p + 1} = \sqrt{n_p + 1}\eta\Omega_0$. There are two small differences between the photon momentum and magnetic field gradient cases. The first is a global phase difference of i for the sidebands between the two cases, and also a relative phase of -1 between the two sideband terms which is only present in the magnetic field

gradient case. These phases can easily be compensated for if required by adjusting the phase of the field. The second is a shift in the resonant frequency of all of the transitions by an amount $-\nu_z\eta^2$. For typical parameters this shift is small, and in practice the resonant frequencies are found experimentally and so the shift goes unnoticed.

Applying a driving field therefore allows for transitions between the polaron spin states $|\downarrow_p\rangle$ and $|\uparrow_p\rangle$ with no change in polaron motional state, as well as transitions that change the spin and motional states by one quanta by setting the detuning to either be resonant with the carrier frequency, or detuned by $\pm\nu_z$. The relative coupling strength of the sidebands to the carrier is given by the effective Lamb-Dicke parameter $\eta = \mu_B\partial_z B z_0/\hbar\nu_z$, which is proportional to the magnetic field gradient, as well as the square root of the phonon number n_p. We can apply the polaron transformation U_p to each of the Hamiltonians given in this section, which allows us to drop the p subscripts in the states and operators.

3.2.4 Driving motional sidebands with microwaves

To demonstrate spin-motion coupling with $^{171}\mathrm{Yb}^+$ in our magnetic field gradient setup, an ion is first prepared in $|0\rangle$, after which a microwave field is applied to couple the $|0\rangle \leftrightarrow |+1\rangle$ transition with frequency $\omega_{\mu\mathrm{w}} = \omega_B + \delta_{\mu\mathrm{w}}$, where $\omega_B = \omega_0 + \mu_B B_0/\hbar - \nu_z\eta^2$ and $\delta_{\mu\mathrm{w}}$ is the detuning from the carrier. By scanning $\delta_{\mu\mathrm{w}}$ over a range covering $\pm\nu_z$, peaks corresponding to the three terms in Eq. 3.24 should be observed, with the replacements $|\downarrow_p\rangle \to |0\rangle$ and $|\uparrow_p\rangle \to |+1\rangle$.

Fig. 3.4 shows the result of such an experiment, where the trap frequency has been set to $\nu_z/2\pi = 265\,\mathrm{kHz}$, giving an effective Lamb-Dicke parameter of $\eta = 0.013$. This gives an extra frequency shift due to the gradient of $-\nu_z\eta^2/2\pi = -46\,\mathrm{Hz}$. The carrier Rabi frequency is $\Omega_0/2\pi = 62.7\,\mathrm{kHz}$, giving relative sideband Rabi frequencies $\sqrt{n}\eta\Omega_0 = \sqrt{n}\times 2\pi \times 0.83\,\mathrm{kHz}$. For a pulse time of $200\,\mu\mathrm{s}$, the three peaks are clearly visible, thereby demonstrating spin-motion coupling with long-wavelength radiation using a magnetic field gradient. Since the ion has only been Doppler cooled, it is in a thermal state with mean phonon number $\bar{n}$. By summing the probabilities to make a transition for each n level and weighting them according to a thermal distribution, $\bar{n}$ can be estimated. This procedure is discussed in more detail in Sec. 5.3. We find that $\bar{n} \approx 60$.

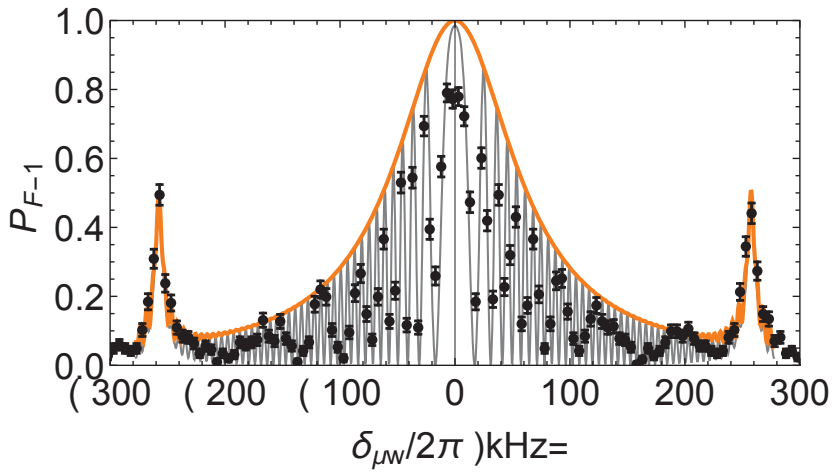


Fig. 3.4 Probability of exciting an ion to F=1 as a function of frequency for a 200 μs microwave pulse, clearly showing the resolved motional sidebands due to the magnetic field gradient. The sideband peaks are separated in frequency from the carrier by the secular frequency $\nu_z/2\pi = 265$ kHz minus a Stark shift of approximately 7.4 kHz. The additional structure in the carrier peak is due to the fact that the pulse time is longer than the π-time of 7.8 μs, and can be seen from Eq. 2.23. The orange curve is the sum of the carrier envelope given by $\Omega_0^2/\sqrt{\Omega_0^2 + \delta_{\mu w}}$ with the sideband terms (discussed in Sec. 5.3) for $\bar{n} = 60$. The grey curve shows the fine structure of the carrier from Eq. 2.23, which is randomly sampled by the data due to the large step size and therefore unresolved.

3.3 Multiple ions in a magnetic field gradient

The theory presented in the previous sections describes a single ion in a magnetic field gradient. When extending this theory to multiple ions in a linear string, there are some extra features that are not present in the equivalent photon momentum case. The first is individual addressing in frequency space, which is immediately apparent for qubits with magnetic field dependent energy splittings that have different positions in a magnetic field gradient. A less apparent feature is an undriven Ising-type spin-spin coupling between each ion pair due to the gradient. This coupling can be used to create entangled states of multiple ions and has been used to implement a CNOT gate between nearest-neighbour and next-nearest-neighbour ions [44]. In this section, the theory of multiple ions in a magnetic field gradient will be presented. It will be shown that as well as individual addressing of qubits, the gradient allows transitions between the ions' internal states and the shared normal modes of the ion string to be implemented, providing a basis for ions to communicate with one another which can be used to implement multi ion quantum logic gates and create entangled states.

3.3.1 Individual addressing

As discussed in 2.2.2, a string of ions at time t have positions z_j in the z direction, where $j = 1, ..., N$ is the ion number. The positions can be written as $z_j \approx z_j^e + q_j$, where z_j^e are the equilibrium positions and q_j are small displacements about the equilibrium. Considering only the equilibrium positions for now and neglecting the second-order Zeeman shift, the multi-ion generalisation of H_B in Eq. 3.7 is

$$H_B = \sum_{j=1}^{N} \frac{\hbar\omega_0}{2}\Big(|\uparrow_j\rangle\langle\uparrow_j| - |\downarrow_j\rangle\langle\downarrow_j| \Big) + \mu_B\Big(B_0 + z_j^e \partial_z B\Big) |\uparrow_j\rangle\langle\uparrow_j| \,. \tag{3.25}$$

The second term is a site-dependent energy shift of the qubit states, where the shift between a pair of ions i and j is proportional to the distance between them $|z_j^e - z_i^e|$ and the gradient $\partial_z B$. The qubit resonant frequencies are therefore given by

$$\omega_j = \omega_0 + \frac{\mu_B}{\hbar}\Big(B_0 + z_j^e \partial_z B\Big). \tag{3.26}$$

An oscillating field can be made to interact with only one qubit at a time by tuning the frequency ω near to ω_j, as long as the Rabi frequency Ω_0 is much less than the frequency difference between the transitions $|\omega_j - \omega_i|$ for all i, j, as illustrated in Fig.

3.5.

To demonstrate this, we performed an experiment on two ions in which the frequency of a microwave field near resonant with the $|0_j\rangle \leftrightarrow |+1_j\rangle$ transition is varied. The result is shown in Fig. 3.5, and it can be seen that the transition frequencies for the two ions are well separated. A figure of merit for individual addressing is the cross-talk, which characterises the effect of driving a transition in one ion on the other ions in a string. The cross-talk can be calculated as the amount of population transferred in a neighbour ion when a resonant pulse is applied to a given ion for a time t after preparing all ions in the state $|\downarrow_j\rangle$. The amount of population transferred can be found from Eq. 2.23 to be

$$P(\uparrow_{ij}) = \frac{\Omega_0^2}{2(\Omega_0^2 - |\delta_{ij}|^2)}\Big(1 - \cos(t\sqrt{\Omega_0^2 + |\delta_{ij}|^2})\Big), \tag{3.27}$$

where $|\delta_{ij}| = |\omega_i - \omega_j|$ is the frequency difference between the field, which is set to be resonant with ion i, and the resonant frequency of the neighbouring ion j. Since we may want to apply pulses of arbitrary length in time, we can simply take the time average of Eq. 3.27 as the cross-talk parameter, which is therefore $C_{ij} = \Omega_0^2/2(\Omega_0^2 + |\delta_{ij}|^2) \approx \Omega_0^2/2|\delta_{ij}|^2$, where the approximation holds for $|\delta_{ij}| \gg \Omega_0$. For our experiment, the cross-talk value obtained is $C_{12} = 2.7 \times 10^{-4}$. In Ref. [65], individual addressing of an 8 ion string was demonstrated with a cross-talk $< 10^{-5}$ using this method.

Although the cross-talk gives an indication of how well the qubits can be addressed, it depends on the Rabi frequency Ω_0, which can in theory be set to any value, thereby giving any cross-talk value. In practice, the Rabi frequency should be high enough to enable high-fidelity gates to be performed on all qubits, which is achievable if the π-time t_π is much less than the coherence time of the transition. A better parameter to characterise the individual addressability could then be the maximum Rabi frequency achievable for a given cross-talk error, which is given by

$$\Omega_{\max}^{ij} = \sqrt{\frac{2C_{ij}|\delta_{ij}|^2}{1 - 2C_{ij}}}. \tag{3.28}$$

For a desired cross-talk of $C_{12} = 10^{-4}$ between two ions using the same parameters as in Fig. 3.5, the maximum achievable Rabi frequency is therefore $\Omega_{\max}^{12}/2\pi = 38.3\,\text{kHz}$.

This measurement can also be used to infer the magnetic field gradient. An additional measurement of the trap frequency is performed using the method discussed in Sec. 2.5.1, which allows the ion spacing to be calculated using Eq. 2.7 to be $\Delta z = 8.365(2)\,\mu\text{m}$. Neglecting the second-order Zeeman shift, the magnetic field

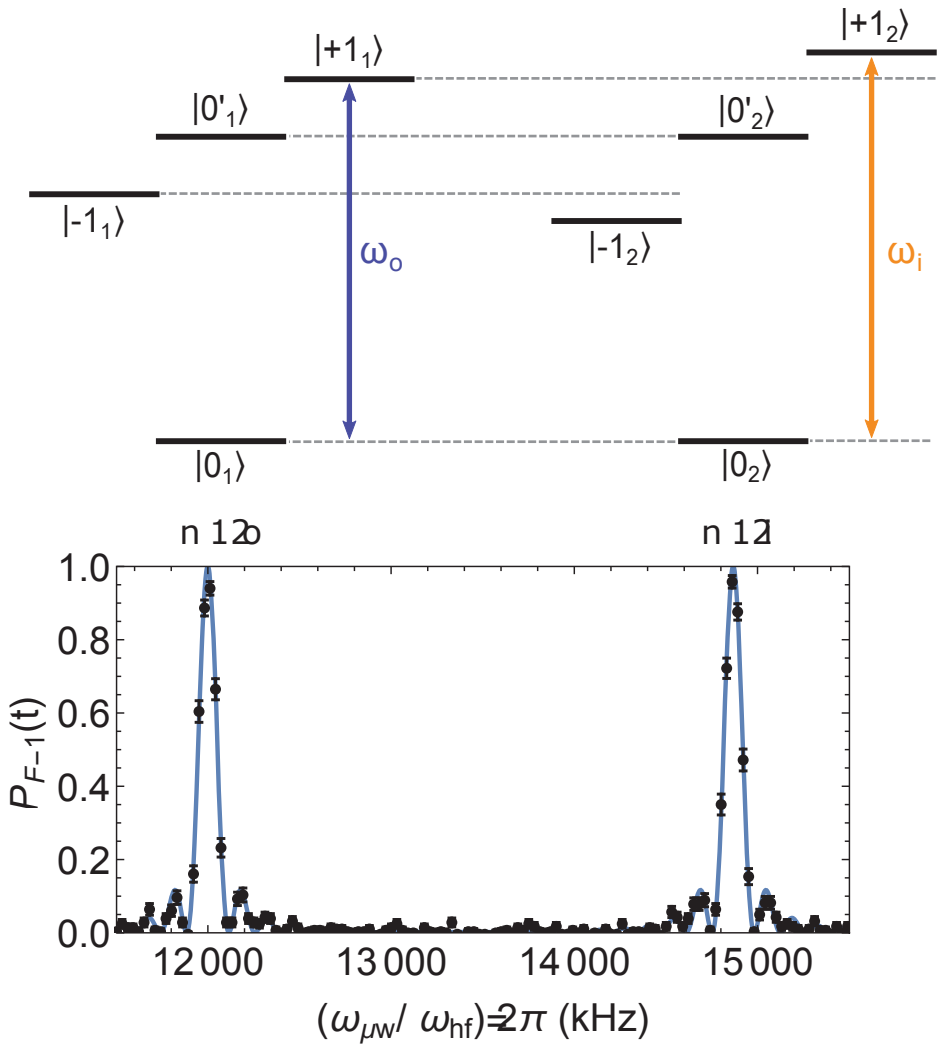


Fig. 3.5 Top: A magnetic field gradient gives rise to site-dependent energy shifts for magnetic field dependent states. In $^{171}\mathrm{Yb}^+$, the $|+1_j\rangle$ and $|-1_j\rangle$ states have first order Zeeman shifts and therefore a transition between $|0_j\rangle \leftrightarrow |+1_j\rangle$ will have a different resonant frequency for each ion j. Bottom: The probability to drive the $|0\rangle \leftrightarrow |+1\rangle$ transition for two ions trapped in a magnetic field gradient. The blue line is a theory curve describing the sum of the two transition probabilities following Eq. 2.23, with a Rabi frequency of $\Omega_0/2\pi = 66.7\,\mathrm{kHz}$. The centre frequencies of the curve are fit to the data, giving a frequency difference of $\Delta\omega_+/2\pi = 2.8679(5)\,\mathrm{MHz}$.

gradient is then given by

$$\partial_z B = \frac{\hbar \Delta\omega_+}{\mu_B \Delta z}. \tag{3.29}$$

We therefore find $\partial_z B = 24.50(1)\,\mathrm{T/m}$*.

3.3.2 Generalising spin-motion coupling to multiple ions

We now consider the ion displacements q_j in the z direction. As described in Sec. 2.2.2, the motional states of a string of trapped ions can be described in terms of a series of normal modes. The normal modes have frequency ν_k, where $k = 1, ..., N$, and the displacements q_j can be written in terms of the normal modes as $q_j = \sum_k S_{jk} z_k^0 (a_k + a_k^\dagger)$, where $z_k^0 = \sqrt{\hbar/2m\nu_k}$, a_k, $a_k^\dagger$ are the ladder operators for the mode k and S_{jk} are normal mode coefficients, as described in Sec. 2.2.2. With these definitions, the Hamiltonian term H_m in Eq. 3.7 can be generalised to the multi-ion case to become

$$\begin{aligned} H_m &= \sum_{j=1}^{N}\sum_{k=1}^{N} S_{jk}\mu_B \partial_z B z_k^0 \left|\uparrow_j\right\rangle \left\langle\uparrow_j\right| (a_k + a_k^\dagger) + \sum_{k=1}^{N} \hbar\nu_k a_k^\dagger a_k \\ &= \sum_{j=1}^{N}\sum_{k=1}^{N} \hbar\nu_k \eta_{jk} \left|\uparrow_j\right\rangle \left\langle\uparrow_j\right| (a_k + a_k^\dagger) + \sum_{k=1}^{N} \hbar\nu_k a_k^\dagger a_k, \end{aligned} \tag{3.30}$$

where we have defined the generalised effective Lamb-Dicke parameter, describing the coupling between ion j and normal mode k, as $\eta_{jk} = S_{jk}\mu_B \partial_z B z_k^0/\hbar\nu_k$. In the multi-ion case, there are many possible displacements of the harmonic oscillator depending on the motional mode and spin configuration. The displaced ladder operators are therefore $b_{jk} = a_k + \eta_{jk}$ and $b_{jk}^\dagger = a_k^\dagger + \eta_{jk}$ and the generalised polaron states are then given by

$$\begin{aligned} \left|\downarrow_{p,j}\right\rangle \left|n_{p,k}\right\rangle &= \left|\downarrow_j\right\rangle \left|n_k\right\rangle, \\ \left|\uparrow_{p,j}\right\rangle \left|n_{p,k}\right\rangle &= e^{-\eta_{jk}(a_k^\dagger - a_k)} \left|\uparrow_j\right\rangle \left|n_k\right\rangle, \end{aligned} \tag{3.31}$$

*this value disagrees slightly with a previously measured value where a Stark shift was not taken into account when measuring the trap frequency.

with corresponding ladder operators given by

$$\begin{aligned} a_{p,k} &= \sum_{j=1}^{N} a_k \left|\downarrow_j\right\rangle \left\langle\downarrow_j\right| + b_{jk} \left|\uparrow_j\right\rangle \left\langle\uparrow_j\right| = a_k + \sum_{j=1}^{N} \eta_{jk} \left|\uparrow_j\right\rangle \left\langle\uparrow_j\right|, \\ a_{p,k}^{\dagger} &= \sum_{j=1}^{N} a_k^{\dagger} \left|\downarrow_j\right\rangle \left\langle\downarrow_j\right| + b_{jk}^{\dagger} \left|\uparrow_j\right\rangle \left\langle\uparrow_j\right| = a_k^{\dagger} + \sum_{j=1}^{N} \eta_{jk} \left|\uparrow_j\right\rangle \left\langle\uparrow_j\right|. \end{aligned} \tag{3.32}$$

With these definitions, Eq. 3.30 becomes

$$\begin{aligned} H_m &= \sum_{k=1}^{N} \left[\hbar\nu_k a_{p,k}^{\dagger} a_{p,k} - \sum_{i=1}^{N}\sum_{j=1}^{N} \hbar\nu_k \eta_{ik}\eta_{jk} \Big(\left|\uparrow_{p,i}\right\rangle \left\langle\uparrow_{p,i}\right| \otimes \left|\uparrow_{p,j}\right\rangle \left\langle\uparrow_{p,j}\right| \Big) \right] \\ &= \sum_{k=1}^{N} \left[\hbar\nu_k a_{p,k}^{\dagger} a_{p,k} - \sum_{j=1}^{N} \hbar\nu_k \eta_{jk}^2 \left|\uparrow_{p,j}\right\rangle \left\langle\uparrow_{p,j}\right| \right] - \sum_{i\neq j}^{N} \hbar J_{ij} \Big(\left|\uparrow_{p,i}\right\rangle \left\langle\uparrow_{p,i}\right| \otimes \left|\uparrow_{p,j}\right\rangle \left\langle\uparrow_{p,j}\right| \Big), \end{aligned} \tag{3.33}$$

where $J_{ij} = \sum_{k=1}^{N} \nu_k \eta_{ik} \eta_{jk}$. The Hamiltonian term in this form is equivalent to the single ion case in Eq. 3.18, except that the energy shift on each ion is now summed over all modes and there is an added third term that, rather than just giving individual energy shifts to each ion, now gives collective pairwise energy shifts, thereby coupling ions together. This is a type of spin-spin coupling and will be discussed further in the next section. For now, however, we will ignore this term and consider the effect of applying an oscillating field to the ion string. Note that just as in the single ion case, we can apply a polaron transformation that allows the p subscripts to be dropped. The multi-ion polaron transformation is given by

$$U_p = \exp\left[\sum_{j=1}^{N}\sum_{k=1}^{N} \eta_{jk}(a_k^{\dagger} - a_k) \left|\uparrow_j\right\rangle \left\langle\uparrow_j\right| \right]. \tag{3.34}$$

An oscillating field can be used to drive transitions between any of the spin states and motional modes by setting the appropriate frequency and amplitude. To see this, we can consider a Hamiltonian identical to Eq. 3.20, which only couples to one of the qubits j, with the others being neglected as off-resonant, which is a good approximation if $\Omega_0 \ll |\omega_j - \omega_i|$ for all i*. We can then follow a similar derivation as in the single ion case. The Hamiltonian can be written in the polaron basis using

*It should also be ensured that $|\omega_j - \omega_i| \gg \nu_k$ for all i, j, k, which is satisfied for typical parameters with a reasonably sized magnetic field gradient.

the identity

$$\begin{aligned}
|\uparrow_j\rangle\langle\downarrow_j| &= |\uparrow_j\rangle\langle\downarrow_j| \bigotimes_{k=1}^{N} \sum_{n_k} |n_k\rangle\langle n_k| \\
&= |\uparrow_{p,j}\rangle\langle\downarrow_{p,j}| \bigotimes_{k=1}^{N} e^{\eta_{jk}(a_{p,k}^\dagger - a_{p,k})} \sum_{n_{p,k}} |n_{p,k}\rangle\langle n_{p,k}| \\
&= \exp\left[\sum_{k=1}^{N} \eta_{jk}(a_{p,k}^\dagger - a_{p,k})\right] |\uparrow_{p,j}\rangle\langle\downarrow_{p,j}|,
\end{aligned} \tag{3.35}$$

and therefore we obtain

$$H_{\text{osc}}^j = \frac{\hbar\Omega_0}{2}\left(\exp\left[\sum_{k=1}^{N} \eta_{jk}(a_{p,k}^\dagger - a_{p,k})\right] |\uparrow_{p,j}\rangle\langle\downarrow_{p,j}| + \text{H.c.}\right)\left(e^{i(\omega t+\phi)} + e^{-i(\omega t+\phi)}\right). \tag{3.36}$$

Ignoring the spin-spin coupling term in H_m, we can transform to the interaction picture with respect to $H_0 = H_B + H_m$ and perform the rotating wave approximation to give

$$\begin{aligned}
H_I^j &= e^{iH_0 t/\hbar} H_{\text{osc}}^j e^{-iH_0 t/\hbar} \\
&= \frac{\hbar\Omega_0}{2}\left(e^{i(\omega_j' - \omega)t} e^{i\phi} \exp\left[\sum_{k=1}^{N} \eta_{jk}(\tilde{a}_{p,k}^\dagger - \tilde{a}_{p,k})\right] |\uparrow_{p,j}\rangle\langle\downarrow_{p,j}| + \text{H.c.}\right),
\end{aligned} \tag{3.37}$$

where $\tilde{a}_{p,k}^\dagger = a_{p,k}^\dagger e^{i\nu_k t}$, $\tilde{a}_{p,k} = a_{p,k} e^{-i\nu_k t}$ and $\omega_j' = \omega_j - \sum_{k=1}^{N} \nu_k \eta_{jk}^2$. This Hamiltonian is similar to the single ion version in Eq. 3.23, except that there is now a summation over all normal modes. The ladder operators for each mode are rotating at frequency ν_k, and as each mode has a different frequency, the transitions are spectrally separated. Therefore as long as $\Omega_0 \ll |\nu_k - \nu_{k\pm1}|$, each mode k can be addressed individually. A transition between $|\downarrow_{p,j}\rangle|n_{p,k}\rangle$ and $|\uparrow_{p,j}\rangle|n_{p,k}+m\rangle$, can be selected by choosing the detuning $\delta_{j,k,m} = \omega - (\omega_j' + m\nu_k)$, resulting in the Hamiltonian

$$H_I^{jk} = \frac{\hbar\Omega_{n_{p,k},n_{p,k}+m}^j}{2}\left(e^{-i\delta_{j,k,m}t} e^{i\phi} |\uparrow_{p,j}\rangle\langle\downarrow_{p,j}| \otimes |n_{p,k}+m\rangle\langle n_{p,k}| + \text{H.c.}\right), \tag{3.38}$$

where $\Omega_{n_{p,k},n_{p,k}+m}^j = \Omega_0 \langle n_{p,k}| e^{\eta_{jk}(a_{p,k}^\dagger - a_{p,k})} |n_{p,k}+m\rangle$. Assuming that we are in the effective Lamb-Dicke regime so that $\eta_{jk}^2 n_{p,k} \ll 1$ and expanding the exponential in

powers of η_{jk}, we obtain a single carrier term for ion j given by

$$H_c^j = \frac{\hbar\Omega_0}{2}\Big(e^{-i\delta_{j,c}t}e^{i\phi}\left|\uparrow_{p,j}\right\rangle\left\langle\downarrow_{p,j}\right| + e^{i\delta_{j,c}t}e^{-i\phi}\left|\downarrow_{p}\right\rangle\left\langle\uparrow_{p}\right|\Big), \tag{3.39}$$

where $\delta_{j,c} = \delta_{j,k,m=0}$. We then get a red and blue sideband term for each ion j and normal mode k, given by

$$\begin{aligned} H_r^{jk} &= -\frac{\hbar\eta_{jk}\Omega_0}{2}\Big(e^{-i\delta_{j,k,r}t}e^{i\phi}a_{p,k}\left|\uparrow_{p,j}\right\rangle\left\langle\downarrow_{p,j}\right| - e^{i\delta_{j,k,r}t}e^{-i\phi}a_{p,k}^\dagger\left|\downarrow_{p,j}\right\rangle\left\langle\uparrow_{p,j}\right|\Big), \\ H_b^{jk} &= +\frac{\hbar\eta_{jk}\Omega_0}{2}\Big(e^{-i\delta_{j,k,b}t}e^{i\phi}a_{p,k}^\dagger\left|\uparrow_{p,j}\right\rangle\left\langle\downarrow_{p,j}\right| - e^{i\delta_{j,k,b}t}e^{-i\phi}a_{p,k}\left|\downarrow_{p,j}\right\rangle\left\langle\uparrow_{p,j}\right|\Big), \end{aligned} \tag{3.40}$$

where $\delta_{j,k,r} = \delta_{j,k,m=-1}$ and $\delta_{j,k,b} = \delta_{j,k,m=+1}$.

We have therefore seen that by adding a magnetic field gradient to a multi ion string, we can drive carrier and sideband transitions between any ion j and any normal mode k using an oscillating field, where the coupling strength is independent of the field's frequency. This is equivalent to the case of photon momentum, except that in the latter case the qubit resonant frequencies are the same and therefore a carrier or sideband transition will be resonant for all ions in the string. Therefore any experiments designed for or demonstrated with photon momentum spin-motion coupling can now be implemented using a magnetic field gradient and long-wavelength radiation.

We can demonstrate the coupling between the spin and motional states of two ions in a similar way to the single ion case. First the ions are prepared in $|00\rangle$, after which a microwave field is applied to couple the $|0_1\rangle \leftrightarrow |+1_1\rangle$ transition with frequency $\omega_{\mu\mathrm{w}} = \omega_1' + \delta_{\mu\mathrm{w}}$, where $\omega_1' = \omega_1 - \nu_1\eta_{11}^2 - \nu_2\eta_{12}^2$. From Sec. 2.2.2, the normal modes for two ions are the centre of mass (COM) mode with frequency $\nu_1 = \nu_z$ and the stretch mode with frequency $\nu_2 = \sqrt{3}\nu_z$. The normal mode coefficients S_{jk} describe the relative ion motion and amplitude for mode k, and are equal for the COM mode as $S_{11} = S_{21} = 1/\sqrt{2}$, and equal and opposite for the stretch mode as $S_{21} = -S_{22} = -1/\sqrt{2}$. We therefore find that $\omega_1' = \omega_1 - (\mu_B\partial_z B)^2/3m\hbar\nu_z^2$.

Fig. 3.6 shows the result of an experiment in which the microwave field detuning $\delta_{\mu\mathrm{w}}$ is scanned over a range including $\pm\sqrt{3}\nu_z$, which covers all 5 transitions including the red and blue sidebands for both the COM and stretch modes and the carrier. The trap frequency is set to $\nu_z/2\pi = 265\,\mathrm{kHz}$ and the relevant effective Lamb-Dicke parameters for ion 1 are therefore $\eta_{11} = 0.009$ and $\eta_{12} = 0.004$.

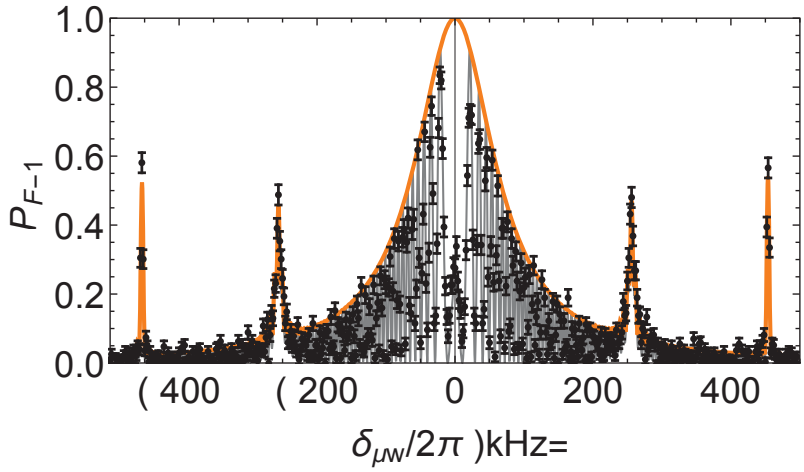


Fig. 3.6 Probability for either ion to be in F=1 as a function of the detuning $\delta_{\mu w}$ of a microwave field applied for 200 μs near resonant with the $|0_1\rangle \leftrightarrow |+1_1\rangle$ transition. Spaced equally either side of the centre carrier peak are the two COM mode sidebands with frequency $\nu_1 = \nu_z = 2\pi \times 265$ kHz, which are Stark shifted towards the carrier by approximately 9 kHz, as well as the two stretch mode sidebands with frequency $\nu_2 = \sqrt{3}\nu_z = 2\pi \times 459$ kHz, which are Stark shifted towards the carrier by approximately 5 kHz. The orange curve is the sum of the carrier envelope $\Omega_0^2/\sqrt{\Omega_0^2 + \delta_{\mu w}^2}$ with the sideband terms (Sec. 5.3) for $\bar{n}_c = 60$ and $\bar{n}_s = 40$, which correspond to approximately twice the Doppler temperatures predicted for these modes (see chapter 5). The grey curve shows the fine structure of the carrier from Eq. 2.23, which is randomly sampled by the data due to the large step size and therefore unresolved.

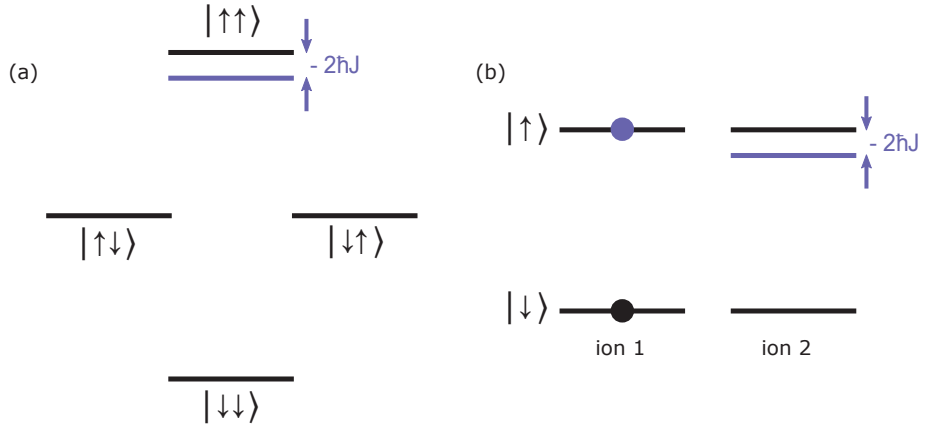


Fig. 3.7 For a two ion spin system, the energies of the collective spin states form a diamond structure as shown in (a). The spin-spin coupling term arising from the magnetic field gradient reduces the energy of the state $|\uparrow\uparrow\rangle$ by an amount $-2\hbar J$. This can be viewed as a conditional energy shift on one of the ions as shown in (b). For example, if ion 1 is in the state $|\uparrow\rangle$, the energy splitting between the spin states of ion 2 is $2\hbar J$ less than if ion 1 is in the state $|\downarrow\rangle$. Therefore if ion 2 is prepared in an equal superposition state and left for a time $t = \pi/2J$, the superposition will acquire a π phase shift only if ion 1 is in the state $|\uparrow\rangle$.

3.3.3 Spin-spin coupling

In the previous section we ignored a spin-spin coupling term in H_m, given by

$$\begin{aligned} H_{ss} &= -\sum_{i\neq j}^{N} \hbar J_{ij} \Big(|\uparrow_i\rangle \langle\uparrow_i| \otimes |\uparrow_j\rangle \langle\uparrow_j| \Big), \\ J_{ij} &= \sum_{k=1}^{N} \nu_k \eta_{ik} \eta_{jk}, \end{aligned} \tag{3.41}$$

where we have now performed the polaron transformation to drop the p subscripts. This coupling between ion pairs can be used to perform conditional quantum logic and thereby generate entangled states. To see this, consider two ions in a magnetic field gradient, as illustrated in Fig. 3.7. The unitary evolution for the Hamiltonian H_{ss} is then given by

$$U_{ss}(t) = e^{iH_{ss}t/\hbar} = e^{-2iJt|\uparrow\uparrow\rangle\langle\uparrow\uparrow|}, \tag{3.42}$$

where we have defined $J = J_{12} = J_{21}$. By evolving this interaction for a time $t = \pi/2J$, the phase of the state $|\uparrow\uparrow\rangle$ will be flipped by $e^{-i\pi} = -1$. A CNOT gate can then be formed by placing the spin-spin interaction between two $\pi/2$ carrier

pulses with a π phase difference. This sequence acting on the four basis states is

$$\begin{aligned}
|{\downarrow\downarrow}\rangle &\xrightarrow{\frac{\pi}{2},\phi=0} \frac{1}{\sqrt{2}}\big(|{\downarrow\downarrow}\rangle + |{\downarrow\uparrow}\rangle\big) \xrightarrow{U_{ss}(\frac{\pi}{J})} \frac{1}{\sqrt{2}}\big(|{\downarrow\downarrow}\rangle + |{\downarrow\uparrow}\rangle\big) \xrightarrow{\frac{\pi}{2},\phi=\pi} |{\downarrow\downarrow}\rangle \\
|{\downarrow\uparrow}\rangle &\xrightarrow{\frac{\pi}{2},\phi=0} \frac{1}{\sqrt{2}}\big(|{\downarrow\downarrow}\rangle - |{\downarrow\uparrow}\rangle\big) \xrightarrow{U_{ss}(\frac{\pi}{J})} \frac{1}{\sqrt{2}}\big(|{\downarrow\downarrow}\rangle - |{\downarrow\uparrow}\rangle\big) \xrightarrow{\frac{\pi}{2},\phi=\pi} |{\downarrow\uparrow}\rangle \\
|{\uparrow\downarrow}\rangle &\xrightarrow{\frac{\pi}{2},\phi=0} \frac{1}{\sqrt{2}}\big(|{\uparrow\downarrow}\rangle + |{\uparrow\uparrow}\rangle\big) \xrightarrow{U_{ss}(\frac{\pi}{J})} \frac{1}{\sqrt{2}}\big(|{\uparrow\downarrow}\rangle - |{\uparrow\uparrow}\rangle\big) \xrightarrow{\frac{\pi}{2},\phi=\pi} |{\uparrow\uparrow}\rangle \\
|{\uparrow\uparrow}\rangle &\xrightarrow{\frac{\pi}{2},\phi=0} \frac{1}{\sqrt{2}}\big(|{\uparrow\downarrow}\rangle - |{\uparrow\uparrow}\rangle\big) \xrightarrow{U_{ss}(\frac{\pi}{J})} \frac{1}{\sqrt{2}}\big(|{\uparrow\downarrow}\rangle + |{\uparrow\uparrow}\rangle\big) \xrightarrow{\frac{\pi}{2},\phi=\pi} |{\uparrow\downarrow}\rangle\,,
\end{aligned} \tag{3.43}$$

which is the truth table for a CNOT gate with ion 1 as the control qubit and ion 2 as the target. This gate has been demonstrated experimentally in Ref. [44] with a fidelity of 0.64(5). The main error source in this implementation was dephasing of the qubit states due to magnetic field noise in the lab. Coherence times of qubits formed of two states with different magnetic moments, as required for the magnetic field gradient scheme, are typically around 1 ms, whereas in Ref. [44] with $\partial_z B \approx 19\,\mathrm{T/m}$ and $\nu_z/2\pi = 123.5\,\mathrm{kHz}$, the nearest-neighbour coupling strength in a three ion string was measured to be $J_{12}/2\pi = 32.9\,\mathrm{Hz}$. To acquire the correct amount of phase to implement a CNOT gate, the interaction must therefore be evolved for $t = \pi/2J_{12} = 7.6\,\mathrm{ms}$, which is almost an order of magnitude longer than the coherence time. Although pulsed dynamical decoupling sequences can be applied to extend the coherence time of these qubits and hence increase the gate fidelity [66], high fidelity gates in the fault tolerant regime are not achievable using the spin-spin coupling with this magnetic field gradient. In our case the gradient of $\approx 24\,\mathrm{T/m}$ is not large enough to reach the potential of high fidelities, and therefore this scheme was not chosen to be used. Since $J \propto \eta^2 \propto (\partial_z B)^2$, the achievable gate fidelity scales favourably when increasing the magnetic field gradient, and so this scheme may be comparable to other schemes for ion traps that incorporate larger magnetic field gradients. As an example, for a two ion string in a magnetic field gradient of $\partial_z B = 150\,\mathrm{T/m}$ and a trap frequency of $\nu/2\pi = 150\,\mathrm{kHz}$, $J_{12}/2\pi = 1.9\,\mathrm{kHz}$ and therefore the interaction time is $t = \pi/2J_{12} = 130\,\mu\mathrm{s}$.

An alternative way to implement two-qubit quantum gates is to use sideband transitions in a similar way to the gates performed using lasers. The theory and experimental realisation of such a gate will be presented in Chapter 6. Importantly, the sideband coupling arising from the magnetic field gradient presented in the previous sections can be used with dressed states, which allow the coherence time

of the qubits to be extended by several orders of magnitude, and are discussed in Chapter 4. When driving such carrier or sideband transitions, the spin-spin coupling term is unwanted and can therefore be an error source. The effect of this term should therefore be considered and will be discussed further in Chapter 4, where it will be shown how this coupling affects the system when dressed states are used.

Chapter 4

Dressed states

4.1 Introduction

A magnetic field gradient produces a coupling between the internal and motional states of trapped ions when the internal states have different magnetic moments. However, states with different magnetic moments are also sensitive to magnetic field noise, causing dephasing of superpositions. This can be problematic for implementing high-fidelity quantum operations where states are required to maintain coherence for times much longer than the operation times (here an operation could for example represent a series of gates, an algorithm or a quantum simulation). By dressing the states with electromagnetic fields, an energy splitting is created between superposition states. This turns the effect of magnetic field noise into a resonant effect, where only noise with frequency near the energy splitting can couple to the system. The effect of noise is thereby greatly reduced, while the magnetic field gradient scheme can still be used. Using dressed states to protect against magnetic field noise in $^{171}Yb^{+}$ was first demonstrated by Timoney et al. in Ref. [47], while other dressed state schemes have also been used for reducing decoherence such as in Refs. [67–70]. A simpler scheme for manipulating a $^{171}Yb^{+}$ dressed-state qubit was then presented in Ref. [71], which forms the background for this work. In this chapter the theory of dressed states for two- and three-level systems is presented and it is shown how these states protect against magnetic field noise. A scheme to create dressed states in $^{171}Yb^{+}$ is presented and a method to prepare and detect these states in one and multiple ions is demonstrated. Finally, lifetime and coherence measurements are performed and it is shown how the coupling between the internal and motional states from the magnetic field gradient is maintained in the dressed basis.

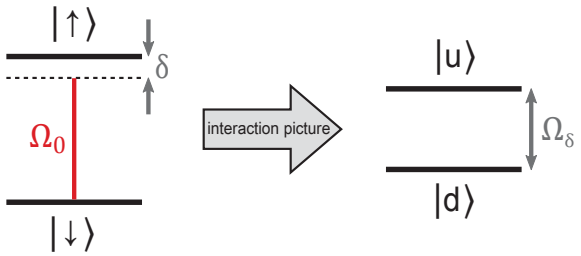


Fig. 4.1 Two levels $|\downarrow\rangle$ and $|\uparrow\rangle$ are dressed by a single field with Rabi frequency Ω_0 and detuning δ. In the interaction picture this system comprises two dressed states $|d\rangle$ and $|u\rangle$ separated in frequency by an amount $\Omega_\delta = \sqrt{\Omega_0^2 + \delta^2}$.

4.2 Dressed state theory

A dressed state is an eigenstate of the Hamiltonian which describes an atomic system being driven by near-resonant electromagnetic fields. In this section, a theoretical description of dressed states for two- and three-level systems will be presented and it will be shown how dressed states have a reduced sensitivity to magnetic field noise.

4.2.1 Dressing a two-level atom

The simplest dressed system comprises a two-level atom interacting with a single near-resonant field. The dynamics of such a system has already been considered in Sec. 2.2.3, however here we will take an alternative approach. For atomic states defined as $|\downarrow\rangle \equiv (0,1)^T$ and $|\uparrow\rangle \equiv (1,0)^T$, the Hamiltonian term in the interaction picture with respect to the energy splitting is given by Eq. 2.16 to be

$$H_{\rm dr}(t) = \frac{\hbar\Omega_0}{2}\Big(|\uparrow\rangle\langle\downarrow| e^{-i\delta t}e^{i\phi} + |\downarrow\rangle\langle\uparrow| e^{i\delta t}e^{-i\phi}\Big), \tag{4.1}$$

where δ is the detuning and ϕ is the phase, as shown in Fig 4.1. Now rather than solve the Schrödinger equation for this Hamiltonian as shown in Sec. 2.2.3, we can instead transform to a rotating frame for which the Hamiltonian is time independent and find the eigenstates and eigenenergies. This can be achieved by moving to an interaction picture with respect to $H_\delta = \hbar\delta\,|\uparrow\rangle\langle\uparrow|$, giving

$$\begin{aligned} H'_{\rm dr} &= e^{iH_\delta t/\hbar}\Big(H_{\rm dr}(t) - H_\delta\Big)e^{-iH_\delta t/\hbar} \\ &= \frac{\hbar\Omega_0}{2}\Big(|\uparrow\rangle\langle\downarrow| e^{i\phi} + |\downarrow\rangle\langle\uparrow| e^{-i\phi}\Big) - \hbar\delta\,|\uparrow\rangle\langle\uparrow| \\ &= \begin{pmatrix} -\hbar\delta & \hbar\Omega_0 e^{i\phi}/2 \\ \hbar\Omega_0 e^{-i\phi}/2 & 0 \end{pmatrix}. \end{aligned} \tag{4.2}$$

The eigenstates of this Hamiltonian are

$$\begin{aligned} |u\rangle &= \frac{\Omega_0}{\sqrt{\Omega_0^2 + (\delta - \Omega_\delta)^2}} \left(|\downarrow\rangle + e^{i\phi} \frac{\Omega_\delta - \delta}{\Omega_0} |\uparrow\rangle \right), \\ |d\rangle &= \frac{\Omega_0}{\sqrt{\Omega_0^2 + (\delta + \Omega_\delta)^2}} \left(|\downarrow\rangle - e^{i\phi} \frac{\Omega_\delta + \delta}{\Omega_0} |\uparrow\rangle \right), \end{aligned} \tag{4.3}$$

where we have defined $\Omega_\delta = \sqrt{\delta^2 + \Omega_0^2}$. The corresponding eigenenergies are

$$\begin{aligned} \epsilon_u &= \frac{\hbar}{2}\big(-\delta + \Omega_\delta \big), \\ \epsilon_d &= \frac{\hbar}{2}\big(-\delta - \Omega_\delta \big), \end{aligned} \tag{4.4}$$

and Eq. 4.2 can then be re-written in terms of the dressed states as

$$H'_{\mathrm{dr}} = -\frac{\hbar\delta}{2}\big(|u\rangle\langle u| + |d\rangle\langle d| \big) + \frac{\hbar\Omega_\delta}{2}\big(|u\rangle\langle u| - |d\rangle\langle d| \big). \tag{4.5}$$

The energies of the dressed states and the populations in $|\uparrow\rangle$ and $|\downarrow\rangle$ as a function of detuning are plotted in Fig. 4.2. In the case that the driving field is resonant ($\delta = 0$), the eigenstates, eigenenergies and Hamiltonian reduce to the simpler form

$$\begin{aligned} |u\rangle &= \frac{1}{\sqrt{2}}\big(|\downarrow\rangle + e^{i\phi} |\uparrow\rangle \big), \\ |d\rangle &= \frac{1}{\sqrt{2}}\big(|\downarrow\rangle - e^{i\phi} |\uparrow\rangle \big), \\ \epsilon_u &= +\frac{\hbar\Omega_0}{2}, \\ \epsilon_d &= -\frac{\hbar\Omega_0}{2}, \\ H'_{\mathrm{dr}} &= \frac{\hbar\Omega_0}{2}\big(|u\rangle\langle u| - |d\rangle\langle d| \big). \end{aligned} \tag{4.6}$$

Since the Hamiltonian H'_{dr} is time independent in this interaction picture, it becomes easier to solve compared to in Sec. 2.2.3. For a state initialised in $|\downarrow\rangle = (|u\rangle + |d\rangle)/\sqrt{2}$

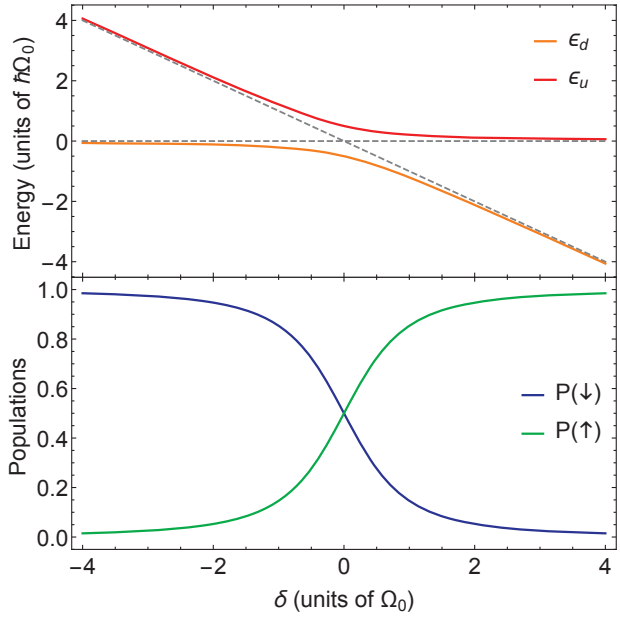


Fig. 4.2 Top: Eigenenergies of the Hamiltonian given in Eq. 4.2 as a function of the detuning δ of the driving field in units of the Rabi frequency Ω_0. The dashed lines show the energies for the case where $\Omega_0 = 0$, which are equal to $\epsilon_u = 0$, $\epsilon_d = -\hbar\delta$ in this interaction frame. An avoided crossing is present when $\Omega_0 \neq 0$, which has a maximum energy gap equal to $\hbar\Omega_0$ at $\delta = 0$. Bottom: Populations of the states $|\downarrow\rangle$ and $|\uparrow\rangle$ making up the dressed state $|u\rangle$ as a function of δ (The populations making up $|d\rangle$ are exactly opposite). In the limit $|\delta| \gg \Omega_0$, the eigenstates are just the un-dressed states $|\uparrow\rangle$ and $|\downarrow\rangle$, while at $\delta = 0$, the eigenstates are the superposition states $(|\downarrow\rangle \pm e^{i\phi}|\uparrow\rangle)/\sqrt{2}$.

and with $\delta = 0$, the time evolution is

$$\begin{aligned} |\psi(t)\rangle &= e^{-iH'_{\rm dr}t/\hbar}\,|\downarrow\rangle \\ &= e^{-i\Omega_0 t(|u\rangle\langle u|-|d\rangle\langle d|)/2}\,|\downarrow\rangle \\ &= \frac{1}{\sqrt{2}}\Big(e^{-i\Omega_0 t/2}\,|u\rangle + e^{i\Omega_0 t/2}\,|d\rangle\Big). \end{aligned} \tag{4.7}$$

We can then calculate the probability to be in the state $|\uparrow\rangle = (|u\rangle - |d\rangle)/\sqrt{2}$ to be

$$P_\uparrow(t) = |\,\langle\uparrow|\psi(t)\rangle\,|^2 = \sin^2(\Omega_0 t/2), \tag{4.8}$$

which indicates Rabi oscillations between the two bare states $|\downarrow\rangle$ and $|\uparrow\rangle$, in agreement with Eq. 2.23.

Arbitrary states and operators can be transformed between the bare state basis $\{|\uparrow\rangle \equiv (1,0)^T, |\downarrow\rangle \equiv (0,1)^T\}$ and the dressed state basis $\{|u\rangle \equiv (1,0)^T, |d\rangle \equiv (0,1)^T\}$ using the unitary operator $U_{\rm dr}$, given by

$$U_{\rm dr} = \begin{pmatrix} k_u^\uparrow & k_d^\uparrow \\ k_u^\downarrow & k_d^\downarrow \end{pmatrix}, \tag{4.9}$$

where the matrix elements are defined by $|u\rangle = k_u^\uparrow|\uparrow\rangle + k_u^\downarrow|\downarrow\rangle$ and $|d\rangle = k_d^\uparrow|\uparrow\rangle + k_d^\downarrow|\downarrow\rangle$, which can be found from Eq. 4.3. An arbitrary state in the bare state basis $|\psi\rangle$ can then be transformed to the dressed basis as $|\psi_{\rm dr}\rangle = U_{\rm dr}^\dagger|\psi\rangle$ and an arbitrary operator $\hat{O}$ can be transformed to the dressed basis as $\hat{O}_{\rm dr} = U_{\rm dr}^\dagger \hat{O} U_{\rm dr}$. Similarly, arbitrary states and operators in the dressed basis can be transformed to the bare state basis as $|\psi\rangle = U_{\rm dr}|\psi_{\rm dr}\rangle$ and $\hat{O} = U_{\rm dr}\hat{O}_{\rm dr}U_{\rm dr}^\dagger$ respectively.

To see how dressed states protect against magnetic field fluctuations, we can write the noise Hamiltonian in Eq. 2.26 ($H_{\rm noise} = \mu_B \Delta B(t)\,|\uparrow\rangle\langle\uparrow|$) in the dressed basis using the unitary transformation $U_{\rm dr}$ to give

$$\begin{aligned} H'_{\rm noise} = U_{\rm dr}^\dagger H_{\rm noise} U_{\rm dr} = -\,\mu_B \Delta B(t)\Bigg[&\frac{\delta}{2\Omega_\delta}\Big(\,|u\rangle\langle u| - |d\rangle\langle d|\,\Big) \\ &- \frac{\Omega_0}{2\Omega_\delta}\Big(\,|u\rangle\langle d| + |d\rangle\langle u|\,\Big)\Bigg]. \end{aligned} \tag{4.10}$$

If we again consider noise of the form $\Delta B(t) = B_0\cos(\omega_f t + \phi_f)$, we can go into the interaction picture with respect to the dressing Hamiltonian $H_{\rm dr}$ (Eq. 4.5). With the condition that the amplitude of the magnetic field noise satisfies $\mu_B B_0/\hbar \ll \Omega_\delta^2/\Omega_0$,

we can make a rotating wave approximation that neglects terms oscillating at $\omega_f + \Omega_\delta$, giving a transformed noise Hamiltonian

$$\begin{aligned} H''_{\text{noise}} = &- \frac{\mu_B \Delta B(t) \delta}{2\Omega_\delta} \Big(|u\rangle \langle u| - |d\rangle \langle d| \Big) \\ &- \frac{\mu_B B_0 \Omega_0}{4\Omega_\delta} \left(|u\rangle \langle d| \, e^{-i(\omega_f - \Omega_\delta)t} e^{-i\phi_f} + |d\rangle \langle u| \, e^{i(\omega_f - \Omega_\delta)t} e^{i\phi_f} \right). \end{aligned} \tag{4.11}$$

For the resonant case $\delta = 0$, the first term in Eq. 4.11 is zero, and the Hamiltonian reduces to

$$H''_{\text{noise}} = -\frac{\mu_B B_0}{4} \left(|u\rangle \langle d| \, e^{-i(\omega_f - \Omega_0)t} e^{-i\phi_f} + |d\rangle \langle u| \, e^{i(\omega_f - \Omega_0)t} e^{i\phi_f} \right). \tag{4.12}$$

This Hamiltonian is analogous to the two-level Rabi Hamiltonian in Eq. 2.16, and therefore the effect is to drive Rabi oscillations between the dressed states $|u\rangle$ and $|d\rangle$ when the noise frequency ω_f is close to the frequency splitting Ω_0. In the case that $|\omega_f - \Omega_0| \gg \mu_B B_0/\hbar$, the noise will have a negligible effect. This results in a large suppression of the effect of noise on the dressed-state qubit $\{|d\rangle, |u\rangle\}$ compared to the un-dressed qubit $\{|\downarrow\rangle, |\uparrow\rangle\}$, as most of the noise frequencies will be decoupled. Furthermore, due to the fact that the noise amplitude generally scales as $1/\omega_f$, increasing the value of Ω_0 will reduce the effects further. For the case that the dressing field is off-resonant, the first term in Eq. 4.11 will be non-zero. This term is analogous to the noise term in the original basis $\{|\downarrow\rangle, |\uparrow\rangle\}$, and therefore allows the noise to couple to the qubit with no frequency dependence. The fraction of noise that can couple to the qubit compared to the un-dressed case is given by δ/Ω_δ. This gives a simple method to calculate the accuracy with which the detuning needs to be set in order to suppress noise to a given level. As an example, to achieve 10% of the effect of noise compared to the un-dressed case, the detuning should approximately satisfy $\delta = \Omega_0/5$. In the limit $|\delta| \gg \Omega_0$, the second term in Eq. 4.11 goes to zero, and the noise can fully couple to the qubit as in the un-dressed case.

Stark shifts

When $\delta \gg \Omega_0$, the dressed states $|u\rangle$ and $|d\rangle$ are nearly the same as the bare states $|\uparrow\rangle$ and $|\downarrow\rangle$, with energy splitting almost equal to the un-dressed case. In this case, it is often approximated that the dressed and bare states are equal, and that the energy of the states has been slightly shifted, known as a Stark shift. The

Stark shift can be found from the dressed state energies $\epsilon_u = \hbar(-\delta + \Omega_\delta)/2$ and $\epsilon_d = \hbar(-\delta - \Omega_\delta)/2$. In the far detuned case, these shifts can be approximated to be $\epsilon_u \approx \hbar\Omega_0^2/4\delta$ and $\epsilon_d \approx -\hbar\Omega_0^2/4\delta$, and therefore the total energy difference between the states is shifted by $\Delta\epsilon = \epsilon_u - \epsilon_d \approx \hbar\Omega_0^2/2\delta$. Stark shifts need to be taken into account when driving sideband transitions, where the applied fields are far detuned from the carrier transition, causing Stark shifts. This is particularly important in chapter 6, where Stark shifts due to the interaction of the two-qubit gate fields can lead to errors in the gate.

4.2.2 Adding an auxiliary state

We now consider the effect of adding an auxiliary state $|a\rangle$ that is not part of the dressed system. Coupling this state to either $|\uparrow\rangle$ or $|\downarrow\rangle$ provides a useful method to transfer population in and out of the dressed states (see Fig. 4.3). To see this, we can look at the Hamiltonian describing a field near resonant with the $|a\rangle \leftrightarrow |\uparrow\rangle$ transition, which after transforming to the interaction picture with respect to the energy splitting and performing the RWA is given by

$$H_a = \frac{\hbar\Omega_a}{2}\Big(|\uparrow\rangle\langle a| e^{-i\delta_a t}e^{i\phi_a} + |a\rangle\langle\uparrow| e^{i\delta_a t}e^{-i\phi_a}\Big), \tag{4.13}$$

where δ_a is the detuning from resonance and Ω_a is the Rabi frequency for this transition. Rotating to the interaction picture with respect to $H_\delta = \hbar\delta\,|\uparrow\rangle\langle\uparrow|$ and transforming to the dressed basis, this becomes

$$H_a' = U_{\rm dr}^\dagger e^{iH_\delta t/\hbar} H_a e^{-iH_\delta t/\hbar} U_{\rm dr} = \frac{\hbar\Omega_a}{2}\Big[\Big((k_u^\uparrow)^*|u\rangle + (k_d^\uparrow)^*|d\rangle\Big)\langle a| e^{-i(\delta_a-\delta)t}e^{i\phi_a} + \text{H.c}\Big]. \tag{4.14}$$

We can then go to the interaction picture with respect to the dressing Hamiltonian $H_{\rm dr}$ (Eq. 4.5), to obtain

$$H_a'' = \frac{\hbar\Omega_a}{2}\Big[(k_u^\uparrow)^*|u\rangle\langle a| e^{-i(\delta_a-\frac{\delta}{2}-\frac{\Omega_\delta}{2})t}e^{i\phi_a} + (k_d^\uparrow)^*|d\rangle\langle a| e^{-i(\delta_a-\frac{\delta}{2}+\frac{\Omega_\delta}{2})t}e^{i\phi_a} + \text{H.c}\Big]. \tag{4.15}$$

From this equation, it can be seen that as long as $\Omega_a \ll \Omega_\delta$, a transition between $|a\rangle$ and either of the two dressed states can be achieved by setting δ_a appropriately. Setting the detuning to $\delta_a = (\delta + \Omega_\delta)/2$ implements a transition to $|u\rangle$ with Rabi frequency $(k_u^\uparrow)^*\Omega_a$, while setting $\delta_a = (\delta - \Omega_\delta)/2$ implements a transition to $|d\rangle$ with Rabi frequency $(k_d^\uparrow)^*\Omega_a$. In the case that the dressing field is resonant ($\delta = 0$), the

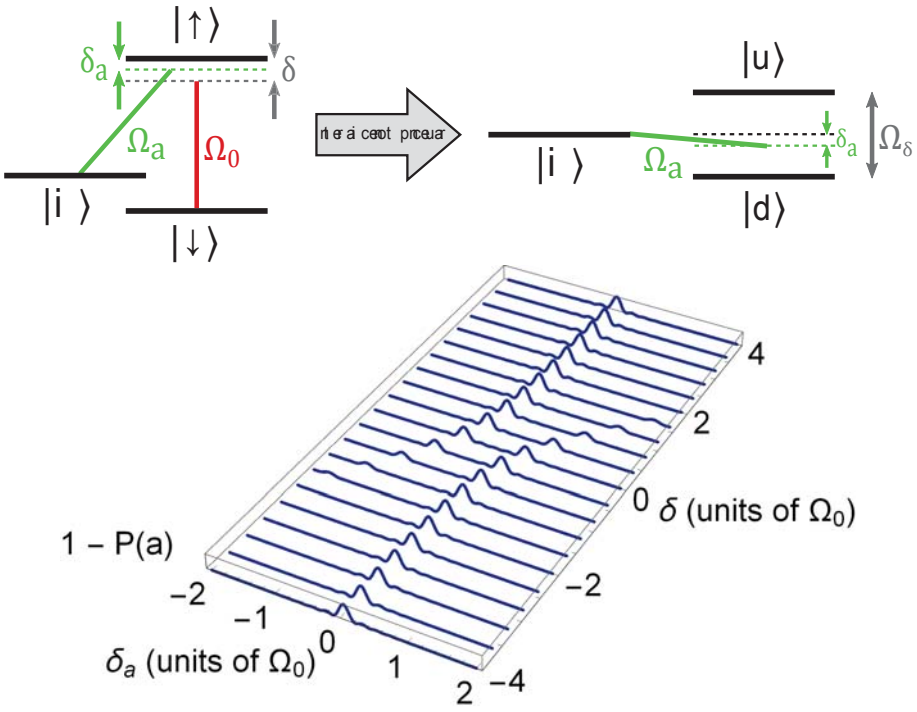


Fig. 4.3 Top: An auxiliary state $|a\rangle$ is coupled to $|\uparrow\rangle$ with Rabi frequency Ω_a and detuning δ_a. In the interaction picture this allows $|a\rangle$ to be coupled to either of the two dressed states for the appropriate detuning. This provides a useful method for transferring population in and out of the dressed states. Bottom: Each blue curve gives the sum of the probabilities to be in the state $|u\rangle$ and $|d\rangle$ as a function of of δ_a, for different values of the dressing field detuning δ. The fields are applied for a time $t = \pi\sqrt{2}/\Omega_a$, corresponding to the π-time for a transition to $|u\rangle$ or $|d\rangle$ when $\delta = 0$. The solutions neglect interference effects between the two transitions, which is a good approximation as long as the difference in frequency between the two peaks is much greater than their widths. For $\delta = 0$, the two dressed state peaks are separated by Ω_0, while for $|\delta| \gg 0$, the single two-level transition peak of the undressed system is recovered.

Rabi frequencies are $\Omega_a/\sqrt{2}$ and the two transitions are separated by Ω_0. Plots of the probability to transfer to either $|u\rangle$ or $|d\rangle$ as a function of δ_a for different values of δ are plotted in Fig. 4.3. It can be seen that in the far detuned limit, the single transition peak corresponding to a transition between the two bare states is recovered.

4.2.3 Dressed states with three levels

A drawback with the two level dressed system is that although the magnetic field noise is decoupled, the dressed state energies depend on Ω_0, and therefore any noise in the dressing field Rabi frequency will couple directly to the states. The effect of such amplitude noise can be described in the same way as the magnetic field noise in Sec. 2.5.4 with the states $\{|\downarrow\rangle, |\uparrow\rangle\}$ replaced with $\{|d\rangle, |u\rangle\}$ and the replacement $\mu_B B_0/\hbar \to \Omega_\delta/2$. By dressing three states with two fields, a dressed state is formed whose energy is independent of the Rabi frequencies, and is therefore protected from both magnetic field and Rabi frequency noise, as will be shown in the following.

Consider three states $|0\rangle \equiv (0,0,1)^T$, $|1\rangle \equiv (0,1,0)^T$ and $|2\rangle \equiv (1,0,0)^T$ in a V-type configuration as shown in Fig. 4.4. Two fields couple the $|0\rangle \leftrightarrow |1\rangle$ and $|0\rangle \leftrightarrow |2\rangle$ transitions with Rabi frequencies Ω_1 and Ω_2 and detunings δ_1 and δ_2. The Hamiltonian is

$$H_{\rm dr}(t) = \frac{\hbar\Omega_1}{2}\Big(|1\rangle\langle 0| e^{-i\delta_1 t}e^{i\phi_1} + \text{H.c}\Big) + \frac{\hbar\Omega_2}{2}\Big(|2\rangle\langle 0| e^{-i\delta_2 t}e^{i\phi_2} + \text{H.c}\Big). \tag{4.16}$$

In a similar way to the two level case, this Hamiltonian can be made time independent by transforming into an interaction picture with respect to $H_\delta = \hbar\delta_1 |1\rangle\langle 1| + \hbar\delta_2 |2\rangle\langle 2|$, giving

$$\begin{aligned} H'_{\rm dr} &= e^{iH_\delta t/\hbar}\Big(H_{\rm dr}(t) - H_\delta\Big)e^{-iH_\delta t/\hbar} \\ &= \frac{\hbar\Omega_1}{2}\Big(|1\rangle\langle 0| e^{i\phi_1} + \text{H.c}\Big) + \frac{\hbar\Omega_2}{2}\Big(|2\rangle\langle 0| e^{i\phi_2} + \text{H.c}\Big) - \hbar\delta_1 |1\rangle\langle 1| - \hbar\delta_2 |2\rangle\langle 2| \\ &= \frac{\hbar}{2}\begin{pmatrix} -2\delta_2 & 0 & \Omega_2 e^{i\phi_2} \\ 0 & -2\delta_1 & \Omega_1 e^{i\phi_1} \\ \Omega_2 e^{-i\phi_2} & \Omega_1 e^{-i\phi_1} & 0 \end{pmatrix}. \end{aligned} \tag{4.17}$$

The three eigenstates are $|u\rangle = k_u^0|0\rangle + k_u^1|1\rangle + k_u^2|2\rangle$, $|d\rangle = k_d^0|0\rangle + k_d^1|1\rangle + k_d^2|2\rangle$

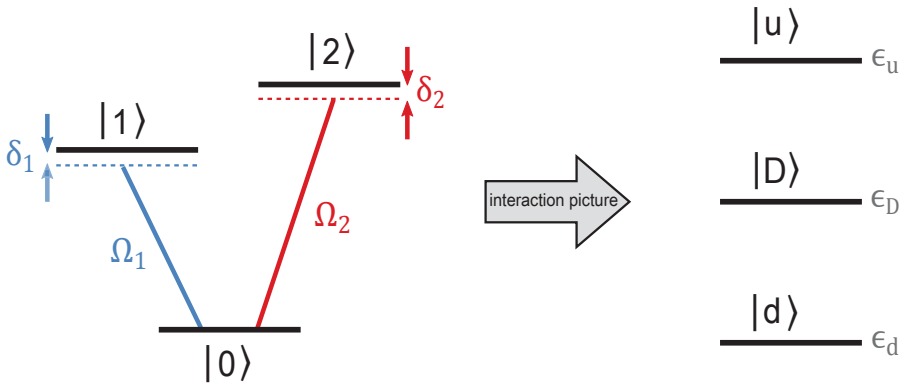


Fig. 4.4 Three levels $|0\rangle$, $|1\rangle$ and $|2\rangle$ are dressed by two fields with Rabi frequencies Ω_1 and Ω_2 and detunings δ_1 and δ_2 as indicated in the figure. In the interaction picture, this system consists of three dressed states $|u\rangle$, $|D\rangle$ and $|d\rangle$. In the case that the detunings are zero and the Rabi frequencies are equal ($\Omega_1 = \Omega_2 = \Omega$), the three dressed states are equally separated in energy by $\hbar\Omega/\sqrt{2}$. The energy of the state $|D\rangle$ is independent of Ω in this case, and consequently this state is protected from noise in both the magnetic field and the amplitude of the dressing fields.

and $|D\rangle = k_D^0 |0\rangle + k_D^1 |1\rangle + k_D^2 |2\rangle$, with corresponding eigenenergies ϵ_u, ϵ_d and ϵ_D. In general, the eigenenergies ϵ_α and coefficients k_α^j cannot be written down in a concise algebraic form*, but can be calculated numerically. In a similar way to the two-level case, arbitrary states and operators can be transformed between the bare state basis and the dressed state basis using the unitary operator $U_{\rm dr}$, given by

$$U_{\rm dr} = \begin{pmatrix} k_u^2 & k_d^2 & k_D^2 \\ k_u^1 & k_d^1 & k_D^1 \\ k_u^0 & k_d^0 & k_D^0 \end{pmatrix}. \tag{4.18}$$

Plots of the dressed state energies and bare state populations making up the dressed states are shown in Fig. 4.5 for the case that the two detunings are equal, equal and opposite, and the case that the Rabi frequencies are unequal. If the Rabi frequencies are unequal, it is useful to define the average Rabi frequency $\Omega_{\rm av} = (\Omega_1 + \Omega_2)/2$ and the difference Rabi frequency $\Delta\Omega = \Omega_2 - \Omega_1$. In the case that both dressing fields are resonant ($\delta_1 = \delta_2 = 0$) and the Rabi frequencies are equal ($\Omega_1 = \Omega_2 = \Omega$), the

*The full analytic solutions are given in Ref. [72]

eigenstates reduce to the simple form

$$\begin{aligned} |u\rangle &= \frac{e^{i\phi_1}}{2}|1\rangle + \frac{e^{i\phi_2}}{2}|2\rangle + \frac{1}{\sqrt{2}}|0\rangle, \\ |d\rangle &= \frac{e^{i\phi_1}}{2}|1\rangle + \frac{e^{i\phi_2}}{2}|2\rangle - \frac{1}{\sqrt{2}}|0\rangle, \\ |D\rangle &= \frac{1}{\sqrt{2}}\Big(e^{i\phi_2}|2\rangle - e^{i\phi_1}|1\rangle\Big), \end{aligned} \tag{4.19}$$

with corresponding eigenenergies

$$\begin{aligned} \epsilon_u &= +\frac{\hbar\Omega}{\sqrt{2}}, \\ \epsilon_d &= -\frac{\hbar\Omega}{\sqrt{2}}, \\ \epsilon_D &= 0. \end{aligned} \tag{4.20}$$

In this case the energy of the dressed state $|D\rangle$ is independent of the dressing field Rabi frequencies and therefore protected from Rabi frequency noise. This makes $|D\rangle$ an appealing state for use as a qubit state, as it is decoupled from both magnetic field and Rabi frequency noise, giving it the potential to exhibit long coherence times when combined with another low noise state.

In a similar way to the two-level case, an auxiliary state $|a\rangle$ can be used to transfer population in and out of the dressed states. As an example, a transition between $|a\rangle$ and $|1\rangle$ will, after moving to the interaction picture with respect to the energy splitting, transforming to the dressed basis, and moving into an interaction picture with respect to the dressed state Hamiltonian $H'_{\mathrm{dr}} = \epsilon_u|u\rangle\langle u| + \epsilon_d|d\rangle\langle d| + \epsilon_D|D\rangle\langle D|$ and H_δ, give a Hamiltonian

$$\begin{aligned} H'_a = &\frac{\hbar\Omega_a}{2}\Big[(k_u^1)^*|u\rangle\langle a|\, e^{-i(\delta_a-\delta_1-\epsilon_u/\hbar)t}e^{i\phi_a} + (k_d^1)^*|d\rangle\langle a|\, e^{-i(\delta_a-\delta_1-\epsilon_d/\hbar)t}e^{i\phi_a} \\ &+ (k_D^1)^*|D\rangle\langle a|\, e^{-i(\delta_a-\delta_1-\epsilon_D/\hbar)t}e^{i\phi_a} + \mathrm{H.c}\Big]. \end{aligned} \tag{4.21}$$

In the resonant case with equal dressing field Rabi frequencies, $(k_u^1)^* = (k_d^1)^* = e^{-i\phi_1}/2$ and $(k_D^1)^* = -e^{-i\phi_1}/\sqrt{2}$. Therefore setting $\delta_a = \epsilon_D/\hbar = 0$ gives rise to a transition between $|a\rangle$ and $|D\rangle$ with Rabi frequency $\Omega_a/\sqrt{2}$, while setting $\delta_a = \epsilon_u/\hbar = \Omega/\sqrt{2}$ or $\delta_a = \epsilon_d/\hbar = -\Omega/\sqrt{2}$ gives rise to transitions between $|a\rangle$ and $|u\rangle$ or $|d\rangle$ respectively,

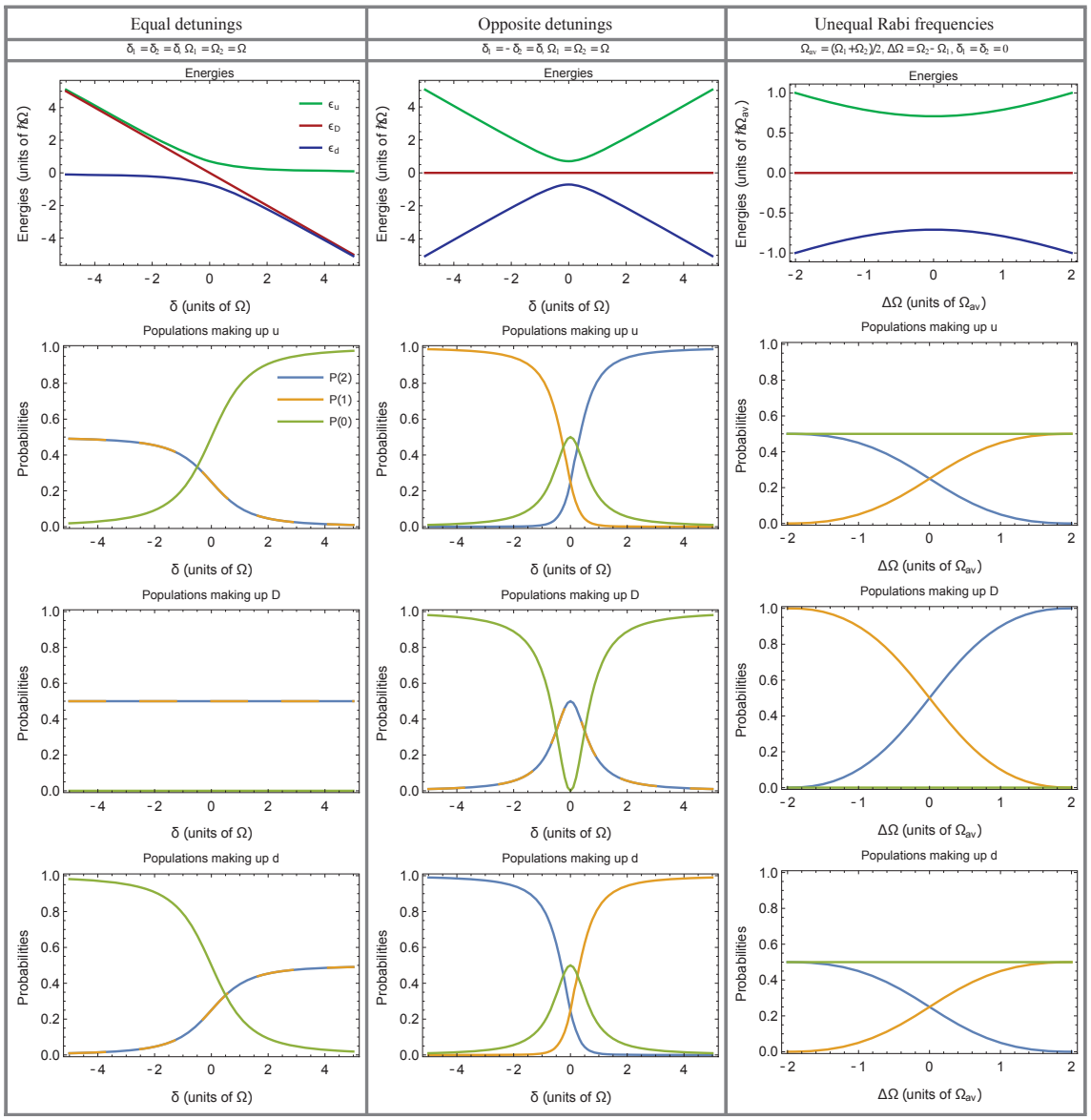


Fig. 4.5 Dressed state energies ϵ_u, ϵ_d and ϵ_D and populations of the bare states $\{|0\rangle, |1\rangle, |2\rangle\}$ making up the dressed states $\{|u\rangle, |d\rangle, |D\rangle\}$ as a function of equal dressing field detunings (left column), opposite detunings (middle column) and unequal Rabi frequencies (right column). If the parameter in question is varied adiabatically, the state populations will follow these curves. The graph in the right column and third row indicates the paths population follows in Stimulated Raman Adiabatic Passage (STIRAP), which allows population to be transferred between two states (in this case $|1\rangle$ and $|2\rangle$) without populating an intermediate state (in this case $|0\rangle$) by adiabatically varying the two Rabi frequencies. By pausing the Rabi frequencies when they are equal, this gives a method to map population between the bare states and dressed states. An interesting alternative case is shown in the centre column and third row, where it can be seen that by varying the dressing field detunings in opposite directions, population can be mapped between $|0\rangle$ and $|D\rangle$, which could also be used to map population between the bare and dressed states.

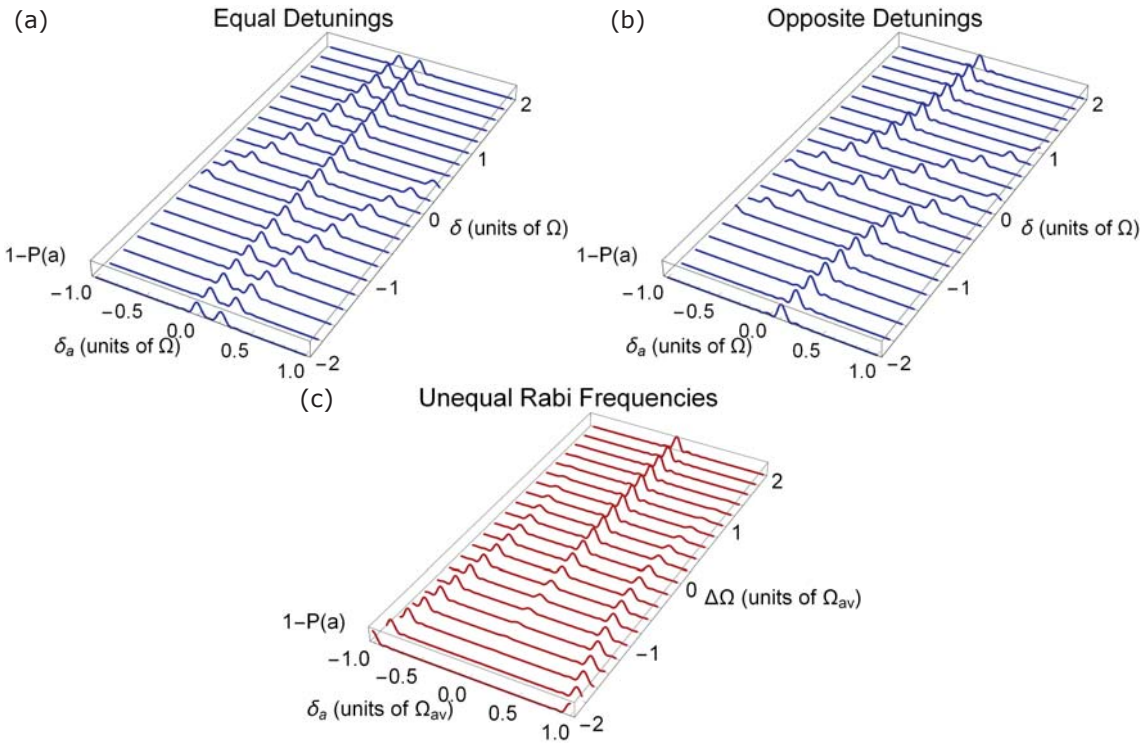


Fig. 4.6 Plots of the probability to transfer from the auxiliary state $|a\rangle$ to one of the three dressed states $|u\rangle$, $|d\rangle$ or $|D\rangle$ as a function of the detuning δ_a and one other parameter, when near resonant with the $|a\rangle \leftrightarrow |1\rangle$ transition. (a) The two dressing field detunings are varied equally as $\delta_1 = \delta_2 = \delta$. (b) The detunings are equal and opposite as $\delta_1 = -\delta_2 = \delta$. (c) The two dressing field Rabi frequencies are varied relative to one another, with average Rabi frequency $\Omega_{\rm av} = (\Omega_1 + \Omega_2)/2$ and difference Rabi frequency $\Delta\Omega = \Omega_2 - \Omega_1$.

with Rabi frequency $\Omega_a/2$. To ensure that only one transition is driven at a time, it should be ensured that $\Omega_a \ll \Omega$. Plots of the probability to transfer from $|a\rangle$ to one of the dressed states for equal and opposite detunings as well as unequal Rabi frequencies are shown in Fig. 4.6. It can be seen that the transition frequencies follow the dressed state energies shown in Fig. 4.5. For the equal and opposite detuning plots (a) and (b), the frequencies and coupling strengths vary in a way so that in the far detuned limit, a single peak corresponding to the bare state transition is recovered. For the varied Rabi frequency plot (c), if $\Delta\Omega \gg 0$, Ω_1 is small and therefore since $|a\rangle$ is coupled to $|1\rangle$ in this example, there is a single peak corresponding to the bare state transition. If $\Delta\Omega \ll 0$, Ω_1 is large and therefore the two-level dressed system is recovered, which can be seen by the two peaks spaced by Ω_1.

4.3 Dressed states in $^{171}Yb^+$

We have seen in the previous section that dressed states can protect against magnetic field noise and that by using a three-level dressed-state system, a dressed state is formed that is also insensitive to noise in the dressing field amplitudes. It has also been shown that population can be transferred into the dressed states from an auxilliary state. We will now consider how this can be applied to the electronic ground states in the $^{171}Yb^+$ ion in order to increase the coherence time of qubits stored in such states. As discussed in Sec. 2.3.3, the electronic ground state manifold of $^{171}Yb^+$ consists of four states, of which $|0\rangle$ and $|0'\rangle$ are insensitive to magnetic fields to first order, while the energies of $|+1\rangle$ and $|-1\rangle$ are linear with magnetic field. In order to drive sideband transitions using the magnetic field gradient, at least one magnetic field sensitive state should be used. It will be shown later in this chapter that such transitions that couple the spin and motional states can also be implemented using dressed states that are formed of one or more magnetic field sensitive states. To decouple the system from magnetic field noise and Rabi frequency noise, we can therefore use the three-level dressed-state scheme discussed in the previous section, and in the following we use the states $|0\rangle$, $|-1\rangle$ and $|+1\rangle$ (indicated in Fig. 4.7), meaning that the two dressing fields are microwave frequency. We therefore make the following associations with the theory presented in the previous section: $|0\rangle \rightarrow |0\rangle$, $|1\rangle \rightarrow |-1\rangle$, $|2\rangle \rightarrow |+1\rangle$ and $|a\rangle \rightarrow |0'\rangle$. An alternative would be to use $|0'\rangle$ instead of $|0\rangle$ as a state that is dressed, in which case the dressing fields would be RF and $|0\rangle$ could be associated as the auxiliary state $|a\rangle$. From Eq. 4.19, with the dressing field detunings set to resonance and the Rabi frequencies equal,

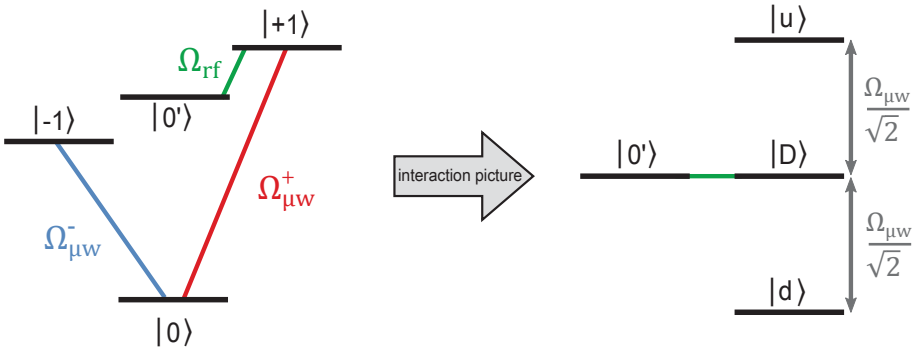


Fig. 4.7 Left: Dressed states in the $^2S_{1/2}$ manifold of $^{171}Yb^{+}$. Here the transitions $|0\rangle \leftrightarrow |+1\rangle$ and $|0\rangle \leftrightarrow |-1\rangle$ are coupled with resonant microwave radiation to obtain the three dressed-states $|u\rangle$, $|d\rangle$ and $|D\rangle$. Right: The resultant energy level diagram in the dressed basis when the Rabi frequencies of the dressing fields are set to be equal ($\Omega^{+}_{\mu w} = \Omega^{-}_{\mu w} = \Omega_{\mu w}$). The energy difference between the dressed-states in this case is given by $\pm\Omega_{\mu w}/\sqrt{2}$.

the Hamiltonian is

$$\begin{aligned} H'_{\mu w} &= \frac{\hbar\Omega_{\mu w}}{2}\Big(|+1\rangle\langle 0| e^{i\phi_+} + |-1\rangle\langle 0| e^{i\phi_-} + \text{H.c}\Big) \\ &= \frac{\hbar\Omega_{\mu w}}{\sqrt{2}}\Big(|u\rangle\langle u| - |d\rangle\langle d| \Big) \end{aligned} \tag{4.22}$$

where the corresponding dressed states are

$$\begin{aligned} |u\rangle &= \frac{e^{i\phi_+}}{2}|+1\rangle + \frac{e^{i\phi_-}}{2}|-1\rangle + \frac{1}{\sqrt{2}}|0\rangle\,, \\ |d\rangle &= \frac{e^{i\phi_+}}{2}|+1\rangle + \frac{e^{i\phi_-}}{2}|-1\rangle - \frac{1}{\sqrt{2}}|0\rangle\,, \\ |D\rangle &= \frac{1}{\sqrt{2}}\Big(e^{i\phi_+}|+1\rangle - e^{i\phi_-}|-1\rangle\Big), \end{aligned} \tag{4.23}$$

with energies $\epsilon_u = +\hbar\Omega_{\mu w}/\sqrt{2}$, $\epsilon_d = -\hbar\Omega_{\mu w}/\sqrt{2}$ and $\epsilon_D = 0$. The fourth state $|0'\rangle$ can then be used as the auxiliary state. Arbitrary rotations between $|0'\rangle$ and any of the three dressed states can be made using a single RF field near resonant with either the $|0'\rangle \leftrightarrow |+1\rangle$ or $|0'\rangle \leftrightarrow |-1\rangle$ transitions. For typical magnetic fields, the frequencies of these transitions are closely spaced, with the difference arising from the second order Zeeman shift $\Delta\omega_{\pm} = |\omega_+ - \omega_-|$. Therefore both transitions should be taken into account. Defining δ_{rf} as the detuning of the RF field from the $|0'\rangle \leftrightarrow |+1\rangle$

transition, the Hamiltonian term is

$$H_{\mathrm{rf}} = \frac{\hbar\Omega_{\mathrm{rf}}}{2}\Big(|+1\rangle \langle 0'| \, e^{-i\delta_{\mathrm{rf}}t} e^{i\phi_{\mathrm{rf}}} + |-1\rangle \langle 0'| \, e^{i(\delta_{\mathrm{rf}}-\Delta\omega_{\pm})t} e^{-i\phi_{\mathrm{rf}}} + \mathrm{H.c}\Big). \tag{4.24}$$

Using Eq. 4.21 we can write this in the dressed basis and transform to the interaction picture with respect to Eq. 4.22 to give

$$\begin{aligned} H'_{\mathrm{rf}} =& \frac{\hbar\Omega_{\mathrm{rf}}}{2\sqrt{2}}\Big(|D\rangle \langle 0'| \left(e^{-i\delta_{\mathrm{rf}}t} e^{i(\phi_{\mathrm{rf}}-\phi_+)} - e^{i(\delta_{\mathrm{rf}}-\Delta\omega_{\pm})t} e^{-i(\phi_{\mathrm{rf}}+\phi_-)}\right) + \mathrm{H.c}\Big) \\ &+ \frac{\hbar\Omega_{\mathrm{rf}}}{4}\Big(|u\rangle \langle 0'| \left(e^{-i(\delta_{\mathrm{rf}}-\frac{\Omega_{\mu\mathrm{w}}}{\sqrt{2}})t} e^{i(\phi_{\mathrm{rf}}-\phi_+)} + e^{i(\delta_{\mathrm{rf}}-\Delta\omega_{\pm}+\frac{\Omega_{\mu\mathrm{w}}}{\sqrt{2}})t} e^{-i(\phi_{\mathrm{rf}}+\phi_-)}\right) \\ &+ |d\rangle \langle 0'| \left(e^{-i(\delta_{\mathrm{rf}}+\frac{\Omega_{\mu\mathrm{w}}}{\sqrt{2}})t} e^{i(\phi_{\mathrm{rf}}-\phi_+)} + e^{i(\delta_{\mathrm{rf}}-\Delta\omega_{\pm}-\frac{\Omega_{\mu\mathrm{w}}}{\sqrt{2}})t} e^{-i(\phi_{\mathrm{rf}}+\phi_-)}\right) + \mathrm{H.c}\Big) \end{aligned} \tag{4.25}$$

There are therefore two transitions from $|0'\rangle$ to each of the three dressed states, totalling six transitions, with each pair separated by $\Delta\omega_{\pm}$. To ensure only a single transition is driven at once, it is required that the RF Rabi frequency satisfies $\Omega_{\mathrm{rf}} \ll \Delta\omega_{\pm}$ as well as the usual condition that $\Omega_{\mathrm{rf}} \ll \Omega_{\mu\mathrm{w}}$. Furthermore, it should be ensured that none of the transitions overlap, for example if $\Delta\omega_{\pm} \approx \Omega_{\mu\mathrm{w}}/\sqrt{2}$, transitions from $|0'\rangle$ to $|u\rangle$ and $|D\rangle$ would have a similar transition frequency.

The state $|D\rangle$ is protected from noise in both the magnetic field and the dressing field Rabi frequency, and the state $|0'\rangle$ is naturally independent of magnetic field to first order. Since it is not part of the dressed system, $|0'\rangle$ is also independent of $\Omega_{\mu\mathrm{w}}$. These two states together therefore form a qubit that is well protected from the environment, giving the potential for long coherence times to be achieved. Using a single RF field and setting $\delta_{\mathrm{rf}} = 0$ or or $\delta_{\mathrm{rf}} = \Delta\omega_{\pm}$, arbitrary rotations in the qubit subspace can be performed in a similar way to a standard two-level system. If $\Omega_{\mathrm{rf}} \ll \Delta\omega_{\pm}$ holds and choosing $\delta_{\mathrm{rf}} = 0$, we can neglect off-resonant terms and the Hamiltonian in Eq. 4.25 reduces to

$$H'_{\mathrm{rf}} = \frac{\hbar\Omega_{\mathrm{rf}}}{2\sqrt{2}}\Big(|D\rangle \langle 0'| \, e^{i(\phi_{\mathrm{rf}}-\phi_+)} + |0'\rangle \langle D| \, e^{-i(\phi_{\mathrm{rf}}-\phi_+)}\Big). \tag{4.26}$$

σ_ϕ-type rotations between the qubit states can therefore be performed by adjusting the phase of the RF field ϕ_{rf}. In principle, the rotation angle can also be changed by adjusting the phase of the microwave dressing field ϕ_+, however this would also change the relative phase of the states making up $|D\rangle$, and therefore would have to be performed adiabatically. In practice, only the relative phase from one pulse to the next is important and so if ϕ_+ is kept constant throughout each experimental

run, it can be ignored (i.e. set to zero).

An interesting alternative regime arises if $\Delta\omega_{\pm} \approx 0$. For $\delta_{\mathrm{rf}} = 0$, Eq. 4.25 then becomes

$$H'_{\mathrm{rf}} = \frac{\hbar\Omega_{\mathrm{rf}}}{2\sqrt{2}}\Big(|D\rangle \langle 0'| \left(e^{i(\phi_{\mathrm{rf}}-\phi_{+})} - e^{-i(\phi_{\mathrm{rf}}+\phi_{-})}\right) + \mathrm{H.c}\Big). \tag{4.27}$$

In this case, the relative phase between the RF and microwave fields becomes important, as it affects the coupling strength between the qubit states. If all three phases are set so that $\phi_{\mathrm{rf}} - \phi_{+} = \phi_{\mathrm{rf}} + \phi_{-} = 0$, the exponential terms cancel and the coupling strength between $|0'\rangle$ and $|D\rangle$ is zero. Alternatively, the phases can be set so that, for example $\phi_{\mathrm{rf}} - \phi_{+} = \phi_{\mathrm{rf}} + \phi_{-} = \pi/2$, in which case the exponential terms add to give a Hamiltonian term

$$H'_{\mathrm{rf}} = \frac{i\hbar\Omega_{\mathrm{rf}}}{\sqrt{2}}\Big(|D\rangle \langle 0'| - |0'\rangle \langle D| \Big). \tag{4.28}$$

This gives a σ_y-type rotation between the qubit states with a Rabi frequency double that of the case in which only a single transition is driven. Other rotation angles cannot be achieved by adjusting the RF phase in this case however, as this will only affect the coupling strength. Similarly by adjusting the phases to the case where the coupling strength to $|D\rangle$ is zero, the resonant coupling strength to $|u\rangle$ and $|d\rangle$ is maximised. This regime therefore has some speed advantages due to the higher Rabi frequencies possible, but is disadvantaged by the fact that arbitrary qubit rotations cannot be implemented in the usual way. Practically, reaching this regime is difficult due to the low magnetic fields that would be required for all ions, especially for the case that the ions are in an axial magnetic field gradient. Another possibility would be to add an off-resonant field to give a Stark shift to $|0'\rangle$, thereby cancelling the non-linear Zeeman shift. To investigate how well the approximation $\Delta\omega_{\pm} \approx 0$ needs to hold, we can consider the case that $\Delta\omega_{\pm}$ is small but non-zero. Setting the phases to $\phi_{\mathrm{rf}} - \phi_{+} = \phi_{\mathrm{rf}} + \phi_{-} = \pi/2$, Eq. 4.25 becomes

$$H'_{\mathrm{rf}} = \frac{i\hbar\Omega_{\mathrm{rf}}}{2\sqrt{2}}\Big(|D\rangle \langle 0'| \left(1 + e^{-i\Delta\omega_{\pm}t}\right) + \mathrm{H.c}\Big). \tag{4.29}$$

The effective Rabi frequency Ω_D therefore oscillates in time between between 0 and $\sqrt{2}\Omega_{\mathrm{rf}}$ at frequency $\Delta\omega_{\pm}$. If $\Delta\omega_{\pm}$ is large compared to Ω_{rf}, this oscillation is fast and can be averaged out in a rotating wave approximation, leading back to Eq. 4.26. However if $\Delta\omega_{\pm}$ is close in frequency to Ω_{rf} but non-zero, the effect will be significant. The condition for reaching the regime in which Eq. 4.28 holds is therefore that the period of oscillation in the Rabi frequency $2\pi/\Delta\omega_{\pm}$ is much longer than the total

length of the operations being performed on the dressed state qubit. This condition applies independently of the Rabi frequency Ω_{rf}.

4.3.1 Magnetic field noise in $^{171}Yb^{+}$

In the $^{171}Yb^{+}$ electronic ground state manifold, the energies of the states $|+1\rangle$ and $|-1\rangle$ depend linearly on the magnetic field. Therefore considering only first order effects, the Hamiltonian term describing the effect of magnetic field noise on the system can be extended from the two-level case described in Sec. 2.5.4 to give

$$H_{\mathrm{noise}} = \mu_B \Delta B(t)\Big(|+1\rangle\langle+1| - |-1\rangle\langle-1| \Big). \tag{4.30}$$

Without the use of dressed states, superpositions of states including either $|+1\rangle$ or $|-1\rangle$ would rapidly dephase as discussed in Sec. 2.5.4. If the three levels $|0\rangle$, $|+1\rangle$ and $|-1\rangle$ are dressed with two microwave fields as discussed in the previous section, and for the case that the dressing field detunings and phases are set to zero and the Rabi frequencies are equal, the noise Hamiltonian term can be written in the dressed state basis as

$$H'_{\mathrm{noise}} = \frac{\mu_B \Delta B(t)}{\sqrt{2}}\Big(|u\rangle\langle D| + |d\rangle\langle D| + \mathrm{H.c}\Big). \tag{4.31}$$

Considering noise of a specific frequency so that $\Delta B(t) = B_0 \cos(\omega_f t + \phi_f)$ and moving to the interaction picture with respect to the dressing Hamiltonian given in Eq. 4.22, this becomes

$$H''_{\mathrm{noise}} = \frac{\mu_B B_0}{2\sqrt{2}}\Big(|u\rangle\langle D|\, e^{-i\left(\omega_f - \frac{\Omega_{\mu\mathrm{w}}}{\sqrt{2}}\right)t} + |d\rangle\langle D|\, e^{i\left(\omega_f - \frac{\Omega_{\mu\mathrm{w}}}{\sqrt{2}}\right)t} + \mathrm{H.c}\Big), \tag{4.32}$$

where we have made a rotating wave approximation that is valid as long as $\mu_B B_0/\hbar \ll \Omega_{\mu\mathrm{w}}/\sqrt{2}$. It can be seen that in a similar way to the two level case, noise at all frequencies except those near $\Omega_{\mu\mathrm{w}}/\sqrt{2}$ have little effect on the system, thereby greatly reducing the effects compared to the undressed case. If the noise frequency ω_f is near $\Omega_{\mu\mathrm{w}}/\sqrt{2}$, it will cause transitions between the dressed state $|D\rangle$ and $|u\rangle$ and $|d\rangle$.

For the ideal case in which the dressing field amplitudes are equal and the detunings are zero, there should therefore be no dephasing of superpositions of the dressed states due to magnetic field noise, but instead the states have a finite lifetime (T_1) due to magnetic field noise near resonant with the dressed-state energy splittings. Therefore in this case the coherence time T_2 should be equal to T_1.

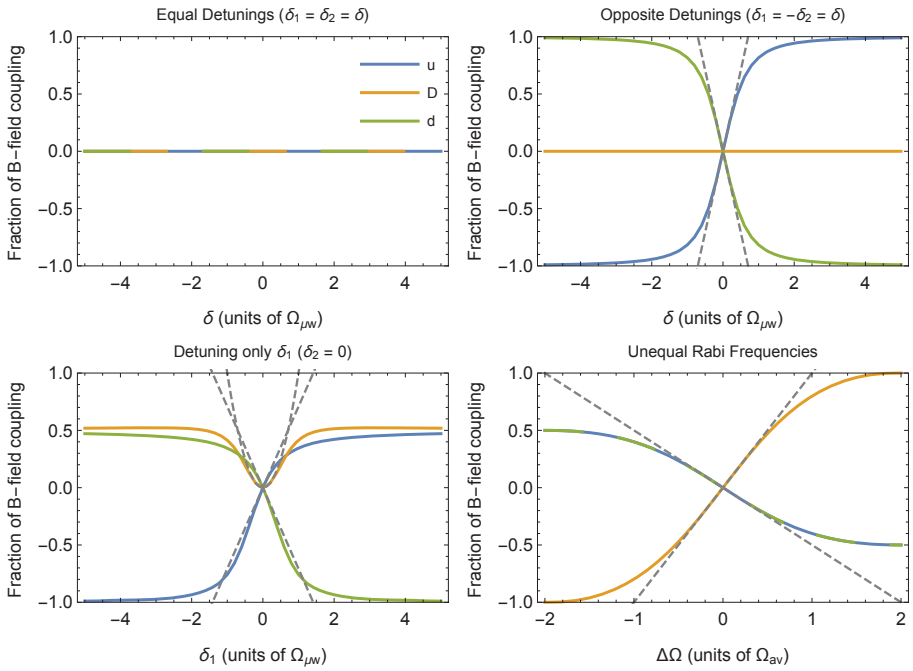


Fig. 4.8 Graphs showing the values of the diagonal matrix elements $|u\rangle\langle u|$, $|d\rangle\langle d|$ and $|D\rangle\langle D|$ for the magnetic field noise Hamiltonian (Eq. 4.30) as a function of various dressing field parameters. The top two graphs show the relative magnitude of the terms compared to the undressed case (i.e. $H'_{\text{noise}}/\mu_B \Delta B(t)$) if the detunings are varied in equal or equal and opposite directions. In the equal case, all three dressed state energies remain insensitive to magnetic field noise, while for the opposite case, the energy of the state $|D\rangle$ remains insensitive and the energies of $|u\rangle$ and $|d\rangle$ become more sensitive. The bottom plots show the matrix elements for the case that only one of the dressing field detunings is varied, or that the dressing field Rabi frequencies are mismatched. The grey dashed lines indicate approximate lowest order approximations for the case that the parameter is much less than $\Omega_{\mu w}$, which are given in Table 4.1.

Parameter	Definitions	$F_u = F_d$	F_D
Equal detunings	$\delta_1 = \delta_2 = \delta$	0	0
Opposite detunings	$\delta_1 = -\delta_2 = \delta$	$\sqrt{2}\lvert\delta\rvert/\Omega_{\mu\mathrm{w}}$	0
Single detuning	$\delta_1 = \delta,\ \delta_2 = 0$	$\lvert\delta\rvert/\sqrt{2}\Omega_{\mu\mathrm{w}}$	$(\lvert\delta\rvert/\Omega_{\mu\mathrm{w}})^2$
Unequal Rabi frequencies	$\Omega_{\mathrm{av}} = (\Omega^+_{\mu\mathrm{w}} + \Omega^-_{\mu\mathrm{w}})/2,$ $\Delta\Omega = \Omega^+_{\mu\mathrm{w}} - \Omega^-_{\mu\mathrm{w}}$	$\Delta\Omega/2\Omega_{\mathrm{av}}$	$\Delta\Omega/\Omega_{\mathrm{av}}$

Table 4.1 The approximate functions for the dressed state energy magnetic field sensitivities F_u, F_d and F_D as a function of various parameters, as indicated in the table. These functions give a good estimate for the case that the parameter is less than approximately 10% of $\Omega_{\mu\mathrm{w}}$, and are shown by the grey dashed lines in Fig. 4.8.

Dephasing of superpositions involving the states $|u\rangle$ and $|d\rangle$ can occur however due to noise in the dressing Rabi frequencies. In practice, the dressing field detunings and Rabi frequencies cannot be set perfectly, and therefore the effect of imperfectly set parameters should be considered. The effects can be seen by transforming H_{noise} in Eq. 4.30 to the dressed basis numerically using the transformation matrix 4.18. The effect of magnetic field noise on the dressed states when varying different parameters can then by seen. In the undressed case, the matrix elements $\langle +1| H_{\mathrm{noise}} |+1\rangle = \mu_B \Delta B(t)$ and $\langle -1| H_{\mathrm{noise}} |-1\rangle = -\mu_B \Delta B(t)$ indicate the energy shift of the states due to magnetic fields, and therefore their sensitivity to magnetic field noise. We can therefore define the fractional sensitivity to dephasing by magnetic field noise for a dressed state $|\beta\rangle$ compared to the undressed case as $F_\beta = \langle\beta| H_{\mathrm{noise}} |\beta\rangle / \mu_B \Delta B(t)$. Fig. 4.8 shows plots of F_u, F_d and F_D as a function of various dressing field parameters. If the parameter in question is small compared to the dressing field Rabi frequency $\Omega_{\mu\mathrm{w}}$, the dependence can be approximated to lowest order, which gives a simple way to calculate the accuracy with which parameters need to be set. The dashed lines in the figures indicate these approximations, and they are given in analytical form in Table 4.1. For the dressed state $|D\rangle$, changing the difference Rabi frequency $\Delta\Omega$ has a linear effect on the sensitivity to magnetic field noise to lowest order. However, changing one or more of the detunings has either no effect or a quadratic effect, and hence $|D\rangle$ can tolerate larger detunings than unequal Rabi frequencies for a given magnetic field sensitivity. For the dressed states $|u\rangle$ and $|d\rangle$, the effect is linear in all cases except for the case of equal detunings, for which the states remain insensitive.

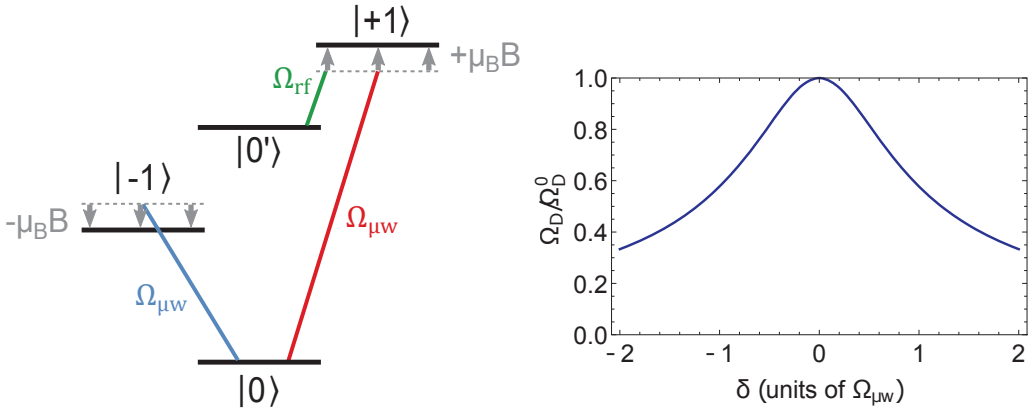


Fig. 4.9 Left: Energy level diagram showing the effect of a magnetic field drift when the dressing fields are initially set to resonance and the RF field is set to $\delta_{\mathrm{rf}} = 0$, corresponding to the resonant frequency of the $|0'\rangle \leftrightarrow |D\rangle$ transition via $|+1\rangle$. A magnetic field drift shifts the energies of the states $|+1\rangle$ and $|-1\rangle$ as indicated in the figure by the grey arrows, causing the dressing fields and RF field to be detuned. With this configuration of detunings, the RF field is still resonant with the same transition to $|D\rangle$, and hence the effect of magnetic field drifts are largely suppressed. Right: One limitation is that the Rabi frequency Ω_D is affected by such a magnetic field drift. The plot shows the ratio of the Rabi frequency for oppositely detuned dressing fields ($\delta_+ = -\delta_- = \delta$) to that when the dressing fields are resonant. It can be seen as long as $\delta \ll \Omega_{\mu\mathrm{w}}$, this change is small.

A useful additional feature of the $\{|0'\rangle, |D\rangle\}$ qubit is that the RF transition frequency $|0'\rangle \leftrightarrow |D\rangle$ is insensitive to magnetic field drifts to first order. This can be seen when considering that a drift in magnetic field will give an equal and opposite energy shift to the states $|+1\rangle$ and $|-1\rangle$ by an amount $\mu_B B$, as seen in Fig. 4.9. If the dressing fields are initially set on resonance, a magnetic field drift is equivalent to detuning the dressing fields equally in opposite directions. As can be seen in Fig. 4.6, this causes the RF transition frequency to $|D\rangle$ to shift by an amount equal to the detuning $\delta = \mu_B B/\hbar$. If the RF field is coupling $|0'\rangle$ to $|+1\rangle$, then the magnetic field drift has moved the energy of $|+1\rangle$ so that the RF detuning δ_{rf} is exactly δ, neglecting the second-order shift in energy of $|0'\rangle$. Therefore, the RF field is always set to the correct frequency for any magnetic field drift. A limitation is that the Rabi frequency of the RF transition to $|D\rangle$ is affected by a magnetic field, a plot of which is shown in Fig. 4.9. This means that although the frequency of the transition between $|0'\rangle$ and $|D\rangle$ is unaffected by a magnetic field drift, the Rabi frequency is affected. However, for small drifts the change in Rabi frequency is small.

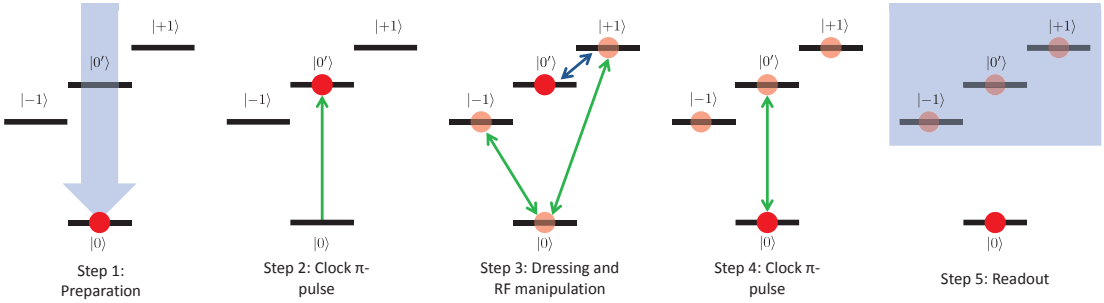


Fig. 4.10 Diagram illustrating the transfer sequence to prepare and detect the dressed-states via the clock transition. After the ion is prepared in $|0\rangle$ by optical pumping, a π-pulse on the clock transition transfers population to $|0'\rangle$. The dressing fields are then turned on and coherent manipulation in the dressed basis is performed using radio frequency fields (light red circles indicate population in the dressed-states). The dressing fields are then turned off and a second π-pulse on the clock transition transfers population from $|0'\rangle$ to $|0\rangle$. Any population that had been transferred to the dressed-states in step 3 will therefore give a bright result when reading out, while population in $|0'\rangle$ will give a dark result.

4.3.2 Preparation and detection of the dressed system

As discussed in Sec. 2.5.2, optical pumping allows the preparation of the state $|0\rangle$, while fluorescence detection gives a binary measurement that discriminates between $|0\rangle$ and $\{|-1\rangle, |0'\rangle, |+1\rangle\}$. To prepare and detect the dressed states, an appropriate transfer sequence to map population is therefore required. A simple method to prepare states in the dressed system after optical pumping to prepare population in $|0\rangle$ is to perform a microwave π-pulse on the $|0\rangle \leftrightarrow |0'\rangle$ clock transition, which prepares the ion in the auxiliary state $|0'\rangle$ (see Fig. 4.10). This step can be performed with high fidelity as the transition is independent of magnetic fields to first order and therefore has a long coherence time $> 1\,\mathrm{s}$. Next, the microwave dressing fields can be applied, dressing the system without affecting populations as $|0'\rangle$ is not coupled. The RF field giving rise to the Hamiltonian in Eq. 4.25 is then applied, which can transfer population to any of the three dressed states. If using the low noise qubit $\{|0'\rangle, |D\rangle\}$, this RF field allows the qubit to be manipulated. After the RF manipulation is complete, the dressing fields are turned off and a second microwave π-pulse swaps population between $|0'\rangle$ and $|0\rangle$. This implements the mapping $|0'\rangle \rightarrow |0\rangle$ and $\{|u\rangle, |D\rangle, |d\rangle\} \rightarrow \{|-1\rangle, |0'\rangle, |+1\rangle\}$, and therefore a measurement discriminates between the auxiliary state $|0'\rangle$ and the dressed states $\{|u\rangle, |D\rangle, |d\rangle\}$. If one wanted to discriminate between different dressed states, extra RF π-pulses could be included into the sequence. For example, a π-pulse swapping

population between $|0'\rangle$ and $|D\rangle$ before the second clock π-pulse (between step 3 and 4 in Fig. 4.10) would result in a measurement that discriminates between $|D\rangle$ and $\{|u\rangle, |0'\rangle, |d\rangle\}$.

To demonstrate this method, we trap a single $^{171}Yb^{+}$ ion in a magnetic field of approximately 9.7 G, which gives measured linear Zeeman shifts of $\omega_+/2\pi = 13.466\,\text{MHz}$, $\omega_-/2\pi = 13.495\,\text{MHz}$ and a second order Zeeman shift of $\Delta\omega_\pm/2\pi = 28.7\,\text{kHz}$. Fig. 4.11 shows a scan of the frequency of an RF field near resonant with the $|0'\rangle \leftrightarrow |\pm1\rangle$ transitions after preparing in $|0'\rangle$ and detecting using the method described above. The RF pulse is applied for 365 μs, corresponding to the measured π-time of the $|0'\rangle \leftrightarrow |D\rangle$ transition. The six peaks corresponding to the six terms in Eq. 4.25 indicate transitions to the dressed states, and the different peak heights are due to the different Rabi frequencies for the different transitions. The microwave dressing fields are applied with equal Rabi frequencies $\Omega_{\mu w}/2\pi = 24.2\,\text{kHz}$, and since $\Delta\omega_\pm > \Omega_{\mu w}/\sqrt{2}$, the two transitions to $|u\rangle$ are crossed. Fig. 4.11 also shows Rabi oscillations between $|0'\rangle$ and $|D\rangle$ when the RF frequency is set to $\delta_{rf} = 0$ and the pulse time is varied. This demonstrates that the qubit $\{|0'\rangle, |D\rangle\}$ can be prepared, manipulated and detected with high fidelity.

The method described here could also be used to prepare and detect the dressed states $|u\rangle$ and $|d\rangle$. This could be useful for the manipulation of a qutrit formed of the states $\{|d\rangle, |D\rangle, |u\rangle\}$, which is well protected from magnetic field noise. The qutrit could also be manipulated using RF pulses between each of the three dressed-states and $|0'\rangle$. As an example, a π-pulse from $|d\rangle$ to $|0'\rangle$, followed by a $\pi/2$ pulse on the $|0'\rangle \leftrightarrow |u\rangle$ transition, and finally a second π-pulse from $|0'\rangle$ to $|d\rangle$ would effectively perform a $\pi/2$ rotation between $|u\rangle$ and $|d\rangle$. Some initial experiments were attempted to implement Rabi oscillations between $|0'\rangle$ and $|u\rangle$ and $|d\rangle$ using the same method as for $|D\rangle$, however, a fast decay in the oscillations was observed. This could be due to the fact that the energies of $|u\rangle$ and $|d\rangle$, unlike $|D\rangle$, are dependent on the dressing field Rabi frequencies $\Omega_{\mu w}$, which are not currently stabilised. Further work is therefore being carried out on investigating the exact cause of the decay, as well as methods to stabilise the amplitude of the microwave fields.

In the preparation and detection method described above, the dressing fields are turned off instantaneously. This can cause mixing of the populations and phases between the states making up the dressed system, which is not an issue if no further coherent manipulation is required, as the detection doesn't discriminate between these states. There may however be situations where one would want to perform further manipulation after turning off the dressing fields. For example it may desirable to map the dressed qubit $\{|0'\rangle, |D\rangle\}$ to the clock qubit $\{|0\rangle, |0'\rangle\}$ for robust

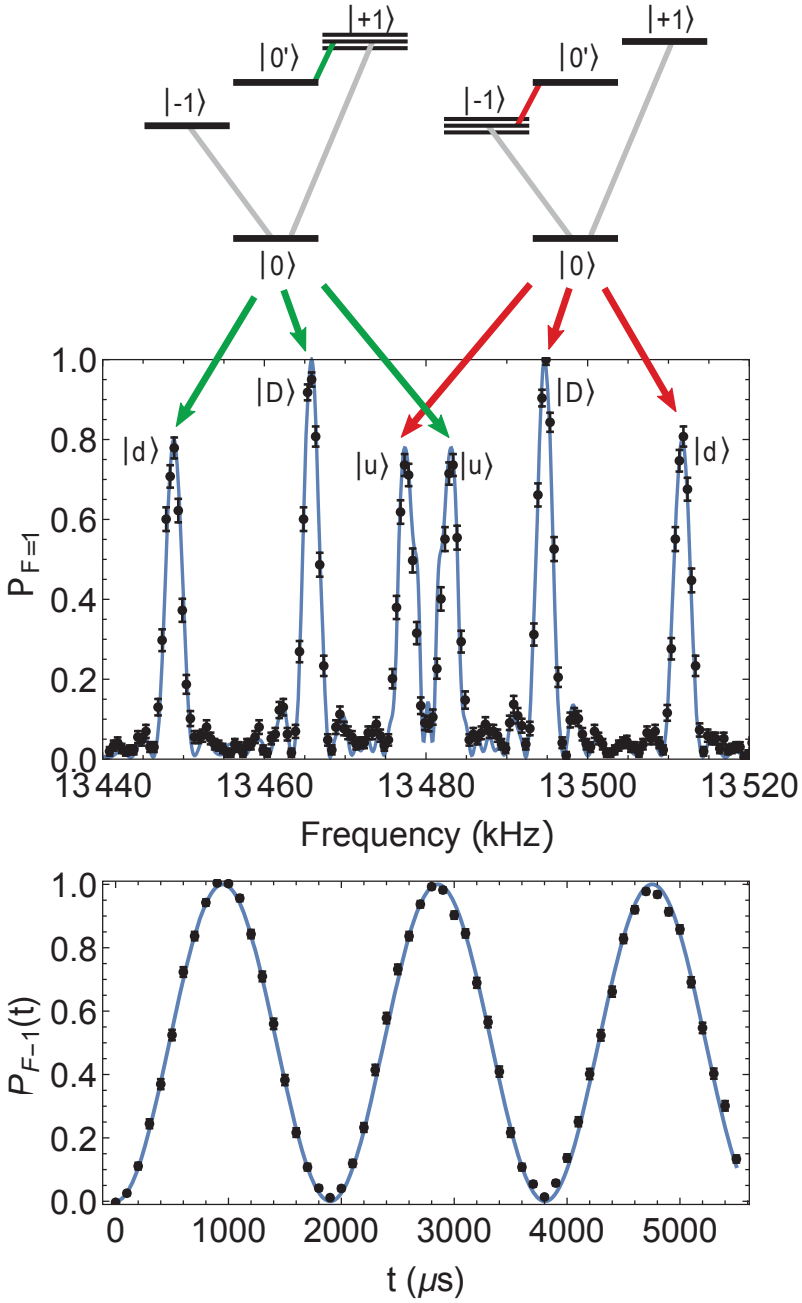


Fig. 4.11 Top: Population in F = 1 after a frequency scan of a single RF field applied for 365 μs, after preparing the ion in $|0'\rangle$ and applying the microwave dressing fields. The blue line is the result of a numerical simulation of the sum of the Hamiltonian terms in Eq. 4.22 and Eq. 4.24 with $\Omega_{\mu w}/2\pi = 24.2\,\text{kHz}$, $\Delta\omega_{\pm}/2\pi = 28.68\,\text{kHz}$ and $\Omega_{rf}/2\pi = 1.94\,\text{kHz}$. The frequency spacing between $|D\rangle$ and $|u\rangle$ and $|d\rangle$ is given by $\Omega_{\mu w}/\sqrt{2} = 2\pi \times 17.1\,\text{kHz}$, and the difference in peak height corresponds to the difference in Rabi frequencies between the transitions. Bottom: Rabi oscillations between $|0'\rangle$ and $|D\rangle$ via $|+1\rangle$. The blue line represents a theory curve describing a resonant Rabi oscillation following Eq. 2.23. The line is fit to the data, giving a Rabi frequency of $\Omega_D/2\pi = 0.5258(4)\,\text{kHz}$.

storage after an entanglement operation in a quantum computing architecture. In this case, an alternative mapping procedure can be used that involves adiabatically ramping the microwave Rabi frequencies in a STIRAP process [47, 71]. This maps $|\pm 1\rangle \rightarrow |D\rangle$ for preparation, and $|D\rangle \rightarrow |\mp 1\rangle$ for readout, with the sign depending on the order in which the dressing field amplitudes are ramped*. With additional π-pulses, this method can therefore allow population to be transferred in and out of the dressed state $|D\rangle$ without disturbing the qubit phase. The STIRAP method is more experimentally challenging as it involves amplitude pulse shaping, and can lead to decoherence as the procedure involves the magnetic field sensitive states $|+1\rangle$ and $|-1\rangle$. The simpler preparation and detection method involving π-pulses on the clock transition was therefore preferred and is used in all dressed state experiments in this thesis. An alternative method to the two discussed so far would allow a mapping from $|0\rangle \rightarrow |D\rangle$ for preparation and $|D\rangle \rightarrow |0\rangle$ for detection or storage. To achieve this, the dressing field detunings could be adiabatically varied from far off resonant to resonant, following the corresponding population curves shown in Fig. 4.5. This method would have the advantage of a direct mapping of the qubit state between the clock and dressed qubits, without the disadvantage of decoherence as no magnetic field sensitive states are involved, and could be investigated experimentally in future work.

4.3.3 Individual addressing of the clock transitions

The method to prepare and detect the dressed states described in the previous section requires π-pulses on the $|0\rangle \leftrightarrow |0'\rangle$ clock transition. For multiple ions in a large magnetic field gradient, the clock transitions become separated in frequency due to the second order Zeeman effect, with the separation given by

$$\Delta\omega_{0,ij} = \omega_0(B_i + d_{ij}\partial_z B) - \omega_0(B_i), \tag{4.33}$$

where B_i is the magnetic field at ion i, $\omega_0(B)$ is clock transition frequency as defined in Sec. 2.3.3 and d_{ij} is the distance between ions i and j. Therefore to prepare $|0'\rangle$ in each ion starting from $|0\rangle$, one of two regimes should be considered. One regime is that the Rabi frequency of the microwave field (Ω_c) driving these transitions is large enough to drive all ions simultaneously, enabling a high fidelity π-pulse in each ($\Omega_c \gg \Delta\omega_{0,ij}$). This regime quickly becomes hard to reach as the ion number is increased for large magnetic field gradients, especially when high fidelities are

*For more information on the STIRAP preparation and detection scheme see the thesis of Dr. Sebastian Weidt [56] or Dr. Kim Lake [59].

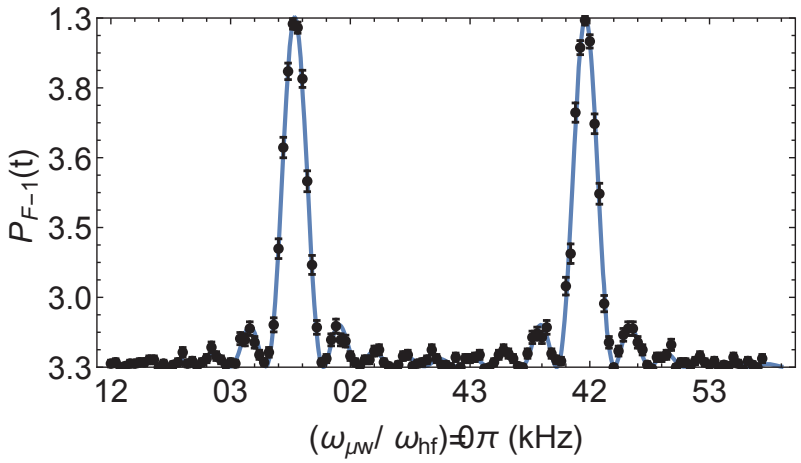


Fig. 4.12 Population in F = 1 after a frequency scan over the $|0\rangle \leftrightarrow |0'\rangle$ clock transition for two ions using a single microwave field. The blue line is a fit to the data for the sum of two transition probabilities, with the Rabi frequency fixed at $\Omega_c/2\pi = 0.69\,\text{kHz}$ and the two transition frequencies as free parameters. The fit gives a separation between the two peaks due to the second order Zeeman effect of $\Delta\omega_{0,12}/2\pi = 12.141(5)\,\text{kHz}$.

required. The second regime is when the Rabi frequency is small enough so that all transitions can be individually addressed ($\Omega_c \ll \Delta\omega_{0,ij}$). In this case, a different microwave field can be used for each transition, and the limitation in fidelity is then given by a combination of the cross-talk between the transitions and the coherence time.

Fig. 4.12 shows a frequency scan over the clock transitions in two ions separated by $d_{12} = 8.3\,\mu\text{m}$ with an offset magnetic field at ion 1 of $B_1 = 9\,\text{G}$, giving a separation of $\Delta\omega_{0,12}/2\pi = 12.141(5)\,\text{kHz}$. For a π-time of $720\,\mu\text{s}$, the cross-talk is $\Omega_c^2/2\Delta\omega_{0,12}^2 = 1.64\times10^{-3}$. To reduce the cross-talk further, $\Delta\omega_{0,12}$ could be increased by either increasing the magnetic field offset B_1 or gradient $\partial_z B$, or lowering the trap frequency ν_z, thereby increasing the ion-ion separation d_{12}.

4.3.4 T_1 and T_2 time measurements

To characterise the dressed states and demonstrate their insensitivity to magnetic field noise, the lifetime (T_1) and coherence time (T_2) should be measured. Transitions between the dressed states can occur when magnetic field noise is resonant with the dressed state energy splitting $\Omega_{\mu w}/\sqrt{2}$, limiting the T_1 time, while fluctuations in the dressing field Rabi frequencies and detunings can limit the T_2 time.

To measure the lifetime of the dressed state $|\beta\rangle \in \{|D\rangle, |u\rangle, |d\rangle\}$, population is first prepared in $|\beta\rangle$ via $|0'\rangle$ using the method described in Sec. 4.3.2. A delay with

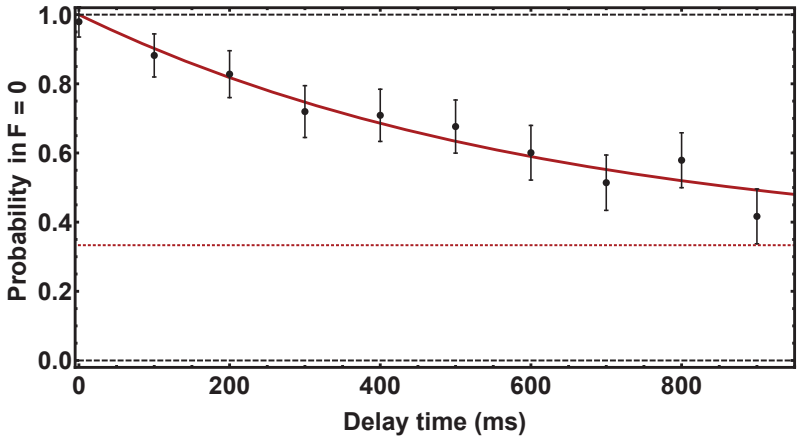


Fig. 4.13 A lifetime (T_1) measurement of the dressed state $|D\rangle$, where $|D\rangle$ is prepared via $|0'\rangle$ and mapped back to $|0\rangle$ via $|0'\rangle$ after a variable delay time. A measurement therefore discriminates between $|D\rangle$ and $\{|u\rangle, |d\rangle, |0'\rangle\}$ assuming the π-pulses are perfect. The red line is a fit to the data using Eq. 4.34, where the lifetime T_1 is the only free parameter, and is found to be $T_1 = 0.63(4)\,\mathrm{s}$. The dashed red line marks 1/3, which is the expected population in $|D\rangle$ if the three dressed states are completely mixed.

variable time is then added, during which the dressing fields are held at constant amplitude. A second RF pulse then transfers population from $|\beta\rangle$ back to $|0'\rangle$, before it is mapped back to $|0\rangle$ and measured. Fig. 4.13 shows the result of an experiment in which the dressed state $|D\rangle$ is prepared and the delay time is varied. The effect of magnetic field fluctuations near resonant with the dressed-state energy splitting in the long time limit is to drive population equally into all three dressed states. Therefore the population in the state $|D\rangle$ should decay to 1/3. The data is therefore fitted to an exponential function that decays to 1/3, given by

$$f_{\mathrm{lifetime}}(t) = \frac{2}{3}e^{-t/T_1} + \frac{1}{3}, \tag{4.34}$$

from which a lifetime of $T_1 = 0.63(4)$s is extracted. The limitation in lifetime is attributed to the finite energy gap between the dressed states. Since noise generally scales inversely with frequency, increasing this energy gap should reduce the amount of magnetic field noise coupling to the system, and thereby increase the lifetime. Increasing the energy splitting can be achieved by increasing the dressing field Rabi frequencies, and larger amplification stages for the microwave generation are therefore being considered.

To measure the coherence time of the qubit $\{|0'\rangle, |\beta\rangle\}$, a Ramsey experiment is performed. After preparing in $|0'\rangle$, a resonant RF $\pi/2$ pulse prepares an equal superposition of $|0'\rangle$ and $|\beta\rangle$. After a delay time t_d, a second $\pi/2$ pulse is applied

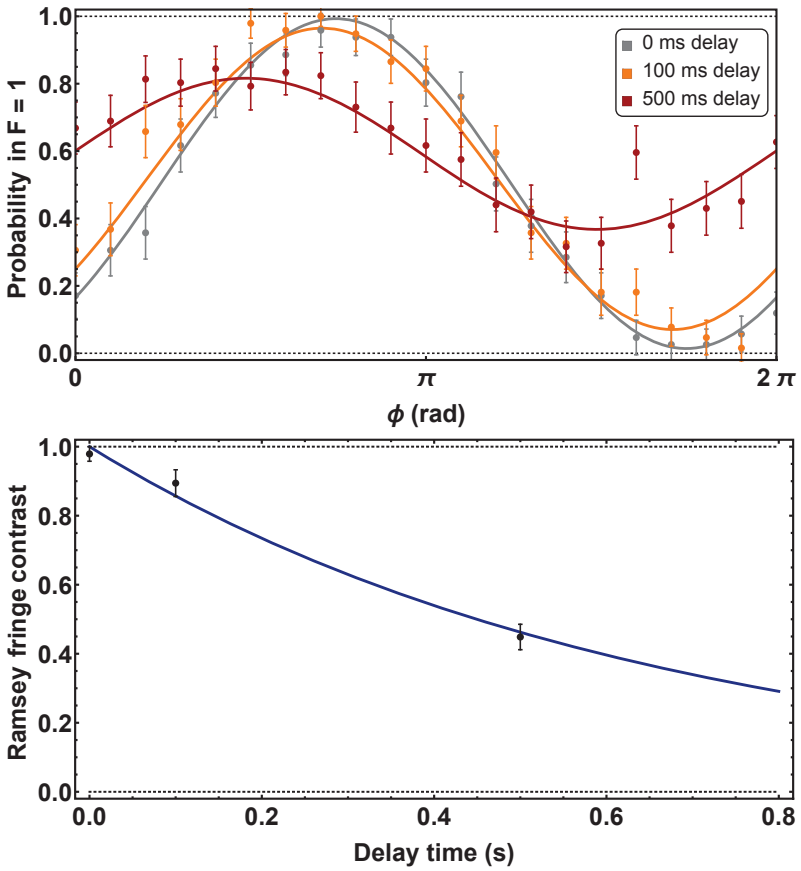


Fig. 4.14 Top: Result of a Ramsey experiment consisting of a $\pi/2$ RF pulse applied to the $|0'\rangle \leftrightarrow |D\rangle$ transition, followed by a delay for a time $t_d/2$, a spin echo RF π-pulse, a second delay for a time $t_d/2$ and finally a second RF $\pi/2$ pulse where the phase ϕ is varied. The grey, orange and red data points correspond to three different delay times as indicated in the legend, and the corresponding lines are the result of a fit to Eq. 4.35, with the amplitude and phase offset as free parameters. The variation in phase offset as the delay time is increased is attributed to slow drifts in the phase of the RF fields. Bottom: Fitted Ramsey fringe contrast for the three delay times for the data in the top graph, where the error bars are the standard errors extracted from the three fits. The blue line is an exponential decay fitted to the three points, giving a coherence time of $T_2 = 0.65(5)\,\mathrm{s}$.

and the phase is varied. As the phase is scanned from 0 to 2π, the population sinusoidally oscillates between $|0'\rangle$ and $|\beta\rangle$ over a full period. Any dephasing of the qubit coherences that occurs during the delay time will cause the amplitude of these Ramsey fringes to be reduced, and so by repeating the experiment for multiple delay times, a plot of the fringe contrast as a function of time can be found, from which the coherence time can be estimated. To remove the effects of slow magnetic field drifts over the course of several experimental repetitions, a spin echo pulse can be included in the middle of the delay. This consists of a single π-pulse with fixed phase at time $t_d/2$, causing the Bloch vector to rotate 180 degrees about an axis in the $x-y$ plane. If there is a slow constant phase rotation around the z axis, which could be due to a shift in the qubit energy, the spin echo pulse will reverse the direction of this rotation. Therefore the phase accumulated during the first half of the delay will be undone by the phase in the second half. Any phase noise that occurs on a timescale faster than t_d will average out during the delay and will therefore not be undone by the spin echo pulse.

Fig. 4.14 shows the result of such an experiment with the qubit $\{|0'\rangle, |D\rangle\}$, where the spin echo pulse has been applied halfway through the delay. As discussed previously, magnetic field fluctuations at the dressed-state energy splitting cause population to be distributed equally amongst the three dressed states. For initial populations $P(0') = P(D) = 1/2$, the populations after long times due to this depolarising effect therefore become $P(0') = 1/2$, $P(D) = P(u) = P(d) = 1/6$. If the coherences have completely dephased, the second $\pi/2$ Ramsey pulse will then transfer half of the population in $|D\rangle$ to $|0'\rangle$ and half of the population in $|0'\rangle$ to $|D\rangle$, giving final populations $P(0') = P(D) = 1/4 + 1/12 = 1/3$ and $P(u) = P(d) = 1/6$. A measurement that discriminates between $|0'\rangle$ and $\{|u\rangle, |d\rangle, |D\rangle\}$ will therefore decay to approximately $2/3$*. Each Ramsey fringe is therefore fitted with the equation

$$f_{\text{Ramsey}}(\phi) = \frac{A}{2}\left(\sin(\phi + \phi_0) - \frac{1}{3}\right) + \frac{2}{3}, \tag{4.35}$$

where A is the amplitude of the fringe and ϕ_0 is the phase offset, both of which are fitting parameters. The amplitude values are plotted as function of delay time, and an exponential fit gives a coherence time of $T_2 = 0.65(5)\,\text{s}$. As discussed in Sec. 4.3.1, both $|D\rangle$ and $|0'\rangle$ are insensitive to noise in the magnetic field and the dressing field Rabi frequencies to first order when the dressing field detunings are zero and

*Note that this value is approximate as in reality the depolarising and dephasing effects will happen simultaneously, and so a more thorough treatment would be required to reach an exact value.

the Rabi frequencies are equal. Experimentally, we saw a strong dependence of the coherence time on the difference Rabi frequency $\Delta\Omega$, and found that we had to set $\Delta\Omega/\Omega_{\text{av}} < 0.01$ in order to achieve the coherence time presented in Fig. 4.14. The detunings were set less accurately at approximately $0.05\Omega_{\text{av}}$. These levels of accuracy are consistent with the theoretical results in Sec. 4.3.1. Since the measured T_1 and T_2 times are equal within statistical errors, it is likely that the measured T_2 time is largely dominated by the lifetime of $|D\rangle$*.

4.4 Combining dressed states with a magnetic field gradient

In Chapter 3, we saw that a magnetic field gradient can give rise to coupling between the internal and motional states of trapped ions and that sideband transitions can be implemented with a coupling strength that is independent of the frequency of the driving radiation. The scheme requires that magnetic field sensitive states be used, and in this chapter we have shown that magnetic field sensitive qubits can be protected using dressed states. In this section the theory of dressed states in $^{171}\text{Yb}^+$ will be combined with the effect of adding a magnetic field gradient, and it will be shown that sideband transitions can be implemented between the dressed states, making them ideal for high-fidelity quantum logic schemes.

4.4.1 Dressed states in a magnetic field gradient

We can generalise the Hamiltonian in Eq. 3.7 to the four-level case in $^{171}\text{Yb}^+$ by noting that the energies of the states $|+1\rangle$ and $|-1\rangle$ are linear in magnetic field and neglecting the second-order Zeeman effect to get

$$\begin{aligned} H_0 &= H_B + H_m, \\ H_B &= \hbar\omega_+ |+1\rangle\langle+1| - \hbar\omega_- |-1\rangle\langle-1| - \hbar\omega_0 |0\rangle\langle 0|, \\ H_m &= \hbar\nu_z\eta\sigma_z\left(a + a^\dagger\right) + \hbar\nu_z a^\dagger a, \end{aligned} \tag{4.36}$$

where we have defined the zero of energy to be the energy of the state $|0'\rangle$ and $\sigma_z = |+1\rangle\langle+1| - |-1\rangle\langle-1|$. We can now follow the same procedure as in the two

*In Sec. 6.3.2, a master equation for depolarisation between $|D\rangle$, $|u\rangle$ and $|d\rangle$ is given (Eq. 6.31). An analytical solution of this equation for a single ion initialised in the state $(|0'\rangle + |D\rangle)/\sqrt{2}$ suggests that it may be possible to achieve a higher coherence time with the upper limit given by $T_2 \leq 3T_1$.

level case, except that now the harmonic oscillator will be displaced in a different direction depending on whether a transition is made to $|+1\rangle$ or $|-1\rangle$. We therefore define two sets of displaced ladder operators as

$$\begin{aligned} b_\pm &= a \pm \eta, \\ b_\pm^\dagger &= a^\dagger \pm \eta. \end{aligned} \tag{4.37}$$

The polaron states and operators are then given by

$$\begin{aligned} |0_p\rangle\,|n_p\rangle &= |0\rangle\,|n\rangle\,, \\ |0'_p\rangle\,|n_p\rangle &= |0'\rangle\,|n\rangle\,, \\ |+1_p\rangle\,|n_p\rangle &= e^{-\eta(a^\dagger - a)}\,|+1\rangle\,|n\rangle\,, \\ |-1_p\rangle\,|n_p\rangle &= e^{\eta(a^\dagger - a)}\,|-1\rangle\,|n\rangle\,, \\ a_p &= a\Big(\,|0\rangle\langle 0| + |0'\rangle\langle 0'|\,\Big) + b_+\,|+1\rangle\langle +1| + b_-\,|-1\rangle\langle -1| \\ &= a + \eta\sigma_z, \\ a_p^\dagger &= a^\dagger\Big(\,|0\rangle\langle 0| + |0'\rangle\langle 0'|\,\Big) + b_+^\dagger\,|+1\rangle\langle +1| + b_-^\dagger\,|-1\rangle\langle -1| \\ &= a^\dagger + \eta\sigma_z, \end{aligned} \tag{4.38}$$

allowing us to re-write H_m as

$$H_m = \hbar\nu_z a_p^\dagger a_p - \hbar\nu_z\eta^2\sigma_{z,p}^2. \tag{4.39}$$

As in the two level case, we can apply a polaron transformation $U_p = e^{\eta\sigma_z(a^\dagger - a)}$ to rotate the polaron states and operators back into the original basis if desired.

With these definitions, the dressing Hamiltonian equivalent to Eq. 4.22 with the microwave field frequencies set to resonance* and in the interaction picture with respect to H_0 is given by

$$H'_{\mu\mathrm{w}} = \frac{\hbar\Omega_{\mu\mathrm{w}}}{2}\Big(\,|+1_p\rangle\langle 0_p|\,e^{i\phi_+}e^{\eta(\tilde{a}_p^\dagger - \tilde{a}_p)} + |-1_p\rangle\langle 0_p|\,e^{i\phi_-}e^{-\eta(\tilde{a}_p^\dagger - \tilde{a}_p)} + \mathrm{H.c}\Big), \tag{4.40}$$

*Here resonance corresponds to the measured frequency in the lab, which includes the energy shift from the gradient in H_m of $-\hbar\nu_z\eta^2$ on both the $|+1\rangle$ and $|-1\rangle$ states.

where $\tilde{a}_p = e^{-i\nu_z t}$. Expanding in powers of η, the zeroth order term is

$$\begin{aligned} H^0_{\mu\mathrm{w}} &= \frac{\hbar\Omega_{\mu\mathrm{w}}}{2}\Big(|+1_p\rangle\langle 0_p| e^{i\phi_+} + |-1_p\rangle\langle 0_p| e^{i\phi_-} + \mathrm{H.c}\Big) \\ &= \frac{\hbar\Omega_{\mu\mathrm{w}}}{\sqrt{2}}\Big(|u_p\rangle\langle u_p| - |d_p\rangle\langle d_p|\Big), \end{aligned} \tag{4.41}$$

which is just the usual dressing Hamiltonian term in the polaron basis with dressed states $|D_p\rangle$, $|u_p\rangle$ and $|d_p\rangle$. The first order term is

$$H^1_{\mu\mathrm{w}} = \frac{\hbar\eta\Omega_{\mu\mathrm{w}}}{2}\Big(a_p^\dagger e^{i\nu_z t} - a_p e^{-i\nu_z t}\Big)\Big(|+1_p\rangle\langle 0_p| e^{i\phi_+} - |-1_p\rangle\langle 0_p| e^{i\phi_-}\Big) + \mathrm{H.c.} \tag{4.42}$$

Crucially, the different effect of the gradient on the states $|+1\rangle$ and $|-1\rangle$ has introduced a minus sign between the two spin state terms. Applying the polaron transformation and writing in the dressed basis we therefore get

$$\begin{aligned} H^1_{\mu\mathrm{w},I} &= \frac{\hbar\eta\Omega_{\mu\mathrm{w}}}{2}\Big(a^\dagger e^{i\nu_z t} - a e^{-i\nu_z t}\Big)\Big(|D\rangle\langle u| - |D\rangle\langle d|\Big) + \mathrm{H.c} \\ &= -\frac{\hbar\eta\Omega_{\mu\mathrm{w}}}{2\sqrt{2}}\Big(a^\dagger e^{i\nu_z t} - a e^{-i\nu_z t}\Big)\Big(S_+ - S_-\Big), \end{aligned} \tag{4.43}$$

where we have defined the three level dressed state ladder operators $S_+ = \sqrt{2}\Big(|u\rangle\langle D| + |D\rangle\langle d|\Big)$ and $S_- = \sqrt{2}\Big(|D\rangle\langle u| + |d\rangle\langle D|\Big)$. Going into the interaction picture with respect to $H^0_{\mu\mathrm{w}}$, this becomes

$$H^1_{\mu\mathrm{w},I} = -\frac{\hbar\eta\Omega_{\mu\mathrm{w}}}{2\sqrt{2}}\Big(a^\dagger e^{i\nu_z t} - a e^{-i\nu_z t}\Big)\Big(S_+ e^{i\frac{\Omega_{\mu\mathrm{w}}}{\sqrt{2}}t} - S_- e^{-i\frac{\Omega_{\mu\mathrm{w}}}{\sqrt{2}}t}\Big). \tag{4.44}$$

Normally, this Hamiltonian would be neglected in a rotating wave approximation as long as $|\nu_z - \Omega_{\mu\mathrm{w}}| \gg 0$. However, for realistic experimental parameters ν_z and $\Omega_{\mu\mathrm{w}}$, this condition may not be fully satisfied and the term can therefore have a small undesired effect, especially in the case of multiple ions. To see this we can perform the Magnus expansion, as described in appendix C, which allows an effective time independent Hamiltonian to be found. Expanding to second order and looking for secular terms, we find in the single ion case

$$H^1_{\mathrm{eff}} = \frac{\hbar\eta^2\Omega^3_{\mu\mathrm{w}}}{\Omega^2_{\mu\mathrm{w}} - 2\nu_z^2} a^\dagger a S_z + \frac{\hbar\eta^2\Omega^2_{\mu\mathrm{w}}\nu_z}{4(\Omega^2_{\mu\mathrm{w}} - 2\nu_z^2)}\Big(S_+S_- + S_-S_+\Big), \tag{4.45}$$

where we have defined $S_z = (|u\rangle\langle u| - |d\rangle\langle d|)/\sqrt{2}$. These terms correspond to Stark shifts of the dressed states, where the first term gives a Stark shift on $|u\rangle$ and $|d\rangle$ that is dependent on the motional state n, while the second term gives a shift to all three of the dressed states. These shifts can be compensated for by either calculating them or measuring them in the experiment and setting the RF detunings accordingly. For the multi-ion case, as well as the generalised version of Eq. 4.45 summed over all ions and normal modes, there is also a cross-coupling term, given by

$$H_{\text{eff}}^1 = \sum_{i\neq j}\sum_k \frac{\hbar\eta_{ik}\eta_{jk}\Omega_{\mu\text{w}}^2\nu_k}{4(\Omega_{\mu\text{w}}^2 - 2\nu_k^2)}\left(S_+^iS_-^j + S_-^iS_+^j\right). \tag{4.46}$$

The operators $S_\pm^iS_\mp^j$ give rise to pairwise transitions between combinations of dressed states. One of these transitions is $|D_iD_j\rangle \leftrightarrow (|u_id_j\rangle + |d_iu_j\rangle)/\sqrt{2}$, which can be an unwanted effect if using the dressed state qubit $\{|0_i'\rangle, |D_i\rangle\}$ in a multi ion string. In this case, this term should be minimised. Alternatively, this term could be used to create an entangled state of two ions in the dressed basis by preparing the state $|D_iD_j\rangle$ and letting the system evolve. It will be seen in the following section that another term contributes to these same transitions between the dressed states, and therefore the transition rates are given by the sum of the contributions by the two terms.

4.4.2 Dressed spin-spin coupling

As shown in Sec. 3.3.3, a magnetic field gradient applied to multiple ions produces a spin-spin coupling term. We will now consider how this term translates to the dressed basis. In the four level $^{171}\text{Yb}^+$ system, the spin-spin coupling Hamiltonian is

$$H_{ss} = -\sum_{i\neq j}\hbar J_{ij}\sigma_z^i\sigma_z^j, \tag{4.47}$$

where $J_{ij} = \sum_k \nu_k\eta_{ik}\eta_{jk}$. We can transform to the dressed basis and go to the interaction picture with respect to $H_{\mu\text{w}}^0$ to give

$$H_{ss} = -\sum_{i\neq j}\frac{\hbar J_{ij}}{4}\left(S_+^iS_+^je^{i\sqrt{2}\Omega_{\mu\text{w}}t} + S_-^iS_-^je^{-i\sqrt{2}\Omega_{\mu\text{w}}t} + S_+^iS_-^j + S_-^iS_+^j\right). \tag{4.48}$$

Terms rotating at $e^{\pm i\sqrt{2}\Omega_{\mu\text{w}}t}$ are cancelled by a rotating wave approximation as long as $J_{ij} \ll \Omega_{\mu\text{w}}$, leaving the terms $S_+^iS_-^j$ and $S_-^iS_+^j$, which are the same transitions as those found in the first order dressing field Hamiltonian H_{eff}^1. This contribution can

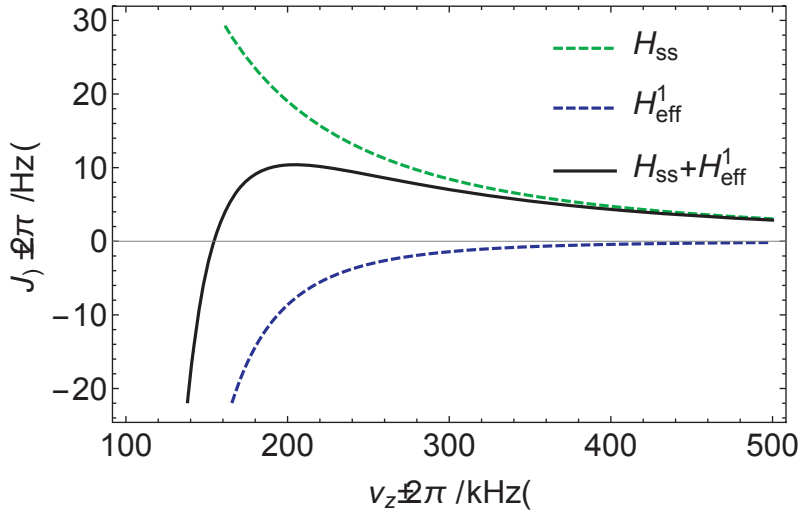


Fig. 4.15 Plot of the transition rate $J_\pm = J^\pm_{12} + J^\pm_{21}$ for the terms $S^1_\pm S^2_\mp$ as a function of the trap frequency for two ions. The green and blue dashed curves show the contributions from the spin-spin coupling (H_{ss}) and dressing field sideband (H^1_{eff}) terms respectively, while the black line shows their sum. The dressing field Rabi frequencies have been set to $\Omega_{\mu\text{w}}/2\pi = 100\,\text{kHz}$, and it can be seen that if ν_z is close to $\Omega_{\mu\text{w}}$, H^1_{eff} dominates, while H_{ss} gives the bigger contribution as ν_z is increased away from $\Omega_{\mu\text{w}}$.

be combined with the transition in Eq. 4.46 to give a final term

$$\begin{aligned} H_\pm = H^1_{\text{eff}} + H_{ss} &= \sum_{i\neq j}\sum_k \frac{\hbar\eta_{ik}\eta_{jk}\nu_k^3}{2(\Omega^2_{\mu\text{w}} - 2\nu_k^2)}\left(S^i_+ S^j_- + S^i_- S^j_+\right) \\ &= \sum_{i\neq j} \hbar J^\pm_{ij}\left(S^i_+ S^j_- + S^i_- S^j_+\right), \end{aligned} \tag{4.49}$$

where we have defined $J^\pm_{ij} = \sum_k \eta_{ik}\eta_{jk}\nu_k^3/2(\Omega^2_{\mu\text{w}} - 2\nu_k^2)$. An example case for two ions is shown in Fig. 4.15, where the two contributions as well as their sum are plotted as a function of ν_z. It can be seen that as long as ν_z is reasonably far in frequency from $\Omega_{\mu\text{w}}$, the spin-spin coupling term dominates the transition rate and the sideband term is a small correction. This interaction is used in Ref. [67] as the basis for a proposal for a quantum simulation of the Haldane phase in spin-1 particles. However, for other purposes it may be an undesirable effect and should be minimised.

4.4.3 Dressed state sidebands

Aside from the effects discussed in the previous two sections, the dressed ions in a magnetic field gradient behave in the same way as in the case with no gradient,

except with the polaron spin and motional states. An RF field coupling $|0'_p\rangle$ and either $|+1_p\rangle$ or $|-1_p\rangle$ will contain sideband terms due to the gradient, and these sideband terms will remain when transforming to the dressed basis, allowing the dressed spin states to be coupled to the motional states. After transforming to the interaction picture with respect to H_0, the Hamiltonian for the RF field in the polaron basis is given by

$$H'_{\mathrm{rf}} = \frac{\hbar\Omega_{\mathrm{rf}}}{2}\Big(|+1_p\rangle \langle 0'_p| \, e^{-i\delta_{\mathrm{rf}}t} e^{i\phi_{\mathrm{rf}}} e^{\eta(\tilde{a}_p^\dagger - \tilde{a}_p)} + |-1_p\rangle \langle 0'_p| \, e^{i(\delta_{\mathrm{rf}} - \Delta\omega_\pm)t} e^{-i\phi_{\mathrm{rf}}} e^{-\eta(\tilde{a}_p^\dagger - \tilde{a}_p)} + \mathrm{H.c}\Big). \tag{4.50}$$

We can then write this in the dressed basis in a similar way to the case with no gradient, which after performing the polaron transformation gives

$$\begin{aligned} H'_{\mathrm{rf}} =& \frac{\hbar\Omega_{\mathrm{rf}}}{2\sqrt{2}}\Big(|D\rangle \langle 0'| \left(e^{-i\delta_{\mathrm{rf}}t} e^{i\phi_{\mathrm{rf}}} e^{\eta(\tilde{a}^\dagger - \tilde{a})} - e^{i(\delta_{\mathrm{rf}} - \Delta\omega_\pm)t} e^{-i\phi_{\mathrm{rf}}} e^{-\eta(\tilde{a}^\dagger - \tilde{a})} \right) + \mathrm{H.c}\Big) \\ &+ \frac{\hbar\Omega_{\mathrm{rf}}}{4}\Big(|u\rangle \langle 0'| \left(e^{-i(\delta_{\mathrm{rf}} - \frac{\Omega_{\mu\mathrm{w}}}{\sqrt{2}})t} e^{i\phi_{\mathrm{rf}}} e^{\eta(\tilde{a}^\dagger - \tilde{a})} + e^{i(\delta_{\mathrm{rf}} - \Delta\omega_\pm + \frac{\Omega_{\mu\mathrm{w}}}{\sqrt{2}})t} e^{-i\phi_{\mathrm{rf}}} e^{-\eta(\tilde{a}^\dagger - \tilde{a})} \right) \\ &+ |d\rangle \langle 0'| \left(e^{-i(\delta_{\mathrm{rf}} + \frac{\Omega_{\mu\mathrm{w}}}{\sqrt{2}})t} e^{i\phi_{\mathrm{rf}}} e^{\eta(\tilde{a}^\dagger - \tilde{a})} + e^{i(\delta_{\mathrm{rf}} - \Delta\omega_\pm - \frac{\Omega_{\mu\mathrm{w}}}{\sqrt{2}})t} e^{-i\phi_{\mathrm{rf}}} e^{-\eta(\tilde{a}^\dagger - \tilde{a})} \right) + \mathrm{H.c}\Big), \end{aligned} \tag{4.51}$$

where we have set the phase of the microwave field to $\phi_+ = 0$ for simplicity. Expanding in powers of η, the zeroth order is identical to Eq. 4.25, while the first order gives red and blue sideband terms, given by

$$\begin{aligned} H^r_{\mathrm{rf}} =& -\frac{\hbar\eta\Omega_{\mathrm{rf}}}{2\sqrt{2}}\Big(|D\rangle \langle 0'| \left(e^{-i\delta_r t} e^{i\phi_{\mathrm{rf}}} a - e^{i(\delta_r - \Delta\omega_\pm)t} e^{-i\phi_{\mathrm{rf}}} a^\dagger \right) + \mathrm{H.c}\Big) \\ &- \frac{\hbar\eta\Omega_{\mathrm{rf}}}{4}\Big(|u\rangle \langle 0'| \left(e^{-i(\delta_r - \frac{\Omega_{\mu\mathrm{w}}}{\sqrt{2}})t} e^{i\phi_{\mathrm{rf}}} a + e^{i(\delta_r - \Delta\omega_\pm + \frac{\Omega_{\mu\mathrm{w}}}{\sqrt{2}})t} e^{-i\phi_{\mathrm{rf}}} a^\dagger \right) \\ &+ |d\rangle \langle 0'| \left(e^{-i(\delta_r + \frac{\Omega_{\mu\mathrm{w}}}{\sqrt{2}})t} e^{i\phi_{\mathrm{rf}}} a + e^{i(\delta_r - \Delta\omega_\pm - \frac{\Omega_{\mu\mathrm{w}}}{\sqrt{2}})t} e^{-i\phi_{\mathrm{rf}}} a^\dagger \right) + \mathrm{H.c}\Big), \end{aligned} \tag{4.52}$$

$$\begin{aligned} H^b_{\mathrm{rf}} =& \frac{\hbar\eta\Omega_{\mathrm{rf}}}{2\sqrt{2}}\Big(|D\rangle \langle 0'| \left(e^{-i\delta_b t} e^{i\phi_{\mathrm{rf}}} a^\dagger - e^{i(\delta_b - \Delta\omega_\pm)t} e^{-i\phi_{\mathrm{rf}}} a \right) + \mathrm{H.c}\Big) \\ &+ \frac{\hbar\eta\Omega_{\mathrm{rf}}}{4}\Big(|u\rangle \langle 0'| \left(e^{-i(\delta_b - \frac{\Omega_{\mu\mathrm{w}}}{\sqrt{2}})t} e^{i\phi_{\mathrm{rf}}} a^\dagger + e^{i(\delta_b - \Delta\omega_\pm + \frac{\Omega_{\mu\mathrm{w}}}{\sqrt{2}})t} e^{-i\phi_{\mathrm{rf}}} a \right) \\ &+ |d\rangle \langle 0'| \left(e^{-i(\delta_b + \frac{\Omega_{\mu\mathrm{w}}}{\sqrt{2}})t} e^{i\phi_{\mathrm{rf}}} a^\dagger + e^{i(\delta_b - \Delta\omega_\pm - \frac{\Omega_{\mu\mathrm{w}}}{\sqrt{2}})t} e^{-i\phi_{\mathrm{rf}}} a \right) + \mathrm{H.c}\Big), \end{aligned} \tag{4.53}$$

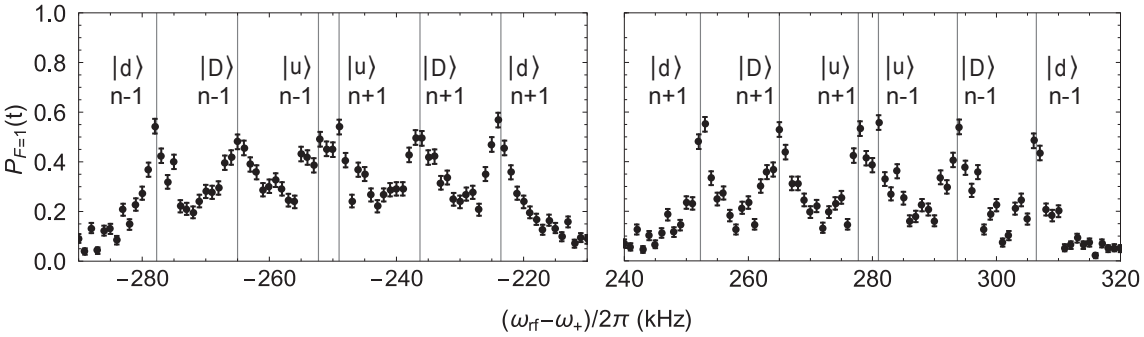


Fig. 4.16 Population in F = 1 after preparing in $|0'\rangle$ and applying an RF field near resonant with the red sidebands (left) or blue sidebands (right) of the dressed state transitions and varying the frequency. The vertical lines show the expected peak positions according to the corresponding dressed state carrier peaks, as shown in Fig. 4.11, which are predicted from Eqs. 4.52 and 4.53. The ion is only Doppler cooled and hence the motion is in a mixed thermal state. Therefore the peak amplitudes are averaged over the response of the sidebands for each n level in the mixture (see Chapter 5 for further details). It can be seen that for sideband transitions from $|0'\rangle$ to $|\beta\rangle$ via $|-1\rangle$, the red (blue) sideband transition takes the motional state from n to $n+1$ $(n-1)$ due to the fact that $|-1\rangle$ is lower in energy than $|0'\rangle$.

where $\delta_r = \delta_{\mathrm{rf}} + \nu_z$ and $\delta_b = \delta_{\mathrm{rf}} - \nu_z$. There are therefore six red and blue sideband transitions corresponding to each of the six carrier transitions to the three dressed states. Note that due to the energy ordering of the states $|-1\rangle$, $|0'\rangle$ and $|+1\rangle$, a red sideband transition from $|0'\rangle$ to a dressed state $|\beta\rangle$ lowers the motional state by one (a) if coupled via $|+1\rangle$ or raises by one $(a^\dagger)$ if coupled via $|+1\rangle$. Fig. 4.16 shows a scan over the red and blue dressed state sideband transitions in a single ion for all six transitions corresponding to the six terms in H^r_{rf} and H^b_{rf}, demonstrating that the dressed states can be coupled to the ion's motional state.

Chapter 5

Sideband cooling

5.1 Introduction

Sideband cooling is a well established technique that allows the motional states of one or more ions to be cooled below the Doppler cooling limit, and ideally close to the ground state. Unlike the mixed thermal states produced by Doppler cooling, the ground state $|n = 0\rangle$ is a pure state, and therefore with further coherent manipulation other pure motional states, such as Fock, coherent and squeezed states, can be created. This makes sideband cooling an invaluable tool for a wide range of trapped ion experiments, many of which require coherent control of the motional degrees of freedom.

To perform sideband cooling, an atomic transition is required with a linewidth much less than the secular frequency of the trap in order to drive specific motional sidebands. This can be realised by either directly driving a narrow linewidth optical transition such as the $S \leftrightarrow D$ transition in calcium [73], or by using a pair of Raman laser beams with a difference frequency equal to the frequency gap between two hyperfine ground states [74]. These two implementations are standard practice in many laboratories, with ground state occupation probabilities reaching 99.9%.

As shown in the previous chapters, a static magnetic field gradient allows sideband transitions to be driven directly between hyperfine ground states using RF and microwave frequency radiation. The use of these transitions for sideband cooling could be advantageous for the scalability of trapped ion experiments, especially when low frequency radiation is used for all coherent operations. Lasers would then only be needed for dissipation, as well as the usual Doppler cooling, state preparation and readout.

In this chapter, sideband cooling of the axial mode of a single ion using long-

wavelength radiation is demonstrated, achieving a ground state preparation fidelity of 88(7)%. Sideband cooling is demonstrated on the dressed state transition $|0'\rangle \leftrightarrow |D\rangle$ at radio frequency. Due to the long coherence time of the dressed state qubit, coherent manipulation of the motional state is possible and is demonstrated in the form of a Rabi oscillation on the blue sideband after cooling to the ground state. The heating rate of a single ion is also measured, and sideband cooling and heating rate measurements are performed on the stretch mode of two ions.

5.2 Doppler cooling

Doppler cooling ideally cools all modes of an ion string to the Doppler temperature, T_D, given by [75]

$$T_D = \frac{\hbar\Gamma}{2k_B}, \tag{5.1}$$

where Γ is the natural linewidth of the cooling transition and k_B is Boltzmann's constant. For the 369 nm $^2S_{1/2} \rightarrow {}^2P_{1/2}$ cooling transition in $^{171}\mathrm{Yb}^+$ with a natural linewidth of $\Gamma/2\pi = 19.6\,\mathrm{MHz}$, $T_D = 471\,\mu\mathrm{K}$. This temperature is achieved when the 369 nm cooling laser is red detuned by $\Gamma/2$ from resonance. The Doppler temperature gives the minimum temperature that can be achieved for ideal Doppler cooling, however in practice non-ideal experimental conditions such as a finite Zeeman shift in the $^2S_{1/2}, F = 1$ manifold or mis-set cooling parameters may result in a higher equilibrium temperature. Doppler cooling produces a thermal motional state ρ_{th}, given by

$$\rho_{\mathrm{th}} = \sum_{n=0}^{\infty} p_n \left|n\right\rangle \left\langle n\right| . \tag{5.2}$$

The populations, p_n, of each motional eigenstate $|n\rangle$ are given by a Boltzmann distribution, which can be written in terms of the average phonon number $\bar{n}$ as [76]

$$p_n = \frac{1}{1+\bar{n}} \left(\frac{\bar{n}}{1+\bar{n}}\right)^n . \tag{5.3}$$

For a given temperature and mode frequency ν_l, $\bar{n}$ can be found to be

$$\bar{n} = \frac{k_B T}{\hbar\nu_l}, \tag{5.4}$$

which can be used to obtain the expected $\bar{n}$ of a motional mode after Doppler cooling.

5.3 Measuring the temperature

The temperature of a motional mode can be measured by driving the sidebands, which have a response that depends on $\bar{n}$. As described in Sec. 3.2.3, in the Lamb-Dicke regime the Rabi frequencies for the first red and blue sidebands of a transition between two states $|\downarrow\rangle|n\rangle$ and $|\uparrow\rangle|n\pm1\rangle$ are given by $\Omega_{n,n-1}=\sqrt{n}\eta\Omega_0$ and $\Omega_{n,n+1}=\sqrt{n+1}\eta\Omega_0$, respectively, where Ω_0 is the carrier Rabi frequency. For a red (blue) sideband interaction detuned from resonance by an amount δ_r (δ_b), the probability to transfer from n to $n-1$ ($n+1$) accompanied by a change in spin state is given by

$$\begin{aligned} P^{\uparrow}_{n,n-1}(t,\delta_r) &= \frac{\Omega^2_{n,n-1}}{\Omega^2_{n,n-1}+\delta_r^2}\left[\frac{1}{2}-\frac{1}{2}\cos\left(t\sqrt{\Omega^2_{n,n-1}+\delta_r^2}\right)\right], \\ P^{\uparrow}_{n,n+1}(t,\delta_b) &= \frac{\Omega^2_{n,n+1}}{\Omega^2_{n,n+1}+\delta_b^2}\left[\frac{1}{2}-\frac{1}{2}\cos\left(t\sqrt{\Omega^2_{n,n+1}+\delta_b^2}\right)\right]. \end{aligned} \tag{5.5}$$

For the thermal state ρ_{th}, the probability to make a transition between two spin states is therefore

$$\begin{aligned} P^{\uparrow}_{\mathrm{rsb}}(t,\delta_r) &= \sum_{n=0}^{\infty} p_n P^{\uparrow}_{n,n-1}(t,\delta_r), \\ P^{\uparrow}_{\mathrm{bsb}}(t,\delta_b) &= \sum_{n=0}^{\infty} p_n P^{\uparrow}_{n,n+1}(t,\delta_b). \end{aligned} \tag{5.6}$$

Eq. 5.6 can be used to infer the temperature of a mode by applying a sideband pulse with variable time or detuning and observing the change in spin-state population.

When $\bar{n}\gg1$, which is typically the case after Doppler cooling, $\Omega_{n,n-1}\approx\Omega_{n,n+1}$, and it is therefore sufficient to only perform an experiment on one of the two sidebands to measure the temperature, as their response will be almost identical. Fig. 5.1 shows the result of such an experiment for a single ion.

For $\bar{n}<1$, which is the regime that can be reached by sideband cooling, the difference between $\Omega_{n,n-1}$ and $\Omega_{n,n+1}$ becomes significant, and the most accurate temperature measurement is then found from the difference between the responses of the two sidebands. For resonant sideband interactions ($\delta_r=\delta_b=0$), we can re-write

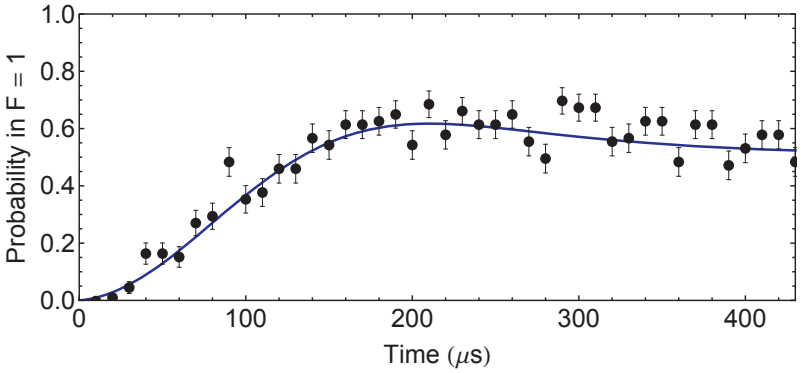


Fig. 5.1 Result of an experiment to determine $\bar{n}$ for the axial mode of a single ion in a trap with secular frequency $\nu_z = 2\pi \times 440\,\text{kHz}$. The bare-state qubit $\{|0\rangle, |+1\rangle\}$ is used, with a coherence time of approximately 2 ms. The experiment consists of 4 ms of Doppler cooling, followed by preparation in $|0\rangle$ and a microwave pulse on the $|0, n\rangle \rightarrow |+1, n+1\rangle$ transition with variable length. The carrier Rabi frequency Ω_0 was independently measured to be 40 kHz, and a theory curve using Eq. 5.6, modified to include decoherence effects is shown where $\bar{n}$ has been set to 80. For this secular frequency, the Doppler limited $\bar{n}$ predicted from Eq. 5.4 is 22. The reason for the discrepancy between the predicted and measured values is most likely due to a combination of linewidth broadening due to the non-zero Zeeman shift between the $^2S_{1/2}$, $F = 1$ states, and imperfect setting of laser power and detuning.

the equation for $P^{\uparrow}_{\text{rsb}}$ in Eq. 5.6 as

$$\begin{aligned} P^{\uparrow}_{\text{rsb}}(t) &= \sum_{n=1}^{\infty} p_n \frac{1}{2}\left(1 - \cos(\Omega_{n,n-1}t)\right) \\ &= \sum_{n=0}^{\infty} p_{n+1} \frac{1}{2}\left(1 - \cos(\Omega_{n,n+1}t)\right) \\ &= \frac{\bar{n}}{\bar{n}+1} \sum_{n=0}^{\infty} p_n \frac{1}{2}\left(1 - \cos(\Omega_{n,n+1}t)\right) \\ &= \frac{\bar{n}}{\bar{n}+1} P^{\uparrow}_{\text{bsb}}(t) \end{aligned} \tag{5.7}$$

allowing us to calculate the ratio between the sideband amplitudes, R, to be

$$R \equiv \frac{P^{\uparrow}_{\text{rsb}}(t)}{P^{\uparrow}_{\text{bsb}}(t)} = \frac{\bar{n}}{\bar{n}+1}. \tag{5.8}$$

This can be re-arranged to give

$$\bar{n} = \frac{R}{1-R}, \tag{5.9}$$

which gives a simple method to calculate $\bar{n}$ by looking at the ratio of the sideband

heights after applying a pulse on each for a fixed length of time. The sideband pulse should be applied for a time that maximizes the difference in heights, which for low $\bar{n}$ is close to the π-time for ground state transition, $t_0 = \pi/\eta\Omega_0$. The temperature can also be measured by performing either a time or frequency scan of the two sidebands and performing a simultaneous fit to Eq. 5.6.

5.4 Sideband cooling

Sideband cooling allows the ions' motional states to be cooled below the minimum temperature achievable with Doppler cooling. A sideband cooling experiment consists of two processes. The first requires a narrow linewidth transition to spectrally resolve the sidebands from the carrier, allowing population to be transferred from $|n\rangle$ to $|n-1\rangle$ by driving a red sideband. The second is a dissipative 'repump', requiring a transition with a fast spontaneous decay rate to take entropy from the system and reset the spin state without affecting the motional state. A schematic of a sideband cooling experiment using long-wavelength radiation is shown in Fig. 5.2. To sideband cool using long-wavelength radiation in $^{171}\mathrm{Yb}^+$, one of the microwave or RF transitions in the $^2S_{1/2}$ ground state can be used for the sideband interaction, and the 369 nm $^2S_{1/2}$, $F = 1 \rightarrow {}^2P_{1/2}$, $F = 1$ transition can be used for the repump. The two processes can either be applied at the same time, known as continuous sideband cooling, or alternately cycled, known as pulsed sideband cooling. The continuous method requires the 2 GHz modulation on the 369 nm laser to be on for the duration of the cooling, which in our experimental setup caused the Toptica 369 nm laser to unlock (see Sec. 2.4.2). We therefore chose to implement the pulsed method, in which the modulation is only applied for a few μs. The difficulty in the continuous method could however be overcome with the newer 369 nm M^2 laser, for which the EOM is situated after the 739 nm light is picked off for locking, and hence is unaffected.

The red sideband interaction can be realised in multiple ways. Using a microwave bare state transition such as $|0\rangle \leftrightarrow |+1\rangle$ is the simplest implementation, as it only requires a single pulse per cycle. However, since the coherence time is short compared to the sideband π-time in the ground state, less population that can be transferred per sideband pulse. A more effective method is to use the dressed state transition $|0'\rangle \leftrightarrow |D\rangle$, as the coherence time issues are eliminated. However, this method has a slightly higher experimental overhead, requiring more pulses and frequencies. Both methods reduce the motional state by transfering population from $F = 0$ to $F = 1$,

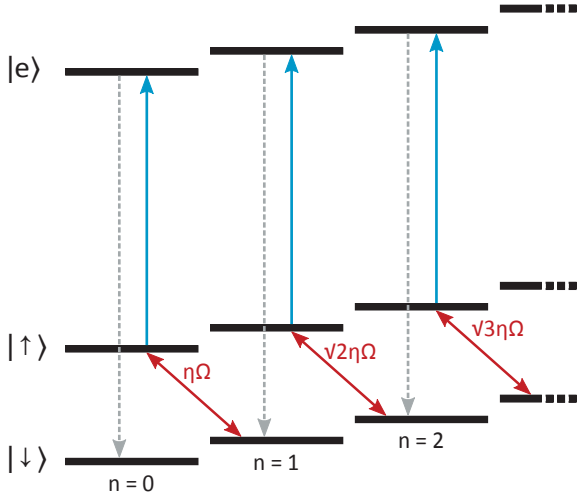


Fig. 5.2 Schematic of a sideband cooling experiment using long-wavelength radiation. For an ion initialised in a spin state $|\downarrow\rangle$ corresponding to one of the hyperfine ground states or dressed states, a microwave or RF pulse is applied on the $|\downarrow, n\rangle \rightarrow |\uparrow, n-1\rangle$ red sideband transition for a time t_p (red arrows). The rate of transfer is n-dependent, and so for a thermal state, the population of each $|n\rangle$ level in the mixture will transfer at different rates, creating a new non-thermal mixed state. The total amount of population transferred from $|\downarrow\rangle$ to $|\uparrow\rangle$ is given in Eq. 5.6. After the sideband pulse, a pulse of laser light is applied, which cycles population between $|\uparrow\rangle$ and a third level $|e\rangle$ (blue arrows). The upper level has a short lifetime and decays quickly to $|\downarrow\rangle$ (dashed grey arrows), thereby resetting the spin state with little effect on the motional state. By repeating this procedure multiple times, the ion will ideally end up in the ground state.

and therefore the repump step is the same in both cases.

The dissipative repump process is identical to the optical pumping scheme discussed in Sec. 2.5.2 to initialise the spin states. With 2 GHz modulation on the 369 nm laser, the $^2S_{1/2}$, $F = 1 \rightarrow {}^2P_{1/2}$, $F = 1$ transition is strongly driven, causing population to quickly decay to $^2S_{1/2}$, $F = 0$. Since the $^2P_{1/2}$, $F = 1$ states can also decay to $^2S_{1/2}$, $F = 1$, photons are scattered with each pulse before the desired spin state is prepared. Each scattering event gives the ion a small increase in energy, known as the recoil energy, given by

$$E_{\text{recoil}} = \frac{\hbar^2 k^2}{2m}. \tag{5.10}$$

This can be written as an increase in the mean phonon number as

$$\Delta\bar{n}_{\text{recoil}} = \alpha \frac{\hbar k^2}{2m\nu_l}, \tag{5.11}$$

where α is the fraction of the recoil energy that heats the mode l, which depends

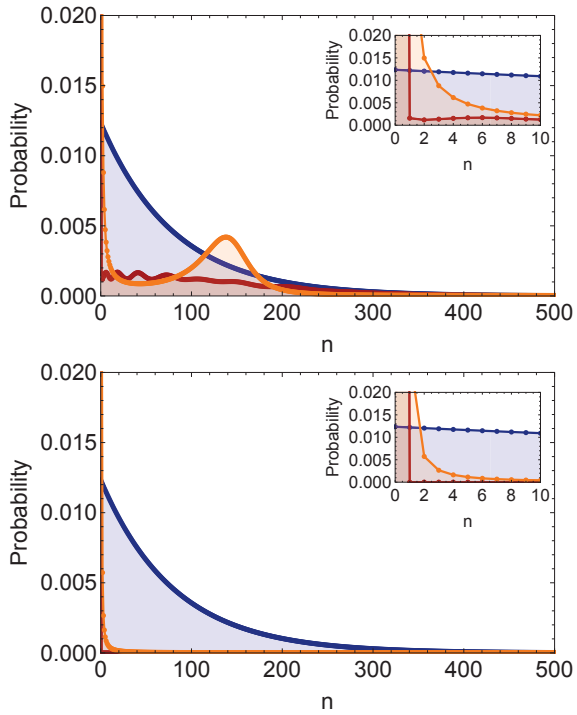


Fig. 5.3 Simulated populations before and after sideband cooling with 100 cycles (top) and 500 cycles (bottom). The blue points show the populations in different n levels before sideband cooling for a thermal state with $\bar{n} = 80$, the orange points show the populations after sideband cooling where the pulse times are fixed at $t_p = \pi/\sqrt{\bar{n}}\eta\Omega$ and the red points show the populations after sideband cooling where the pulse times are varied to match the π-time of each n level in turn. It can be seen that the optimised pulse times have an advantage in both cases, taking $\bar{n}$ (p_0) from 49 (53%) to 35 (71%) in the 100 pulse case and from 3.4 (94%) to 0.33 (99.8%) in the 500 pulse case. In each case the model is simulated with 1000 total $|n\rangle$ states.

on the angle of the laser to the trap axis as well as polarisation and is of order 1/3. To optimise the sideband cooling process, it is therefore important to ensure that the number of photons scattered is minimised. This can be achieved by ensuring that the 369 nm laser with 2 GHz modulation is set exactly on resonance, and that the carrier frequency driving the $^2S_{1/2}$, $F = 1 \rightarrow {}^2P_{1/2}$, $F = 0$ transition is strongly suppressed. In our experiment the repump pulse is applied for 6 μs, for which a rate equations simulation* predicts an average of 3 photons scattered per cycle. For an axial trap frequency of $\nu_z/2\pi = 440$ kHz, this gives an average increase in mean phonon number of $\Delta\bar{n}_{\text{recoil}} \approx 0.006$ per repump pulse.

In the simplest case, the time of each sideband pulse in the sequence would be fixed, for example to $t_p = \pi/\sqrt{\bar{n}}\eta\Omega$, corresponding to the '$\pi$-time' of the thermal state with average phonon number $\bar{n}$. However, since the populations are changing

*written by Dr. Simon Webster

after each pulse, it is more effective to change the pulse time in each cycle of the sequence. The sideband cooling process including the effect of varying pulse times was modelled using Python*. For a given number of pulses and neglecting effects such as off-resonant coupling and decoherence, an optimised sequence for a given number of pulses $n_{\max}$ was found by setting each pulse time to the π-time of each n level in turn, starting at $n_{\max}$ and decreasing to $n = 1$ (the π-time for a transition from n to $n-1$ is given by $t_n = \pi/\sqrt{n}\eta\Omega$). Absent decoherence, this method transfers all of the population from Fock states up to $n = n_{\max}$ into $n = 0$. Therefore, the theoretical fidelity of preparing the ground state is given by the total amount of population up to $n_{\max}$. For an initial $\bar{n}$ of 80, this gives approximately 71% for $n_{\max} = 100$ and 99.8% for $n_{\max} = 500$. Although increasing the number of pulses will reduce $\bar{n}$, for a large number of pulses the reduction becomes small, and it may be desirable to reduce the total number of pulses used in order to reduce the total time of the sideband cooling. The total sideband cooling time for the optimised case is given by

$$t_{\text{cool}} = n_{\max} t_{\text{r}} + \sum_{n=1}^{n_{\max}} t_n, \tag{5.12}$$

where the repump time t_{r} is the time required to reset the spin state, which includes the application of the 369 nm laser and any additional coherent manipulation that may be required, for example to prepare the dressed state qubit. Figure 5.3 shows the modelled populations before and after sideband cooling using both a fixed pulse time and the optimised varying pulse times in the cases of 100 and 500 pulses. It can be seen that the optimised sequence has a clear advantage, taking the ground state occupation probability p_0 from 94 % to 99.8 % in the 500 pulse case.

The above analysis assumes perfect population transfer according to Eq. 5.6. In reality, however, there will be other processes that affect the populations, resulting in less efficient cooling. The most significant of these are dephasing, off-resonant coupling to the carrier transition and heating of the motional mode. In the case of dephasing, the reduction in efficiency arises due to the fact that less population is transferred per sideband pulse. For a resonant sideband interaction, the probability to make a transition from n to $n-1$ accompanied by a change in spin state with dephasing can be found from Eq. A.11 to be

$$P^{\uparrow}_{n,n-1}(t) = \frac{1}{2}\left[1 - e^{-\Gamma t/2}\left(\cos(\Omega_{\Gamma,n,n-1}t/2) + \frac{\Gamma}{\Omega_{\Gamma,n,n-1}}\sin(\Omega_{\Gamma,n,n-1}t/2)\right)\right], \tag{5.13}$$

*code written by Andrea Rodriguez

where $\Gamma = 1/\tau$ is the dephasing rate, τ is the coherence time and $\Omega_{\Gamma,n,n-1} = \sqrt{4\Omega_{n,n-1}^2 - \Gamma^2}$. Off-resonant coupling to the carrier causes the spin state to change without affecting the motional state. The probability to make a spin flip for a carrier transition with detuning δ_c (ignoring dephasing) is given by

$$P_{n,n}^{\uparrow}(t,\delta_c) = \frac{\Omega_0^2}{\Omega_0^2+\delta_c^2}\left(\frac{1}{2} - \frac{1}{2}\cos\left(t\sqrt{\Omega_0^2+\delta_c^2}\right)\right), \tag{5.14}$$

where for a resonant sideband interaction, $\delta_c = \pm\nu_l$. Eqs. 5.13 and 5.14 can be used to estimate the effect of dephasing and off-resonant carrier coupling on the sideband cooling for a given set of parameters Ω_0, ν_l and Γ.

In the case of heating of the motional state, the solution is easiest solved numerically. The effect of heating on the temperature measurements and motional state manipulation is discussed in Sec. 5.4.2.

5.4.1 Sideband cooling with dressed states

The dressed state qubit $\{|0'\rangle, |D\rangle\}$ has a significantly longer coherence time than qubits formed from magnetic field sensitive states. Therefore by cooling on the red sideband of the $|0'\rangle \leftrightarrow |D\rangle$ transition, more population can be transferred per cycle compared to the bare state case. This makes the cooling rate faster compared to the bare state case for a fixed sideband Rabi frequency, which for a given heating rate allows lower temperatures to be reached.

The dressed-state qubit was prepared and detected using the method described in Sec. 4.3.2. A microwave π-pulse on the $|0\rangle \leftrightarrow |0'\rangle$ transition was applied before and after the dressed sideband interaction, in each case taking 14 μs. The second pulse was performed to ensure that photons are only scattered in the repump step if a transition from $|0'\rangle$ to $|D\rangle$ has been made, thereby reducing the energy gained from photon recoil. The dressing fields were applied with equal Rabi frequencies $\Omega_{\mu w}/2\pi = 32$ kHz and the trap frequency was measured to be $\nu_z/2\pi = 426.7(1)$ kHz. The initial temperature after 4 ms of Dopppler cooling was measured to be $\bar{n} = 65(5)$.

With a measured 2nd order Zeeman shift of $\Delta\omega_{\pm}/2\pi = 34$ kHz, the nearest transition from $|0'\rangle \leftrightarrow |D\rangle$ is the $|0'\rangle \leftrightarrow |u\rangle$ transition, which is detuned by $(\Delta\omega_{\pm} - \Omega_{\mu w}/\sqrt{2})/2\pi = 11.4$ kHz. For the RF carrier, it must therefore be ensured that $\Omega_D \ll (\Delta\omega_{\pm} - \Omega_{\mu w}/\sqrt{2})$. However, for the sidebands, it is sufficient that $\sqrt{\bar{n}}\eta\Omega_D \ll (\Delta\omega_{\pm} - \Omega_{\mu w}/\sqrt{2})$, meaning that larger values of Ω_D can be used. To measure Ω_D, an RF field was applied with equal and opposite detuning from the $|0'\rangle \leftrightarrow |+1\rangle$ and $|0'\rangle \leftrightarrow |-1\rangle$ bare state transitions. For $\Omega_{rf} \gg \Delta\omega_{\pm}$, the population oscillates

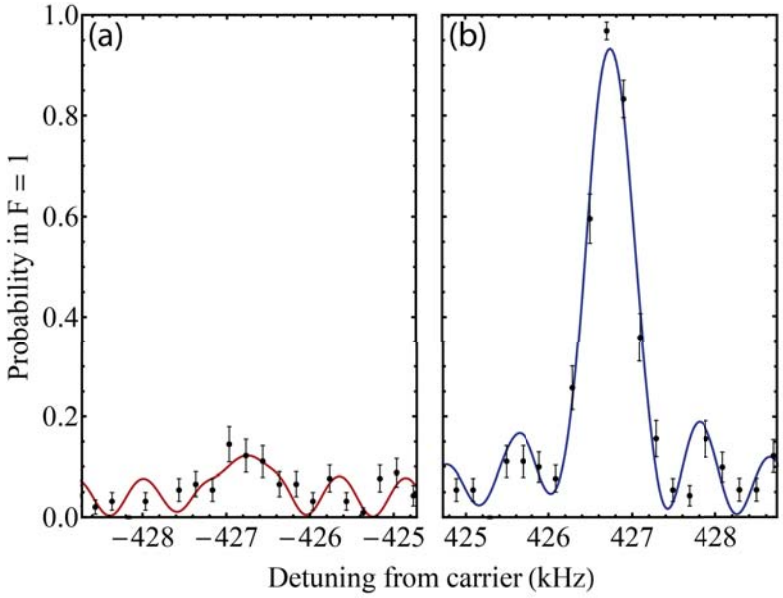


Fig. 5.4 Population in F = 1 after (a) a frequency scan over the red sideband and (b) a frequency scan over the blue sideband, both after sideband cooling. The red and blue lines are the result of a numerical simulation of the system where we have set $\nu_z/2\pi = 426.7\,\text{kHz}$, $\Omega_{\mu\text{w}}/2\pi = 32\,\text{kHz}$, $\Omega_D/2\pi = 61.2\,\text{kHz}$ and a probe pulse time of $1270\,\mu\text{s}$ with $\bar{n}$ as the only free parameter. The simulation does not take into account heating effects. A least-squares fit gives $\bar{n} = 0.13(4)$, corresponding to a ground state occupation probability of $p_0 = 0.88(3)$.

between $|0'\rangle$ and $(|{+1}\rangle + e^{i\phi}\,|{-1}\rangle)/\sqrt{2}$ with frequency $\sqrt{2}\Omega_{\text{rf}}$. This can then be used to obtain $\Omega_D = \Omega_{\text{rf}}/\sqrt{2}$. Using this method, $\Omega_D/2\pi$ was measured to be 61.2 kHz. The sideband cooling was applied in 500 steps using the optimised pulse times method, resulting in a total cooling time calculated from Eq. 5.12 of 71 ms, where $t_{\text{r}} = 38\,\mu\text{s}$ including both the optical repumping and the two microwave π-pulses.

Fig 5.4 shows the result of a frequency scan over both the red and blue sidebands after the sideband cooling is applied, using a probe pulse time of $1270\,\mu\text{s}$, which is close to t_0. Since the dressed-state system consists of six carrier transitions and six red and blue sidebands, the response is more complex than that given in Eq. 5.6, and so a numerical simulation of the system was performed. The simulation integrates the Schrödinger equation for the bare state Hamiltonians given in Eqs. 4.22 and 4.24, as well as the associated sideband terms, over a given frequency range for an initial state $|0', n\rangle$ for n ranging from 0 to n_{max}. The resulting curves are assigned weights p_n which can be fitted with Eq 5.5 to give $\bar{n}$. Using the parameters given in the previous paragraph, a least-squares fit to the data gives $\bar{n} = 0.13(4)$, corresponding to a ground state occupation probability of $p_0 = 0.88(3)$. The $|n\rangle$ levels simulated ranged from $n = 0$ to $n_{\text{max}} = 2$, which for $\bar{n} = 0.13$ contains 99.8% of the population.

5.4.2 Heating

Motional modes of trapped ions heat at an approximately constant rate $\dot{\bar{n}}$. The heating can have various sources, which can either be from noisy electronics (for example on the voltage supplies for the trap electrodes), or from other unknown sources. The unknown sources are thought to stem from electrical noise on the surface of the trap electrodes, but the exact noise mechanism is not known, and hence heating from such a source is termed 'anomalous' heating [77, 78]. Not only does heating limit the maximum ground-state population probability achievable with sideband cooling, but it is also a cause of infidelity in two-qubit logic gates and quantum simulations that incorporate the phonon modes. The heating rate is therefore an important parameter to measure for all future experiments.

The heating rate of an ion in our trap had previously been measured using the Doppler recool method [58]. This method looks at the arrival times of photons after switching off the cooling laser for a variable delay time, and matches to theory to extract $\dot{\bar{n}}$. The method does not require sideband cooling, making it simple to implement, but gives a less accurate temperature measurement. The scaled spectral noise density, given by $\nu_z S_E(\nu_z) = 4\dot{\bar{n}}\hbar m\nu_z^2/e^2$, was found to be $2.3(6) \times 10^{-4}\,\mathrm{V^2m^{-2}}$. This would correspond to a heating rate of $6700\,\mathrm{s^{-1}}$ at a secular frequency of $\nu_z/2\pi = 426.7(1)\,\mathrm{kHz}$. For this heating rate, the ion would gain ≈ 8.6 quanta during a single sideband pulse for the parameters used in Sec 5.4.1, making cooling to the ground state impossible. For this reason, significant effort was made to reduce the heating rate before sideband cooling was attempted. This included removing sources of electromagnetic noise in the vicinity of the experiment by replacing noise-inducing electronics, and using a well separated ground for important low-noise electronics. We also developed a new low noise multi-channel voltage supply for the static voltage trap electrodes*.

To measure the new heating rate of the ion we modified the sideband cooling sequence experiment described in section 5.4.1 to include a variable delay time. The delay is inserted after the sideband cooling but before the RF probe pulse, during which the ion heats at a rate $\dot{\bar{n}}$. By performing the experiment for delay times of 0 ms, 5 ms and 10 ms, a heating rate can be extracted. The measured temperature for each delay time is shown in Fig. 5.5. A fit to the data gives a heating rate of $41(7)\,\mathrm{s^{-1}}$, which corresponds to a gain of 1 phonon every 24 ms. This heating rate gives a scaled electric-field noise density of $\nu_z S_E(\nu_z) = 1.4(2) \times 10^{-6}\,\mathrm{V^2m^{-2}}$, which is a reduction of more than two orders of magnitude compared to the previously

*designed by Dr. Bjoern Lekitsch

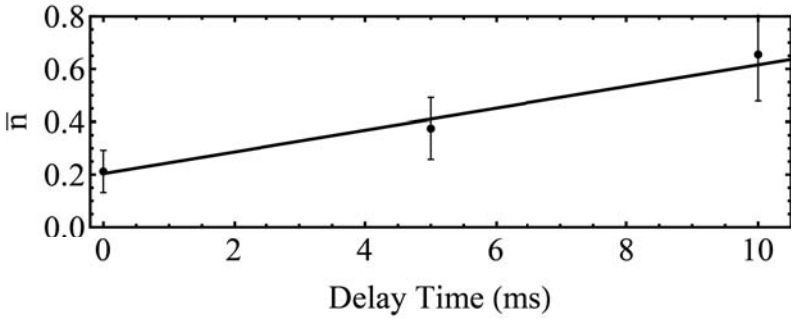


Fig. 5.5 To measure the heating rate $\dot{\bar{n}}$ a variable delay is introduced after sideband cooling. For each of the three delay times a scan over the red and blue sidebands is taken, as in Fig. 5.4, allowing $\bar{n}$ to be determined. The black line is a fit to the data which gives a heating rate of $\dot{\bar{n}} = 41(7)\,\mathrm{s}^{-1}$, or 1 phonon in 24 ms, for the axial secular frequency of $\nu_z/2\pi = 426.7(1)\,\mathrm{kHz}$.

measured value.

To model the effects of motional heating on an experiment, we can use a Lindblad master equation of the form

$$\frac{d\rho}{dt} = -\frac{i}{\hbar}[H,\rho] - \mathcal{L}(\rho), \tag{5.15}$$

where $\mathcal{L}(\rho)$ is given by

$$\mathcal{L}(\rho) = \sum_{j=1}^{2}\left(C_j\rho C_j^\dagger - \frac{1}{2}C_j^\dagger C_j\rho - \frac{1}{2}\rho C_j^\dagger C_j\right). \tag{5.16}$$

The relaxation operators for an ion coupled to a thermal environment with coupling strength Γ and mean phonon number in thermal equilibrium $\bar{n}_{\mathrm{th}}$ are given by $C_1 = \sqrt{\Gamma(1+\bar{n}_{\mathrm{th}})}a$ and $C_2 = \sqrt{\Gamma\bar{n}_{\mathrm{th}}}a^\dagger$ [31]. In the case that the temperature of the environment is much greater than that of the ion*, we can approximate that $\Gamma(1+\bar{n}_{\mathrm{th}}) \approx \Gamma\bar{n}_{\mathrm{th}} = \dot{\bar{n}}$, and the relaxation operators are then reduced to

$$\begin{aligned} C_1 &= \sqrt{\dot{\bar{n}}}a \\ C_2 &= \sqrt{\dot{\bar{n}}}a^\dagger. \end{aligned} \tag{5.17}$$

A simple experiment that demonstrates coherent control of the motional state is a Rabi oscillation between $|n=0\rangle$ and $|n=1\rangle$, which can be achieved with a blue sideband interaction after sideband cooling to the ground state. Coherent evolution requires that the coherence time is much greater than the ground state sideband

*This is always true for Doppler cooled ions with temperatures in the mK region.

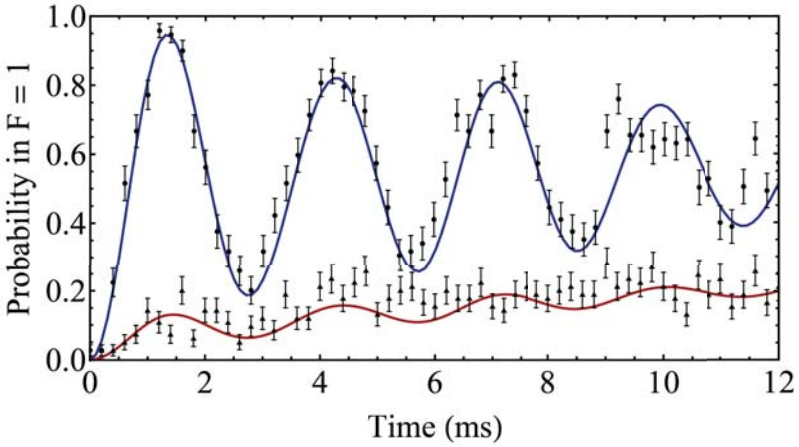


Fig. 5.6 Result of an experiment to demonstrate coherent control of the motional state of a single trapped ion. The graph shows the population in $F = 1$ after ground state cooling, preparing in $|0'\rangle$ and applying an RF pulse for a variable time, resonant with the blue (circles) and red (triangles) motional sidebands of the $|0'\rangle \leftrightarrow |D\rangle$ transition. The solid red and blue lines are the result of a numerical simulation of Eq. 5.15 for a two-level system and a single motional mode. The heating rate and initial thermal state are set to the measured values of $\dot{\bar{n}} = 41\,\mathrm{s}^{-1}$ and $\bar{n} = 0.13$ respectively, and the ground state sideband Rabi frequency is set to $\eta\Omega_0/2\pi = 0.35\,\mathrm{kHz}$.

π-time t_0, and therefore the dressed state qubit $\{|0'\rangle, |D\rangle\}$ should be used. Fig. 5.6 shows the result of such an experiment using both the red and the blue sidebands, and the data is overlaid with a numerical simulation of Eq. 5.15 using the initial $\bar{n}$ and heating rate parameters measured in the previous sections*. The data can be seen to match the simulation well, indicating that this is a good model for a motional mode undergoing heating.

5.4.3 Sideband cooling two ions

As explained in Sec. 2.2.2, the addition of a second ion adds an extra motional mode in each spatial direction. In the axial direction these are the centre of mass (COM) and stretch modes with frequencies $\nu_c = \nu_z$ and $\nu_s = \sqrt{3}\nu_z$ respectively. Due to their separation in frequency, the two modes can be addressed and cooled individually as long as $\eta\Omega \ll (\sqrt{3} - 1)\nu_z$. The stretch mode generally has a lower heating rate than the COM mode, even when scaling out the dependence on frequency. This makes it attractive for use in experiments that require the use of a motional mode, for example a two-qubit gate. The reduced heating rate can be understood from the type of electric field fluctuation that is required to excite each mode. In the case of

*code written by Dr. Simon Webster

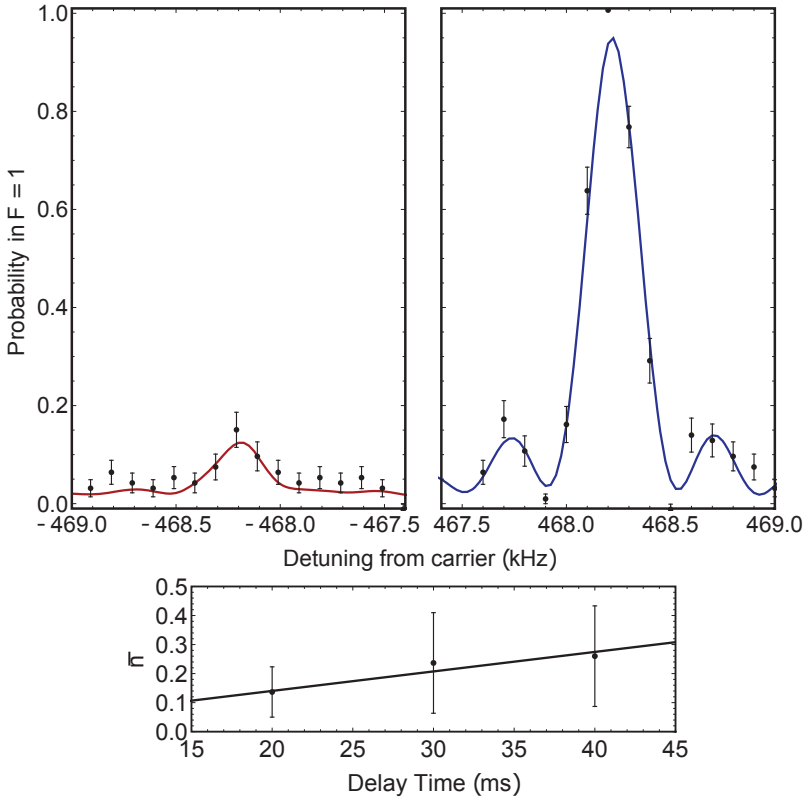


Fig. 5.7 Top: Scan over the stretch mode red and blue sidebands of the $|0'\rangle \leftrightarrow |D\rangle$ transition of one ion in a pair after sideband cooling on the stretch red sideband of the bare state $|0\rangle \leftrightarrow |+1\rangle$ transition in the same ion. The dressed state transition was used in the final probe pulse in order to reduce decoherence effects that would cause a greater uncertainty in the temperature measurement. The microwave sideband cooling consisted of 500 pulses using the optimised pulse times, with Rabi frequency $\Omega_{+1}/2\pi = 80\,\mathrm{kHz}$. For the probe pulse, a Rabi frequency of $\Omega_D/2\pi = 45\,\mathrm{kHz}$ was used and the RF probe pulse was applied for $2750\,\mu\mathrm{s}$. The fit is the result of a numerical simulation of the dressed system taking into account off-resonant coupling to the carrier transitions, as discussed in Sec. 5.4.1, giving $\bar{n} = 0.14(3)$. Bottom: Heating rate measurement on the stretch mode, consisting of three individual sideband measurements as described above, with a variable delay inserted between the cooling and measurement. A linear fit gives a heating rate of $\dot{\bar{n}} = 7(2)\,\mathrm{s}^{-1}$ for a stretch mode frequency $\nu_s/2\pi = 468.2\,\mathrm{kHz}$.

the COM mode, any electric field fluctuation at the resonant frequency could cause an excitation of the motional state, whereas for the stretch mode the fluctuation must also push the two ions in equal and opposite directions, which is much less likely.

In anticipation of performing a two-qubit gate, it was decided that the $|0\rangle \leftrightarrow |+1\rangle$ bare state transition of one ion in the pair should be used to cool the stretch mode. Sideband cooling on this transition requires only a single microwave field and a single microwave pulse per cycle, and hence is less demanding experimentally. However, the efficiency of the cooling is reduced due to the significantly shorter coherence time ($T_2 \approx 1\,\mathrm{ms}$), compared to the dressed state case. The reduction in efficiency per pulse can be estimated from Eq. 5.13, which for measured parameters $\nu_s/2\pi = 468.2\,\mathrm{kHz}$ and $\Omega_{+1}/2\pi = 80\,\mathrm{kHz}$ gives $P_{+1} = 0.72$ for a transition with Rabi frequency $\eta_s\Omega_{+1}$ and pulse time $t_\pi = \pi/\eta_s\Omega_{+1}$. As will be seen in the next chapter, the two-qubit gate scheme used is insensitive to the motional temperature to first order, and therefore the simplification of using the bare state transition was considered to outweigh the small reduction in gate fidelity from the slightly higher expected temperature after sideband cooling. Fig. 5.7 shows a measurement of the temperature of the stretch mode of a two ion string after sideband cooling, achieving a mean phonon number of $\bar{n} = 0.14(3)$, corresponding to a ground state occupation probability of $p_0 = 88(2)\%$. This result is similar to the single ion case, which could be due to the lower heating rate on the stretch mode balanced with the less efficient cooling method.

To measure the heating rate of the stretch mode, a similar experiment to that described in section 5.4.2 was performed, and the result is also shown in Fig. 5.7, giving a heating rate of $\dot{\bar{n}}_s = 7(2)\,\mathrm{s}^{-1}$. This value can be compared to the heating rate of a single ion by calculating the expected heating rate for the same frequency for a single ion. The scaling of heating rates with frequency is discussed in Sec. 6.3.2, and using Eq. 6.29, the equivalent heating rate for a single ion would be $\approx 35\,\mathrm{s}^{-1}$. The stretch mode heating rate is therefore approximately five times lower than for a single ion, thereby confirming that the stretch mode has a significantly lower heating rate for a given frequency.

Chapter 6

Two ion entanglement

6.1 Introduction

A two-qubit gate is a key operation in the circuit model of quantum computing, creating entanglement and thereby allowing the full Hilbert space of a multi-qubit system to be utilised for a computation. In most experimental realisations it is also the hardest to implement, and lower fidelities are typically achieved compared with the other elementary operations. In trapped ions, there is no significant natural coupling between the spin states of different ions, and therefore the coupling has to be engineered, either through the collective motional modes of ions in a shared trap or using photonic interactions. As discussed in Chapter 3, the coupling between the spin and motional states for the microwave and radio frequency fields that interact directly with hyperfine qubits is negligible, and therefore two-photon Raman transitions in the optical frequency regime are often used. The most successful type of two ion gates so far realised are geometric phase gates, for which the motional state of a pair of ions are driven in circles in phase space, with the direction and magnitude dependent on the spin state. The states then pick up a phase proportional to the area enclosed by the trajectory of the motional state in phase space, which allows a two-qubit gate to be realised between the two ions. Importantly, to first order the gate is insensitive to the temperature of the initial motional state, which relaxes the experimental requirements required to achieve high fidelities. Geometric phase gates can either be performed in the σ_z or the σ_x basis, the latter of which is known as a Mølmer-Sørensen gate. Using optical frequency fields, impressive fidelities of 0.999 [40] and 0.993 [79] have been achieved using the two gate types respectively.

In this chapter, it will be shown how a Mølmer-Sørensen type geometric phase gate can be implemented using long-wavelength radiation and a magnetic field gradient.

The gate is performed on the dressed state qubit as discussed in Chapter 4, thereby significantly increasing the coherence time and consequently allowing high-fidelities to be reached, despite the relatively small spin-motion coupling strength from the gradient compared to optical schemes. A demonstration of such a gate is presented, and the gate is characterised, indicating a Bell state fidelity of 0.985(12).

6.2 Spin-motion entanglement with a single ion

The two-qubit gate scheme used in this work is that proposed by Mølmer and Sørensen in Ref. [30], in which the red and blue sidebands in both ions are driven simultaneously. The effect of such an interaction is easiest to understand by first considering a single ion and single motional mode. In this case, the spin and motion become entangled, while the geometric phase responsible for creating entanglement in the multi-ion case is global and can be ignored. The simplicity compared to the multi-ion case also makes it a useful experiment to test and characterise the Mølmer-Sørensen interaction. In this section, the theory of the Mølmer-Sørensen interaction will be presented and it will be shown that the interaction can be implemented using the dressed-state qubit $\{|0'\rangle, |D\rangle\}$, introduced in chapter 4, in $^{171}\mathrm{Yb}^{+}$. Finally, results from a demonstration of such an experiment will be presented.

6.2.1 The Mølmer-Sørensen interaction

To understand the effect of the Mølmer-Sørensen interaction, we can consider a two-level ion with states $|\downarrow\rangle$ and $|\uparrow\rangle$ as well as a single motional mode with states $|n\rangle$. As shown in Chapter 3, applying a magnetic field gradient to such a system allows sideband transitions to be driven with a coupling strength proportional to the effective Lamb-Dicke parameter η. The Mølmer-Sørensen interaction is created by combining the red and blue sideband Hamiltonian terms in Eq. 3.24, with equal carrier Rabi frequencies Ω_0 and equal and opposite 'symmetric' detunings ($\delta = \delta_r = -\delta_b$), as shown in Fig. 6.1. With these definitions and after performing the polaron transformation to drop the p subscripts, we obtain a Hamiltonian

$$H_{\mathrm{MS}} = \frac{\hbar\eta\Omega_0}{2}\Big[e^{i\delta t}a^{\dagger}\Big(|\uparrow\rangle\langle\downarrow| e^{i\phi_b} - |\downarrow\rangle\langle\uparrow| e^{-i\phi_r}\Big) - e^{-i\delta t}a\Big(|\downarrow\rangle\langle\uparrow| e^{-i\phi_b} - |\uparrow\rangle\langle\downarrow| e^{i\phi_r}\Big)\Big], \tag{6.1}$$

where ϕ_r and ϕ_b are the phases of the fields driving the red and blue sidebands respectively. This Hamiltonian can be factorised by defining the spin phase $\phi_s =$

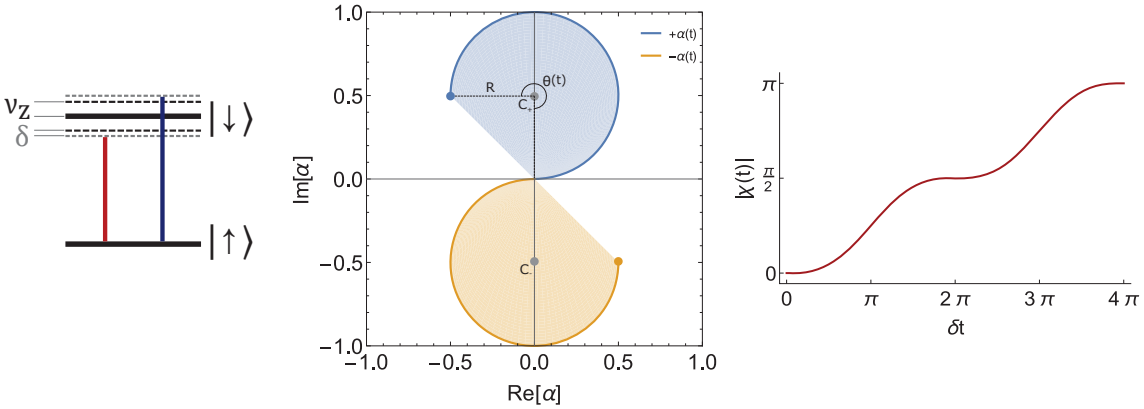


Fig. 6.1 Left: Energy level diagram indicating the fields required for the Mølmer-Sørensen interaction. Middle: Trajectories of the displacements $\pm\alpha(t)$ in phase space, which correspond to the paths taken if the ion is in either $|{\leftarrow_\phi}\rangle$ or $|{\rightarrow_\phi}\rangle$. The angle in this case is $\theta(t) = \delta t = 3\pi/2$. Right: The magnitude of the geometric phase $|\chi(t)|$ as a function of the angle δt rotated around $C_\pm$. The value is twice the area of the circular segment enclosed by $\alpha(t)$, as indicated by the shading in the middle diagram.

$(\phi_r + \phi_b)/2$ and the motional phase $\phi_m = (\phi_r - \phi_b)/2$ so that $\phi_r = \phi_s + \phi_m$ and $\phi_b = \phi_s - \phi_m$. H_{MS} then becomes

$$\begin{aligned} H_{\text{MS}} &= \frac{\hbar\eta\Omega_0}{2}\Big(|{\uparrow}\rangle\langle{\downarrow}|\, e^{i\phi_s} - |{\downarrow}\rangle\langle{\uparrow}|\, e^{-i\phi_s}\Big)\Big(a^\dagger e^{i\delta t}e^{-i\phi_m} - ae^{-i\delta t}e^{i\phi_m}\Big) \\ &= -\frac{i\hbar\eta\Omega_0}{2}S_\phi\Big(a^\dagger e^{i\delta t}e^{-i\phi_m} - ae^{-i\delta t}e^{i\phi_m}\Big), \end{aligned} \tag{6.2}$$

where we have defined the Mølmer-Sørensen spin operator $S_\phi = i\Big(|{\uparrow}\rangle\langle{\downarrow}|\, e^{i\phi_s} - |{\downarrow}\rangle\langle{\uparrow}|\, e^{-i\phi_s}\Big)$. The eigenstates of the spin operator are the superposition states $|{\leftarrow_\phi}\rangle = \Big(|{\downarrow}\rangle + ie^{i\phi_s}|{\uparrow}\rangle\Big)/\sqrt{2}$ and $|{\rightarrow_\phi}\rangle = \Big(|{\downarrow}\rangle - ie^{i\phi_s}|{\uparrow}\rangle\Big)/\sqrt{2}$, and S_ϕ can therefore be written in terms of its eigenstates as $S_\phi = |{\leftarrow_\phi}\rangle\langle{\leftarrow_\phi}| - |{\rightarrow_\phi}\rangle\langle{\rightarrow_\phi}|$. The Hamiltonian in Eq. 6.2 is time dependent and its effects are not immediately apparent. To see its effect, the resulting unitary operator can be found using the Magnus expansion, as described in Appendix C. In this case the unitary operator is exactly solvable, as terms in the expansion above second order are zero. The unitary operator is found to be

$$\begin{aligned} U_{\text{MS}}(t) &= \exp\Big(S_\phi(\alpha(t)a^\dagger - \alpha^*(t)a)\Big)\exp\Big(i\chi(t)S_\phi^2\Big) \\ &= e^{i\chi(t)}\Big(|{\leftarrow_\phi}\rangle\langle{\leftarrow_\phi}|\, D(\alpha(t)) + |{\rightarrow_\phi}\rangle\langle{\rightarrow_\phi}|\, D(-\alpha(t))\Big), \end{aligned} \tag{6.3}$$

where we have defined

$$\begin{aligned}\alpha(t) &= -\frac{i\eta\Omega_0}{2\delta}e^{-i\phi_m}\Big(e^{i\delta t}-1\Big),\\ \chi(t) &= -\frac{\eta^2\Omega_0^2}{4\delta^2}\Big(\delta t-\sin(\delta t)\Big),\end{aligned} \tag{6.4}$$

and $D(\alpha)=e^{\alpha a^\dagger-\alpha^* a}$ is the usual displacement operator. The effect of the interaction is therefore to displace the ion's motional state by $\alpha(t)$ or $-\alpha(t)$, with the sign depending on the spin eigenstate. The displacement follows a circular trajectory in the complex plane, as shown in Fig. 6.1, centred around the point $C_\pm=\pm\alpha(t=\pi/\delta)/2=\pm i\eta\Omega_0 e^{-i\phi_m}/2\delta$ with radius $R=\eta\Omega_0/2\delta$. At time t, the displacement has rotated by an angle $\theta(t)=\delta t$ around $C_\pm$, starting at $\alpha(0)=0$. The trajectory therefore completes q circles at times $t_q=2\pi q/\delta$. With these definitions, the parameters in Eq. 6.4 can be re-written as

$$\begin{aligned}\pm\alpha(t) &= -C_\pm\Big(e^{i\theta(t)}-1\Big)\\ \chi(t) &= -R^2\Big(\theta(t)-\sin(\theta(t))\Big).\end{aligned} \tag{6.5}$$

In this form, it can be seen that $|\chi(t)|$ is equal to twice the area of the circular segment enclosed by the trajectory of $\alpha(t)$. The states therefore pick up a phase proportional to this area, which is known as a geometric phase. The displacements can also be written in terms of the expectation values of the position and momentum operators using the relations $\langle z(t)\rangle_\alpha=\sqrt{2\hbar/m\nu_z}\mathrm{Re}[\alpha(t)]$ and $\langle p(t)\rangle_\alpha=\sqrt{2\hbar m\nu_z}\mathrm{Im}[\alpha(t)]$. The geometric phase is then equal to $A/\hbar$, where A is the area enclosed by the elipse segment in phase space (z,p). In the single ion case, the phase is global and therefore has no effect, however it will be seen later in the chapter that this phase allows multiple ions to be entangled. Crucially, the displacement $\alpha(t)$ and the geometric phase $\chi(t)$ are independent of the ion's initial motional state as long as the motion remains in the Lamb-Dicke regime. This makes the interaction much more robust compared to schemes where a particular motional state is required, making it appealing for high-fidelity gate operations.

If the ion is prepared in a superposition of the spin eigenstates such as $|\downarrow\rangle=(|\leftarrow_\phi\rangle+|\rightarrow_\phi\rangle)/\sqrt{2}$, the motional state will move in a superposition of the two trajectories $\pm\alpha(t)$. If the spin and motional states are initialised to $|\downarrow\rangle\,|n=0\rangle$, the

state at time t will be

$$|\psi_{\text{cat}}(t)\rangle = \frac{1}{\sqrt{2}}\Big(|{\leftarrow_\phi}\rangle\, |\alpha(t)\rangle + |{\rightarrow_\phi}\rangle\, |{-\alpha(t)}\rangle \Big), \tag{6.6}$$

which is known as a Schrödinger cat state. Since only the ion's spin states are detected in our experiment, it is useful to calculate the reduced density matrix $\rho^{(s)}_{\text{cat}}(t)$ describing only the spin degree of freedom. This can be found by tracing over the motional states of the full density matrix $\rho_{\text{cat}}(t) = |\psi_{\text{cat}}(t)\rangle\, \langle\psi_{\text{cat}}(t)|$ to obtain

$$\begin{aligned}
\rho^{(s)}_{\text{cat}}(t) &= \sum_{n=0}^{\infty} \langle n|\, \rho_{\text{cat}}(t)\, |n\rangle \\
&= \frac{1}{2}\Big(|{\leftarrow_\phi}\rangle\, \langle{\leftarrow_\phi}| + |{\rightarrow_\phi}\rangle\, \langle{\rightarrow_\phi}| \Big) + \frac{e^{-2|\alpha(t)|^2}}{2}\Big(|{\leftarrow_\phi}\rangle\, \langle{\rightarrow_\phi}| + |{\rightarrow_\phi}\rangle\, \langle{\leftarrow_\phi}| \Big) \\
&= \frac{1}{2}\Big(1 + e^{-2|\alpha(t)|^2}\Big)\, |{\downarrow}\rangle\, \langle{\downarrow}| + \frac{1}{2}\Big(1 - e^{-2|\alpha(t)|^2}\Big)\, |{\uparrow}\rangle\, \langle{\uparrow}|
\end{aligned} \tag{6.7}$$

The spin therefore evolves from the pure state $|{\downarrow}\rangle\, \langle{\downarrow}|$ towards the maximally mixed state $\rho_I = (|{\downarrow}\rangle\, \langle{\downarrow}| + |{\uparrow}\rangle\, \langle{\uparrow}|)/2$, before turning back at $t = \pi/\delta$ and returning to $|{\downarrow}\rangle$ at $t = 2\pi/\delta$. The probability to be in the state $|{\uparrow}\rangle$ is therefore given by

$$P(\uparrow) = \langle{\uparrow}|\, \rho^{(s)}_{\text{cat}}(t)\, |{\uparrow}\rangle = \frac{1}{2}\Big(1 - e^{-2|\alpha(t)|^2}\Big). \tag{6.8}$$

In the above, we have assumed that the ion's motion is in the ground state $|n = 0\rangle$. If instead the motion is in a thermal state with mean phonon number $\bar{n}$, the density matrix at time t is

$$\rho_{\text{th}}(t) = \sum_{n=0}^{\infty} p_n\, |\psi_n(t)\rangle\, \langle\psi_n(t)|\,, \tag{6.9}$$

where $p_n = (1/(1+\bar{n}))(\bar{n}/(1+\bar{n}))^n$ from Eq. 5.3 and $|\psi_n(t)\rangle$ is given by

$$|\psi_n(t)\rangle = \frac{1}{\sqrt{2}}\Big(|{\leftarrow_\phi}\rangle\, D(\alpha(t))\, |n\rangle + |{\rightarrow_\phi}\rangle\, D(-\alpha(t))\, |n\rangle \Big). \tag{6.10}$$

We can then trace over the motional state in a similar way to the pure state case to obtain

$$\rho^{(s)}_{\text{th}}(t) = \frac{1}{2}\Big(1 + e^{-2|\alpha(t)|^2(1+2\bar{n})}\Big)\, |{\downarrow}\rangle\, \langle{\downarrow}| + \frac{1}{2}\Big(1 - e^{-2|\alpha(t)|^2(1+2\bar{n})}\Big)\, |{\uparrow}\rangle\, \langle{\uparrow}|\,, \tag{6.11}$$

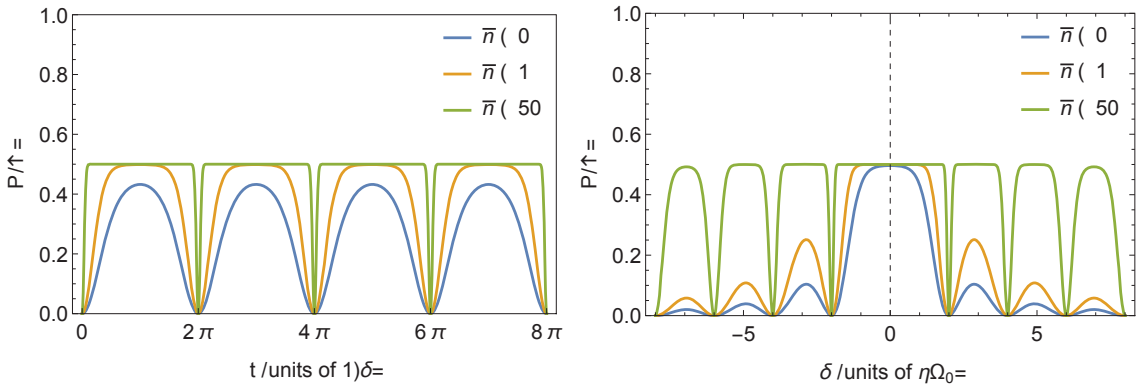


Fig. 6.2 Probability to be in the state $|\uparrow\rangle$ as a function of t (left) and δ (right, $t = \pi/\eta\Omega_0$) for the cases that the ion is prepared in the ground state or thermal states with $\bar{n} = 1$ and $\bar{n} = 50$. In all cases, the dips where $P(\uparrow) = 0$ occur at the instances when the motional state has completed an integer number of loops in phase space. The maxima occur when the motional state has completed half a loop, which causes the spin state to be almost completely mixed when tracing over the motion.

and therefore the probability to be in the state $|\uparrow\rangle$ is

$$P_{\text{th}}(\uparrow) = \langle\uparrow| \rho_{\text{th}}^{(s)}(t) |\uparrow\rangle = \frac{1}{2}\left(1 - e^{-2|\alpha(t)|^2(1+2\bar{n})}\right). \tag{6.12}$$

The probability $P_{\text{th}}(\uparrow)$ for different values of $\bar{n}$ is plotted as a function of time and symmetric detuning in Fig. 6.2. It can be seen that although the displacement is independent of the motional state, the features become narrower as the temperature increases. This is due to the smaller overlap between two displaced thermal states compared to coherent states. Therefore, if it is required that an integer number of loops in phase space are completed, a higher temperature means that the time and detuning have to be set more accurately.

Off-resonant fields such as those driving sideband transitions cause Stark shifts, which can be calculated using the two-level dressed picture described in Sec. 4.2.1. For the Mølmer-Sørensen interaction, the two fields have detunings $\delta_r = \delta$ and $\delta_b = -\delta$, and therefore the total Stark shift is $\Delta\epsilon = \hbar\Omega_0^2/2\delta - \hbar\Omega_0^2/2\delta = 0$. This vanishing Stark shift is an added benefit for the two-level Mølmer-Sørensen interaction, as the symmetric detuning δ can be set independently of the carrier Rabi frequency. However it will be seen in the following section that when using the dressed state qubit $\{|0'\rangle, |D\rangle\}$, added complications lead to a non-zero Stark shift.

6.2.2 Spin-motion entanglement with the dressed-state qubit

In Chapter 4, it was shown that the sideband transitions can be driven between the state $|0'\rangle$ and the dressed state $|D\rangle$ in $^{171}\mathrm{Yb}^{+}$ using an RF field coupling the $|0'\rangle \leftrightarrow |+1\rangle$ transition*. The advantage of these states compared to the bare states is that they are much less sensitive to magnetic field noise and hence have a much longer coherence time, allowing coherent operations to be performed with high fidelity. The Mølmer-Sørensen interaction can therefore be performed on this transition with the replacements $|\downarrow\rangle \rightarrow |0'\rangle$, $|\uparrow\rangle \rightarrow |D\rangle$ and $\Omega_0 \rightarrow \Omega_D = \Omega_{\mathrm{rf}}/\sqrt{2}$. In the dressed state case unlike the simpler two level case, a non-zero Stark shift arises due to the other dressed state carrier transitions present when driving the sidebands of one of the dressed states. For symmetry reasons similar to the two level case, Stark shifts of the three dressed states connected to $|0'\rangle$ via $|+1\rangle$ are cancelled by the symmetrically detuned sideband fields. However, Stark shifts of the three transitions connected via $|-1\rangle$ are not cancelled completely and therefore cause the frequency of the $|0'\rangle \leftrightarrow |D\rangle$ transition to shift. With the approximations $\pm\delta_c \approx \pm\nu_z$ and $|\delta_c| \gg \Omega_D, \Omega_{\mu\mathrm{w}}$, the total shift is given by

$$\begin{aligned}\frac{\Delta\epsilon_{0'\leftrightarrow D}}{\hbar} =& \frac{\Omega_D^2}{2}\left(\frac{1}{\nu_z - \Delta\omega_\pm} - \frac{1}{\nu_z + \Delta\omega_\pm}\right) \\ &+ \frac{\Omega_{ud}^2}{4}\left(\frac{1}{\nu_z + \Omega_{\mu\mathrm{w}}/\sqrt{2} - \Delta\omega_\pm} + \frac{1}{\nu_z - \Omega_{\mu\mathrm{w}}/\sqrt{2} - \Delta\omega_\pm}\right. \\ &\left. - \frac{1}{\nu_z + \Omega_{\mu\mathrm{w}}/\sqrt{2} + \Delta\omega_\pm} - \frac{1}{\nu_z - \Omega_{\mu\mathrm{w}}/\sqrt{2} + \Delta\omega_\pm}\right) \\ \approx& \frac{3\Omega_{\mathrm{rf}}^2\Delta\omega_\pm}{4\nu_z^2},\end{aligned} \tag{6.13}$$

where $\Omega_{ud} = \Omega_{\mathrm{rf}}/2$ is the Rabi frequency of the $|0'\rangle \leftrightarrow |u\rangle$ and $|0'\rangle \leftrightarrow |d\rangle$ transitions. To compensate for this shift, the detunings of the Mølmer-Sørensen fields should be set to $\delta_r = \delta + \Delta\epsilon_{0'\leftrightarrow D}/\hbar$ and $\delta_b = -\delta + \Delta\epsilon_{0'\leftrightarrow D}/\hbar$, so that they are symmetric about the Stark shifted carrier transition. This can be achieved by accurately measuring the transition frequency of the un-shifted carrier transition and calculating the expected shift using Eq. 6.13. For the single ion case, this typically sets the detunings to within the required accuracy, however for the two-qubit gate the Stark shifts need to be set more accurately and therefore further methods to optimise the detunings were developed, which are discussed later in the chapter. Fig. 6.3 shows the result

*The $|0'\rangle \leftrightarrow |-1\rangle$ transition could also be used.

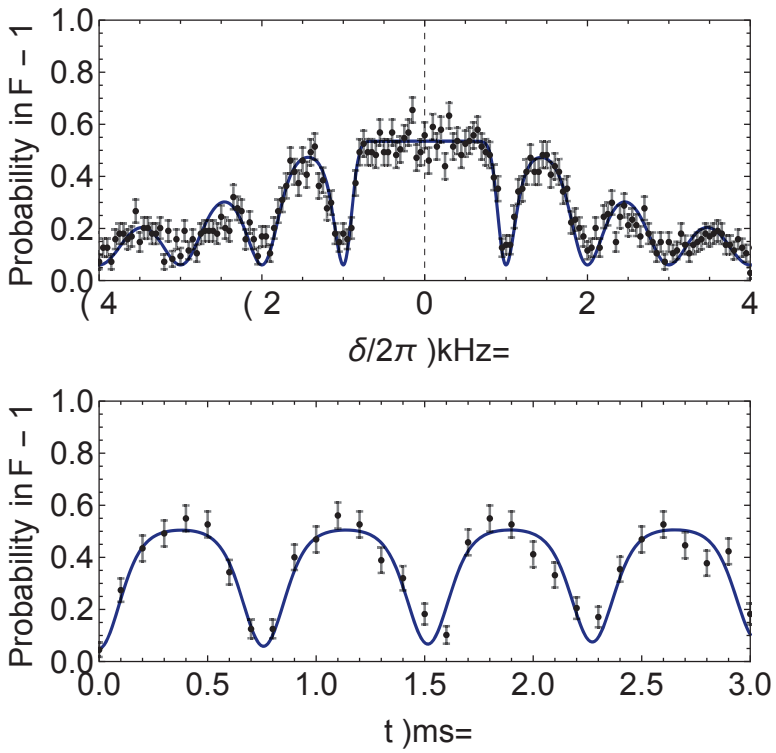


Fig. 6.3 Top: Probability to be in F = 1 as a function of the symmetric detuning δ of the two Mølmer-Sørensen fields applied for $t = 1$ ms after preparing one ion in a two ion string in the state $|0'\rangle$. The fields are tuned close to the stretch mode of motion with frequency $\nu_s = \sqrt{3}\nu_z = 465.7(1)$ kHz and the ions are only Doppler cooled. The second ion is prepared in $|0\rangle$ and is not dressed and therefore does not participate in the interaction. The blue line is a theory curve following Eq. 6.12, where the baseline and amplitude have been scaled to account for off-resonant coupling to the carrier transition. The parameters used in the theory curve are $\Omega_D/2\pi = 41$ kHz and $\bar{n} = 40$, which is approximately twice the Doppler temperature. At $\delta = 0$, the maximum displacement between the two thermal states is $2|\alpha(t)| = 2 \times 0.52$. Bottom: Probability to be in F = 1 as a function of the time t that the Mølmer-Sørensen fields are applied for, where the symmetric detuning is fixed at $\delta/2\pi = 1.32$ kHz.

of an experiment in which the Mølmer-Sørensen fields were applied for a time t after preparing a single ion in $|0'\rangle$ while either keeping the time fixed and varying the detuning or keeping the detuning fixed and varying the time. The data can be seen to match the theory curves well, demonstrating that the Mølmer-Sørensen interaction is working as expected and that Schrödinger cat type states where the spin and motional degrees of freedom are entangled have been created.

6.3 Two-ion entanglement

6.3.1 Mølmer-Sørensen interaction for multiple ions

The Mølmer-Sørensen interaction can be generalised to multiple ions by applying red and blue sideband fields to each ion with detunings close to one of the normal modes of the ion string, as shown in Fig. 6.4. In the following, we will assume that the symmetric detuning δ_k is equal for each ion and only interacts with the selected mode k, neglecting the other modes as off resonant. This is a good assumption for the case that $\eta_{jk}\Omega_j \ll |\nu_k - \nu_{k+1}|$, however some schemes such as those presented in Refs. [80, 81] utilise the coupling to all motional modes. With the single mode assumption, the generalised version of Eq. 6.2 is given by

$$H^k_{\mathrm{MS}} = -\sum_{j=1}^{N} \frac{i\hbar\eta_{jk}\Omega_j}{2} S_{\phi j}\Big(a_k^\dagger e^{i\delta_k t} e^{-i\phi_{mj}} - a_k e^{-i\delta_k t} e^{i\phi_{mj}}\Big), \tag{6.14}$$

where $S_{\phi j} = i\Big(|\uparrow_j\rangle\langle\downarrow_j| e^{i\phi_{sj}} - |\downarrow_j\rangle\langle\uparrow_j| e^{-i\phi_{sj}}\Big)$ is the Mølmer-Sørensen spin operator for ion j with spin eigenstates $|\leftarrow_{\phi j}\rangle = \Big(|\downarrow_j\rangle + ie^{i\phi_{sj}}|\uparrow_j\rangle\Big)/\sqrt{2}$ and $|\rightarrow_{\phi j}\rangle = \Big(|\downarrow_j\rangle - ie^{i\phi_{sj}}|\uparrow_j\rangle\Big)/\sqrt{2}$, and $\phi_{sj} = (\phi_{rj} + \phi_{bj})/2$ and $\phi_{mj} = (\phi_{rj} - \phi_{bj})/2$ are the spin and motional phases for ion j. The unitary operator for the multi-ion case can be found using the Magnus expansion in a similar way to the single ion case to give

$$U^k_{\mathrm{MS}} = \exp\Big(\sum_{j=1}^{N} S_{\phi j}(\alpha_{jk}(t)a_k^\dagger - \alpha^*_{jk}(t)a_k) - \sum_{i,j=1}^{N} i\chi_{ijk}(t) S_{\phi i} S_{\phi j}\Big), \tag{6.15}$$

where the generalised displacements $\alpha_{jk}(t)$ and geometric phases $\chi_{ijk}(t)$ are given by

$$\begin{aligned}
\alpha_{jk}(t) &= \frac{i\eta_{jk}\Omega_j}{2\delta_k} e^{-i\phi_{mj}}\Big(e^{i\delta_k t} - 1\Big), \\
\chi_{ijk}(t) &= \frac{\eta_{ik}\eta_{jk}\Omega_i\Omega_j}{4\delta_k^2}\Big(\delta_k t\cos(\Delta\phi_{mij}) - \sin(\Delta\phi_{mij}) - \sin(\delta_k t - \Delta\phi_{mij})\Big),
\end{aligned} \tag{6.16}$$

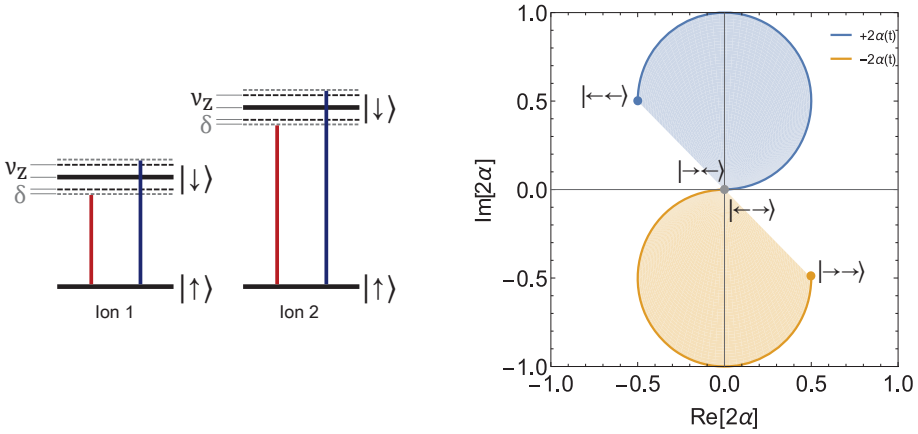


Fig. 6.4 Left: The Mølmer-Sørensen interaction is implemented by applying two fields to each ion with the same symmetric detuning δ_k from the red and blue sidebands of normal mode k. The magnetic field gradient causes the resonant frequency of the qubits to be different, and hence four fields are needed in total for a pair of ions. Right: If the detuning is close to the COM mode, the motional state moves in circles in the complex plane following the path $\pm 2\alpha_c$ if the spins are in the states $|{\leftarrow}{\leftarrow}\rangle$ or $|{\rightarrow}{\rightarrow}\rangle$, while there is no displacement if the spin states are $|{\leftarrow}{\rightarrow}\rangle$ or $|{\rightarrow}{\leftarrow}\rangle$ (the opposite set of states are affected if the stretch mode is used instead). The states that do move acquire a geometric phase $\chi_c(t)$ equal to the area enclosed by the displacement in phase space (z, p), which can be used to create entanglement between the two ions.

where $\Delta\phi_{mij} = \phi_{mi} - \phi_{mj}$. A key difference between the multi-ion case and the single ion case is the additional cross coupling terms proportional to $S_{\phi i}S_{\phi j}$. When $i = j$, these terms just give rise to global geometric phases in the same way as the single ion case, however when $i \neq j$, the phases are dependent on the spin state of the ion pair i, j. A state dependent phase such as this can be used to create an entangled state between a pair of ions. To see this, we can consider a pair of ions and a single motional mode, which could either be the centre of mass (COM) or stretch mode. The generalised effective Lamb-Dicke parameters in this case are $\eta_{11} = \eta_c$, $\eta_{12} = \eta_c$, $\eta_{21} = -\eta_s$ and $\eta_{22} = \eta_s$, where η_c and η_s are the magnitude of the effective Lamb-Dicke parameters for the COM and stretch mode respectively. For equal Rabi frequencies $\Omega_1 = \Omega_2 = \Omega$ and setting the spin and motional phases to

zero ($\phi_{sj} = \phi_{mj} = 0$), the two ion unitary operator for mode k can be written as

$$\begin{aligned} U^k_{\mathrm{MS}} = e^{-4i\chi_k(t)} D\Big(\alpha_{1k}(t) + \alpha_{2k}(t)\Big) \left|{\leftarrow\leftarrow}\right\rangle \left\langle{\leftarrow\leftarrow}\right| \\ + e^{-4i\chi_k(t)} D\Big(-\alpha_{1k}(t) - \alpha_{2k}(t)\Big) \left|{\rightarrow\rightarrow}\right\rangle \left\langle{\rightarrow\rightarrow}\right| \\ + D\Big(\alpha_{1k}(t) - \alpha_{2k}(t)\Big) \left|{\leftarrow\rightarrow}\right\rangle \left\langle{\leftarrow\rightarrow}\right| \\ + D\Big(-\alpha_{1k}(t) + \alpha_{2k}(t)\Big) \left|{\rightarrow\leftarrow}\right\rangle \left\langle{\rightarrow\leftarrow}\right|, \end{aligned} \tag{6.17}$$

where $\chi_k(t) = \chi_{ijk}(t)$ for all i, j. For the COM mode we get $\alpha_{1c}(t) = \alpha_{2c}(t) = \alpha_c(t)$, and therefore the motional state follows the displacements $\pm 2\alpha_c(t)$ when the spin is in the states $\left|{\leftarrow\leftarrow}\right\rangle$ and $\left|{\rightarrow\rightarrow}\right\rangle$ respectively, while the displacements for the states $\left|{\leftarrow\rightarrow}\right\rangle$ and $\left|{\rightarrow\leftarrow}\right\rangle$ cancel. For the stretch mode, we get $-\alpha_{1s}(t) = \alpha_{2s}(t) = \alpha_s(t)$, and therefore the motional state is displaced by $\pm 2\alpha_s(t)$ for the states $\left|{\leftarrow\rightarrow}\right\rangle$ and $\left|{\rightarrow\leftarrow}\right\rangle$, while the displacements cancel for the states $\left|{\leftarrow\leftarrow}\right\rangle$ and $\left|{\rightarrow\rightarrow}\right\rangle$. In either case, a relative phase of $e^{-4i\chi_k(t)}$ is acquired between the two sets of states $\{\left|{\leftarrow\leftarrow}\right\rangle, \left|{\rightarrow\rightarrow}\right\rangle\}$ and $\{\left|{\leftarrow\rightarrow}\right\rangle, \left|{\rightarrow\leftarrow}\right\rangle\}$. If the ions are prepared in the state $\left|{\downarrow\downarrow}\right\rangle \left|n = 0\right\rangle$, the states at time t for the two modes are therefore

$$\begin{aligned} \left|\psi_c(t)\right\rangle =& e^{-4i\chi_c(t)}\Big(\left|{\leftarrow\leftarrow}\right\rangle \left|2\alpha_c(t)\right\rangle + \left|{\rightarrow\rightarrow}\right\rangle \left|-2\alpha_c(t)\right\rangle\Big) \\ &+ \Big(\left|{\leftarrow\rightarrow}\right\rangle + \left|{\rightarrow\leftarrow}\right\rangle\Big) \left|n = 0\right\rangle \\ \left|\psi_s(t)\right\rangle =& e^{-4i\chi_s(t)}\Big(\left|{\leftarrow\leftarrow}\right\rangle + \left|{\rightarrow\rightarrow}\right\rangle\Big) \left|n = 0\right\rangle \\ &+ \Big(\left|{\leftarrow\rightarrow}\right\rangle \left|2\alpha_s(t)\right\rangle + \left|{\rightarrow\leftarrow}\right\rangle \left|-2\alpha_s(t)\right\rangle\Big). \end{aligned} \tag{6.18}$$

At times $t_q = 2\pi q/\delta_k$, where q is an integer, the motional state has completed a loop so that $\pm 2\alpha_k(t_q) = 0$, and hence the spin and motional states decouple. The geometric phases acquired at such times for the two modes are then found from Eq. 6.16 to be $\chi_{c,q} = q\pi\eta_c^2\Omega^2/2\delta_c^2$ and $\chi_{s,q} = -q\pi\eta_s^2\Omega^2/2\delta_s^2$. To create a maximally entangled state at t_q, the parameters should be chosen so that $\chi_{k,q} = \pm\pi/8$. This can be achieved by setting the detuning to be

$$\delta_k = \pm 2\sqrt{q}\eta_k\Omega. \tag{6.19}$$

With these choices for the time and detuning, the Mølmer-Sørensen unitary operator reduces to

$$U_{\mathrm{MS}} = \exp\Big(\pm\frac{i\pi}{4}S_{y1}S_{y2}\Big) = \frac{1}{\sqrt{2}}\begin{pmatrix} 1 & 0 & 0 & \mp i \\ 0 & 1 & \pm i & 0 \\ 0 & \pm i & 1 & 0 \\ \mp i & 0 & 0 & 1 \end{pmatrix}, \tag{6.20}$$

where the $\pm$ sign in the exponential depends on which mode is used and whether the detuning is chosen to be positive of negative and we have ignored a global phase. The operation of such a gate on the four input basis states gives the following truth table:

$$\begin{aligned} |{\downarrow\downarrow}\rangle &\rightarrow \frac{1}{\sqrt{2}}\Big(|{\downarrow\downarrow}\rangle \mp i\,|{\uparrow\uparrow}\rangle\Big), \\ |{\downarrow\uparrow}\rangle &\rightarrow \frac{1}{\sqrt{2}}\Big(|{\downarrow\uparrow}\rangle \pm i\,|{\uparrow\downarrow}\rangle\Big), \\ |{\uparrow\downarrow}\rangle &\rightarrow \frac{1}{\sqrt{2}}\Big(|{\uparrow\downarrow}\rangle \pm i\,|{\downarrow\uparrow}\rangle\Big), \\ |{\uparrow\uparrow}\rangle &\rightarrow \frac{1}{\sqrt{2}}\Big(|{\uparrow\uparrow}\rangle \mp i\,|{\downarrow\downarrow}\rangle\Big). \end{aligned} \tag{6.21}$$

It can be seen that the gate creates maximally entangled Bell states for all input basis states, while the motional state is decoupled. Therefore, it has been shown that the Mølmer-Sørensen interaction applied to a pair of ions can create maximally entangled spin states. The gate is equivalent to a CNOT gate and can be transformed using the following sequence of single qubit gates:

$$U_{\mathrm{CNOT}} = (\mathbb{I}\otimes H)\cdot(R_{-\frac{\pi}{2}}\otimes R_{-\frac{\pi}{2}})\cdot(H_y\otimes H_y)\cdot U_{\mathrm{MS}}\cdot(H_y\otimes H_y)\cdot(\mathbb{I}\otimes H), \tag{6.22}$$

where $R_\phi = \mathrm{diag}(1, e^{i\phi})$ is a single ion phase shift, H is a Hadamard gate and $H_y = R_{-\frac{\pi}{2}}\cdot H\cdot R_{\frac{\pi}{2}}$ is a Hadamard gate rotated to the y-basis. This can be verified by taking Eq. 6.20 and multiplying the matrices as described. The Mølmer-Sørensen gate is therefore suitable as a two-qubit gate for universal quantum computing.

In the derivation of the unitary evolution described above we set the spin and motional phases to zero. If we instead set the spin and motional phases to be non-zero but equal for both ions, the result is that the spin eigenstates and hence the relative phase of the final Bell state change. The change in motional phase also

causes the centre point of the two circles in phase space to rotate by an angle ϕ_m around the origin. If the phases are not equal for the two ions, the displacements in Eq. 6.17 don't cancel for any of the spin states, and consequently the geometric phases for the two modes at times t_q become $\chi_{c,q}(t) = q\pi\eta_c^2\Omega^2\cos(\Delta\phi_{m12})/2\delta_c^2$ and $\chi_{s,q}(t) = -q\pi\eta_s^2\Omega^2\cos(\Delta\phi_{m12})/2\delta_s^2$. The effect at times t_q is therefore to effectively weaken the interaction. If the phases are set so that $\Delta\phi_{m12} = \pi/2$, the gate has no effect, while if they are set so that $\Delta\phi_{m12} = \pi$, the opposite set of spin states are displaced and the geometric phase has the opposite sign, compared to the case where $\Delta\phi_{m12} = 0$. It should therefore be ensured that the spin and motional phases are fixed and their difference is equal to either 0 or π in order for the interaction to work correctly. For ions in a magnetic field gradient, the qubit frequencies of the two ions are different. This means that there are four detunings that need to be set for the gate (δ_{r1}, δ_{b1}, δ_{r2} and δ_{b2}). If $\delta_{b1} - \delta_{r1} \neq \delta_{b2} - \delta_{r2}$, the phase difference $\Delta\phi_{m12}$ becomes time-dependent, which would be detrimental to the gate for the reasons mentioned above. It should therefore be ensured that the two frequency differences are exactly equal to ensure that the phase relationship between the two sets of Mølmer-Sørensen fields can be kept constant.

In a similar way to the two ion case, we can find the reduced density matrix $\rho_k^{(s)}(t)$ describing only the spin states by tracing over the motional state. As an example we can choose to perform the gate on the stretch motional mode so that the states $|{\leftarrow}{\rightarrow}\rangle$ and $|{\rightarrow}{\leftarrow}\rangle$ move in circles in phase space. Starting with the spins in the state $|{\downarrow}{\downarrow}\rangle$ and the motion in a thermal state, the density matrix is

$$\begin{aligned}\rho_{\mathrm{th},s} =& \sum_{n=0}^{\infty} p_n \left|\psi_{n,s}(t)\right\rangle \left\langle\psi_{n,s}(t)\right|, \\ \left|\psi_{n,s}(t)\right\rangle =& e^{-4i\chi_s(t)}\Big(\left|{\leftarrow}{\leftarrow}\right\rangle + \left|{\rightarrow}{\rightarrow}\right\rangle\Big)\left|n\right\rangle \\ &+ \Big(\left|{\leftarrow}{\rightarrow}\right\rangle D(2\alpha_s(t)) + \left|{\rightarrow}{\leftarrow}\right\rangle D(-2\alpha_s(t))\Big)\left|n\right\rangle.\end{aligned} \tag{6.23}$$

The reduced density matrix can then be found as $\rho_{\mathrm{th},s}^{(s)} = \sum_{m=0}^{\infty}\langle m|\,\rho_{\mathrm{th},s}\,|m\rangle$. The magnitude of the density matrix elements at three different times during the gate evolution are plotted in Fig. 6.5. The diagonal elements of the density matrix give

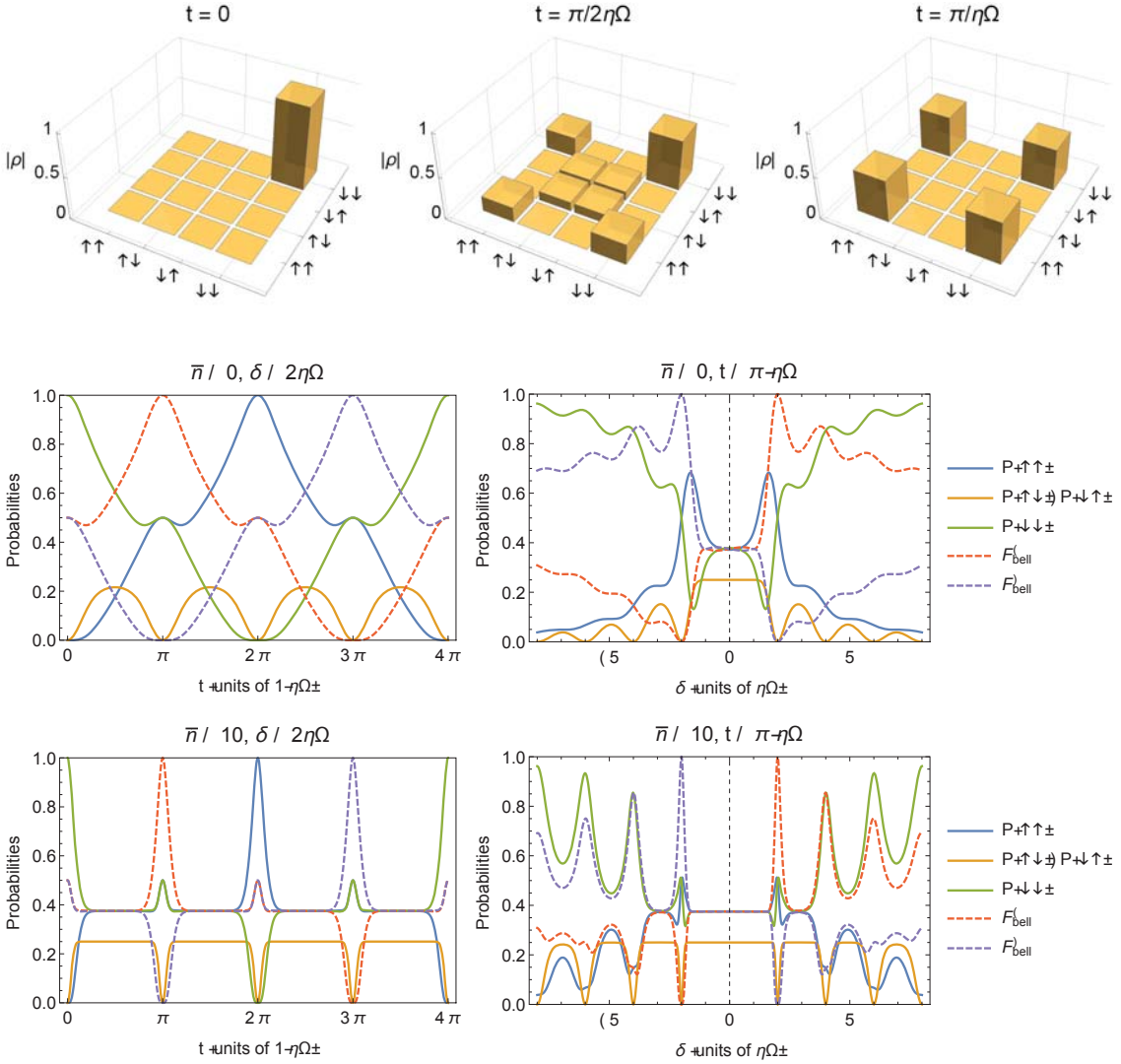


Fig. 6.5 Top: Plots of the magnitude of the reduced density matrix elements for three different times after applying the Mølmer-Sørensen interaction to a pair of ions with symmetric detuning $\delta = 2\eta\Omega$. With this detuning, a maximally entangled state will be formed after the motional state has completed a single loop in phase space at time $t_g = 2\pi/\delta = \pi/\eta\Omega$. The first and last plot show the density matrix before and after the gate interaction, showing that the spin state evolves from $|\downarrow\downarrow\rangle$ to the maximally entangled state $(|\downarrow\downarrow\rangle + e^{i\phi}|\uparrow\uparrow\rangle)/\sqrt{2}$. The middle plot shows the state halfway through the evolution, which is a mixed state after tracing over the motional degrees of freedom. Bottom: State populations and Bell state fidelities as a function of time (left) and symmetric detuning (right) for the Mølmer-Sørensen interaction applied to a pair of ions, following Eqs. 6.24 and 6.27. In the top row the motional state is prepared in the ground state $|n = 0\rangle$, while in the bottom row the motional state is in a thermal state with $\bar{n} = 10$. It can be seen that while the gate still works in the thermal case, the features are narrower and therefore the detuning and time have to be set more accurately compared to the ground state case to achieve a given gate fidelity.

the state populations, which are found to be

$$\begin{aligned} P(\uparrow\uparrow) &= \frac{1}{8}\Big(3 + e^{-|4\alpha_s(t)|^2(\bar{n}+\frac{1}{2})} - 4\cos(4\chi_s(t))e^{-|2\alpha_s(t)|^2(\bar{n}+\frac{1}{2})}\Big), \\ P(\uparrow\downarrow) = P(\downarrow\uparrow) &= \frac{1}{8}\Big(1 - e^{-|4\alpha_s(t)|^2(\bar{n}+\frac{1}{2})}\Big) \\ P(\downarrow\downarrow) &= \frac{1}{8}\Big(3 + e^{-|4\alpha_s(t)|^2(\bar{n}+\frac{1}{2})} + 4\cos(4\chi_s(t))e^{-|2\alpha_s(t)|^2(\bar{n}+\frac{1}{2})}\Big). \end{aligned} \tag{6.24}$$

Plots of the populations as a function of both time and detuning are plotted in Fig. 6.5. These functions are useful to compare with experimental data to see if the Mølmer-Sørensen interaction is working correctly and to measure and set experimental parameters such as the symmetric detuning and Rabi frequencies.

There are several measures that can be used to estimate the gate fidelity. A simple measure is given by the overlap of the density matrix with the Bell state $|\psi_\phi\rangle = (|\downarrow\downarrow\rangle + e^{i\phi}|\uparrow\uparrow\rangle)/\sqrt{2}$. Here ϕ is the phase of the Bell state, which is predicted to be either $\pi/2$ or $-\pi/2$ depending on which motional mode is used and the sign of the symmetric detuning. A more precise method is to perform process tomography, where the output state is characterised for every input state and the average fidelity is taken. This would require individual ion detection, and so was not used here, but would be an interesting further experiment to carry out. For an arbitrary density matrix ρ with matrix elements $\rho_{ij,kl}$, where $i, j, k, l \in \{\downarrow, \uparrow\}$, the Bell state fidelity is

$$\begin{aligned} \mathcal{F}_{\text{bell}} = \langle\psi_\phi|\,\rho\,|\psi_\phi\rangle &= \frac{1}{2}\Big(\rho_{\uparrow\uparrow,\uparrow\uparrow} + \rho_{\downarrow\downarrow,\downarrow\downarrow} + e^{i\phi}\rho_{\downarrow\downarrow,\uparrow\uparrow} + e^{-i\phi}\rho_{\uparrow\uparrow,\downarrow\downarrow}\Big) \\ &= \frac{1}{2}\Big(\rho_{\uparrow\uparrow,\uparrow\uparrow} + \rho_{\downarrow\downarrow,\downarrow\downarrow} + 2|\rho_{\uparrow\uparrow,\downarrow\downarrow}|\cos(\phi - \phi_{\uparrow\uparrow,\downarrow\downarrow})\Big), \end{aligned} \tag{6.25}$$

where we have written the off diagonal matrix elements in polar form as $\rho_{\uparrow\uparrow,\downarrow\downarrow} = \rho^*_{\downarrow\downarrow,\uparrow\uparrow} = |\rho_{\uparrow\uparrow,\downarrow\downarrow}|e^{i\phi_{\uparrow\uparrow,\downarrow\downarrow}}$. The phase of the Bell state is usually unimportant, as any phase difference from a desired Bell state can be corrected with single qubit rotations. In this case, we can ignore the cosine term in Eq. 6.25 and the fidelity becomes

$$\mathcal{F}_{\text{bell}} = \frac{1}{2}\Big(\rho_{\uparrow\uparrow,\uparrow\uparrow} + \rho_{\downarrow\downarrow,\downarrow\downarrow} + 2|\rho_{\uparrow\uparrow,\downarrow\downarrow}|\Big). \tag{6.26}$$

The theoretical gate fidelity as a function of time can be calculated from the reduced density matrix $\rho^{(s)}_{\text{th},s}$ to be

$$\mathcal{F}^{\pm}_{\text{bell}} = \frac{1}{8}\Big(3 + e^{-|4\alpha_s(t)|^2(\bar{n}+\frac{1}{2})} \pm 4\sin(4\chi_s(t))e^{-|2\alpha_s(t)|^2(\bar{n}+\frac{1}{2})}\Big), \tag{6.27}$$

where the $\pm$ sign corresponds to the two Bell states $(|\downarrow\downarrow\rangle \pm i\,|\uparrow\uparrow\rangle)/\sqrt{2}$. The fidelity as a function of time and detuning is plotted in Fig. 6.5.

In the same way as in the single ion case, the Mølmer-Sørensen interaction can be performed on multiple dressed-state qubits $\{|0'_j\rangle, |D_j\rangle\}$, where j is the ion number, with the replacements $|\downarrow_j\rangle \rightarrow |0'_j\rangle$, $|\uparrow_j\rangle \rightarrow |D_j\rangle$ and $\Omega \rightarrow \Omega_D = \Omega_{\mathrm{rf}}/\sqrt{2}$. The Stark shifts for the two ions can be calculated using Eq. 6.13, where the 2nd order Zeeman shifts $\Delta\omega_\pm$ are different for the two ions due to the magnetic field gradient.

6.3.2 Sources of Error

There are various sources of error that could lead to a Bell state infidelity for the Mølmer-Sørensen gate. These errors can be grouped into two broad categories, namely mis-set gate parameters and limiting errors such as motional heating and dephasing. The infidelity due to limiting errors indicates the maximum fidelity achievable when the gate parameters are perfectly set, and is determined by system parameters that are set or have been characterised in previous chapters. In the following sections, the main sources of error are discussed and the resulting gate infidelities are calculated.

Motional heating

Motional heating causes the populations in the Fock states $|n\rangle$ to change, which can change the path of the displaced motional states in phase space and cause the paths to not completely close at the end of the gate. The gate infidelity due to heating can be calculated by solving the master equation given in Eq. 5.15 with the Mølmer-Sørensen Hamiltonian. An analytical solution is derived in Ref. [31], which for two ions gives an infidelity

$$\varepsilon_{\mathrm{heating}} = 1 - \frac{1}{8}\Big(3 + 4e^{-\frac{\dot{\bar{n}}\pi}{2\sqrt{q}\eta_k\Omega}} + e^{-\frac{2\dot{\bar{n}}\pi}{\sqrt{q}\eta_k\Omega}}\Big). \tag{6.28}$$

The infidelity can be reduced by increasing the speed of the gate compared to the heating rate (i.e. increasing the ratio $\eta_k\Omega/\dot{\bar{n}}$), or by increasing the number of loops q. By increasing the number of loops, the displacements in phase space per loop get smaller and hence the sensitivity to heating reduces. If q is large, the gate becomes largely insensitive to heating, however, the gate time also increases as $\sqrt{q}$, and therefore other sources of error may become more significant in this regime.

In chapter 5, the heating rates for a single ion and the stretch mode of two ions were measured. The heating rate of the COM mode of two ions should be equal

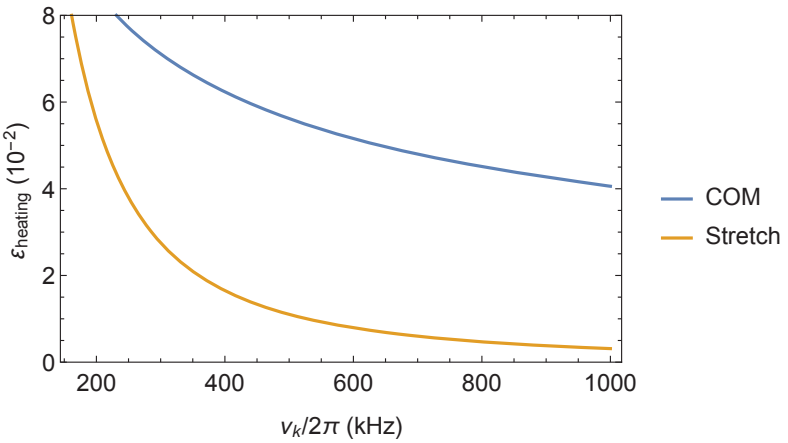


Fig. 6.6 Heating rate error $\epsilon_{\text{heating}}$ as given by Eq. 6.28 as a function of the mode frequency ν_k for the COM and stretch modes of a two ion string using the measured heating rates for the two modes. The Rabi frequency has been fixed as $\Omega/2\pi = 35\,\text{kHz}$ and q has been set to 1. Since η_k decreases with ν_k, this means that although the error decreases for larger mode frequencies, the gate time increases.

to the single ion heating rate for a given trap frequency. For the COM mode, the heating rate as a function of mode frequency follows the relation [82]

$$\dot{\bar{n}}_c(\nu_z) = \frac{e^2}{4m\hbar\nu_z^2}\nu_z S_E(\nu_z), \tag{6.29}$$

where $\nu_z S_E(\nu_z)$ is the scaled spectral noise density of the electric field, which is assumed to be independent of the trap frequency and constant, and can be found by measuring $\dot{\bar{n}}_c$ for the COM mode at a particular trap frequency. From our previous measurements in Chapter 5, we find $\nu_z S_E(\nu_z) = 1.4(2)\times 10^{-6}\ \text{V}^2\text{m}^{-2}$. For the stretch mode, an estimate for the heating rate as a function of the mode frequency is given by [83]

$$\begin{aligned}\dot{\bar{n}}_s(\nu_s) &= \frac{e^2}{4m\hbar\nu_s^2}\frac{\nu_z S_E(\nu_z)}{d^2}\Delta z^2 \\ &= \frac{e^2}{4m\hbar\nu_s^{10/3}}\frac{\nu_z S_E(\nu_z)}{d^2}\left(\frac{3e^2}{2\pi\epsilon_0 m}\right)^{2/3},\end{aligned} \tag{6.30}$$

where d is the ion-electrode distance and Δz is the ion-ion spacing. For our ion-electrode distance of $d = 310\,\mu\text{m}$ and stretch mode frequency $\nu_s/2\pi = 468.2\,\text{kHz}$, Eq. 6.30 predicts a heating rate of $\dot{\bar{n}}_s = 0.025\,\text{s}^{-1}$. This is over two orders of magnitude lower than the value of $\dot{\bar{n}}_s = 7(2)\,\text{s}^{-1}$ measured in Sec. 5.4.3. The reason for the large discrepancy is unknown, but could be caused by a noise spectrum that does

not scale as 1/f, or for noise that is correlated between the trap electrodes, both of which are not taken into account in the model leading to Eq. 6.30. An interesting further experiment would be to measure the scaling of the stretch mode heating rate with frequency. Fig. 6.6 shows plots of the gate infidelity due to heating $\epsilon_{\text{heating}}$ as a function of the mode frequency ν_k for the COM and stretch modes using the measured heating rates. The stretch mode heating rate follows the frequency scaling of Eq. 6.30, with an extra constant multiplying factor to account for the discrepancy between predicted and observed heating rates.

Dephasing and depolarisation

A common source of error for the Mølmer-Sørensen gate is dephasing of the qubits due to magnetic field noise. As shown in Chapter 4, the use of dressed states suppresses the effects of magnetic field noise as the energies of the dressed states are independent of the magnetic field. Noise can still couple to the system however by driving transitions between the dressed states if the noise frequency is near-resonant with the dressed-state energy splitting. The effect of magnetic field noise in this case is therefore depolarisation rather than dephasing. As discussed in Sec. 4.3.1, magnetic field noise can also cause dephasing of the dressed-state qubit $\{|0'\rangle, |D\rangle\}$ if the detunings and Rabi frequencies of the dressing fields are not set correctly. After setting these parameters to within the expected tolerance based on the theory described in Sec. 4.3.1, the lifetime of $|D\rangle$ and the coherence time of the qubit $\{|0'\rangle, |D\rangle\}$ were measured in Sec. 4.3.4 and found to be equal within statistical errors at approximately 0.65 s. This indicates that depolarisation is indeed the dominant effect due to magnetic field noise in our system.

The effect of both dephasing and depolarisation on the gate fidelity can be estimated using a master equation approach. To estimate the effects, a numerical simulation is performed using a Lindblad master equation of the form

$$\dot{\rho}(t) = \frac{i}{\hbar}[H, \rho(t)] + \sum_{jk} \Big(C_{jk}\rho(t)C_{jk}^{\dagger} - \frac{1}{2}C_{jk}^{\dagger}C_{jk}\rho(t) - \frac{1}{2}\rho(t)C_{jk}^{\dagger}C_{jk} \Big), \tag{6.31}$$

where H is the Hamiltonian and C_{jk} are Lindblad operators acting on ion j. For dephasing, there is one Lindblad operator per ion ($k = 1$), given by [84]

$$C_{j1} = \sqrt{\frac{\Gamma}{2}} \Big(|D_j\rangle \langle D_j| - |0'_j\rangle \langle 0'_j| \Big), \tag{6.32}$$

where $\Gamma = 1/T_2$ is the measured dephasing rate. In the case of depolarisation, there are six Lindblad operators ($k = 6$), which are given by [84]

$$\begin{aligned}
C_{j1} &= \sqrt{\frac{\gamma_1}{6}}\big(\,|u_j\rangle\langle D_j| + |D_j\rangle\langle u_j|\,\big),\\
C_{j2} &= \sqrt{\frac{\gamma_1}{6}}\big(\,|d_j\rangle\langle D_j| + |D_j\rangle\langle d_j|\,\big),\\
C_{j3} &= \sqrt{\frac{\gamma_1}{6}}\big(i\,|u_j\rangle\langle D_j| - i\,|D_j\rangle\langle u_j|\,\big),\\
C_{j4} &= \sqrt{\frac{\gamma_1}{6}}\big(i\,|d_j\rangle\langle D_j| - i\,|D_j\rangle\langle d_j|\,\big),\\
C_{j5} &= \sqrt{\frac{\gamma_2}{6}}\big(\,|u_j\rangle\langle u_j| - |D_j\rangle\langle D_j|\,\big),\\
C_{j6} &= \sqrt{\frac{\gamma_2}{6}}\big(\,|d_j\rangle\langle d_j| - |D_j\rangle\langle D_j|\,\big),
\end{aligned} \tag{6.33}$$

where γ_1 and γ_2 are two decay rates. The six Lindblad operators for depolarisation correspond to σ_x, σ_y and σ_z type rotations between $|D\rangle$ and $|u\rangle$ as well as $|D\rangle$ and $|d\rangle$. The σ_z type rotations would occur if there were fluctuations in the relative energies of the dressed states, which could for example be caused by fluctuations in the microwave dressing field Rabi frequencies. We neglect these effects in the following, and therefore set $\gamma_1 = 1/T_1$ as the measured lifetime of $|D\rangle$ and $\gamma_2 = 0$. The factor of 6 in the square root differs from Ref. [84] by a factor of 3/2, which is due to the fact that here there are two levels coupled to $|D\rangle$ rather than one as in the case of a qubit. The additional factor was found by solving Eq. 6.31 analytically for a single ion. A worst-case scenario for the gate fidelity can then be found by initialising two four-level ions in the Bell state $|\psi\rangle = (|0'0'\rangle - i\,|DD\rangle)/\sqrt{2}$ and simulating the decay due to depolarisation following Eq. 6.31 with no Hamiltonian term. Fig. 6.7 shows the result of such a simulation for the measured lifetime $T_1 = 0.63(4)\,\mathrm{s}$. An additional exponential decay is overlaid with the simulated curve, which is an approximate analytical expression for the gate fidelity as a function of time in the form

$$\mathcal{F}_{\mathrm{depolarisation}} = \mathcal{F}_0 + (1 - \mathcal{F}_0)e^{-\gamma_0 t/T_1}, \tag{6.34}$$

where we find $\mathcal{F}_0 = 0.2778$ and $\gamma_0 = 0.92$ give a good agreement with the simulation on short timescales (similar to expected gate times), as shown in Fig. 6.7. Substituting in the equation for the gate time, we therefore find the error due to depolarisation is

$$\varepsilon_{\mathrm{depolarisation}} = (1 - \mathcal{F}_0)(1 - e^{-\frac{\pi\gamma_0\sqrt{q}}{T_1\eta_k\Omega}}). \tag{6.35}$$

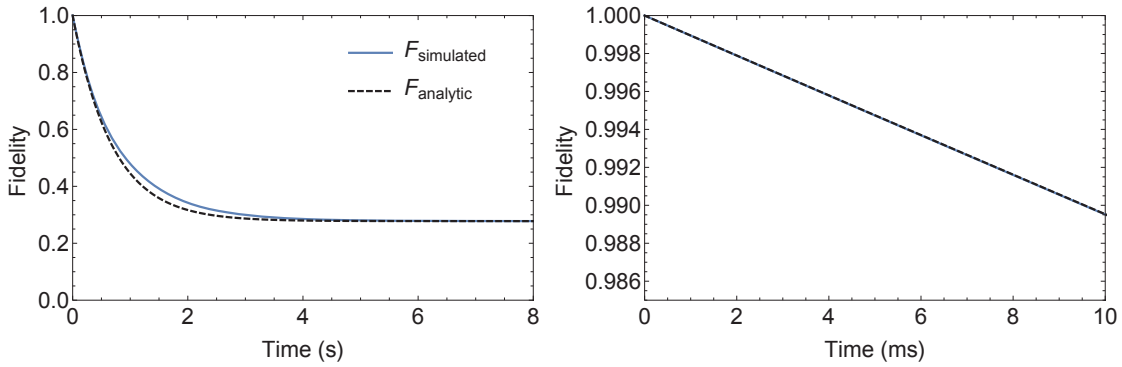


Fig. 6.7 Result of a numerical simulation of Eq. 6.31 for two four-level ions initially prepared in the Bell state $|\psi\rangle = (|0'0'\rangle - i\,|DD\rangle)/\sqrt{2}$. The blue curve is the numerical simulation, while the black dashed curve is the analytical expression given by Eq. 6.34. The simulated and analytic expressions can be seen to be in good agreement, especially on shorter timescales as shown in the right plot, which shows the expected fidelity on similar timescales to the expected gate time for our parameters.

As expected for a fixed lifetime, the gate infidelity from depolarisation can only be reduced by performing a faster gate (i.e. increasing $\eta_k\Omega$ or reducing q).

Carrier coupling

Off-resonant coupling of the Mølmer-Sørensen fields to the carrier transitions leads to small oscillations of the populations in time at a frequency approximately equal to the detuning from the carrier δ_c. Unlike the previous errors, this is a coherent process and so does not necessarily give rise to any gate infidelity. If the gate was applied for a time that is an integer multiple of the off-resonant carrier oscillation period $2\pi/\delta_c$, the infidelity from carrier coupling would be zero. However, achieving such accuracy is not typically possible experimentally, as any small change in the carrier detuning would be amplified after the many oscillations required to reach the gate time*. Furthermore, in the dressed-state scheme there are six carrier transitions to consider, each with slightly different detunings. Finding a time when the amplitude of all six oscillations are zero would therefore be challenging. If the gate is not performed with such accuracy, the coupling to the carrier becomes an error term, which is calculated in Ref. [31] to be approximately $N\Omega_\beta^2/2\delta_\beta^2$ for each carrier transition $|0'\rangle \leftrightarrow |\beta\rangle$, where N is the number of ions. We can approximate that the six carrier detunings are all equal to the mode frequency ν_k, which is valid as long as $\delta, \Omega_{\mu\text{w}} \ll \nu_k$. Using the fact that $\Omega_D = \Omega_{\text{rf}}/\sqrt{2}$ and $\Omega_{ud} = \Omega_{\text{rf}}/2$, the carrier coupling error is therefore

*for typical parameters the gate time is on the order of 1000 periods of the mode oscillation

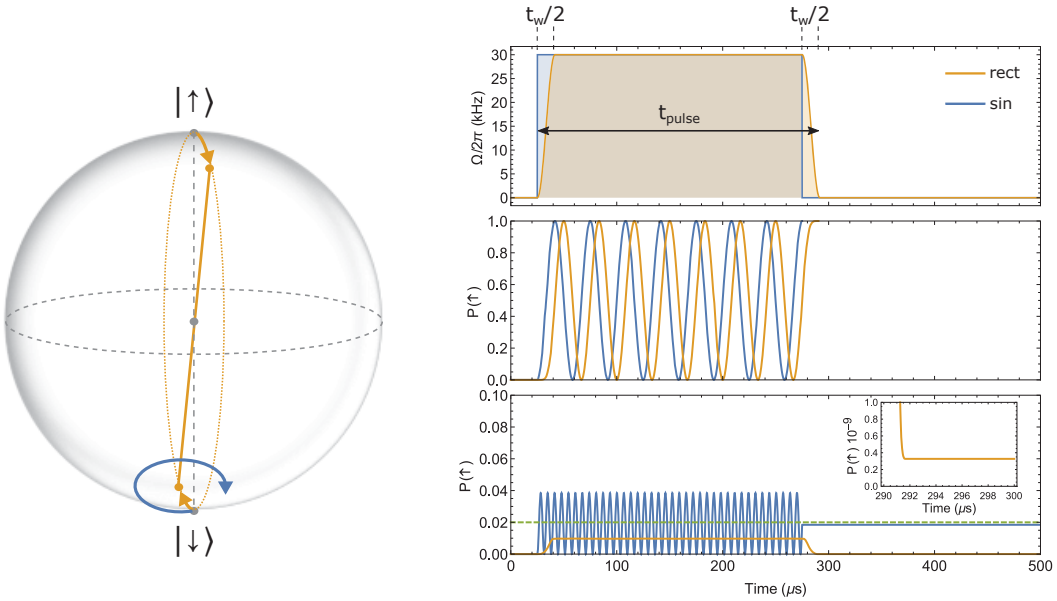


Fig. 6.8 Effect of modulating the Rabi frequency of an off-resonant field applied to a two-level system. Left: On the Bloch sphere, an off-resonant field causes the state vector to rotate around an axis aligned with the dressed-state eigenvectors which is at an angle θ from z (for $\phi = 0$), shown by the solid orange line. If the field is turned on instantaneously, a state initialised in $|\downarrow\rangle$ rotates around the circle shown in blue. At the end of the pulse, the state vector could therefore be at any angle between 0 and 2θ due to imperfect timing. If the field is instead ramped up at the start of the pulse and ramped down at the end of the pulse slowly compared to π/δ, the state vector adiabatically follows the spin eigenstates, returning to $|\downarrow\rangle$ at the end of the pulse. Right: Plots of a numerical simulation of a single field applied to a two level system with either a square pulse shape (blue) or a shaped pulse with $\sin^2$ type ramp profile (orange) as described by Eq. 6.37. The top graph shows the Rabi frequency as a function of time, which in both cases has a maximum of $\Omega_{\max}/2\pi = 30\,\text{kHz}$. The window length t_w is set to $2\pi/\Omega_{\max}$, so that the two ramps at the beginning and end of the pulse each last half a period of the maximum Rabi frequency. The pulse areas have been set equal so that a for a resonant pulse, a rotation of 15π is achieved. The middle graph shows the population $P(\uparrow)$ as a function of time for a resonant pulse, while the bottom graph shows the same for when the detuning is set to $\delta = 5\Omega_{\max}$. For this detuning, the window length t_w satisfies the adiabatic condition as $t_w = 10\pi/\delta$. It can be seen that although the shaped resonant pulse transfers population in the same way as the square pulse, the off-resonant pulse has a significantly reduced error. The inset in the bottom graph shows a zoom of $P(\uparrow)$ for the shaped case at the end of the pulse, showing that the maximum population is on the order 10^{-9}. The dashed green line shows the average error for an unshaped pulse, which is approximately given by $\Omega_{\max}^2/2\delta^2$.

$$\varepsilon_{\text{carrier}} \approx \frac{\Omega_D^2}{\nu_k^2} + \frac{4\Omega_{ud}^2}{\nu_k^2} = \frac{2\Omega_{\text{rf}}^2}{\nu_k^2}. \tag{6.36}$$

It can be seen that the carrier coupling error can be reduced by either increasing the mode frequency ν_k or decreasing the Rabi frequency Ω_{rf}.

In our setup, the magnetic field gradient of 24.5 T/m gives a fairly small effective Lamb-Dicke parameter for typical trap frequencies, and therefore the ratio of sideband to carrier Rabi frequencies is also small. This means that the parameter regime required for a reasonably fast, high-fidelity gate results in a large carrier coupling infidelity on the order of a few %. The error due to carrier coupling can however be largely suppressed by modulating the amplitude of the Mølmer-Sørensen fields in time so that they are smoothly turned on and off, rather than the usual square pulse. This can be understood by considering the positions of the two level dressed-state eigenvectors given in Eq. 4.3 on the Bloch sphere. The Bloch vector can be described using two angles θ and ϕ, for which the dressed-state eigenvectors can be written as $|d\rangle = \cos(\theta/2)\,|\downarrow\rangle + e^{i\phi}\sin(\theta/2)\,|\uparrow\rangle$ and $|u\rangle = \sin(\theta/2)\,|\downarrow\rangle - e^{i\phi}\cos\theta/2\,|\uparrow\rangle$. If the Rabi frequency $\Omega_0 = 0$, the dressed states $|u\rangle$ and $|d\rangle$ are equal to the bare states $|\downarrow\rangle$ and $|\uparrow\rangle$ and therefore $\theta = \phi = 0$. If $\delta \gg \Omega_0$ and Ω_0 is increased, we find $\theta \approx -2\arccos(2\delta/\sqrt{4\delta^2 + \Omega_0^2})$, while ϕ is set by the phase of the field. If the ion is initialised in the state $|\downarrow\rangle$ and an off-resonant field is applied instantaneously, the state vector will rotate around the axis on the Bloch sphere at angle (θ, ϕ) corresponding to the dressed-state eigenvectors with frequency $\Omega_\delta = \sqrt{\delta^2 + \Omega_0^2}$, as shown in Fig. 6.8. If however, the Rabi frequency is increased slowly, the state vector follows the eigenstate and there is no oscillation. The field can then be ramped back down, returning all population to $|\downarrow\rangle$ at the end of the pulse. For sufficiently large detuning, $\Omega_\delta \approx \delta$ and the condition for adiabatic following is approximately $t_w \gg \pi/\delta$. For zero detuning, the eigenvectors instantaneously jump to $|u\rangle = (|\downarrow\rangle + |\uparrow\rangle)/\sqrt{2}$ and $|d\rangle = (|\downarrow\rangle - |\uparrow\rangle)/\sqrt{2}$, and therefore the ramp speed for adiabatic following becomes infinitely slow. Consequently, a shaped pulse can perform in the same way as a square pulse when resonant, while having a significantly reduced error when off-resonant.

The exact shape of the ramp is not crucial, as long as the adiabatic condition $t_w \gg \delta$ is met. A $\sin^2$ profile was therefore chosen. The Rabi frequency is therefore modulated as

$$\Omega(t) = \begin{cases} \Omega_{\max}\sin^2\left(\frac{\pi t}{t_w}\right) & 0 \le t < \frac{t_w}{2} \\ \Omega_{\max} & \frac{t_w}{2} \le t < t_{\text{pulse}} - \frac{t_w}{2} \\ \Omega_{\max}\sin^2\left(\frac{\pi(t - t_{\text{pulse}})}{t_w}\right) & t_{\text{pulse}} - \frac{t_w}{2} \le t < t_{\text{pulse}} \end{cases}. \tag{6.37}$$

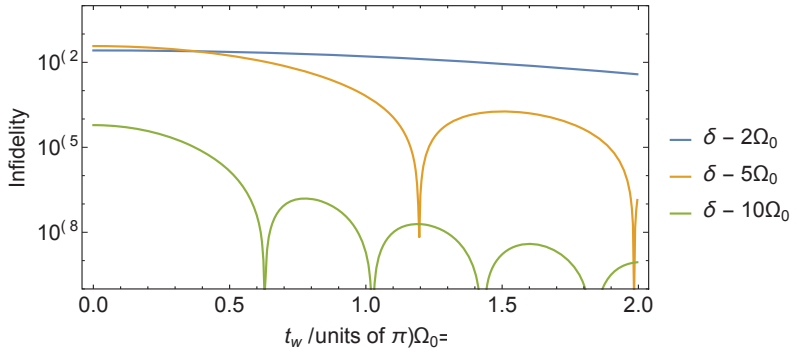


Fig. 6.9 Infidelity defined as the amount of population remaining in $|\uparrow\rangle$ after applying a $\sin^2$ shaped pulse as a function of the window length t_w for different values of δ. The maximum value of t_w in this case is $2\pi/\Omega_0$, corresponding to $t_w = t_{\text{pulse}}$. It can be seen that the error can be reduced by several orders of magnitude when using pulse shaping.

This profile is illustrated in Fig. 6.8. To observe the effect of pulse shaping, a numerical simulation of a two level system interacting with a field was performed, where both square and $\sin^2$ shaped pulses were tested. The results are shown in Fig. 6.8, where it can be seen the amount of population transferred between the two states is reduced by several orders of magnitude when an off-resonant field is applied. Fig. 6.9 shows the population remaining in $|\uparrow\rangle$ after applying a shaped pulse equivalent to a π-pulse when $\delta_c = 0$ as a function of the window length t_w for different detunings.

To test the pulse shaping, we prepare a single ion in $|0'\rangle$ and apply an RF pulse with fixed length near the $|0'\rangle \leftrightarrow |D\rangle$ transition and vary the detuning. The resulting population for both a square and shaped pulse are shown in Fig. 6.10 along with a numerical simulation with the measured parameters. It can be seen that the data and simulation curves match well, demonstrating that the shaped pulse is having the desired effect.

Incorrect symmetric detuning

If the symmetric detuning δ of the Mølmer-Sørensen fields is set incorrectly, the loops in phase space will not exactly close at the gate time and the geometric phase will not be exactly equal to $\pi/8$. As well as arising from mis-set parameters, such an error can also arise if there is a drift in the trap frequency. To calculate the gate infidelity for small detuning errors, we can set $\delta = \delta_0 + \Delta\delta$, where $\delta_0 = 2\sqrt{q}\eta\Omega$ and $\Delta\delta$ is the symmetric detuning error, and expand Eq. 6.27 in powers of $\Delta\delta$. To lowest order in $\Delta\delta$, we get

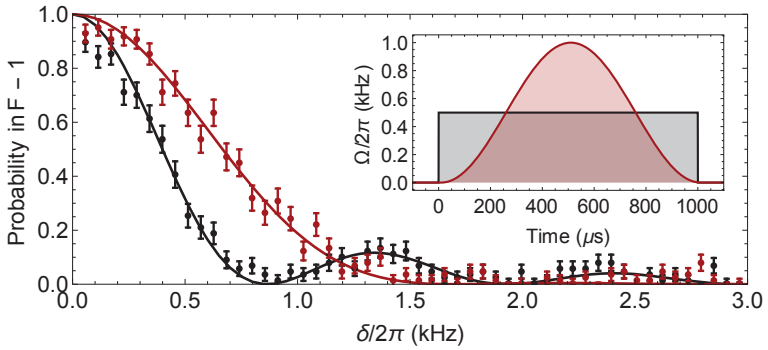


Fig. 6.10 Population in F = 1 after preparing in $|0'\rangle$ and applying an RF pulse to the $|0'\rangle \leftrightarrow |D\rangle$ transition while scanning the detuning. The black points are for a square pulse with Rabi frequency $\Omega_D/2\pi = 0.5\,\text{kHz}$, while the red points are for a shaped $\sin^2$ pulse following Eq. 6.37, where the window length has been set equal to the pulse length so that $t_w = t_{\text{pulse}} = 1\,\text{ms}$ and the maximum Rabi frequency is $\Omega_{\text{max}} = 2\Omega_D$. The Rabi frequency for the two cases as a function of time are shown in the inset. The solid lines are the result of numerically simulating a two level system driven by a single field with Rabi frequency either constant at Ω_D for the pulse duration or varied following Eq. 6.37.

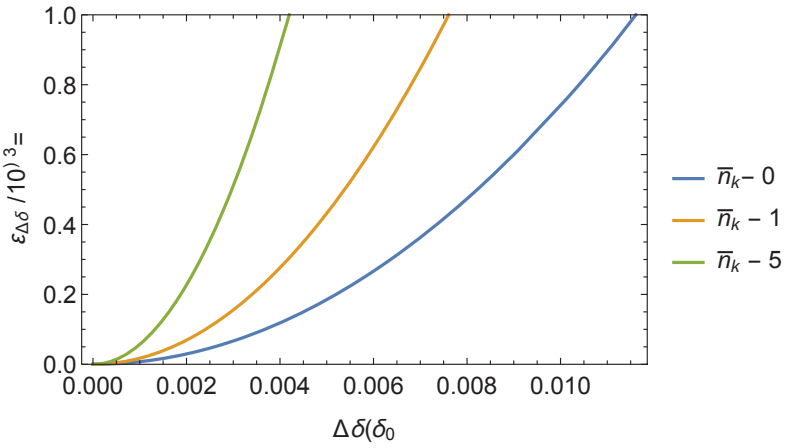


Fig. 6.11 Gate infidelity $\varepsilon_{\Delta\delta}$ as a function of the fractional symmetric detuning error $\Delta\delta/\delta_0$. It can be seen that for a higher mean phonon number $\bar{n}_k$, the detuning error should be smaller to achieve a given fidelity. It is therefore advantageous to sideband cool the motional state as low as possible to reduce the error.

$$\varepsilon_{\Delta\delta} = 1 - \mathcal{F}_{\text{bell}} = \Delta\delta^2 \left(\frac{\pi^2}{\eta_k^2 \Omega^2}\right)\left(\frac{1 + 2q(1 + 2\bar{n}_k)}{16q}\right) + O(\Delta\delta^3). \tag{6.38}$$

The error $\varepsilon_{\Delta\delta}$ is plotted in Fig. 6.11. It can be seen that for higher values of $\bar{n}_k$, the fractional detuning error $\Delta\delta/\delta_0$ should be set more accurately to achieve the same gate fidelity. This is apparent when looking at the plots of fidelity in Fig. 6.5 for the $\bar{n} = 0$ and $\bar{n} = 10$ cases, where it can be seen that the feature surrounding the correct gate detuning is much narrower in the hotter case. It is therefore advantageous to sideband cool the motional state to a low $\bar{n}$ in order to achieve a high-fidelity gate. If the mode is in the ground state, the symmetric detuning should be kept below $\Delta\delta \approx 0.01\delta_0$ to ensure the infidelity is less than 10^{-3}.

Incorrect asymmetric detuning

Gate infidelities can also arise if the 'asymmetric detuning' is set incorrectly. For a single ion, the two sideband detunings are ideally set to $\delta_r = \delta_0$ and $\delta_b = -\delta_0$, where δ_0 is the symmetric gate detuning. An asymmetric detuning $\Delta\delta$ is then defined as the case where $\delta_r = \delta_0 + \Delta\delta$ and $\delta_b = -\delta_0 + \Delta\delta$. For two ions, there are four main asymmetric detuning errors, namely both ions have equal asymmetric detunings, both have opposite asymmetric detunings, and two cases where only one of the ions has an asymmetric detuning. Such errors can occur if the Stark shift for each ion is not set correctly, or if there is a drift in the qubit frequency. The infidelity from asymmetric detuning errors cannot be calculated in a simple analytic way in the same way as the symmetric detuning error, as when deriving the Mølmer-Sørensen Hamiltonian we have already assumed that $\delta_r = -\delta_b$. To estimate the error, a numerical simulation of the gate can be performed for the case that the motion is in the ground state. The overlap with the Bell state $|\psi_\phi\rangle = (|0'0'\rangle + e^{i\phi}|DD\rangle)/\sqrt{2}$ at t_g is then calculated and the Bell state fidelity is maximised as a function of ϕ. This then allows any variation in phase of the produced Bell state to be taken into account, which could be corrected using single qubit rotations if required. Fig. 6.12 shows the resulting infidelity as a function of $\Delta\delta$ for the four different cases. It can be seen that the worst case is when both ions have equal asymmetric detuning, in which case it can be seen that we require $\Delta\delta \lesssim 0.04\delta_0$ for the infidelity to be below 10^{-2}.

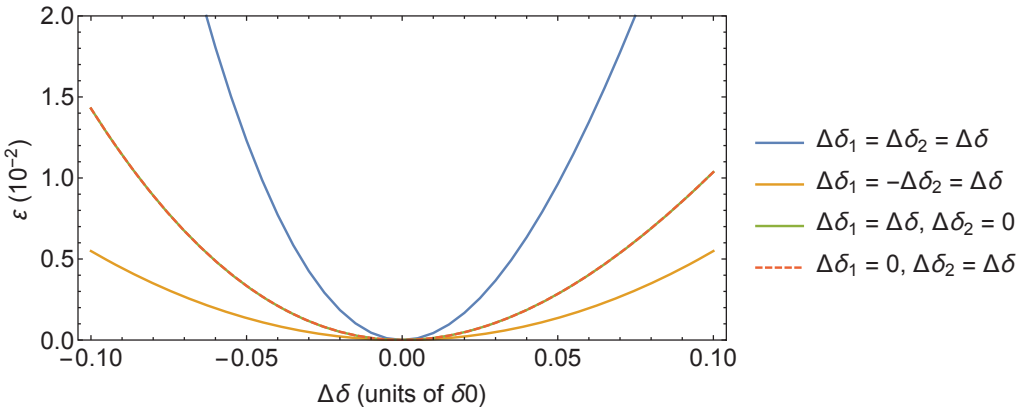


Fig. 6.12 Gate infidelity as a function of incorrectly set asymmetric detunings. The four curves represent the four different ways that the asymmetric detuning can be mis-set. The symmetric detuning is set to $\delta_0 = 2\eta\Omega$, corresponding to a single loop gate and the gate time is set to $t_g = 2\pi/\delta_0$. The infidelities can also be compensated by slightly adjusting the symmetric detuning or gate time.

Nonlinear Kerr coupling

The nonlinearity of the Coulomb interaction gives rise to a 'Kerr' coupling between axial and radial normal modes for which the ions have relative motion, such as the stretch axial mode and the rocking radial modes for a two ion string [85, 86]. If the gate is performed on the axial stretch mode, the mode frequency therefore depends on the motional state $|n_r\rangle$ of the rocking mode. If the rocking mode is only Doppler cooled so that it is in a thermal state with mean phonon number $\bar{n}_r$, the stretch mode frequency fluctuates between experimental runs, which consequently becomes a symmetric detuning error for the gate. The Kerr coupling Hamiltonian for a pair of ions is given by [85, 86]

$$H_{\text{kerr}} = \hbar K a_s a_s^\dagger a_r a_r^\dagger, \tag{6.39}$$

where $a_s, a_s^\dagger$ and $a_r, a_r^\dagger$ are ladder operators for the stretch mode and rocking mode respectively. The coupling coefficient K is given by [86]

$$K = -\nu_s \left(\frac{1}{2} + \frac{\nu_s^2/2}{4\nu_r^2 - \nu_s^2}\right)\left(\frac{\nu_z}{\nu_r}\right)\left(\frac{2\hbar\nu_z}{\alpha^2 mc^2}\right)^{\frac{1}{3}}, \tag{6.40}$$

where $\nu_r = \sqrt{\nu_\perp^2 - \nu_z^2}$ is the rocking mode frequency, $\nu_\perp$ could correspond to either radial mode frequency ν_x or ν_y, α is the fine structure constant and c is the speed of light. The stretch mode frequency is therefore modified by $\Delta\nu_s = Kn_r$. This is the same as a symmetric detuning error, and can therefore be substituted into Eq.

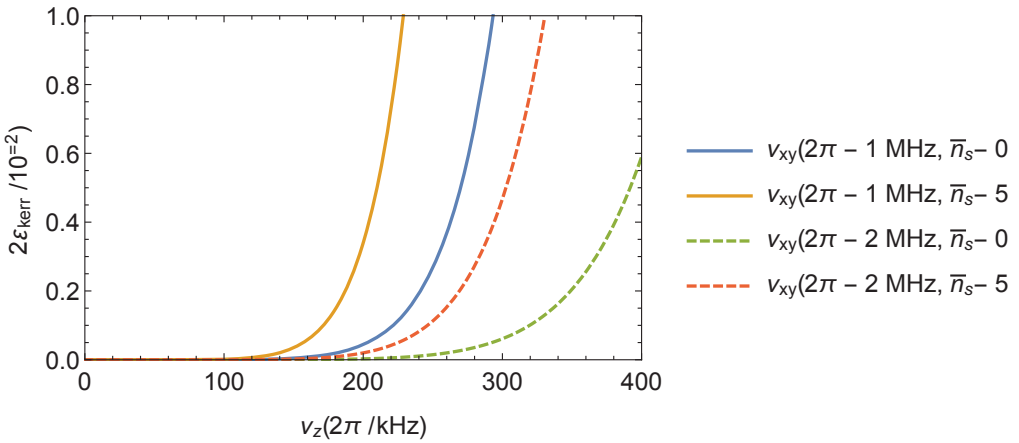


Fig. 6.13 Gate infidelity $2\varepsilon_{\text{kerr}}$ due to the Kerr coupling between the stretch and rocking modes in a two ion string. The Rabi frequency is fixed at $\Omega/2\pi = 35\,\text{kHz}$ and the solid and dashed lines represent two different radial mode frequencies $\nu_\perp/2\pi = 1\,\text{MHz}$ and $2\,\text{MHz}$ respectively. The rocking modes are assumed to be at the Doppler temperature, as given by Eq. 5.1 and the two curves for each radial mode frequency represent the stretch mode being in a thermal state with $\bar{n}_s = 0, 5$. The infidelity is twice the Kerr coupling error due to the two radial modes, which are approximated to be the same frequency. The curves take into account the reduction in effective Lamb-Dicke parameter with increasing trap frequency, making the q loop gate time longer for a fixed Ω.

6.38 to find the gate infidelity. If the rocking mode is in a thermal state with mean phonon number $\bar{n}_r$, the error is thermally distributed with a different value for each experimental run. The average error can therefore be calculated by the variance of the thermal distribution, which is given by $\text{Var}(n_r) = \bar{n}_r(2\bar{n}_r + 1)$. The average infidelity is then found to be [87]

$$\varepsilon_{\text{kerr}} = K^2\bar{n}_r(2\bar{n}_r + 1)\left(\frac{\pi^2}{\eta_s^2\Omega^2}\right)\left(\frac{1 + 2q(1 + 2\bar{n}_s)}{16q}\right). \tag{6.41}$$

There are two radial modes in the x and y directions which are generally almost the same frequency, both of which have an associated rocking mode. The total error from Kerr coupling is therefore approximately $2\varepsilon_{\text{kerr}}$. Plots of $2\varepsilon_{\text{kerr}}$ are shown in Fig. 6.13.

Spin-spin coupling

An error term arises from the spin-spin coupling due to the magnetic field gradient, whose effect in the dressed basis is derived in Sec. 4.4.2. The effect is to drive population between $|DD\rangle$ and $(|ud\rangle + |du\rangle)/\sqrt{2}$ at a rate $2J_{12}^{\pm} = \sum_k \eta_{1k}\eta_{2k}\nu_k^3/(\Omega_{\mu\text{w}}^2 -$

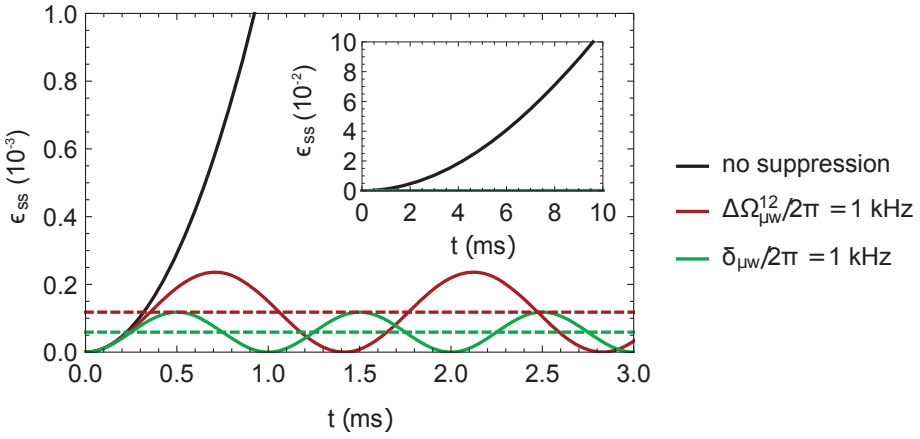


Fig. 6.14 Gate infidelity due to spin-spin coupling as a function of time, where the trap frequency has been set to $\nu_z/2\pi = 265\,\text{kHz}$ and the dressing field Rabi frequencies are $\Omega_{\mu w}/2\pi = 20\,\text{kHz}$. The black curve shows the error when all dressing field detunings are resonant and Rabi frequencies equal, in which case the spin-spin coupling is a resonant effect. By either changing the difference between the dressing field Rabi frequencies for the two ions (red) or by detuning the dressing fields (green) by 1 kHz, the error can be significantly suppressed. The dashed lines show the average error as given in Eq. 6.44.

$2\nu_k^2$). A simple error model is then found by equating the infidelity with the loss of population from $|DD\rangle$ when coupled to a state outside of the two qubits with frequency $4J_{12}^{\pm}$. The error is then given by

$$\varepsilon_{ss} = \frac{1}{4}\left(1 - \cos\left(\frac{4J_{12}^{\pm}\pi\sqrt{q}}{\eta_k\Omega}\right)\right). \tag{6.42}$$

This can be a significant error for typical gate parameters, however, the coupling can be largely suppressed by adjusting the parameters to change the dressed state energies. To see this, we can write the operators S_+ and S_- for arbitrary dressed state energies ϵ_u, ϵ_d and ϵ_D in the interaction picture with respect to the dressing Hamiltonian to get

$$\begin{aligned} S_+ &= \sqrt{2}\Big(e^{i(\epsilon_u-\epsilon_D)/\hbar}\,|u\rangle\langle D| + e^{i(\epsilon_D-\epsilon_d)/\hbar}\,|D\rangle\langle d|\Big), \\ S_- &= \sqrt{2}\Big(e^{i(\epsilon_D-\epsilon_u)/\hbar}\,|D\rangle\langle u| + e^{i(\epsilon_d-\epsilon_D)/\hbar}\,|d\rangle\langle D|\Big). \end{aligned} \tag{6.43}$$

The terms coupling to $|DD\rangle$ in the spin-spin coupling operators $S_+^i S_-^j$ are then rotating at frequencies $\Delta_{ij}^{\pm} = \pm(\epsilon_u^i + \epsilon_d^j)/\hbar \mp (\epsilon_D^i + \epsilon_D^j)/\hbar$. If the dressing fields are all set to resonance and the dressing field Rabi frequencies are all equal, $\epsilon_u^j = \Omega_{\mu w}^j/\sqrt{2}$, $\epsilon_d^j = -\Omega_{\mu w}^j/\sqrt{2}$ and $\epsilon_D^j = 0$, and therefore $\Delta_{ij}^{\pm} = 0$. Therefore the spin-spin interaction

is a resonant effect. If however the dressed state energies are set in a way that makes $\Delta_{ij}^{\pm} \neq 0$, the coupling is off-resonant and is therefore suppressed. The coupling can be neglected as off-resonant if the condition $\Delta_{ij}^{\pm} \gg J_{ij}^{\pm}$ is met. There are two distinct ways to alter the dressed state energies to have the desired effect with a pair of ions. The first is to detune the dressing fields equally for both ions by an amount $\delta_{\mu\mathrm{w}}$. The rotation frequency of the spin-spin coupling term is then $\Delta_{12}^{\pm} = \pm\delta_{\mu\mathrm{w}}$. Alternatively, the dressing Rabi frequencies can be set to be different by an amount $\Delta\Omega_{\mu\mathrm{w}} = \Omega_{\mu\mathrm{w}}^{1} - \Omega_{\mu\mathrm{w}}^{2}$*. The rotation frequency is then $\Delta_{12}^{\pm} = \pm\Delta\Omega_{\mu\mathrm{w}}/\sqrt{2}$. Fig. 6.14 shows the effect of the spin-spin coupling on the gate infidelity as a function of time for the case that the coupling is resonant and off-resonant. If the coupling is off resonant, the average error can be found to be

$$\varepsilon_{ss} \approx \frac{|J_{12}^{\pm}|^2}{|\Delta_{12}^{\pm}|^2}. \tag{6.44}$$

Other errors

Other sources of error considered are small compared to the errors discussed in the previous sections, giving contributions to the gate infidelity below 10^{-7}. Error terms that can be significant in some implementations of the Mølmer-Sørensen gate are deviations from the Lamb-Dicke regime and coupling to spectator motional modes, as discussed in Ref. [31]. In our case the effective Lamb-Dicke parameter η is small compared to the Lamb-Dicke parameters η_l that can be achieved with lasers, and hence such errors are negligibly small ($\sim 10^{-7}$). If a similar experiment was carried out where a larger magnetic field gradient was used, these errors may become significant and should then be taken into account. Errors can also arise due to approximations in the dressed-state picture. In the derivation of the dressed state Hamiltonians discussed in Chapter 4, some approximations were made and hence some Hamiltonian terms were neglected. These terms may have a small effect on the gate, which can lead to errors. The error terms can be found by performing the Magnus expansion on the full Hamiltonian, which has been shown analytically in Ref. [88]. With the exception of the spin-spin coupling error discussed in the previous section, all such errors were found to be below 10^{-8} for typical parameters.

Total infidelity

The total infidelity can be estimated by adding together all of the errors discussed in the previous sections. The measured gate infidelity will likely be higher than

*Note that the Rabi frequencies of the two dressing fields for a given ion should still be equal.

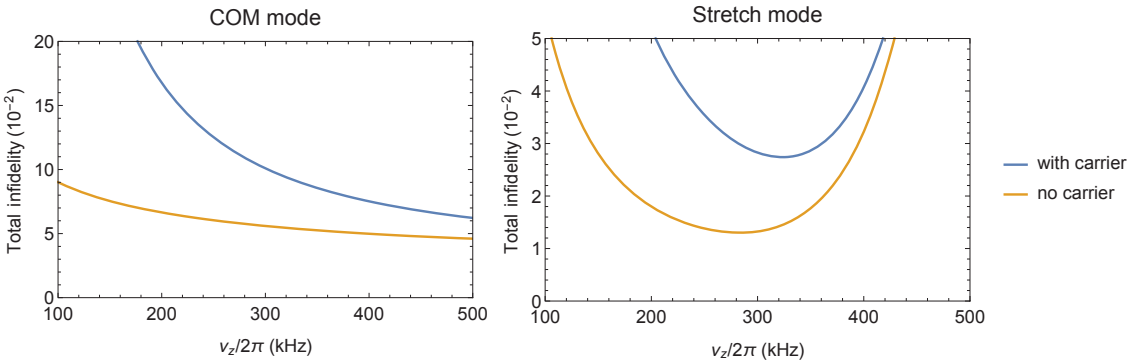


Fig. 6.15 Total gate infidelity as a function of the trap frequency obtained by summing the errors described in the previous sections for the COM mode (left) and the stretch mode (right). Errors due to mis-set detunings have not been included, and it has been assumed that the spin-spin coupling error is suppressed sufficiently to be neglected. The blue curve shows the total infidelity when using a square pulse shape, while the orange shows the infidelity without the carrier coupling error, which could be achieved by shaping the amplitude of the Mølmer-Sørensen fields. The parameters used correspond to typical measured values and are set to $\Omega/2\pi = 45\,\text{kHz}$, $\bar{n} = 0.14$, $\nu_\perp/2\pi = 1.5\,\text{MHz}$. The depolarisation time and heating rates are set to those measured in Chapters 4 and 5 respectively.

this value as some systematic and experimental effects may have not been taken into account, but it gives a lower bound and a good idea of what is achievable for a given set of parameters. Fig. 6.15 shows the total infidelity as a function of trap frequency for both the COM and stretch modes for a set of parameters given in the figure caption. It can be seen that the lowest infidelity of approximately 0.015 is achieved when using the stretch mode with trap frequency in the range 250 kHz to 350 kHz. To obtain this infidelity, it has been assumed that pulse shaping has been used to completely neglect the error from carrier coupling, and that the dressing field Rabi frequencies differ between the two ions by $\approx 1\,\text{kHz}$ to suppress the spin-spin coupling.

6.3.3 Experimental Results

The gate is performed on the stretch motional mode with frequency $\nu_s/2\pi = 459.34(1)\,\text{kHz}$. To implement the gate, the stretch mode is therefore first sideband cooled to approximately $\bar{n}_s \approx 0.14$ using the microwave sideband cooling technique as discussed in Sec. 5.4.3, where the sideband pulses are resonant with the red sideband of the $|0\rangle \leftrightarrow |{+}1\rangle$ transition. This cooling technique was chosen as it requires less fields and pulses, and a small but finite temperature is not a significant source of error. After cooling, the ions are prepared in the state $|0'0'\rangle$ using optical

pumping and two microwave π-pulses on each of the clock transitions with pulse times of 700 μs and 685 μs respectively. The four microwave dressing fields and the four RF Mølmer-Sørensen fields are then applied. The dressing field Rabi frequencies are set to $\Omega_{\mu w1}/2\pi = 20.5\,\text{kHz}$ for ion 1 and $\Omega_{\mu w2}/2\pi = 21.6\,\text{kHz}$, where the Rabi frequencies of the two fields in each ion have been matched to within 0.5%. The difference in Rabi frequency was chosen to suppress the spin-spin coupling error, causing the coupling to be off-resonant by $\Delta_{12}^{\pm}/2\pi = 778\,\text{Hz}$. The spin-spin coupling frequency is calculated to be $J_{12}^{\pm}/2\pi = 3.8\,\text{Hz}$, which therefore gives a suppressed error of $\varepsilon_{ss} \approx 2\times10^{-5}$. The Rabi frequencies for the four Mølmer-Sørensen fields are set to $\Omega_{rf}/2\pi = 64.2\,\text{kHz}$, corresponding to a dressed state Rabi frequency $\Omega_D = \Omega_{rf}/\sqrt{2} = 2\pi \times 45.4\,\text{kHz}$ and all four fields are set equal to within 1 kHz. The pulse amplitudes are shaped in a $\sin^2$ profile as discussed previously in the chapter, with a window length of $t_w = 20\,\mu$s. With these parameters, it can be seen that $\delta_c \approx \nu_s \approx 10\Omega_D$, and $t_w \approx 2\pi/\Omega_D$. Therefore the infidelity from carrier coupling is below 10^{-8} and can be neglected. To set the gate detunings correctly, the $|0'\rangle \leftrightarrow |D\rangle$ carrier transitions are first measured to an accuracy of $\approx 20\,\text{Hz}$, and the optimum Stark shifts and symmetric detuning for a single loop gate are calculated using Eqs. 6.13 and 6.19. A scan of the gate pulse time is then performed, and any mis-set symmetric detuning can be inferred from the time at which the populations $P_{0'D} + P_{D0'}$ dip to zero, as can be seen in Fig. 6.5. To optimise the asymmetric detunings, the pulse time is set to $2t_g$ and each of the four asymmetric detuning types, as discussed in Sec. 6.3.2, are scanned. These processes are then iterated until the populations at t_g are optimised towards the ideal values of $P_{0'0'} = P_{DD} = 0.5$ and $P_{0'D} + P_{D0'} = 0$. Fig. 6.16 shows the resulting populations when varying the pulse time. It can be seen that the data fits the theory curves well, demonstrating that the Mølmer-Sørensen interaction is working correctly. The populations at the gate time $t_g = \pi/\eta\Omega_D = 2.7\,\text{ms}$ are measured separately with 1300 repetitions, giving $P_{0'0'} + P_{DD} = 0.997(8)$, which is consistent with the production of the Bell state $|\psi_\phi\rangle = (|0'0'\rangle + e^{i\phi}|DD\rangle)/\sqrt{2}$. The populations on their own however are not enough to verify that the state is entangled and extract a Bell state fidelity, as the state could be mixed to some degree. Therefore a further measurement is required to enable the Bell state fidelity to be calculated, which will be discussed in the following section.

Gate characterisation

As can be seen from Eq. 6.25, the Bell state fidelity can be calculated from the density matrix elements $\rho_{\uparrow\uparrow,\uparrow\uparrow}$, $\rho_{\downarrow\downarrow,\downarrow\downarrow}$, $\rho_{\uparrow\uparrow,\downarrow\downarrow}$ and $\rho_{\downarrow\downarrow,\uparrow\uparrow}$. The diagonal matrix elements

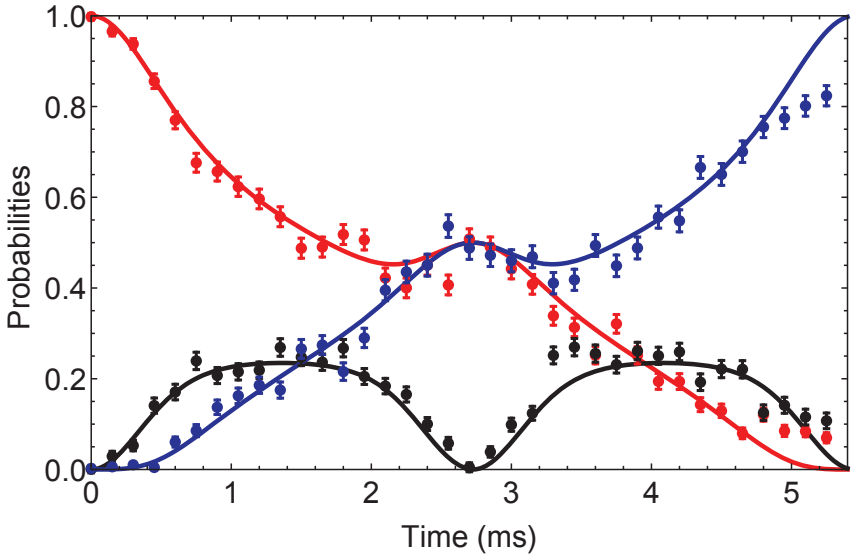


Fig. 6.16 Measured probabilities for zero (red), one (black) and two (blue) ions to be in $F = 1$ for the Mølmer-Sørensen interaction when the pulse time is varied. These are equivalent to the probabilities $P_{0'0'}$, $P_{0'D} + P_{D0'}$ and P_{DD} respectively if errors due to mapping between dressed and bare states and lifetime effects are neglected. The solid lines are theory curves following Eqs. 6.24 with $\bar{n} = 0$. The symmetric detuning is set to $\delta = 2\eta\Omega_D = 2\pi \times 370\,\text{Hz}$. At the gate time $t_g = 2.7\,\text{ms}$, the populations can be seen to approach the ideal values of $P_{0'0'} = P_{DD} = 0.5$ and $P_{0'D} + P_{D0'} = 0$, consistent with the production of the Bell state $|\psi_s\rangle = (|0'0'\rangle + e^{i\phi}\,|DD\rangle)/\sqrt{2}$.

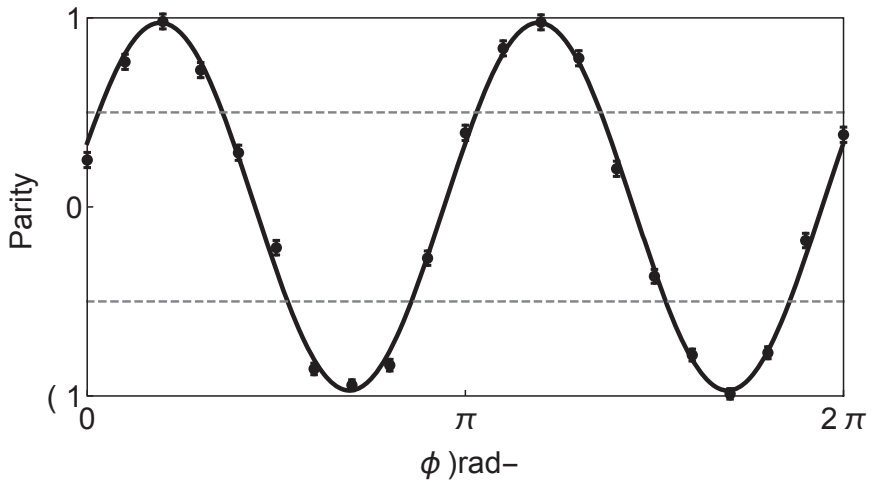


Fig. 6.17 Parity $\Pi = P_{0'0'} - P_{0'D} - P_{D0'} + P_{DD}$ of the two dressed-state qubits after applying the Mølmer-Sørensen interaction for a time t_g followed by a parity pulse on both carrier transitions and varying the carrier field phases equally. Each point is the result of 800 repetitions. The data is fit to the function $A_0 + A\cos(2\phi + \phi_0)$, which can be compared with Eq. 6.46 to see that $A \to 2|\rho^i_{\uparrow\uparrow,\downarrow\downarrow}|$. A fit to the data gives $A = 0.972(17)$, which together with the measured populations at t_g gives a Bell state fidelity of $\mathcal{F}_{\text{bell}} = 0.985(12)$.

$\rho_{\uparrow\uparrow,\uparrow\uparrow}$ and $\rho_{\downarrow\downarrow,\downarrow\downarrow}$ are given by the populations $P_{\uparrow\uparrow}$ and $P_{\downarrow\downarrow}$ which can be measured directly from an experiment such as that shown in Fig. 6.16. To measure the off diagonal density matrix elements $\rho_{\uparrow\uparrow,\downarrow\downarrow}$ and $\rho_{\downarrow\downarrow,\uparrow\uparrow}$, a further experiment should be performed after the gate interaction. As shown in Ref. [33], these matrix elements can be measured by applying $\pi/2$ carrier pulses to both ions and varying the phase on both equally. From Eq. 2.23, the unitary operator for a $\pi/2$ pulse on a single ion with phase ϕ_p is given by

$$U_p\Big(t = \frac{\pi}{2\Omega}, \phi_p\Big) = \frac{1}{\sqrt{2}} \begin{pmatrix} 1 & -ie^{i\phi_p} \\ -ie^{-i\phi_p} & 1 \end{pmatrix}. \tag{6.45}$$

If the phases are set to be equal for the carrier fields for both ions, the total unitary operator for a $\pi/2$ pulse on each ion is $U_p(\phi_p) \otimes U_p(\phi_p)$. The parity Π is defined the sum of the populations in the even parity states $|\uparrow\uparrow\rangle$ and $|\downarrow\downarrow\rangle$ minus the sum of the populations in the odd parity states $|\uparrow\downarrow\rangle$ and $|\downarrow\uparrow\rangle$. The parity signal as a function of ϕ_p after applying the two $\pi/2$ pulses to an arbitrary initial state ρ^i is therefore given by

$$\begin{aligned}\Pi(\phi_p) &= \langle\uparrow\uparrow|\,\rho_p(\phi_p)\,|\uparrow\uparrow\rangle + \langle\downarrow\downarrow|\,\rho_p(\phi_p)\,|\downarrow\downarrow\rangle - \langle\uparrow\downarrow|\,\rho_p(\phi_p)\,|\uparrow\downarrow\rangle - \langle\downarrow\uparrow|\,\rho_p(\phi_p)\,|\downarrow\uparrow\rangle \\ &= \rho^i_{\uparrow\downarrow,\downarrow\uparrow} + \rho^i_{\downarrow\uparrow,\uparrow\downarrow} - e^{2i\phi_p}\rho^i_{\downarrow\downarrow,\uparrow\uparrow} - e^{-2i\phi_p}\rho^i_{\uparrow\uparrow,\downarrow\downarrow} \\ &= 2|\rho^i_{\uparrow\downarrow,\downarrow\uparrow}|\cos(\phi_{\uparrow\downarrow,\downarrow\uparrow}) - 2|\rho^i_{\uparrow\uparrow,\downarrow\downarrow}|\cos(\phi_{\uparrow\uparrow,\downarrow\downarrow} + 2\phi_p),\end{aligned} \tag{6.46}$$

where $\rho_p(\phi_p) = (U_p(\phi_p) \otimes U_p(\phi_p))\rho^i(U_p^\dagger(\phi_p) \otimes U_p^\dagger(\phi_p))$. The parity signal therefore oscillates with frequency $2\phi_p$, phase offset $\phi_{\uparrow\uparrow,\downarrow\downarrow}$ and amplitude $2|\rho^i_{\uparrow\uparrow,\downarrow\downarrow}|$, allowing the magnitude and phase of $\rho^i_{\uparrow\uparrow,\downarrow\downarrow}$ to be extracted. The additional term in Eq. 6.46 gives an offset to the parity curve if the density matrix elements $\rho^i_{\uparrow\downarrow,\downarrow\uparrow}$ are non-zero. Fig. 6.17 shows the parity signal after applying the gate to the two dressed state qubits as discussed in the previous section for a time t_g, followed by a $\pi/2$ pulse on both carrier transitions $|0'\rangle \leftrightarrow |D\rangle$ lasting 425 μs and varying the phase of both fields equally. The data is fit to the function $A_0 + A\cos(2\phi_p + \phi_0)$, which can be compared with Eq. 6.46 to give the magnitude of the off-diagonal density matrix elements as $A = |\rho^i_{\uparrow\uparrow,\downarrow\downarrow}| = |\rho^i_{\downarrow\downarrow,\uparrow\uparrow}| = 0.972(17)$. Inserting this into Eq. 6.26 along with the measured populations, the Bell state fidelity is $\mathcal{F}_{\text{bell}} = 0.985(12)$.

From the experimental parameters used, the measured gate infidelity can be broken down into individual parts from different error sources, as described in Sec. 6.3.2. These estimated errors are given in Table. 6.1. It can be seen that the largest estimated contribution to the error is from motional heating. The measured gate fidelity differs from the predicted value by approximately 2×10^{-3}, which is well within the error of the measurement. Any difference between the two values could also arise due to mis-set gate parameters such as the symmetric and asymmetric detunings.

In Appendix D, a 'gate recipe' is described, which outlines the procedure used to implement the two-qubit gate presented in this chapter. It has been attempted to make the steps as generic as possible, so that the recipe could be followed for future experiments where different parameters are used.

In this chapter, a two-qubit gate using the Mølmer-Sørensen interaction has been demonstrated with a Bell state fidelity of $\mathcal{F}_{\text{Bell}} = 0.985(12)$. The gate is implemented using only microwave and RF fields, making it a promising candidate for use in a large scale quantum computing architecture. The infidelity measured agrees well with the predicted errors from the measured motional heating rate, lifetime and coherence time, and such errors can be reduced with further work. The next steps to increase the fidelity further, as well as an outline of how this two-qubit gate scheme

Source	Error (10^{-2})
Motional heating	0.96
Depolarisation	0.27
Carrier coupling	$< 10^{-8}$
Kerr coupling	0.08
Spin-spin coupling	$< 10^{-5}$
Total	**1.31**

Table 6.1 Error budget for the two-qubit gate, which has a measured infidelity of $(1.5 \pm 1.2) \times 10^{-2}$. The errors are calculated from equations given in Sec. 6.3.2. The predicted infidelity from the sum of errors in the table matches the measured infidelity to within the error in the measurement. Any difference between the predicted and measured values could be due to mis-set gate parameters.

would fit into a large scale quantum computing architecture, are discussed in the following chapter.

Chapter 7

Conclusion

The work described in this thesis centres around a new method for performing the fundamental operations required for a quantum computer using long-wavelength radiation. The method uses the combination of a static magnetic field gradient to couple the internal and motional states of the trapped ions, and dressed states to protect the qubits from magnetic field noise. With this combination, sideband cooling of a single ion to $\bar{n} = 0.13(4)$ was demonstrated, as well as a two-qubit quantum logic gate with a Bell state fidelity of $\mathcal{F}_{\text{Bell}} = 0.985(12)$. These two results represent the coldest temperature and highest fidelity two-qubit gate achieved in trapped ions using long-wavelength radiation, making this scheme a promising candidate for use in a scalable quantum computing architecture. The result has also made it possible to design a scheme for a trapped ion quantum computer based on long-wavelength radiation, where there is no correlation between the number of microwave and RF fields applied with the number of qubits. This idea is discussed in further detail in Sec. 7.3.

7.1 Summary

In chapter 3 it was shown that by adding a static magnetic field gradient to an ion trap experiment, a transition that couples the internal and motional states of a trapped ion can be performed with a coupling strength that is independent of the frequency of the radiation applied. This can then be used to perform multi-qubit gates using long-wavelength radiation. Furthermore, for multiple ions in a linear trap the gradient additionally allows qubits to be individually addressed in frequency space, in contrast to the traditional approach in which lasers are tightly focussed to address ions in position space. It was then shown in chapter 4 that dressed states can help suppress

noise coupling to the magnetic field sensitive qubits required for the magnetic field gradient scheme. A scalable preparation and detection method was demonstrated for the dressed-state qubit $\{|0'\rangle, |D\rangle\}$, and the T_1 and T_2 times were measured to be 0.63(4) s and 0.65(5) s respectively. The coherence time is nearly three orders of magnitude larger than the bare magnetic field sensitive states, and is comparable with the coherence times of magnetic field insensitive clock qubits. With further work, it should be possible to increase the lifetime and coherence time to 2 s and above, as demonstrated in Ref. [89]. With these lifetime and coherence time measurements, high-fidelity single qubit gates between $|0'\rangle$ and $|D\rangle$ in the fault-tolerant regime should be possible, and are indicated by the Rabi oscillations demonstrated in chapter 4. To fully characterise the single-qubit gates and properly measure the fidelity, a randomised benchmarking experiment could be performed, which would be an interesting experiment for future investigation. In chapter 5, the dressed state and magnetic field gradient schemes were combined to implement sideband cooling to the ground state of motion in a single ion using long-wavelength radiation. The mean phonon number after sideband cooling was measured to be $\bar{n} = 0.13(4)$. The heating rate of a single ion in the trap was also measured to be $41(7)\,\mathrm{s}^{-1}$ at an axial trap frequency of $\nu_z/2\pi = 426.7(1)\,\mathrm{kHz}$, which is almost two-orders of magnitude lower than a previously measured value. The improvement is attributed to a highly stable voltage supply and filtering system designed for applying the DC voltages to the trap electrodes, as well as an effort to remove sources of electrical noise in the laboratory. The stretch mode of a two ion string was also sideband cooled, reaching a mean phonon number of $\bar{n} = 0.14(3)$. The heating rate of this mode was measured and found to be five times less than the single ion heating rate after scaling out the dependence on trap frequency. Finally in chapter 6, a Mølmer-Sørensen two-qubit gate was implemented with two dressed-state qubits using long-wavelength radiation. The Bell state fidelity was measured to be $\mathcal{F}_{\mathrm{Bell}} = 0.985(12)$, which is approaching the regime required for fault-tolerant quantum computation. The current limitations in gate fidelity are motional heating and depolarisation, both of which could be reduced dramatically with an increased magnetic field gradient. This demonstration shows that this gate scheme, in which dressed-states are used to protect qubits that can be coupled by a magnetic field gradient, is a promising candidate for use in a scalable trapped ion quantum computing architecture.

7.2 Future work

The next step for this scheme is to push the gate fidelity further into the fault-tolerant regime, thereby further demonstrating the potential for long-wavelength radiation quantum computing. If the single and two qubit gate infidelities can be reduced below 10^{-3} in a single system, this scheme would surpass the best results achieved by Raman laser gates so far. The best way to achieve this would be to increase the magnetic field gradient. For the gradient of 24.5 T/m used in this work, the effective Lamb-Dicke parameter is typically in the range 0.001 to 0.01. In comparison, the Lamb-Dicke parameter used in Raman laser gates is typically on the order 0.1. A small effective Lamb-Dicke parameter causes sideband transitions to have narrow widths in frequency and hence high demands are placed on the stability of parameters such as the magnetic field and trap frequency. Furthermore, the gate time is longer and therefore decohering processes have a larger effect. If the gradient was increased so that the effective Lamb-Dicke parameter was comparable with the Lamb-Dicke parameter for Raman laser gates, these errors should be able to be reduced to 10^{-3} and below. A simple way to create a higher magnetic field gradient would be to modify or redesign the trap used in this work so that the magnets are closer together. A simulation shows that by moving the magnets so that the distance between the ion and magnets is 2.4 mm, a magnetic field gradient of 150 T/m would be produced. This should be straightforward to achieve in a redesigned trap. An alternative would be to design a new macroscopic trap in which the endcap electrodes are made from permanent magnet material, thereby incorporating the magnetic field gradient into the trap design. With a gradient of 150 T/m, the infidelity of a two-qubit gate using reasonable parameters could be reduced to below 10^{-3}*. Although this would allow a high-fidelity two-qubit gate to be realised, a more scalable demonstration could be performed on a microfabricated chip trap. Significant effort in our group is currently being put into developing methods to create the required high magnetic field gradients on microfabricated chip traps. A promising method is to apply large currents to current carrying structures buried below the electrode layers. This allows high gradients to be created at the position of the ion string. Several traps based on

*With parameters $\partial_z B = 150\,\mathrm{T/m}$, $\Omega_D/2\pi = 100\,\mathrm{kHz}$, $\nu_z/2\pi = 500\,\mathrm{kHz}$ and $\nu_r/2\pi = 3\,\mathrm{MHz}$, the predicted fidelity for a single loop gate on the stretch mode of two ions is 0.9992 using the coherence time and heating rate measured in this work, based on the error terms presented in chapter 6. Numerical simulations of the system by Itsik Cohen have however found additional infidelities for the gate which are thought to arise from higher order terms in the Magnus expansion of the full system Hamiltonian (see appendix C). The source of this additional error is currently under investigation and a method to suppress the effect is being developed. However, even with this error included, parameters can be found for which the infidelity is below 10^{-3}.

this design have been fabricated and initial tests have successfully passed up to 10 amps of current through the buried wires. Simulations of the magnetic field produced by the applied currents give magnetic field gradients up to 150 T/m. Current effort is therefore focussed on setting up experiments to test the new microfabricated traps in order to perform a high-fidelity two-qubit gate based on the scheme discussed in this work.

7.3 Scalability

To advance the work described in this thesis beyond proof-of-principle, a scalable quantum computer design should be developed. The design should meet all of the requirements described by DiVicenzo (shown in Sec. 1.1.1) and be scalable to arbitrarily many ions. This has been the focus of work carried out in our group and a 'blueprint' for a trapped ion quantum computer based on the static magnetic field gradient scheme has been developed in Ref. [48]. An outline of the architecture is presented in the following.

Trap structure

The design is based on the idea of Kieplinski in Ref. [23] where ions are loaded, manipulated, stored and detected in separate zones, and shuttled between zones. The design makes use of the surface code error correction scheme, for which the two-qubit gates are only required to be performed between nearest-neighbour ions and is well suited to a 2D layout of connected X-junctions. Due to electrical and fabrication constraints, the trapping structure cannot be arbitrarily large, and is therefore split into individual modules, each containing a 6×6 array of connected X-junctions, as shown in Fig. 7.1. Each module has a corresponding compact helical resonator beneath the chip for application of the trap RF voltage, as well as on-chip digital-to-analogue converters (DACs), which generate the required DC voltages, which are connected to the trap electrodes via buried wires. The X-junctions have an optimised electrode geometry for shuttling and separation following Ref. [90], as well as backside loading capabilities to reduce charge build up on the electrodes due to coating from the atomic ovens [91]. On-chip photodetectors in specific detection zones collect ion fluorescence for qubit readout, and a single laser beam can be passed back and fourth over detection zones in a module without interacting with ions in other zones. The modules are aligned together mechanically using xyz piezo stages, and simulations in Ref. [48] show that misalignments of up to 10 μm in each spatial

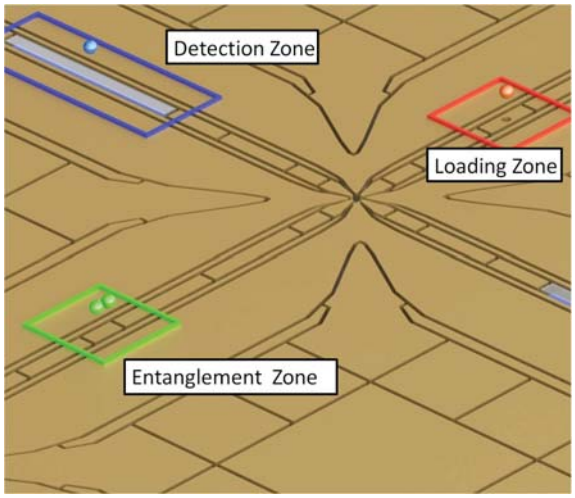


Fig. 7.1 Computer generated image of a single X-junction forming part of a 6×6 array in a module for the scalable architecture. Three zones are indicated in different arms of the junction, where different operations can be carried out as discussed in the text. Image taken from Ref. [48].

direction are acceptable. The $^{171}Yb^{+}$ ions used for storing and processing quantum information are sympathetically cooled by a different ion species in between gate and shuttling operations. A potential candidate ion species for efficient sympathetic cooling is Barium due to the similar masses, and co-trapping the two ion species is a current goal in our group.

Magnetic field

In designated entanglement zones, magnetic field gradients are applied using a copper current carrying wire structure buried beneath the electrode layer of the chips. The wire structure is designed so that only four current connections are required per module to supply the required current to all entanglement zones. Simulations show that magnetic field gradients of 150 T/m can be expected for 10 A applied, which has been successfully tested in prototype versions of the chip. In addition to the magnetic field gradients, local magnetic field offsets can be applied to each zone with extra current wires. The currents can be applied individually to each zone, controlled by on-chip DACs, which allows individual control of the magnetic field in each entanglement zone.

Coherent control

As mentioned, current wires allow individual control of the magnetic field in each entanglement zone. Since the energy of the $|-1\rangle$ and $|+1\rangle$ states in $^{171}Yb^{+}$ are linearly

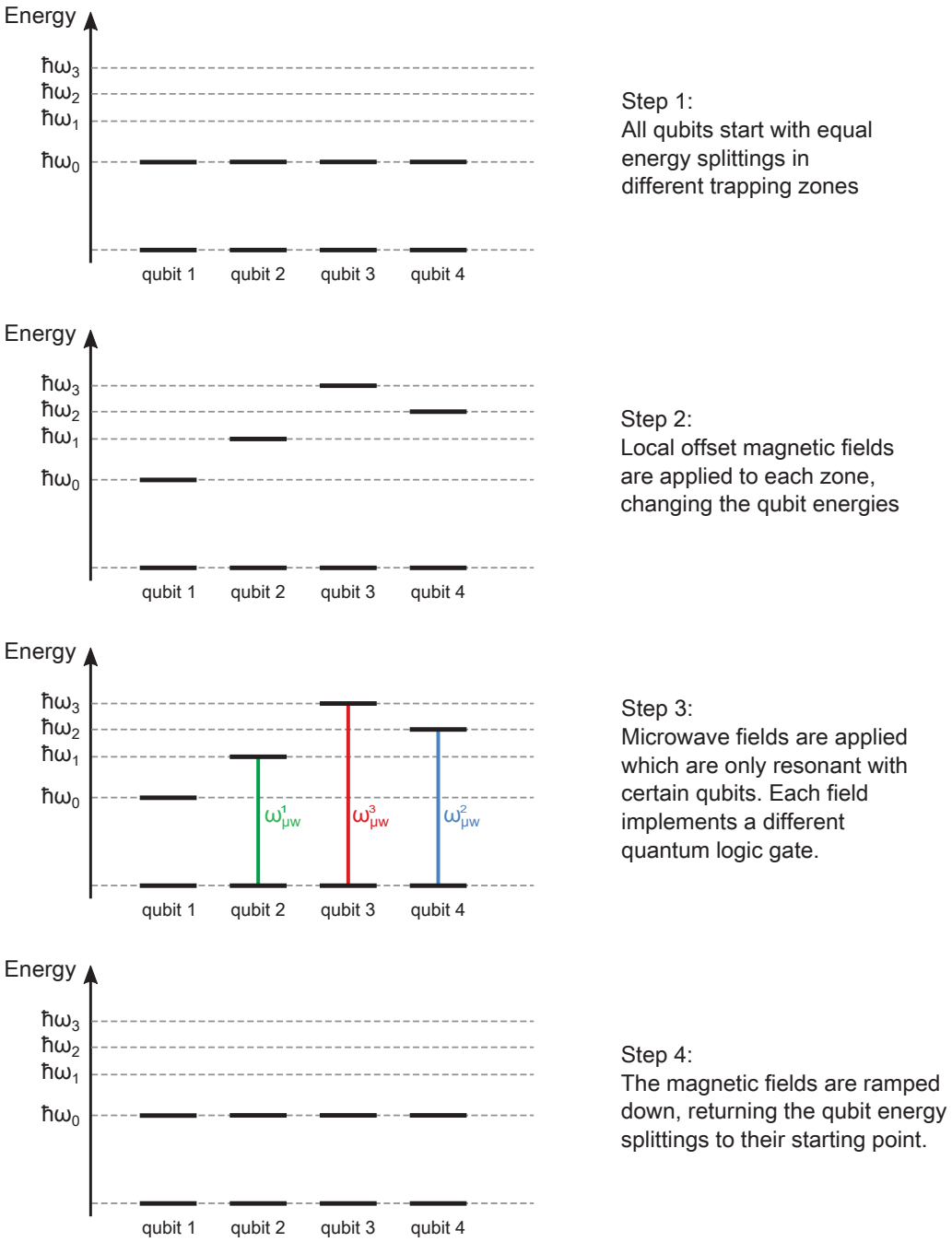


Fig. 7.2 Example experimental sequence to implement simultaneous single qubit gates for four qubits in the scalable architecture using local magnetic field control. In this simple case, the qubits are formed of one state that is independent of the magnetic field and one state that is linearly proportional, such as the $\{|0\rangle, |+1\rangle\}$ qubit in $^{171}Yb^{+}$.

dependent on the magnetic field, the transition frequencies of the ions in different zones can therefore be individually controlled. This allows coherent operations to be applied only to specific zones in the array using a single set of microwave and RF fields per operation, which can be applied globally using standard emitters. The simplest example can be seen if using a magnetic field sensitive qubit such as $\{|0\rangle, |+1\rangle\}$ and only performing single qubit operations. Initially, the magnetic field in all zones would be at a set value B_0, such that the resonant frequency of the qubits, ω_0, is far off-resonant with the frequency of a microwave field $\omega_{\mu\mathrm{w}}$. To implement a single qubit gate, firstly the magnetic field in the chosen zones is ramped up to a higher value, B_1, such that $\omega_1 = \omega_{\mu\mathrm{w}}$. Next the microwave field at frequency $\omega_{\mu\mathrm{w}}$ is applied for a time t_{pulse} and phase ϕ, both of which can be varied to implement a specific qubit rotation. After the interaction, the magnetic field is lowered back to B_0, completing the operation. The change in magnetic field will impart an additional phase on the qubit, however if the ramp profile is identical for every repetition, the phase shift can be measured and corrected by first performing the sequence with no microwave field applied. Additional operations could also be introduced on other qubits simultaneously by defining additional magnetic fields B_j for the jth operation, corresponding to qubit frequencies ω_j, which are resonant with different microwave fields at frequencies $\omega^j_{\mu\mathrm{w}} = \omega_j$. This is illustrated in Fig. 7.2. Multi-qubit gates can be performed in the same way, where the resonant frequencies of each ion pair will be separated by the gradient and therefore multiple sets of fields will be required for a single two-qubit gate operation, as discussed in chapter 6.

For the dressed-state qubit $\{|0'\rangle, |D\rangle\}$, the qubit energy splitting cannot be changed just by ramping the magnetic field in the same way as the $\{|0\rangle, |+1\rangle\}$ qubit, as the energy and populations making up $|D\rangle$ also depend on the detuning of the microwave dressing fields, as discussed in chapter 4. One possibility would be to vary the detuning of the dressing fields so that they follow the resonant frequency of the $|0\rangle \leftrightarrow |\pm 1\rangle$ transitions as the magnetic field is changed, however this would be hard to achieve to an accuracy that would be required for high-fidelity operations. A more appealing method is to map the qubit from the clock qubit $\{|0\rangle, |0'\rangle\}$ to the dressed-state qubit after the magnetic field has been ramped from B_0 to B_j, and back to the clock qubit before the magnetic field is ramped down again. This way the clock qubit acts as a memory qubit, while the dressed-state qubit is used for single- and two-qubit quantum logic operations, as shown in Fig. 7.3. There are various ways such a mapping could be achieved. One way is to first apply a π-pulse to transfer population from $|0\rangle \rightarrow |+1\rangle$, followed by a half STIRAP sequence, as discussed in Sec. 4.3.2. This then maps $|+1\rangle \rightarrow |D\rangle$. After the dressed-state manipulation is

complete, the second half of the STIRAP maps $|D\rangle \rightarrow |-1\rangle$, followed by a second π-pulse to map $|-1\rangle \rightarrow |0\rangle$. Another possible method was discussed in Sec. 4.3.2, in which the dressing field detunings are varied in equal and opposite directions to map $|0\rangle \leftrightarrow |D\rangle$ directly. This method has the advantages of a direct mapping and reduced sensitivity to magnetic field noise, but has yet to be investigated experimentally. Additionally, by comparing the two cases in Fig. 7.3 with the dressing field detuning variations required for the direct mapping between the two qubits, it can be seen that by ramping the magnetic field adiabatically, the dressing field detunings will change in equal and opposite directions, and will therefore map between the two qubits automatically. This gives a strong advantage to the direct mapping method for the scalable architecture, and would be an interesting experiment to carry out in the near future.

When performing shuttling operations, the ions will experience a large variation in magnetic field due to the magnetic field gradient. If one or more of the qubit states is sensitive to magnetic fields, the qubit will acquire a phase due to the varying magnetic field, which could be detrimental if the phase is unknown. To minimise the phase acquired, it would be useful to use the $\{|0\rangle, |0'\rangle\}$ clock qubit, as it has only a small sensitivity to the magnetic field from the second order Zeeman shift. This should not add any additional overhead as the mapping is also required for locally controlled gates when using dressed-state qubits, as discussed in the previous paragraph. As long as the ion trajectory is identical for each shuttling operation, the phase acquired from shuttling due to the second order Zeeman shift can be measured using a Ramsey experiment, and therefore corrected.

It has therefore been shown that the dressed-state two-qubit gate scheme demonstrated in this work is compatible with a realistic architecture for a large scale trapped ion quantum computer based on long-wavelength radiation. Importantly, the scheme removes the correlation between the number of fields applied and the number of qubits, which are instead tuned into resonance with global fields using local magnetic field shifts. Further work in the group is aiming to build a 'demonstrator device' based on the blueprint, where all of the basic operations can be performed in a single experiment that has a modular design and could therefore easily be scaled to a large number of ions. This work will be an exciting further step towards the realisation of a large scale quantum computer.

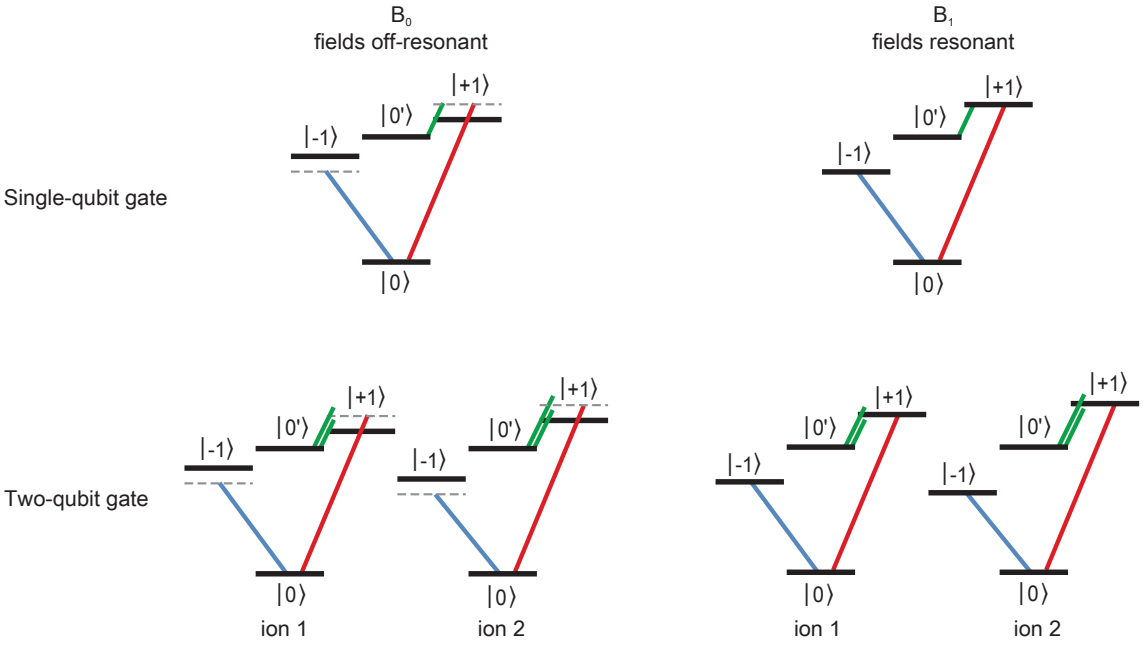


Fig. 7.3 Diagrams showing how single-qubit (top) and two-qubit (bottom) gates can be implemented with dressed-state qubits when the magnetic field offset is locally controlled in each trapping zone. The left diagrams show the case where the magnetic field offset is at the lower value B_0, in which case the microwave dressing fields and RF gate fields are off-resonant. Note that the ions are still in a magnetic field gradient, and therefore the resonant frequencies in the two ion case are separated. For the right diagrams, the magnetic field offset has been increased to B_1, where all fields are now resonant. The magnetic field cannot trivially be ramped between the two cases with the dressing fields on continuously, as this would affect the energy and populations making up $|D\rangle$. However, in the particular case shown where the dressing field frequencies are initially set off-resonant, the change in detunings of the dressing fields as the magnetic field is ramped would automatically map the clock qubit to the dressed-state qubit.

References

[1] G.E. Moore. Cramming more components onto integrated circuits. *Proceedings of the IEEE*, 86(1):82–85, Jan 1998.

[2] G.E. Moore. Progress in digital integrated electronics. In *Electron Devices Meeting, 1975 International*, volume 21, pages 11–13, 1975.

[3] Jack Dongarra. Performance of various computers using standard linear equations software. Computer Science Technical Report Number CS - 89 – 85, 2015.

[4] R. P. Feynman. Simulating physics with computers. *International Journal of Theoretical Physics*, 21:467–488, 1982.

[5] D. Deutsch. Quantum theory, the church-turing principle and the universal quantum computer. *Proc. R. Soc. Lond. A*, 400:97–117, 1985.

[6] P. W. Shor. Algorithms for quantum computation: discrete logarithms and factoring. In *Proceedings of the 35th Annual Symposium on Foundations of Computer Science*, SFCS '94, pages 124–134. IEEE Computer Society, 1994.

[7] Lov K. Grover. A fast quantum mechanical algorithm for database search. In *STOC '96 Proceedings of the twenty-eighth annual ACM symposium on Theory of computing*, pages 212–219, 1996.

[8] P. W. Shor. Fault-tolerant quantum computation. *Proc. 37th Annual Symposium on Foundations of Computer Science, IEEE Computer Society Press*, pages 56–65, 1996.

[9] A. M. Steane. Error correcting codes in quantum theory. *Phys. Rev. Lett.*, 77:793–797, Jul 1996.

[10] E. Knill. Quantum computing with realistically noisy devices. *Nature*, 434:39–44, 2005.

[11] Austin G. Fowler, Ashley M. Stephens, and Peter Groszkowski. High-threshold universal quantum computation on the surface code. *Phys. Rev. A*, 80:052312, Nov 2009.

[12] Naomi H. Nickerson, Ying Li, and Simon C. Benjamin. Topological quantum computing with a very noisy network and local error rates approaching one percent. *Nat Commun*, 4, 2013.

[13] David P. DiVincenzo. The physical implementation of quantum computation. *Fortschritte der Physik*, 48(9-11):771–783, 2000.

[14] Gavin K. Brennen, Carlton M. Caves, Poul S. Jessen, and Ivan H. Deutsch. Quantum logic gates in optical lattices. *Phys. Rev. Lett.*, 82:1060–1063, Feb 1999.

[15] J. I. Cirac and P. Zoller. Quantum computations with cold trapped ions. *Phys. Rev. Lett.*, 74:4091–4094, May 1995.

[16] E. Knill, R. Laflamme, and G. J. Milburm. A scheme for efficient quantum computation with linear optics. *Nature*, 409:46–52, 2000.

[17] J. Clarke and F. K. Wilhelm. Superconducting quantum bits. *Nature*, 453:1031–1042, 2008.

[18] Daniel Loss and David P. DiVincenzo. Quantum computation with quantum dots. *Phys. Rev. A*, 57:120–126, Jan 1998.

[19] T. D. Ladd, F. Jelezko, R. Laflamme, Y. Nakamura, C. Monroe, and J. L. O'Brien. Quantum computers. *Nature*, 464:45–53, 2010.

[20] D. J. Wineland, R. E. Drullinger, and F. L. Walls. Radiation-pressure cooling of bound resonant absorbers. *Phys. Rev. Lett.*, 40, 1978.

[21] W. Neuhauser, M. Hohenstatt, P. E. Toschek, and H. Dehmelt. Localized visible ba^+ mono-ion oscillator. *Phys. Rev. A*, 22:1137–1140, Sep 1980.

[22] M. G. Raizen, J. M. Gilligan, J. C. Bergquist, W. M. Itano, and D. J. Wineland. Ionic crystals in a linear paul trap. *Phys. Rev. A*, 45:6493–6501, May 1992.

[23] D. Kielpinski, C.R. Monroe, and D.J. Wineland. Architecture for a large-scale ion-trap quantum computer. *Nature*, 417:709–711, 2002.

[24] D. Hucul, I. V. Inlek, G. Vittorini, C. Crocker, S. Debnath, S. M. Clark, and C. Monroe. Modular entanglement of atomic qubits using photons and phonons. *Nat. Phys.*, 11:37–42, 2015.

[25] J. C. Bergquist, Randall G. Hulet, Wayne M. Itano, and D. J. Wineland. Observation of quantum jumps in a single atom. *Phys. Rev. Lett.*, 57:1699–1702, Oct 1986.

[26] F. Diedrich, J. C. Bergquist, Wayne M. Itano, and D. J. Wineland. Laser cooling to the zero-point energy of motion. *Phys. Rev. Lett.*, 62:403–406, Jan 1989.

[27] C. Monroe, D. M. Meekhof, B. E. King, W. M. Itano, and D. J. Wineland. Demonstration of a fundamental quantum logic gate. *Phys. Rev. Lett.*, 75:4714–4717, Dec 1995.

[28] Q. A. Turchette, C. S. Wood, B. E. King, C. J. Myatt, D. Leibfried, W. M. Itano, C. Monroe, and D. J. Wineland. Deterministic entanglement of two trapped ions. *Phys. Rev. Lett.*, 81:3631–3634, Oct 1998.

[29] Anders Sørensen and Klaus Mølmer. Quantum computation with ions in thermal motion. *Phys. Rev. Lett.*, 82:1971–1974, Mar 1999.

[30] Klaus Mølmer and Anders Sørensen. Multiparticle entanglement of hot trapped ions. *Phys. Rev. Lett.*, 82:1835–1838, Mar 1999.

[31] Anders Sørensen and Klaus Mølmer. Entanglement and quantum computation with ions in thermal motion. *Phys. Rev. A*, 62:022311, Jul 2000.

[32] S. Schneider G. J. Milburn and D. F. V. James. Ion trap quantum computing with warm ions. *Fortschr. Phys.*, 48:801–810, 2000.

[33] C. A. Sacket, D. Kielpinski, B. E. King, C. Langer, V. Meyer, C. J. Myatt, M. Rowe, Q. A. Turchette, W. M. Itano, D. J. Wineland, and C. Monroe. Experimental entanglement of four particles. *Nature*, 404:256–259, 2000.

[34] D. Leibfried, B. DeMarco, V. Meyer, D. Lucas, M. Barrett, J. Britton, W. M. Itano, B. Jelenkovic, C. Langer, T. Rosenband, and D. J. Wineland. Experimental demonstration of a robust, high-fidelity geometric two ion-qubit phase gate. *Nature*, 422:412–415, 2003.

[35] W. K. Hensinger, S. Olmschenk, D. Stick, D. Hucul, M. Yeo, M. Acton, L. Deslauriers, C. Monroe, and J. Rabchuk. T-junction ion trap array for two-dimensional ion shuttling, storage, and manipulation. *Appl. Phys. Lett.*, 88, 2006.

[36] R. B. Blakestad, C. Ospelkaus, A. P. VanDevender, J. M. Amini, J. Britton, D. Leibfried, and D. J. Wineland. High-fidelity transport of trapped-ion qubits through an **X**-junction trap array. *Phys. Rev. Lett.*, 102:153002, Apr 2009.

[37] R. Bowler, J. Gaebler, Y. Lin, T. R. Tan, D. Hanneke, J. D. Jost, J. P. Home, D. Leibfried, and D. J. Wineland. Coherent diabatic ion transport and separation in a multizone trap array. *Phys. Rev. Lett.*, 109:080502, Aug 2012.

[38] A. Walther, F. Ziesel, T. Ruster, S. T. Dawkins, K. Ott, M. Hettrich, K. Singer, F. Schmidt-Kaler, and U. Poschinger. Controlling fast transport of cold trapped ions. *Phys. Rev. Lett.*, 109:080501, Aug 2012.

[39] T. P. Harty, D. T. C. Allcock, C. J. Ballance, L. Guidoni, H. A. Janacek, N. M. Linke, D. N. Stacey, and D. M. Lucas. High-fidelity preparation, gates, memory, and readout of a trapped-ion quantum bit. *Phys. Rev. Lett.*, 113:220501, Nov 2014.

[40] C. J. Ballance, T. P. Harty, N. M. Linke, and D. M. Lucas. High-fidelity two-qubit quantum logic gates using trapped calcium-43 ions. *arXiv:1406.5473 [quant-ph]*, 2014.

[41] Nitzan Akerman, Nir Navon, Shlomi Kotler, Yinnon Glickman, and Roee Ozeri. Universal gate-set for trapped-ion qubits using a narrow linewidth diode laser. *arXiv*, 1505.02503 [quant-ph].

[42] Florian Mintert and Christof Wunderlich. Ion-trap quantum logic using long-wavelength radiation. *Phys. Rev. Lett.*, 87(25):257904, Nov 2001.

[43] M. Johanning, A. Braun, N. Timoney, V. Elman, W. Neuhauser, and Chr. Wunderlich. Individual addressing of trapped ions and coupling of motional and spin states using rf radiation. *Phys. Rev. Lett.*, 102:073004, Feb 2009.

[44] A. Khromova, Ch. Piltz, B. Scharfenberger, T. F. Gloger, M. Johanning, A. F. Varón, and Ch. Wunderlich. Designer spin pseudomolecule implemented with trapped ions in a magnetic gradient. *Phys. Rev. Lett.*, 108:220502, Jun 2012.

[45] C. Ospelkaus, C. E. Langer, J. M. Amini, K. R. Brown, D. Leibfried, and D. J. Wineland. Trapped-ion quantum logic gates based on oscillating magnetic fields. *Phys. Rev. Lett.*, 101(9):090502, Aug 2008.

[46] C. Ospelkaus, U. Warring, Y. Colombe, K. R. Brown, J. M. Amini, D. Leibfried, and D. J. Wineland. Microwave quantum logic gates for trapped ions. *Nature*, 476(7359):181–184, 2011.

[47] N. Timoney, I. Baumgart, M. Johanning, A. F. Varon, M. B. Plenio, A. Retzker, and Ch. Wunderlich. Quantum gates and memory using microwave-dressed states. *Nature*, 476:185–188, 2011.

[48] B. Lekitsch, S. Weidt, A. G. Fowler, K. Mølmer, S. J. Devitt, Ch. Wunderlich, and W. K. Hensinger. Blueprint for a microwave ion trap quantum computer. *arXiv:1508.00420*, 2015.

[49] Charles Donald. Development of an ion trap quantum information processor. *Ph.D. thesis, University of Oxford*, 2000.

[50] H. G. Dehmelt. Radiofrequency spectroscopy of stored ions. *Adv. At. Mol. Phys.*, 3:53, 1967.

[51] R. F. Wuerker, H. Shelton, and R. V. Langmuir. Electrodynamic containment of charged particles. *Journal of Applied Physics*, 30(3), 1959.

[52] D.F.V. James. Quantum dynamics of cold trapped ions with application to quantum computation. *Applied Physics B*, 66(2):181–190, 1998.

[53] G. Breit and I. I. Rabi. Measurement of nuclear spin. *Phys. Rev.*, 38:2082–2083, Dec 1931.

[54] R. Sterling. Ytterbium ion trapping and microfabrication of ion trap arrays. *Ph.D. thesis, University of Sussex*, 2011.

[55] A. Nizamani. Yb^+ ion trapping and optimum planar trap geometries for scalable quantum technology. *Ph.D. thesis, University of Sussex*, 2011.

[56] S. Weidt. Towards microwave based ion trap quantum technology. *Ph.D. thesis, University of Sussex*, 2013.

[57] J. Randall. Quantum logic in trapped ions using microwaves and dressed states. *MRes project report, Imperial College London*, 2012.

[58] J. McLoughlin. Development and implementation of an Yb^+ ion trap experiment towards coherent manipulation and entanglement. *Ph.D. thesis, University of Sussex*, 2011.

[59] K. Lake. Towards high fidelity entanglement with dressed state qubits. *Ph.D. thesis, University of Sussex*, 2014.

[60] J. Siverns. Yb ion trap experimental set-up and two-dimensional ion trap surface array design towards analogue quantum simulations. *Ph.D. thesis, University of Sussex*, 2011.

[61] D. Murgia. A scalable approach to quantum logic operations. *MRes thesis, Imperial College London*, 2014.

[62] Rachel Noek, Geert Vrijsen, Daniel Gaultney, Emily Mount, Taehyun Kim, Peter Maunz, and Jungsang Kim. High speed, high fidelity detection of an atomic hyperfine qubit. *Opt. Lett.*, 38(22):4735–4738, Nov 2013.

[63] Roee Ozeri. The trapped-ion qubit tool box. *Contemporary Physics*, 52(6):531–550, 2011.

[64] P. Carruthers and M. M. Nieto. Coherent states and the forced quantum oscillator. *American Journal of Physics*, 33(7), 1965.

[65] C. Piltz, T. Sriarunothai, A. F. Varón, and C. Wunderlich. A trapped-ion-based quantum byte with 10^{-5} next-neighbour cross-talk. *Nat. Commun*, 5:4679, 2014.

[66] Ch. Piltz, B. Scharfenberger, A. Khromova, A. F. Varón, and Ch. Wunderlich. Protecting conditional quantum gates by robust dynamical decoupling. *Phys. Rev. Lett.*, 110:200501, May 2013.

[67] I. Cohen and A. Retzker. Proposal for verification of the haldane phase using trapped ions. *Phys. Rev. Lett.*, 112:040503, Jan 2014.

[68] Alejandro Bermudez, Tobias Schaetz, and Diego Porras. Photon-assisted-tunneling toolbox for quantum simulations in ion traps. *New Journal of Physics*, 14:053049, 2012.

[69] T. R. Tan, J. P. Gaebler, R. Bowler, Y. Lin, J. D. Jost, D. Leibfried, and D. J. Wineland. Demonstration of a dressed-state phase gate for trapped ions. *Phys. Rev. Lett.*, 110:263002, Jun 2013.

[70] Nir Navon, Shlomi Kotler, Nitzan Akerman, Yinnon Glickman, Ido Almog, and Roee Ozeri. Addressing two-level systems variably coupled to an oscillating field. *Phys. Rev. Lett.*, 111:073001, Aug 2013.

[71] S. C. Webster, S. Weidt, K. Lake, J. J. McLoughlin, and W. K. Hensinger. Simple manipulation of a microwave dressed-state ion qubit. *Phys. Rev. Lett.*, 111:140501, Oct 2013.

[72] M. P. Fewell, B. W. Shore, and K. Bergmann. Coherent population transfer among three states: Full algebraic solutions and the relevance of non adiabatic proceses to transfer by delayed pulses. *Aust. J. Phys.*, 50:281–308, 1997.

[73] Ch. Roos, Th. Zeiger, H. Rohde, H. C. Nägerl, J. Eschner, D. Leibfried, F. Schmidt-Kaler, and R. Blatt. Quantum state engineering on an optical transition and decoherence in a paul trap. *Phys. Rev. Lett.*, 83:4713–4716, Dec 1999.

[74] C. Monroe, D. M. Meekhof, B. E. King, S. R. Jefferts, W. M. Itano, D. J. Wineland, and P. Gould. Resolved-sideband raman cooling of a bound atom to the 3D zero-point energy. *Phys. Rev. Lett.*, 75:4011–4014, 1995.

[75] H. Metcalf and P. Van Der Straten. Laser cooling and trapping. *Springer*, ISBN 9780387987268, 1999.

[76] R. Loudon. The quantum theory of light. *Oxford University Press*, 2000.

[77] Marcus D. Hughes, Bjoern Lekitsch, Jiddu A. Broersma, and Winfried K. Hensinger. Microfabricated ion traps. *Contemporary Physics*, 52(6):505–529, 2011.

[78] N Daniilidis, S Narayanan, SA Möller, R Clark, TE Lee, PJ Leek, A Wallraff, St Schulz, F Schmidt-Kaler, and H Häffner. Fabrication and heating rate study of microscopic surface electrode ion traps. *New Journal of Physics*, 13(1):013032, 2011.

[79] Jan Benhelm, Gerhard Kirchmair, Christian F. Roos, and Rainer Blatt. Towards fault-tolerant quantum computing with trapped ions. *Nat. Phys*, 4:463–466, 2008.

[80] K. Kim, M.-S. Chang, R. Islam, S. Korenblit, L.-M. Duan, and C. Monroe. Entanglement and tunable spin-spin couplings between trapped ions using multiple transverse modes. *Phys. Rev. Lett.*, 103:120502, Sep 2009.

[81] P. Jurcevic, B. P. Lanyon, P. Hauke, C. Hempel, P. Zoller, R. Blatt, and C. F Roos. Quasiparticle engineering and entanglement propagation in a quantum many-body system. *Nature*, 511:202–205, July 2014.

[82] Marcus D. Hughes, Bjoern Lekitsch, Jiddu A. Broersma, and Winfried K. Hensinger. Microfabricated ion traps. *Contemporary Physics*, 52(6):505–529, 2011.

[83] B. E. King, C .S. Wood, C .J. Myatt, Q. A. Turchette, D. Leibfried, W. M. Itano, C. Monroe, and D. J. Wineland. Cooling the collective motion of trapped ions to initialize a quantum register. *Phys. Rev. Lett.*, 81:1525–1528, 1998.

[84] K M Fonseca Romero and R Lo Franco. Simple non-markovian microscopic models for the depolarizing channel of a single qubit. *Physica Scripta*, 86(6):065004, 2012.

[85] C. F. Roos, T. Monz, K. Kim, M. Riebe, H. Häffner, D. F. V. James, and R. Blatt. Nonlinear coupling of continuous variables at the single quantum level. *Phys. Rev. A*, 77:040302, Apr 2008.

[86] X. Rebecca Nie, Christian F. Roos, and Daniel F.V. James. Theory of cross phase modulation for the vibrational modes of trapped ions. *Physics Letters A*, 373(4):422 – 425, 2009.

[87] C. J. Ballance. High-fidelity quantum logic in ca^{+}. *Ph.D. thesis, University of Oxford*, 2014.

[88] Gatis Mikelsons, Itsik Cohen, Alex Retzker, and Martin B Plenio. Universal set of gates for microwave dressed-state quantum computing. *New Journal of Physics*, 17(5):053032, 2015.

[89] A. Retzker M. B. Plenio Ch. Wunderlich I. Baumgart, J.-M. Cai. Ultrasensitive magnetometer using a single atom. *arXiv:1411.7893 [quant-ph]*, 2014.

[90] A.H. Nizamani and W.K. Hensinger. Optimum electrode configurations for fast ion separation in microfabricated surface ion traps. *Applied Physics B*, 106(2):327–338, 2012.

[91] J M Amini, H Uys, J H Wesenberg, S Seidelin, J Britton, J J Bollinger, D Leibfried, C Ospelkaus, A P VanDevender, and D J Wineland. Toward scalable ion traps for quantum information processing. *New Journal of Physics*, 12(3):033031, 2010.

[92] S Blanes, F Casas, J A Oteo, and J Ros. A pedagogical approach to the magnus expansion. *European Journal of Physics*, 31(4):907, 2010.

Appendix A

Pure dephasing of a driven two-level atom

In this appendix, the dynamics of a resonantly driven two-level atom undergoing pure dephasing is derived. Here pure dephasing means that the off-diagonal elements of the density matrix decay exponentially at a fixed rate, which is a useful approximation for some data analysis such as fitting a decaying Rabi oscillation. However, such an approximation cannot be used in calculations such as in the case of dressed states, where the decoupling takes advantage of the spectrum of noise in the lab, which is not taken into account in this simple model. Defining the two atomic states as $|0\rangle = (0,1)^T$ and $|1\rangle = (1,0)^T$, the density matrix at time t is

$$\rho(t) = \begin{pmatrix} \rho_{00}(t) & \rho_{01}(t) \\ \rho_{10}(t) & \rho_{11}(t) \end{pmatrix}. \tag{A.1}$$

The time evolution of the density matrix is described by a Lindblad master equation of the form

$$\dot{\rho}(t) = \frac{i}{\hbar}[H, \rho(t)] + C\rho(t)C^\dagger - \frac{1}{2}C^\dagger C\rho(t) - \frac{1}{2}\rho(t)C^\dagger C, \tag{A.2}$$

where the relaxation operators for pure dephasing are

$$C = C^\dagger = \sqrt{\frac{\Gamma}{2}}\sigma_z. \tag{A.3}$$

Here Γ is the dephasing rate, which is related to the dephasing time (or coherence time), τ, as $\tau = 1/\Gamma$. For a resonant driving field with Rabi frequency Ω_0 and setting the phase to zero, the Hamiltonian is $H = \hbar\Omega_0\sigma_x/2$, and the commutator term in

Eq. A.2 is therefore

$$-\frac{i}{\hbar}[H,\rho(t)] = -\frac{i\Omega_0}{2}\begin{pmatrix} \rho_{10}(t)-\rho_{01}(t) & \rho_{11}(t)-\rho_{00}(t) \\ \rho_{00}(t)-\rho_{11}(t) & \rho_{01}(t)-\rho_{00}(t) \end{pmatrix}. \tag{A.4}$$

Together with the relaxation terms and using the fact that $\rho_{00}(t)+\rho_{11}(t)=1$ and $\rho_{01}(t)=\rho_{10}^*(t)$, we arrive at the optical Bloch equations

$$\begin{aligned} \dot{\rho}_{00}(t) &= -\dot{\rho}_{11}(t) = -\frac{i\Omega_0}{2}\Big(\rho_{10}(t)-\rho_{01}(t)\Big) \\ \dot{\rho}_{01}(t) &= \dot{\rho}_{10}^*(t) = -\frac{i\Omega_0}{2}\Big(\rho_{11}(t)-\rho_{00}(t)\Big) - \Gamma\rho_{01}(t). \end{aligned} \tag{A.5}$$

To solve these equations, we can use trial solution of the form

$$\rho_{ij}(t) = \rho_{ij}(0)e^{\lambda t}, \tag{A.6}$$

which leads to four simultaneous equations that can be written in matrix form as

$$\begin{pmatrix} -\lambda & 0 & i\Omega_0/2 & -i\Omega_0/2 \\ 0 & -\lambda & -i\Omega_0/2 & i\Omega_0/2 \\ i\Omega_0/2 & -i\Omega_0/2 & -\lambda-\Gamma & 0 \\ -i\Omega_0/2 & i\Omega_0/2 & 0 & -\lambda-\Gamma \end{pmatrix} \cdot \begin{pmatrix} \rho_{00}(0) \\ \rho_{11}(0) \\ \rho_{01}(0) \\ \rho_{10}(0) \end{pmatrix} = 0. \tag{A.7}$$

The eigenvalues of this matrix are

$$\begin{aligned} \lambda_1 &= 0 \\ \lambda_2 &= -\Gamma \\ \lambda_3 &= -\frac{1}{2}(\Gamma + i\Omega_\Gamma) \\ \lambda_4 &= -\frac{1}{2}(\Gamma - i\Omega_\Gamma), \end{aligned} \tag{A.8}$$

where we have defined $\Omega_\Gamma = \sqrt{4\Omega_0^2-\Gamma^2}$. The general solutions to Eqs. A.5 are then

$$\rho_{ij}(t) = k_{ij}^{(1)} + k_{ij}^{(2)}e^{-\Gamma t} + k_{ij}^{(3)}e^{-(\Gamma+i\Omega_\Gamma)t/2} + k_{ij}^{(4)}e^{-(\Gamma-i\Omega_\Gamma)t/2}, \tag{A.9}$$

where $k_{ij}^{(s)}$ are constants to be found from initial conditions. An interesting case is when all of the population is initialised in the state $|0\rangle$, giving the initial conditions $\rho_{00}(0)=1$, $\rho_{01}(0)=\rho_{10}(0)=\rho_{11}(0)=0$. For each $\rho_{ij}(t)$ there are four unknown constants $k_{ij}^{(s)}$, and we therefore need four initial conditions for each. The remaining

three initial conditions for each $\rho_{ij}(t)$ can be found by inserting the known initial conditions into Eqs. A.5 to find the initial first, second and third order derivatives, giving

$$\begin{aligned}
\dot{\rho}_{00}(0) &= -\dot{\rho}_{11}(0) = 0, \\
\dot{\rho}_{01}(0) &= \dot{\rho}^*_{10}(0) = i\Omega_0/2, \\
\ddot{\rho}_{00}(0) &= -\ddot{\rho}_{11}(0) = -\Omega_0^2/2, \\
\ddot{\rho}_{01}(0) &= \ddot{\rho}^*_{10}(0) = -i\Omega_0\Gamma/2, \\
\dddot{\rho}_{00}(0) &= -\dddot{\rho}_{11}(0) = \Omega_0^2\Gamma/2, \\
\dddot{\rho}_{01}(0) &= \dddot{\rho}^*_{10}(0) = -i\Omega_0(\Omega_0^2 - \Gamma^2)/2.
\end{aligned} \tag{A.10}$$

By differentiating Eq. A.9 and using Eqs. A.10, we can find four simultaneous equations for each $\rho_{ij}(0)$, which can be solved for each $k_{ij}^{(s)}$ and subsequently substituted back into Eq. A.9. The population in state $|1\rangle$ is then found to be

$$P_1(t) = \rho_{11}(t) = \frac{1}{2}\left[1 - e^{-\Gamma t/2}\left(\cos(\Omega_\Gamma t/2) + \frac{\Gamma}{\Omega_\Gamma}\sin(\Omega_\Gamma t/2)\right)\right], \tag{A.11}$$

while the off-diagonal density matrix elements evolve as

$$\rho_{01}(t) = \rho^*_{10}(t) = -\frac{\Omega_0}{2\Omega_\Gamma}\left(1 - e^{i\Omega_\Gamma t}\right)e^{-(\Gamma + i\Omega_\Gamma)t/2}, \tag{A.12}$$

where $\Omega_\Gamma = \sqrt{4\Omega_0^2 - \Gamma^2}$. Eqs. A.11 and A.12 are plotted in Fig. A.1 for a range of ratios Γ/Ω_0.

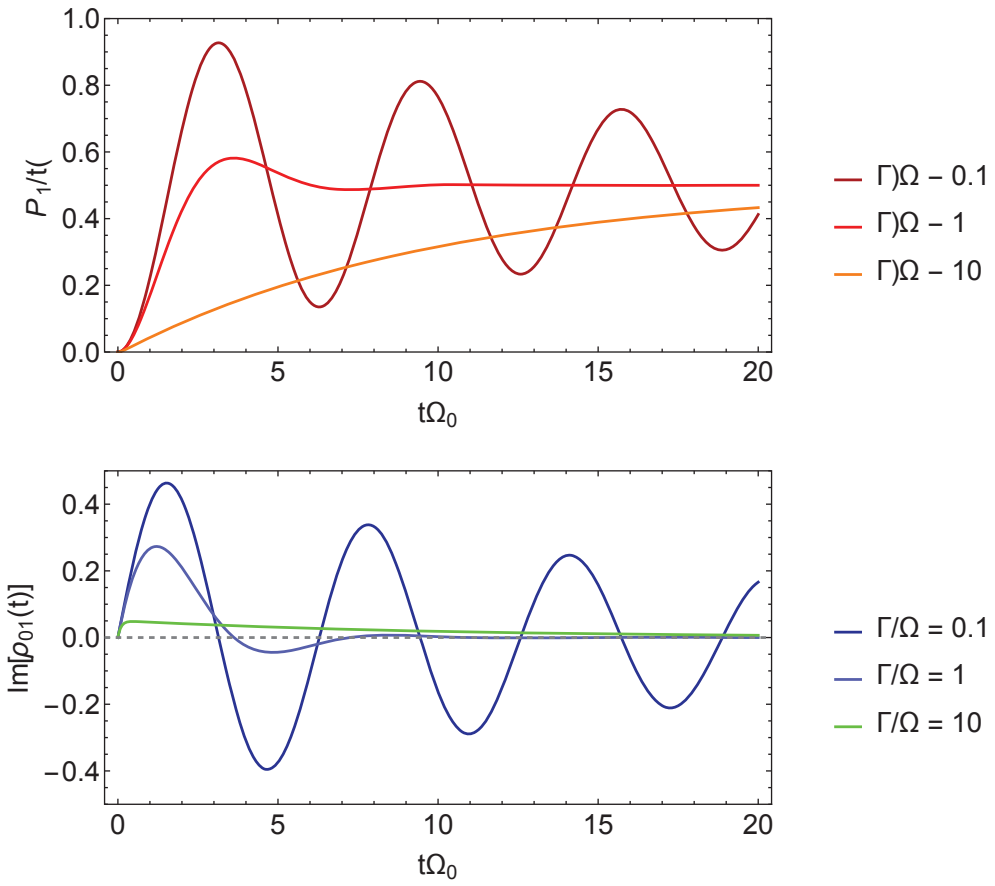


Fig. A.1 Top: Population in $|1\rangle$ as a function of time (scaled to Ω_0) resulting from Eq. A.11 for three values of Γ/Ω_0. Bottom: The imaginary part of the off-diagonal density matrix element $\rho_{01}(t)$ for the same parameters ($Re[\rho_{01}(t)] = 0$) resulting from Eq. A.12, showing the time evolution of the coherences.

Appendix B

Normalising detection errors

This appendix describes the procedure to normalise out detection errors from measured data, and how to calculate the associated error in the estimated probability. In the ideal case, ions' spin states could be discriminated perfectly by setting a threshold for the number of photons detected. In practice however, the photon histograms corresponding to the different spin states might have some overlap. The overlap is due to a mixture of effects including experimental issues such as background scatter, atomic effects such as off-resonant coupling, as well as the statistical nature of the Poissonian photon distributions as discussed in Sec. 2.5.2. In particular, when detecting ions using a PMT, only the total photon count can be recorded, and the histograms for one and two (or more) ions often have a significant overlap. Advanced algorithms for quantum computing such as error correction require that the detection error is within the fault-tolerant regime. However for operations such as sequences of one- and two-qubit gates or quantum simulations, detection is the final step in the pulse sequence and therefore the single-shot detection error does not need to be in the fault-tolerant regime as long as the experiment can be repeated multiple times. If the errors are known, a linear map can be found that, for multiple repetitions of an experiment, allows the state probabilities to be calculated from the measurements. In the following, the procedure to calculate this linear map for one and two ions will be described.

B.1 Single ion

Consider a two-level ion with states $|\downarrow\rangle$ and $|\uparrow\rangle$. A fluorescence detection measurement gives n photons, and for a threshold t_1, if $n \leq t_1$, the measurement result is 0, whereas if $n > t_1$, the measurement result is 1. If the detection was perfect, a measurement

result of 0 would correspond to the ion being in the state $|\downarrow\rangle$, while a measurement result of 1 would correspond to the ion being in the state $|\uparrow\rangle$. To find the detection errors, we assume we can prepare the states $|\downarrow\rangle$ and $|\uparrow\rangle$ perfectly, and measure the number of photons collected after preparing each state for N repetitions. After thresholding the results, the detection errors are given by the conditional probabilities $P(0|\uparrow)$ and $P(1|\downarrow)$, where $P(a|b)$ is defined the probability of measuring a, given that b occured. The relationship between the measurement and state probabilities is therefore given by

$$\begin{aligned}\begin{pmatrix} P(1) \\ P(0) \end{pmatrix} &= \begin{pmatrix} P(1|\uparrow) & P(1|\downarrow) \\ P(0|\uparrow) & P(0|\downarrow) \end{pmatrix} \begin{pmatrix} P(\uparrow) \\ P(\downarrow) \end{pmatrix} \\ &= \mathbf{M_2} \begin{pmatrix} P(\uparrow) \\ P(\downarrow) \end{pmatrix},\end{aligned} \tag{B.1}$$

where it can be seen that $P(0|\uparrow) = 1 - P(1|\uparrow)$ and $P(1|\downarrow) = 1 - P(0|\downarrow)$. The error matrix can then be inverted to allow the state probabilities to be calculated from the measurements as

$$\begin{pmatrix} P(\uparrow) \\ P(\downarrow) \end{pmatrix} = \mathbf{M_2^{-1}} \begin{pmatrix} P(1) \\ P(0) \end{pmatrix}. \tag{B.2}$$

B.2 Two ions

For two ions, there are four possible spin states $|\downarrow\downarrow\rangle$, $|\downarrow\uparrow\rangle$, $|\uparrow\downarrow\rangle$ and $|\uparrow\uparrow\rangle$. For PMT detection, there are only three possible measurements corresponding to zero, one or two ions fluorescing. In this case two thresholds t_1 and t_2 are set, and for a measurement giving n photons, $n \leq t_1$ gives 0, $t_1 < n \leq t_2$ gives 1 and $n > t_2$ gives 2. The individual addressability of the ions provided by the magnetic field gradient allows all four spin states to be prepared, and consequently all six detection errors to be found. The linear map is then

$$\begin{pmatrix} P(2) \\ P(1) \\ P(0) \end{pmatrix} = \mathbf{M_3} \begin{pmatrix} P(\uparrow\uparrow) \\ P(\uparrow\downarrow) + P(\downarrow\uparrow) \\ P(\downarrow\downarrow) \end{pmatrix}, \tag{B.3}$$

where

$$\mathbf{M_3} = \begin{pmatrix} P(2|\uparrow\uparrow) & P(2|\uparrow\downarrow) & P(2|\downarrow\downarrow) \\ P(1|\uparrow\uparrow) & P(1|\uparrow\downarrow) & P(1|\downarrow\downarrow) \\ P(0|\uparrow\uparrow) & P(0|\uparrow\downarrow) & P(0|\downarrow\downarrow) \end{pmatrix}. \tag{B.4}$$

The state probabilities can then be found as

$$\begin{pmatrix} P(\uparrow\uparrow) \\ P(\uparrow\downarrow) + P(\downarrow\uparrow) \\ P(\downarrow\downarrow) \end{pmatrix} = \mathbf{M_3^{-1}} \begin{pmatrix} P(2) \\ P(1) \\ P(0) \end{pmatrix}. \tag{B.5}$$

B.3 Probability estimation and errors

In the single ion case, the measurement is a Bernoulli trial with outcome $X \in \{0, 1\}$. For N measurements, the probability to measure $X = 1$, $P(1)$, can be estimated to be

$$P(1) = \frac{Z}{N} \pm z\sqrt{\frac{P(1)[1 - P(1)]}{N}}, \tag{B.6}$$

where $Z = \sum_{i=1}^{N} X_i$ is the number of measurements with outcome 1 and z is approximately equal to 1 for a confidence interval of one standard deviation. The values of $P(1)$ and $P(0) = 1 - P(1)$ are then transformed using Eq. B.2 to find the maximum likelihood estimators of $P(\uparrow)$ and $P(\downarrow)$. The positive and negative errors represented by the confidence interval in Eq. B.6 can then be transformed in the same way to give errors to the probabilities $P(\uparrow)$ and $P(\downarrow)$. For the two ion case, the measurement is a multinomial distribution with three possibilities. The probabilities $P(0)$, $P(1)$ and $P(2)$ as well as their confidence intervals can be estimated in the same way as the single ion case, and the estimate and error transformed to find the maximum likelihood estimators of $P(\downarrow\downarrow)$, $P(\downarrow\uparrow) + P(\uparrow\downarrow)$ and $P(\uparrow\uparrow)$ using Eq. B.5. This procedure is used for all ion fluorescence data measured in this thesis.

Appendix C

Magnus Expansion

The Magnus expansion allows the unitary evolution operator for a time-dependent Hamiltonian to be expanded and consequently approximated to a given order in the Hamiltonian. It is an alternative to time-dependent perturbation theory, and offers the advantage that it preserves the unitarity of the propagator. A detailed description of the Magnus expansion can be found in Ref. [92] and is summarised in the following. The unitary evolution operator for an arbitrary time-dependent Hamiltonian $H(t)$ between times t_0 and t can be written as

$$U(t) = \mathcal{T}\left(\exp\left[-\frac{i}{\hbar}\int_{t_0}^{t} dt' H(t')\right]\right), \tag{C.1}$$

where $\mathcal{T}$ is the time ordering operator, which is defined as

$$\mathcal{T}(H(t')H(t'')) = \begin{cases} H(t')H(t'') & \text{for} \quad t' > t'' \\ H(t'')H(t') & \text{for} \quad t' < t''. \end{cases} \tag{C.2}$$

The Magnus expansion is then given by

$$U(t) = \exp\left[-\frac{i}{\hbar}\int_{t_0}^{t} dt' H(t') - \frac{1}{2\hbar^2}\int_{t_0}^{t} dt' \int_{t_0}^{t'} dt''[H(t'), H(t'')] + ...\right], \tag{C.3}$$

where we have included terms up to second order. In this thesis, terms higher than second order are not considered. For the Mølmer-Sørensen Hamiltonian in Eq. 6.14, terms in the Magnus expansion that are third order or higher are equal to zero, and therefore the solution given by the terms shown in Eq. C.3 is exact. When additional Hamiltonian terms are added, as is the case for the dressed-state Mølmer-Sørensen gate discussed in this work, terms in the Magnus expansion may be non-zero to infinite order. The approximate solution is also complex to calculate due to the

multiple cross-terms that arise when calculating the commutators in the expansion terms that are second order or higher. Calculation of such terms that could affect the operation of the gate is the focus of Ref. [88]. This leads to multiple terms that either cause population to 'leak' out of the dressed state qubit subspace, or to cause Stark shifts of the qubit state energies. With the exception of the spin-spin coupling term derived in Sec. 4.4.2, these terms have a negligible effect on the gate for typical parameters. As shown in Sec. 6.3.2, the spin-spin coupling can be heavily suppressed with careful choice of dressing parameters.

Appendix D

Gate recipe

This appendix provides a 'recipe' for implementing the Mølmer-Sørensen gate with dressed-state qubits in a magnetic field gradient, with references to the relevant parts of the thesis. Before attempting the gate, the following experiments should be carried out:

- The magnetic field gradient should be maximised following the procedure outlined in Sec. 2.5.6 and measured as shown in Sec. 3.3.1. This allows the effective Lamb-Dicke parameter as a function of the mode frequency to be calculated as

$$\eta_k = \frac{1}{\sqrt{2}} \frac{\mu_B \partial_z B}{\hbar \nu_k} \sqrt{\frac{\hbar}{2m\nu_k}}, \tag{D.1}$$

  where k is the mode number (COM or stretch for two ions). The offset magnetic field should also be adjusted to ensure that the two $|0\rangle \leftrightarrow |0'\rangle$ clock transitions can be individually addressed as discussed in Sec. 4.3.3.

- The theoretical gate fidelity should be calculated following Sec. 6.3.2, taking into account all error sources. Parameters such as the trap frequency should be set to optimise the fidelity.

- State preparation and detection should be characterised and optimised to give the best fidelity for two ions, as discussed in Sec. 2.5.2.

- Dressed states should be implemented and it should be checked that Rabi oscillations between $|0'\rangle$ and $|D\rangle$ can be carried out. A scan such as that shown in Fig. 4.11 should be performed and it should be checked that the peaks corresponding to transitions between $|0'\rangle$ and $|D\rangle$ are well separated from other

transition frequencies. The T_1 and T_2 times should be measured and recorded following Sec. 4.3.4.

- Sideband cooling should be implemented using the mode selected for the gate following Sec. 5.4.3. In this work the mode was sideband cooled on the $|0\rangle \leftrightarrow |+1\rangle$ transition. The final $\bar{n}$ after sideband cooling should be measured as well as the heating rate.

- Pulse shaping of the gate fields should be set up if desired following Sec. 6.3.2.

After the above experiments have been carried out, the gate can be attempted. There are also a series of experiments required to set up the gate on a daily basis, which typically takes around 1 - 2 hours. These should be carried out in order according to the following:

1. Measure the trap frequency accurately using the method discussed in Sec. 2.5.1. We measure the frequency with an accuracy of approximately 20 Hz.

2. Take state detection histograms with a high number of repetitions (1000 - 5000) to be used for error normalisation.

3. Measure the resonant frequency of the $|0\rangle \leftrightarrow |\pm 1\rangle$ transitions in both ions for the dressing fields. The frequencies should be measured to an accuracy less than $0.01\Omega_{\mu\mathrm{w}}$, where $\Omega_{\mu\mathrm{w}}$ is the final Rabi frequency used for the dressing fields. We measure the frequencies to an accuracy of 0.2 kHz by turning the Rabi frequencies down to 4.2 kHz, and afterwards increase them back to the desired value $\Omega_{\mu\mathrm{w}}/2\pi \approx 21$ kHz.

4. Measure and set the dressing field Rabi frequencies by adjusting the corresponding powers of the microwave fields. The two Rabi frequencies in each ion should be equalised to within $0.005\Omega_{\mathrm{av}}$, where $\Omega_{\mathrm{av}} = (\Omega^{+}_{\mu\mathrm{w}} + \Omega^{-}_{\mu\mathrm{w}})/2$ is the average Rabi frequency of the two dressing fields in a single ion, and the difference between the Rabi frequencies between the two ions should be adjusted to suppress the spin-spin coupling error according to Eq. 6.44. Due to the non-linear response of microwave amplifiers, there can be a change in output power depending on the number of fields input. Therefore we set the power of each dressing field with all four fields turned on, but with three fields set to a frequency that is not resonant with any transitions in the ions.

5. Measure the resonant frequency of the $|0'\rangle \leftrightarrow |D\rangle$ transition via $|+1\rangle$ for each ion in turn by applying an RF field close to the $|0'\rangle \leftrightarrow |\pm 1\rangle$ transitions with the dressing fields turned on after preparing in $|0'\rangle$. We measure the frequency to an accuracy of 20 Hz by turning the Rabi frequency down to 0.25 Hz.

6. Measure and set the dressed state Rabi frequencies by adjusting the corresponding powers of the RF fields. For the sideband interactions, the condition $\eta\Omega_D \ll \Omega_{\mu\mathrm{w}}$ should be met, while for the carrier interaction, the equivalent condition is $\Omega_D \ll \Omega_{\mu\mathrm{w}}$. Therefore the high powers used for the gate fields cannot be measured with the dressed state carrier transition $|0'\rangle \leftrightarrow |D\rangle$. Instead, the Rabi frequency can be measured by setting the RF frequency to $(\omega_- + \omega_+)/2$ and performing a time scan with the dressing fields turned off. For $\Omega_{\mathrm{rf}} \gg \Delta_\pm$, where $\Delta_\pm = \omega_- - \omega_+$ is the second order Zeeman shift, oscillations between $|0'\rangle$ and $(|+1\rangle + e^{i\phi}|-1\rangle)/\sqrt{2}$ will be observed with frequency approximately equal to $\sqrt{2}\Omega_{\mathrm{rf}} = 2\Omega_D$. The Rabi frequencies are equalised to within 1 kHz.

7. Perform a Ramsey experiment as described in Sec. 4.3.4 with a reasonably long delay (we typically use 100 ms) and check that the contrast is as expected for the previously measured T_2 time. If it is not as expected, a mistake may have occured when setting the dressing field powers or detunings.

8. Using the measured values of ν_z, Ω_{rf} and $\Delta\omega_\pm$, calculate the Stark shifted carrier transition frequency using the formula (from Eq. 6.13)

$$\omega_{\mathrm{stark}} = \omega_+ + \frac{3\Omega_{\mathrm{rf}}^2 \Delta\omega_\pm}{4\nu_k^2}, \tag{D.2}$$

where ν_k is either the COM or stretch mode frequency. Next, calculate the required symmetric gate detuning for a single loop gate, given by

$$\delta_k = 2\eta_k\Omega_D, \tag{D.3}$$

and set the four RF fields detunings from the Stark shifted carrier frequency to $\pm\nu_k \pm \delta_k$.

Following these steps, a time scan of the gate pulse can be performed with sideband cooling turned on, and the measured populations can be compared with the theory curves in Eqs. 6.24. This allows any symmetric detuning error to be identified and corrected. If the populations do not match the theory for any symmetric detuning error, there may be some asymmetric detuning errors. The populations can

be compared with a numerical simulation which can take into account asymmetric detuning errors, although different combinations of the four asymmetric detuning types may give similar results. An alternative method is, once the symmetric detuning is thought to be approximately correct, to set the pulse time to $2t_g$, where $t_g = 2\pi/\delta_k$ is the single loop gate time, and to scan the four asymmetric detunings in turn to optimise the population to the predicted values $P_{DD} = 1$, $P_{0'0'} = P_{0'D} = P_{D0'} = 0$. Once the symmetric and asymmetric detunings have been optimised, the populations can be measured at t_g. Following this, a parity sequence can be performed where the gate is followed by a $\pi/2$ carrier pulse on each ion and the phases are varied. If the phase relationships between fields of different frequency are well defined, the carrier pulses can be performed at the unshifted carrier frequencies ω_+. This is the case for an arbitrary waveform generator (AWG) where the phases are set at the pulse start time and the multi-tone waveform is identical in every repeat of the experiment. However, if the phases are not well defined, the carrier pulses should be performed at the shifted carrier frequencies, as defined in Eq. D.2. This is the case for the DDS boards described in Sec. 2.4.3, which continuously output and are turned on and off using external switches, and therefore have no well defined phase relationship between fields of different frequency.